Method Optimization for Fourier Transform Infrared Imaging of Hippocampal Sections from Background and 3xTg (AD model) Mice

by:

Zahra Abyat

A Thesis submitted to the Faculty of Graduate Studies of
The University of Manitoba
in partial fulfillment of the requirement of the degree of
MASTER OF SCIENCE

Faculty of Engineering
Graduate Program of Biomedical Engineering
University of Manitoba
Winnipeg

Table of Contents

List of Tables

List of Figures

Abstract

The creatine/phosphocreatine system, regulated by Creatine kinase, plays a vital role in maintaining energy balance in the brain. Energy metabolism and the function of creatine kinase are known to be affected in Alzheimer's diseased brain and cells exposed to the amyloid peptide. In Alzheimer's disease (AD), the brain and cells that contain amyloid peptide deposits show dysfunctional energy metabolism and impaired creatine kinase activity. Creatine kinase is an important regulator of the creatine/phosphocreatine system that keeps the energy balance in these tissues. Therefore, we hypothesize that an enriched creatine diet provides neuroprotection in early, preclinical AD. Previous publications from our lab indicate increased creatine levels in brain tissue of AD mice. Given that hypo-metabolism likely precedes neurodegeneration and plaque formation, use of creatine to target hypo-metabolism could be a promising approach for altering or decelerating the onset of AD. Infrared spectrochemical imaging was used to examine hippocampal, cortical, and cerebellum tissue from 9-month-old mice expressing triple mutations of PSI_{M146V}, APP_{Swe} and tau_{P301L} transgenes, that progressively develop plaques and tangles. These transgenic mice were used to evaluate the effect of creatine diet (3% w/w) on the development of neurodegeneration. A total of 12 mice (n = 6 background & n = 6 transgenic) were used in this study. These animals were each divided into two groups (n = 3) to be fed regular or creatine-enriched diets. Creatine deposits suggestive of altered energetic status were detected by infrared spectrochemical imaging in all the animals. However, the creatine appearance and crystal morphology was affected by the freeze-thaw procedure involved in sample preparation. Long-term freeze storage also affected creatine crystallization as indicated by a series of freeze storage and freeze-thaw experiments. Creatine crystals can get washed away or migrate from tissue surface during the freeze-thaw procedure as creatine is highly soluble in water. Freeze-thaw experiments

confirmed that the sample preparation methods, i.e., methods of tissue acquisition, freezing, storage, and transport affect the formation of the crystals.

Acknowledgments

I would first like to thank my thesis advisor Professor Kathleen Gough of the Department of Chemistry at the University of Manitoba. Professor Gough was always supportive throughout my thesis research and writing. Her guidance and expert advice have been invaluable throughout all the stages of this work.

I would also like to express my gratitude to Professor Benedict C. Albensi from the Department of Pharmacology and Therapeutics at the University of Manitoba. I would like to thank Professor Albensi for extensive discussions and invaluable suggestions that have contributed to the development of this thesis.

I would also like to thank members of Dr. Albensi's lab; Claudia Perez, Wanda Snow for their support in data collection.

In memory of late Dr. Philip Hultin. Although no longer with us this thesis benefitted from his useful comments and advice as a member of my advisory committee.

I would like to thank members of our lab: Tanvy Vakil, Sarvesh K. Ramlochun, Negar Atefi Godwin Ajaezi, Nicole Pogorzelec, and Gorkem Bakir.

I would like to thank the Department of Chemistry and the Graduate Program of Biomedical Engineering at the University of Manitoba for providing all the facilities that permitted the completion of this thesis.

I would like to thank my boyfriend, Dr. Kirill Levin, for being so supportive while I was writing my thesis. Thanks for taking the time to help with some of the figures and all the constructive suggestions. Thanks for the emotional support and for being so understanding.

I am indebted to my family, my mother, and father for their continuous support and for providing me the opportunities to chase my dreams. This journey would not have been possible without them.

This thesis is dedicated to:

My parents for their endless love, support, and encouragement.

Chapter 1. Introduction to Thesis

1.1 FTIR Imaging of control and AD Mice

Alzheimer's disease (AD) is a neurodegenerative disease that causes 60-80 % of dementia cases (Alzheimer's Association, 2018). AD is characterized by amyloid plaques and neurofibrillary tangles that lead to neuron loss. Plaques are composed of amyloid Aβ peptides, whereas neurofibrillary tangles are composed of mis-folded tau proteins. The Aβ peptides are proteolytic derivatives of the transmembrane amyloid precursor protein while the tau is axonal microtubule-associated protein (Bloom, 2014). In AD, the progressive loss of neurons of the hippocampus damages the synapses that mediate memory and cognition and causes a decline in memory and cognitive function (Tanaka et al., 2008).

Mitochondrial dysfunction and energy depletion play a vital role in AD pathogenesis (Brewer and Wallimann, 2000). Because memory formation is an energy demanding task, certain types of memories such as spatial memory are dependent on efficient mitochondrial function. Given that creatine is a crucial regulator of the cell's energy status, creatine may be beneficial to learning and memory via altering brain bioenergetics. Creatine supplementation has been reported to be neuroprotective in several neurodegenerative diseases such as Parkinson's disease, Huntington's disease and multiple sclerosis (MS). However, the mechanism by which oral creatine administration benefits humans remains poorly understood. To broaden our knowledge of creatine supplementation benefits on neurodegeneration, we investigated the effects of creatine ingestion in transgenic (3xTg) Alzheimer's mice and compared it with background mice (C57BL/6 background mice that were used to generate the 3xTg mice). Creatine levels post-sacrifice were examined with Fourier-Transform infrared spectroscopy (FTIR) of brain tissue sections. It is hypothesized that infrared spectroscopy would provide us some knowledge of the molecular

mechanisms of creatine-induced enhancements. This is possible owing to our ability to use FTIR to assess the creatine levels in brain tissue at the molecular level.

1.2 FTIR Spectroscopy

In infrared (IR) spectroscopy, IR radiation is passed through a sample, where some of the light is absorbed while the remaining light is transmitted. The absorbed energy excites the vibrations of molecules resulting in a quantum mechanical transition to a higher energy level. An absorbance spectrum is generated based on the energy difference of transitions between vibrational energy levels. Every molecule has a unique spectrum or fingerprint since different molecular structures produce different infrared spectra. Therefore, infrared spectroscopy can be used for qualitative identification of any material. Also, a quantitative assessment is possible by measuring the magnitude (height, band area) of the peaks in the spectrum. In fact, with modern software algorithms, IR has become an excellent quantitative analysis tool (Griffiths, 2007).

FTIR spectroscopy is useful technique for detection of biochemical changes caused by pathology even at earlier stages of the disease (Correia et al., 2016). FTIR is a valuable tool for molecular fingerprinting due to its simplicity and the capability to analyze several biomolecules simultaneously. FTIR spectroscopy is a highly sensitive and reproducible analytical technique for identification and quantification of structural moieties of biomolecules based on their IR absorption spectra. This could enable the identification of biochemical pathway alterations linked to neurodegenerative diseases (Correia et al., 2016).

There are various sources of IR light including globar, synchrotron and quantum cascade lasers (QCLs). An FTIR instrument can be operated either in transmission or transflectance sampling mode. FTIR spectroscopy is explained in more detail in chapter 3 of this thesis. An FTIR

microscope can be used to generate image contrast based on the intrinsic biochemical composition of the tissue. FTIR microscopy does not require pre-analytical chemical modification, whereas other techniques, for example immunohistochemistry, use fluorescence and dyes for sample visualization that may interfere with sample chemical composition (Baker et al., 2014). On the other hand, vibrational spectroscopy monitors intrinsic spectroscopic properties of a sample without affecting its composition.

FTIR images are comparable to results from histological staining protocols and can be analyzed by non-spectroscopists (Baker et al., 2014). Thus it is suitable for a clinical environment. FTIR spectroscopy allows disease diagnosis without compromising the molecular composition of the tissue. Also, FTIR spectroscopy is cost-effective, fast and can be operated in an automated fashion. FTIR imaging provides spatially resolved structural and compositional information which can be used to obtain diagnostic markers for diseases (Baker et al., 2014).

FTIR imaging has some limitations and special considerations. The IR diffraction limit is about 1 μm at best. Advantages and associated limitations of the FTIR technique are described in chapter 3. Key among these are sample preparation and storage which become an important factor in this thesis as explained in chapters 4 and 5.

1.3 Problem statement

There has been an enormous effort on the development of neuroprotective agents for the reduction and delay of Alzheimer's disease (Chiang and Koo, 2014). Targeting of metabolic mechanisms has emerged as an important technique for preventing or slowing the onset of AD. Hypo-metabolism occurs very early in the disease process and before the hallmarks of the AD appear (Costantini et al., 2008). We hypothesize that a creatine-enriched diet may have neuroprotective

effects in Alzheimer's disease through creatine-induced mitochondrial energy maintenance. While the exact effect of amyloid beta (Aβ) on neurons continues to be a research area, it is hypothesized that mitochondria are involved in AD through accelerating neuron apoptosis. Studies suggest that Aβ can cause neuron apoptosis directly by increasing oxidative stress and reducing energy availability (Sultana & Butterfield, 2008). It has been hypothesized that a creatine-enriched diet could delay the progress of MS and neuron apoptosis by lowering the extent of energy depletion in these cells (Chamberlain et al., 2017).

In this thesis the cell bioenergetics is investigated by evaluating creatine levels as a marker of impaired energy metabolism in transgenic mouse (3xTg) model brains. The creatine levels in transgenic mouse brains are compared with background mouse brains. Creatine levels are estimated by FTIR imaging of *ex vivo*, snap-frozen, untreated brain tissue sections extracted from hippocampus and cortex of transgenic mice model. We hypothesize that the high spatial resolution possible with FTIR i.e. 5.5 μm may provide a measurement of creatine levels that is reflective of the *in vivo* condition.

1.4 Objective of research

Given that AD is a multifactorial disease, a multi-analyte profiling approach of brain tissue may provide a better understanding of the mechanism and biological signatures of disease, in order to permit the development of therapeutics for preventing or at least slowing the progress of AD. FTIR spectroscopy serves as a useful and straightforward metabolic fingerprinting tool.

Originally the objective of this study was to identify neurodegeneration in Alzheimer's disease in transgenic mice. FTIR imaging was used to assess the distribution of a disease marker for altered energy metabolism, i.e., creatine. The effect of a potential therapeutic, i.e., creatine

ingestion, on this disease marker was assessed to establish whether a creatine enriched diet may be used as a therapeutic for the prevention or delay of disease pathology in AD. Infrared spectra of brain tissue were analyzed to relate the disease pathology to markers such as creatine deposition and localization in the brains of AD mice and background mice. The mouse models used in this research are described in chapter 3.

During the course of this study, several inconsistencies in creatine crystal morphology and creatine distribution were observed. The creatine distribution was not consistent in brain tissue sections from the same animal or even tissue sections that were mounted on the same imaging slide. It was challenging to obtain spectra of creatine molecules consistently since the creatine spectral biomarker was found to be dependent on sample preparation methods. These inconsistencies lead to another objective i.e. methods development. Consequently, the exploratory pilot study was re-directed towards optimizing a sample preparation methodology that would yield consistent and reproducible creatine spectra that are truly reflective of the *in vivo* state. This is presented in chapter 5. This exploratory pilot study is intended to contribute to the future development of a working methodology for sample preparation that would improve multivariate brain tissue analysis with FTIR spectroscopy.

Chapter 2: Characteristics of AD Pathology

2.0 Epidemiology of Alzheimer's Disease

Dementia is a syndrome that is caused by neurodegenerative diseases that impair memory, thinking and ability to perform daily tasks. Dementia is not normal aging and is the leading cause of disability and dependence in the elderly (AD Association, 2015). The population of people living with dementia worldwide is estimated at 47 million and is projected to triple by 2050 (WHO, 2017).

Alzheimer's disease is the most common cause of dementia and accounts for 60-70 % of dementia cases (AD Association, 2015). It is estimated that 5.7 million Americans live with AD dementia. In 2015, AD was the sixth leading cause of death in people of age ≥ 65 years in the United States. In America, total dementia healthcare cost for people ≥ 65 years is estimated to be 277 billion US$ in 2018 (AD Association report, 2018). In Canada, 564,000 Canadians are currently living with dementia, and this number is projected to rise to 937,000 in the next 15 years. The annual caregiving cost for dementia in Canada is estimated to be $ 10.4 billion (Canada AD Association website, 2018). Given the global prevalence of AD, an enormous amount of research has been conducted to improve the understanding of the disease. This study aims to evaluate the disease at a molecular level attempting to potentially improve the disease therapeutic strategies.

2.1 Pathology of AD

AD is characterized by a progressive loss of brain cells that typically presents as a progressive loss of short-term memory. Neuronal loss and brain atrophy begin decades before clinical symptoms emerge. Brain atrophy results in disconnection in cortical areas of the brain affected by AD resulting in a progressive decline in cognitive function and disability. In the mild to moderate AD, atrophy extends to the cerebral cortex causing eminent memory loss along with personality and

mood changes. In late onset AD, cortex atrophy affects areas that control speech, reasoning, sensory processing, and conscious thought (Frisoni et al., 2010).

2.2 Hallmarks of AD

AD is characterized by several neuropathological hallmarks including: aggregated Aβ plaques derived from amyloid precursor proteins (APP), neurofibrillary tangles (NFT), glial responses, inflammation, and neuronal degeneration. Aβ plaques and NFTs develop with normal aging and a variety of neurodegenerative diseases (Serrano-Pozo et al*.,* 2011). In AD, these lesions are in brain regions that correspond to clinical symptoms. However, the presence of plaques and tangles is not enough to distinguish demented from non-demented individuals. Instead, it is the spatiotemporal pattern of these lesions that define AD (Jack, C. R et al., 2011). Autopsy studies have correlated neuropathology to cognitive impairments (Nelson et al., 2009). However, Aβ plaque pathology is not always associated with cognitive decline (Jack, C. R et al., 2009).

2.3 Genetics of AD

AD is classified based on the age of onset. The early onset form, sometimes referred to as pre-senile AD, occurs before the age of 65 years and is a familial type (FAD), whereas the late-onset AD occurs after the age of 65 years and is frequently sporadic (Rocchi et al., 2009). Familial AD is an early onset AD caused by inherited genetic mutations within families. These mutations are explained in the following section (2.3.1). Familial AD accounts for 5 % of total AD cases while the remaining 95 % are mostly sporadic late onset cases (Rocchi et al., 2009).

2.3.1 Familial AD

Familial AD (FAD) is commonly caused by mutations in amyloid precursor protein (APP) in chromosome 21, presenilin-1 (PS1) gene on chromosome 14 and presenilin-2 (PS2) gene on chromosome 1 (Rocchi et al., 2009). Senile plaques (SPs) and (NFTs) are considered the signature pathological markers of AD (Goate, 1991 and Sherrington, 1995). APP is a transmembrane protein that is involved in neuronal plasticity. Amyloid metabolism leads to Aβ formation; the main component of senile plaques (Turner, 2003 & Selkoe,1994).

Aβ is a 38-43 amino acid proteolytic fragment of APP that is generated throughout the lifecycle of mammalian cells. Normally, APP is cleaved by α-secretase and β-secretase and subsequently by γ-secretase. The α-secretase cleavage is non-amyloidogenic, whereas the β-secretase cleavage is amyloidogenic. There are various proteolytic derivatives of APP; however, the largest known APP contains 770 amino acids. Figure 2.1 A shows a single transmembrane protein with 700-770 amino acids. APP undergoes cleavage by either α-secretase (cleavage after residue 687, Figure 2.1.B) or by β-secretase (cleavage after residue 671, Figure 2.1C) generating membrane-associated C-terminal fragments, i.e., the C83 (APP-CTF α) or C99 (APP-CTF β) respectively. These C83 and C99 fragments then become substrates for γ-secretase cleavage. The γ-secretase cleavage results in the formation of the p3 peptide from APP-CTF α fragment and Aβ peptide from APP-CTF β fragment **(**Selkoe, 2004). The γ-cleavage with APP-CTF β fragment produces both Aβ40 and Aβ42; however, Aβ42 is more toxic (Suzhen, 2012). The longer Aβ42 amino acids are hydrophobic and tend to aggregate into plaques. These plaques may aggregate and extend throughout the limbic and association cortices (Selkoe, 2004). Various models are attempting to explain the plaque formation and AD pathology. Aβ plaques are believed to be involved in the development and progress of AD; however, the mechanism is not understood. APP

and Aβ peptides are believed to be involved in a chain of events such as disturbed calcium homeostasis, generation of free radicals, apoptosis, activation of microglia and astrocytes, inflammation, hyperphosphorylation of the microtubule-associated protein, i.e., tau and its polymerization into neurofibrillary tangles and other toxic events.

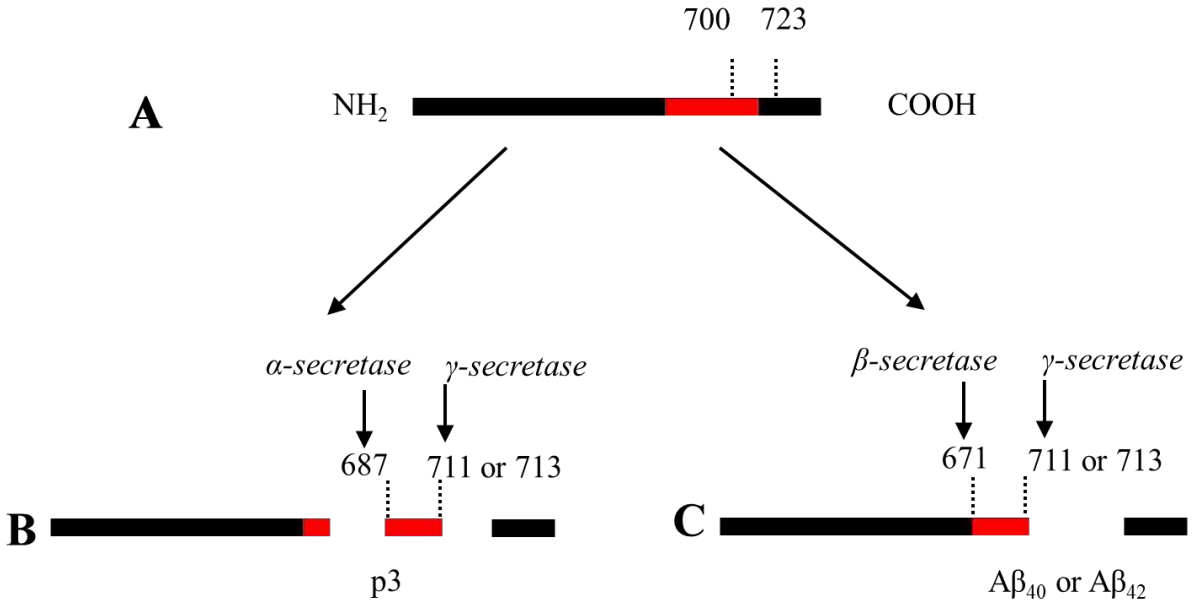

Figure 2.1 Schematic diagram of APP and its principal proteolytic derivatives. A) Single transmembrane protein with 700-770 amino acids. B) A by-product of normal processing of APP (APP-α). C) A by-product of abnormal processing APP, β-secretase cleavage producing: Aβ40 and Aβ42. This figure was produced based on available literature (Selkoe, 2004)
.

2.3.2 Sporadic AD

Sporadic AD has a complex etiology, and thus genetic factors alone are not indicative of disease development. Genetic factors combined with environmental risk factors can give rise to AD pathology. Risk factors include diet, cardiovascular diseases, mild cognitive impairments (MCI), age and head trauma (Liu, 2013). The ε4 allele of apolipoprotein E (APOE) is one of the major genetic risk factors for the sporadic AD. APOE is a multifunctional protein which is synthesized

and secreted by astrocytes, microglia, oligodendrocytes, and ependymal layer cells. APOE has several functions such as neuron repair, maintaining synaptic connections and toxin scavenging. The APOE gene encodes three alleles: APOE2, APOE3, and APOE4 (Xu et al., 2000). Prevailing theories suggest that APOE genes influence AD pathogenesis mainly by affecting Aβ metabolism that triggers a set of downstream events that ultimately causes AD. It is not clear whether the APOE4 allele influences AD pathogenesis by the gain of toxic function or loss of protective role, or by both. APOE regulates not only the clearance but also Aβ aggregation (Holtzman, 2004).

2.4 Pathogenesis of AD

Despite the countless investigations, understanding AD pathogenesis has proven challenging. Two of the main theories, considered the heart of AD pathogenesis are the amyloid cascade hypothesis and the mitochondrial cascade hypothesis. The amyloid cascade hypothesis assumes that AD is always primary amyloidosis, while the mitochondrial cascade hypothesis that implies most AD cases are secondary amyloidosis (Xu et al., 2000).

2.4.1 Amyloid Cascade Hypothesis (ACH)

The amyloid cascade hypothesis states that Aβ formation is the first event in amyloidosis, which may lead to alteration in phosphorylation of tau proteins and their microtubule binding capacity, leading to neurofibrillary tangle formation, cell death and ultimately dementia (Armstrong, 2011). The ACH proposes that these mutations alter APP processing and lead to an increase in Aβ42 and Aβ40. Excessive production of Aβ peptides result in plaque formation (aggregated Aβ) that induces neurodegeneration, and this neuronal loss results in dementia. The ACH assumes that Aβ

deposition is the first pathological event, which leads to NFTs, cell apoptosis and eventually dementia (Holtzman, 2004).

2.4.2 Mitochondrial Cascade Hypothesis

The mitochondrial cascade hypothesis suggests that non-Mendelian genetic factors account for the non-autosomal dominant AD (late onset AD). Based on this theory, Aβ is a marker of brain dementia and not the sole cause of AD. This hypothesis proposes that mitochondrial dysfunction in AD brain leads to Aβ plaque formation and tau phosphorylation. (Xu et al., 2000 and Kim et al*.,* 2009).

2.5 Mitochondrial Creatine Kinase and AD

The brain has a high energy demand, for which creatine is an essential regulator. Neurons consume a high amount of energy for various functions, such as the establishment of ionic gradients, neurotransmitter exocytosis, and synaptic function. AD brains are characterized by hypo-metabolism. The AD brains experience reduction in cerebral glucose metabolism decades before the clinical pathology (Wolozin, 2004). Creatine is an important molecule that is associated with energy production (Harris *et al*., 2003).

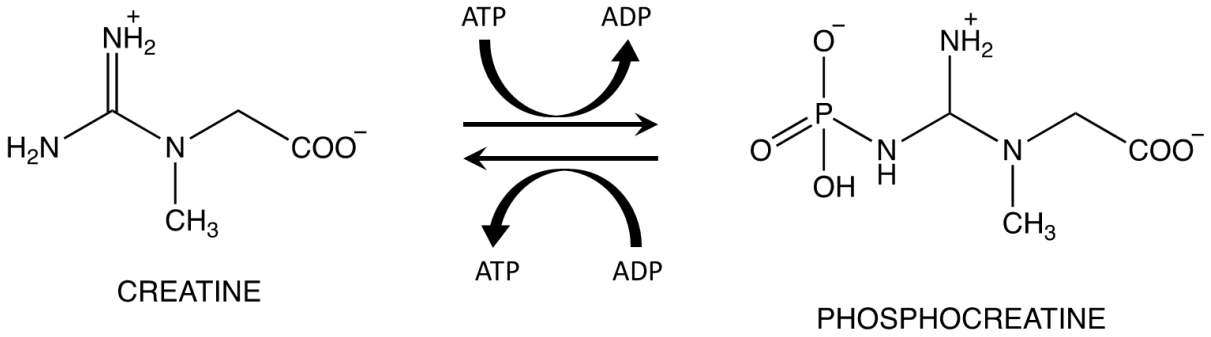

Figure 2.2. Phospho-creatine ATP interaction.

Through the mitochondrial creatine kinase (CK) enzyme, phosphocreatine acts as an energy shuttle connecting the sites of ATP production and utilization. The creatine kinase enzyme transfers a phosphate group to ADP, thus forming ATP. The Phosphocreatine/CK acts as a rapidly mobilizable energy reserve that recycles adenosine triphosphate. The mitochondrial CK generates ATP from phosphocreatine and ADP immediately following an intense muscular or neuronal effort. In this way, a constant ATP/ADP ratio is maintained even during high workloads and ischemic conditions (Otellin et al., 2003).

ATP synthesis from phosphocreatine is 12 times faster than oxidative phosphorylation (Harris et al. 2003 and Wallimann et al., 1992). This is why athletes and bodybuilders use creatine monohydrate to support short duration high-intensity exercises. Phosphocreatine is particularly vital in tissues such as muscles and brain that have fluctuating energy demands. The spontaneous conversion of ADP to ATP by phosphocreatine requires continuous replacement of creatine, which occurs by endogenous synthesis and diet. Dietary sources of creatine are restricted to animal sources of food, i.e. meat (Hersh and Rodgers, 2008).

Creatine is endogenously synthesized by a two-step mechanism that involves: L-arginine glycine amidinotransferase (AGAT) and N-guanidinoacetate methyltransferase (GAMT) as per the reaction below (Hersh and Rodgers, 2008):

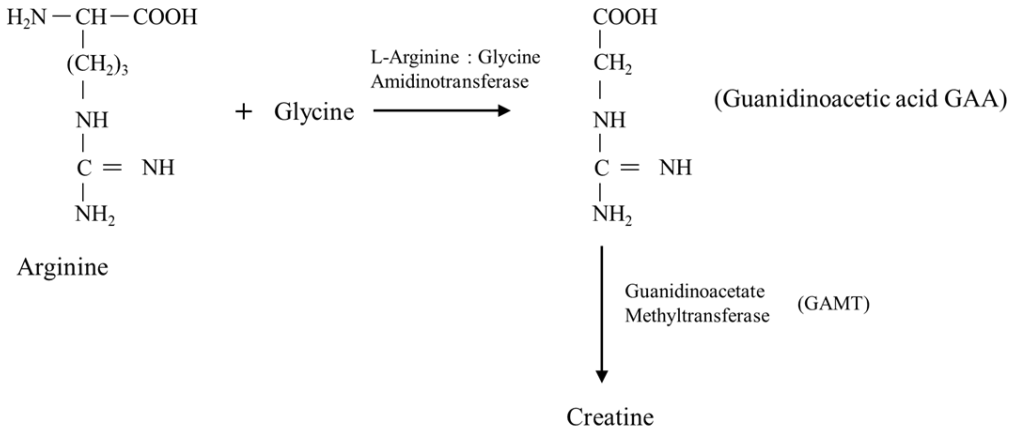

Figure 2.3. Creatine synthesis through AGAT & GAMT (Hersh and Rodgers, 2008).

2.5.1 Creatine Kinase, a promoter of cell survival

There have been several studies investigating the neurobehavioral consequences of creatine supplementation in humans and mouse models, reporting on possible cognitive enhancement.

Chamberlain et al. reported that creatine enhances mitochondrial-mediated oligodendrocyte survival post a demyelinating injury, which is typically experienced in MS. Chronic demyelination occurs in MS especially in the progressive phase of MS where there is a continuous accumulation of clinical disability (Chamberlain et al., 2017). The prognosis of secondary progressive MS is worse compared to relapsing-remitting MS. Most of the available therapies focus on the suppression of inflammation, which is helpful in relapse-remitting MS but not progressive MS. Reduction of inflammation decreases the severity of relapse-remitting MS but

does not overcome the transition to secondary progressive MS. It has been reported that 80 % of patients with relapsing-remitting MS tend to develop secondary progressive MS (My-MS website, 2018). In relapsing-remitting MS, oligodendrocytes can re-myelinate due to the availability of oligodendrocyte precursor cells, unlike progressive MS where re-myelination fails. Creatine was administered both *in vivo* (spinal cord demyelination surgery in mice) and *in vitro* (oligodendrocyte lineage cells) to investigate the role of creatine in neuro-protection, possibly by promoting oligodendrocyte viability (Chamberlain et al., 2017). The study reported that creatine treated oligodendrocyte lineage cells had increased mitochondrial membrane potential and oligodendrocyte mitochondrial ATP production compared with controls (*in vitro)*. This result was further supported by their *in vivo* studies of a mouse model deficient in the creatine-synthesizing enzyme guanidinoacetate-methyltransferase (GAMT). Creatine injection in GAMT-deficient mice with a demyelinating lesion reduced the apoptosis of oligodendrocytes. Thus, creatine has been shown to promote oligodendrocyte viability during CNS re-myelination, suggesting the therapeutic potential of creatine in promoting cell survival and neuroprotection in MS (Chamberlain et al., 2017).

In another study, creatine was orally supplemented to vegetarian subjects who lacked a dietary creatine intake, in order to investigate the role of creatine in brain function (Rae et al., 2013). The study involved 45 young adult vegetarian subjects in a double-blind, placebo-controlled, cross-over design. The vegetarian subjects in this study were on a five-gram daily creatine diet for six weeks. The intelligence and working memory of these subjects were assessed post creatine dietary enrichment. Creatine ingestion improved both working memory and

intelligence scores of these vegetarian subjects, suggesting that creatine is involved in brain plasticity (Rae et al., 2013).

Another study reported the beneficial effects of creatine supplementation against traumatic brain injury (Sullivan et al., 2000). A creatine diet was selected for this study because it is a commonly available food supplement and is used by athletes, regardless of their activity level, to boost strength and performance. The effect of creatine ingestion on brain tissue damage was examined after inducing an experimental traumatic brain injury (TBI) on mouse and rat models. Rats and mice on a four-week creatine-enriched diet experienced a reduction in cortical damage by as much as 50% in rats and 36% in mice. This neuroprotection effect is linked to creatine-induced maintenance of mitochondrial energy. Creatine ingestion tends to compensate for the reduction in cellular ATP levels caused by traumatic injury. They proposed that a creatine-enriched diet stabilizes the CK that is associated with mitochondrial adenine nucleotide translocator (ANT; the mitochondrial ADP/ATP carrier) which in turn blocks the calcium-induced opening of the mitochondrial permeability transition pore (MPTP) after TBI. This neuroprotection mechanism was demonstrated by the increase in mitochondrial energy, a decrease in reactive oxygen species and calcium, and maintenance of ATP levels. Thus, creatine ingestion is advantageous particularly to athletes who are at a higher risk of experiencing head injuries. Creatine is a food supplement consumed by 75 % of professional sports players. Creatine is used by athletes to ensure a phosphocreatine pool that can act as a phosphate reservoir, to regenerate ATP and thereby decrease muscular fatigue and enhance recovery following a high-intensity exercise. Apart from improving skeletal muscle function, creatine serves as a temporal buffer for various cells such as neurons that have a fluctuating energy demand (Sullivan et al., 2000).

Oral creatine supplementation has been studied in Huntington's (HD) disease where it is reported to slow down the development of neurodegeneration (Bender et al., 2005). Perturbation of the glutamate-glutamine (Glu-Gln) cycle is involved in the pathogenesis of Huntington's disease. Glu is the primary excitatory neurotransmitter released into the synaptic cleft, which is a space between two neurons that allows for information to be relayed between neurons via a chemical signal. It is critical that Glu levels are always maintained at a low level to reduce excitotoxicity (Bender et al., 2005). This is accomplished by either Glu transporter enzymes or the Gln synthetase, a glutaminase enzyme, which is ATP dependent. 60-80% of the energy supply to the brain is consumed by Glu neurotransmission. The effect of creatine supplementation was examined in 20 Huntington's Disease (HD) patients. Brain metabolite levels were used as markers of HD, wherein proton magnetic resonance spectroscopy (H-MRS) was used for evaluating the effect of a creatine diet. H-MRS showed a 15.6 % reduction in Glx, i.e. (combined Glu and Gln) and 7.8 % reduction in Glu after creatine enrichment. This reduction in cortical Glx and Glu was due to the enhanced energy-dependent conversion of Glu to Gln via Glu-Gln cycle. Thus, creatine has therapeutic potential in HD possibly through overcoming Glu-mediated excitotoxicity (Bender et al., 2005).

Creatine supplementation is also beneficial in the treatment of amyotrophic lateral sclerosis (ALS) in mice with the superoxide dismutase 1 (SOD1) mutation (Klivenyi et al., 1999). ALS is a motor neuron disease that is characterized by degeneration and death of motor neurons in the spinal cord, brainstem, and motor cortex. Mice with the G93A human SOD1 mutation have altered electron transport enzymes and exhibit loss of mitochondrial membrane potential. Thus, they are a mouse model that represents a type of mitochondrial dysfunction pathology. These transgenic mice develop progressive paralysis and motor neuron loss. Transgenic SOD1 mice, supplemented

with 1% or 2% creatine diet, exhibited improved motor performance and extended survival. This improvement was a function of creatine dosage. Creatine administration also protected 4-month old SOD1 mice from loss of both motor neurons and substantia nigra neurons. Creatine ingestion protected SOD1 mice from oxidative damage as evidenced by the lower level of 3-nitrotyrosine, which is a marker of peroxynitrite-mediated nitration in motor neurons. At four months of age, mice on the 1 % creatine did not experience a rise in spinal cord 3-nitrotyrosine levels compared to mice fed an un-supplemented diet (Klivenyi et al., 1999).

Chapter 3. FTIR Spectroscopy of Background (C57BL/6) & Transgenic (3xTg) Mice

3.1 Infrared Spectroscopy

3.1.1 Working Principles of Infrared Spectroscopy

Various spectroscopy techniques provide information about architecture, symmetry, electronic state energies, vibrational and rotational states of the molecules. The spectroscopic methods most frequently used in biomedicine are infrared, NMR, Raman, UV/Vis circular dichroism and fluorescence spectroscopy (Larkin, 2011). Infrared (IR) spectroscopy has been used to characterize various types of samples since the 1940s. IR vibrational spectroscopy uses the light of the mid-infrared region of the electromagnetic spectrum, wavelengths range from 4000 to 400 cm^{-1} or 2.5 to 25 × 10^{-6} m as presented in Figure 3.1.

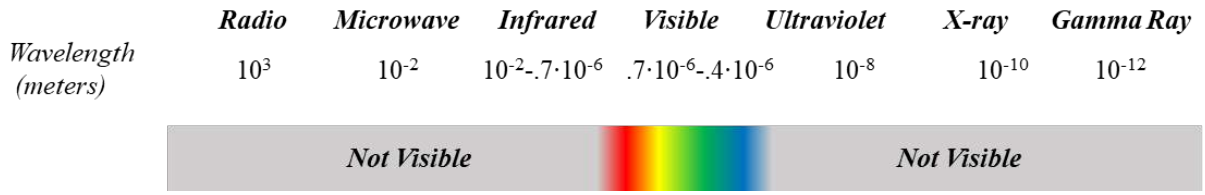

Figure 3.1. Schematic of the electromagnetic spectrum, showing energies of the mid IR region (Z.Abyat).

The infrared absorption process can be described by considering two atoms connected by a spring-like a bond. The bond can stretch and contract, changing the distance between the atoms and the potential energy of the molecule. The stretching and contraction of a diatomic molecule can be modeled by the harmonic oscillations of a spring.

The classical vibrational frequency of a diatomic molecule is

$$\nu = \frac{1}{2\pi}\sqrt{k / \mu} \qquad \text{..... (3.1)}$$

where k is the force constant related to spring stiffness or strength of the bond and μ is the reduced mass (Larkin, 2011).

$$\frac{1}{\mu} = \frac{1}{m1} + \frac{1}{m2} \quad \text{..... (3.2)}$$

where m_1 and m_2 are atomic masses of individual atoms. The vibrational energy levels for diatomic molecules are calculated using the harmonic oscillator model. A harmonic oscillator obeys Hooke's law that assumes that a system displaced from equilibrium responds with a restoring force whose magnitude is proportional to the displacement (Larkin, 2011). When a molecule absorbs infrared light, it can transit from one energy level to another; which is is probed by spectroscopy. As per Figure 3.2, a plot of the energy of a diatomic molecule as a function of the distance is a parabola that is symmetric about the equilibrium internuclear distance.

In the case of the harmonic potential, these energy states are equidistant and have energy levels E given by:

$$E_i = \left(v + \frac{1}{2}\right) h \upsilon_i \qquad \text{where } v = 0, 1, 2\text{.....(3.3)}$$

Here υ_i is the fundamental frequency of a mode and v is the vibrational quantum number (Larkin, 2011). The harmonic oscillator is a good approximation for energy levels of molecules in the ground state, i.e. the lowest energy level. As quantum number increases, the molecular vibrations become anharmonic. In the harmonic oscillator model only fundamental transitions are allowed, i.e., only transitions to adjacent energy level ($\Delta v = \pm 1$) while in the anharmonic oscillator model overtones($\Delta v \geq \pm 2$), and combination (multiples of different fundamental modes) bands can occur (R. Dyer,1965).

Infrared light is used to excite vibrations in molecules. The amount of infrared light absorbed to induce these vibrations provides information about the identity and the structure of the molecules (R. Dyer, 1965, Chapter 2). This information is obtained from the infrared absorption spectrum of the examined molecules. The spectrum is a plot of the amount of energy absorbed by the sample versus the wavelength of the incident radiation. Infrared absorption peaks can be reported in either wavenumbers or wavelengths. The positions and the relative strengths of these absorption peaks provide information about the structure and composition of the molecule (R. Dyer,1965, Chapter 2).

When infrared radiation is absorbed, a quantum-mechanical transition occurs, and the molecule transitions from a lower energy level to a higher energy level. The quantity of energy absorbed is equivalent to the difference in energy between the two vibrational energy levels (equation 3.4). Photons of specific energy may be absorbed (or emitted) by a molecule (Lambert et al., 1987, Chapter 6).

$$\Delta E = E_2 - E_1 = hc/\lambda = h\nu \ldots\ldots\ldots\ldots\ldots\ldots\ldots\ldots (3.4)$$

$$\nu = c/\lambda \ldots\ldots\ldots\ldots\ldots\ldots\ldots\ldots\ldots\ldots\ldots\ldots\ldots\ldots (3.5)$$

where h is Planck's constant (6.63×10^{-34} Js), ν is the frequency of light, c is the speed of light in vacuum and λ is the wavelength.

For infrared active molecules, the transitions from the ground state to a first excited state, i.e., fundamental transitions, are the most probable ones. Transitions to higher energy levels, i.e. non-fundamental transitions (overtones and combination), may occur but are less likely.

Combination bands are possible, if the incident infrared light excites more than one vibrational mode simultaneously. The vibrational modes are well described with the harmonic and anharmonic oscillator model derived from simple mechanics (R. Dyer,1965, Chapter 2). Figure 3.2 shows the potential energy diagram for the harmonic and anharmonic oscillator.

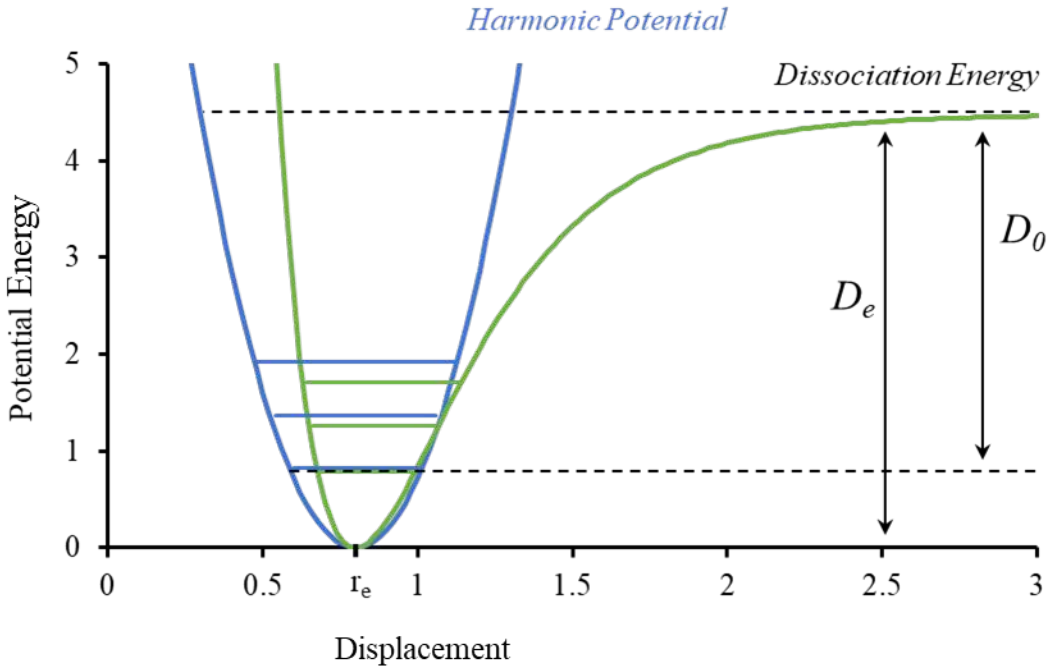

Figure 3.2. Potential energy curve for harmonic & anharmonic oscillator model.
Note: The curves were generated in Excel using D_e = 4.48eV and D_0 = 3.66 eV, where v is a transition from v=0 (vibrational ground state) to v= 1 (1^{st} vibrational energy level), D_0 is the energy required for dissociation and D_e is the theoretical energy required to break the bond.

IR information is obtained through normal or fundamental modes as well as the combinations and overtones of the molecular vibrations (Lambert et al., 1987, Chapter 6). A normal mode of vibration is one in which every atom exhibits a simple harmonic oscillation about its equilibrium position. These normal mode bands arise from fundamental molecular vibrations

such as symmetric and anti-symmetric stretching, bending, scissoring, twisting, wagging, rocking and deformation. The various vibrations require distinct, quantized energies ($h\nu$) at frequency ν. When infrared light is incident on a molecule, a photon with frequency that matches a natural vibrational frequency of the molecule can be absorbed (Lambert et al., 1987, Chapter 6). The number of fundamental vibrational modes is dependent on the internal degrees of freedom, which are 3N-6 and 3N-5 for vibrations of non-linear and linear molecules, respectively; N is the number of atoms in a molecule. Only the vibrations that change the dipole moment of the molecule result in the absorption of infrared energy. Thus, small symmetrical molecules will display simpler spectra. For example, the C=C stretch vibrations of ethylene and the symmetric C-H stretches of methane do not result in absorption bands in the infrared spectrum.

3.2 Dispersive Spectrometers

Dispersive spectrometers are sometimes referred to as grating or scanning spectrometers. In dispersive instruments, the infrared radiation from a broadband source is directed to a prism or diffraction grating (Larkin, 2011). The source, usually a globar or black body radiator made of a high resistance substance, emits thermal radiation when an electric current is applied. The slit separates the various wavelengths of light in the spectral range and directs each wavelength individually onto the detector. The detector measures the amount of radiation absorbed at each wavelength. Most dispersive spectrometers are double beam instruments that measure the energy difference between a sample and a reference. The detector then generates an electronic ratio of the sample signal versus a reference signal for each frequency. The detector measurements are sequential; one spectral frequency is measured at a time from the sample and the reference. The frequencies in dispersive instruments are adjusted by rotating the grating. The dispersive

instrumentation is inefficient and has been replaced by interferometer instrumentation, i.e., FTIR spectrometers, owing to numerous performance advantages discussed in section 3.3.1.

3.3 Michelson Interferometer

A spectrometer involves a light source, an optical system, a detector, and a sample holder. Infrared light from the source hits the detector which measures the intensity of the emergent beam (Griffiths,1975). The optical system for FTIR spectrometer is based on the Michelson interferometer. The Michelson interferometer is a device that splits the radiation beam into two paths and then recombines the two paths once a path difference has been established. This leads to interference between the two beams. The detector measures the variation in the intensity of the beam emerging from the interferometer as a function of path difference (Chapter 2, Griffiths,1975).

Figure 3.3 depicts a Michelson interferometer for FTIR. The interferometer includes two mutually perpendicular plane mirrors, one of which is a movable mirror. The beam splitter splits the light to the stationary mirror and the movable mirror. A beam from the source is partially reflected to the fixed mirror at point F (Figure 3.3A) or is partially transmitted to the movable mirror at point M (Figure 3.3B). The beams returning to the beam splitter then recombine where the recombined beam intensity ranges from fully constructive to fully destructive, for a single wavelength. Half of the recombined light will be directed to the detector via the sample while the other half will be lost. Only the output beam traveling to the detector is of interest in spectroscopy. The light intensity measured by the detector is a function of displacement of the moving mirror. The recombined light generates an interference pattern as per Figure 3.3C, i.e. a cosine wave, if a monochromatic light source is used. When a broad range of infrared light is passed through the

interferometer, the signal at the detector is a superposition of many cosine waves at many frequencies (Figure 3.3D). This creates a signal pattern that is called an interferogram. The interferogram is converted by a Fourier transform (FT) operation to a spectrum in units of energy, hence the name Fourier transform spectroscopy. The spectra can be displayed to show either absorbance or transmittance of each infrared wavelength at it passes through the sample (Chapter 2, Griffiths, 1975).

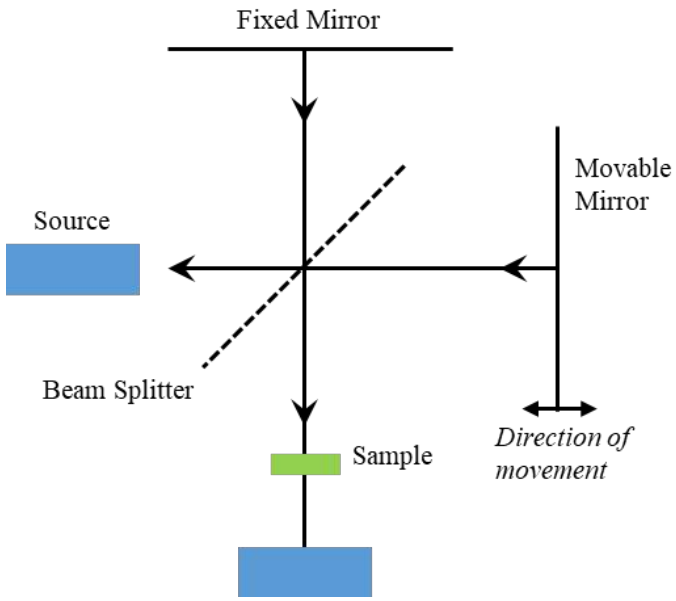

Figure 3.3. Schematic of the main parts of the Michelson interferometer

3.3A. Output beam from the fixed mirror

Arrows show path of light reflected from the fixed mirror

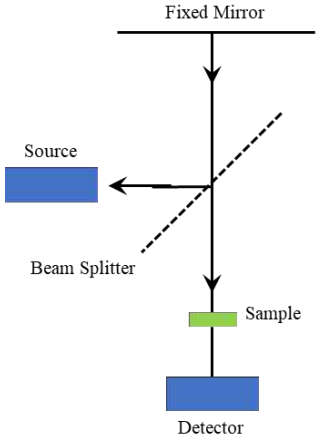

3.3B. Output beam from the moving mirror

Arrows show path of light reflected from the moving mirror

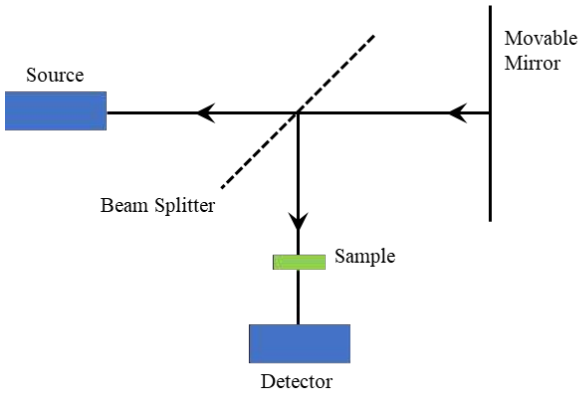

3.3C. Single frequency interferogram

A plot of the signal recorded by the detector versus displacement for one wavelength. This signal is a cosine wave.

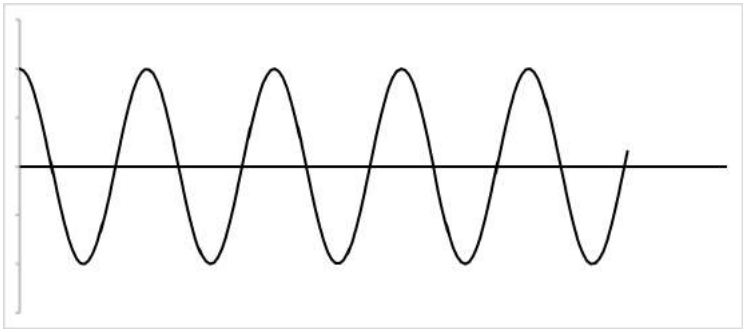

3.3D. Multiple frequency interferogram

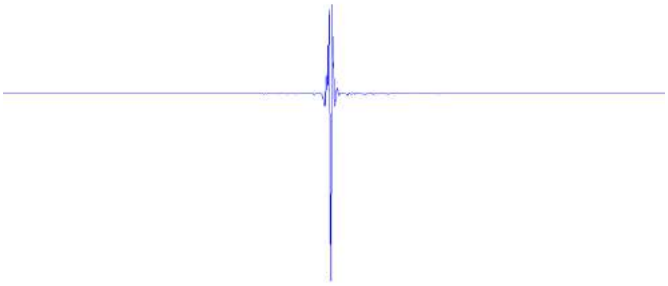

Figure 3.3D is an interferogram generated by FTIR interferometer for the full range of frequencies within the mid-infrared region, the, i.e., wavenumber of 4000 to 400 cm^{-1}. The interferogram is a complex plot of many cosine waves corresponding to the range of frequencies in the mid-IR.

3.3.1 Advantages of FTIR spectroscopy

FTIR spectrometers have several advantages over dispersive spectrometers. These advantages have resulted in the shift to FTIR spectroscopy over the past 50 years.

Multiplex or Fellgett's advantage

The FTIR interferometer measures all the infrared frequencies simultaneously. In contrast, every frequency across the infrared spectrum is measured individually in dispersive interferometers. This makes the dispersive interferometer much slower compared to FTIR interferometer. For example, to scan the mid-infrared region of the spectrum, i.e., from 4000 to 400 cm^{-1} at 1 cm^{-1} resolution, 3600 measurements are required. This translates to a shorter scanning time by a factor of 60 (square root of 3600 scans) for FTIR compared to dispersive spectrometers (Perkins, WD,1986).

Jacquinot's or throughput advantage

The infrared energy (throughput) passing an infrared spectrometer is a function of the area of the source and the angle of the beam passing into the interferometer. The maximum allowable angle of the beam passing through the FTIR interferometer is greater than the dispersive interferometer operating at the same resolution (Perkins, WD, 1986). The infrared light passing through a dispersive interferometer is controlled by a slit which limits the individual frequencies reaching the sample and the detector. However, the infrared light reaching the detector in FTIR spectrometers is controlled by a circular aperture or Jacquinot stop. For a given resolution and wavelength, this circular aperture permits more light through than a slit. The throughput advantage translates to a higher signal to noise ratio in FTIR spectrometers than the dispersive ones (Perkins, WD, 1986).

Precision or the laser advantage

In an FTIR spectrometer, a laser is used to monitor the speed of the moving mirror and the scanning time. The laser also serves a source of wavelength calibration within the instrument. This gives the FTIR spectrometer the advantage of an accurate and reproducible frequency scale that enables the comparison of spectra obtained at different times on the same or different instruments. The spectra obtained from FITR spectrometer are precisely comparable whether they were acquired seven minutes or seven years apart. This capability is not available in dispersive spectrometers. External calibration standards are needed to control the accuracy of a dispersive instrument making the spectra less comparable due to instrumental unknowns during scanning (Perkins, WD, 1986).

3.4 Instrumentation for FTIR Microscope

The FTIR microscope is composed of IR light source, liquid nitrogen cooled mercury cadmium telluride (MCT) detector and a beam splitter. The microscope is coupled to a stage that allows the precise mapping of materials (figure 3.4). The infrared microscope uses reflective optics that ensure coverage of the entire mid-infrared spectral range, i.e., 400 to 4000 cm^{-1} with minimum signal loss. The reflective condensing objectives are of Schwarzschild/Cassegrain design which focuses the incoming light from the interferometer on the sample. The light focused on the sample is then transmitted or reflected depending on the sample and the substrate used to mount the sample. In the transmission mode, the light from the source passes through the sample and then onto the detector. In transflectance mode, after passing through the sample (figure 3.5B), the light reflected from the mirrored substrate (figure 3.5C) then passes through the sample again, before hitting the detector (figure 3.5A). The detector is a focal plane array (FPA) detector which is an array of 64 x 64 pixels (figure 3.6B) where every pixel records a complete infrared spectrum

(Lewis et al., 1995). The FPA-FTIR microscope has several advantages such as fast collection time, high signal to noise ratio and high spatial resolution (5 μm). The FPA consists of the gridwork of individual detectors capable of measuring and collecting signal simultaneously at every point from the sample being examined. The data collection speed is improved by using FPA (focal plane array) detectors that allow the simultaneous spectral acquisition, producing spectral images with good SNR and lateral spatial resolution close to the diffraction limit (Baker et al. 2014). This enables spectroscopists to rapidly obtain a large amount of qualitative and quantitative information about the structure and biochemical composition of a sample.

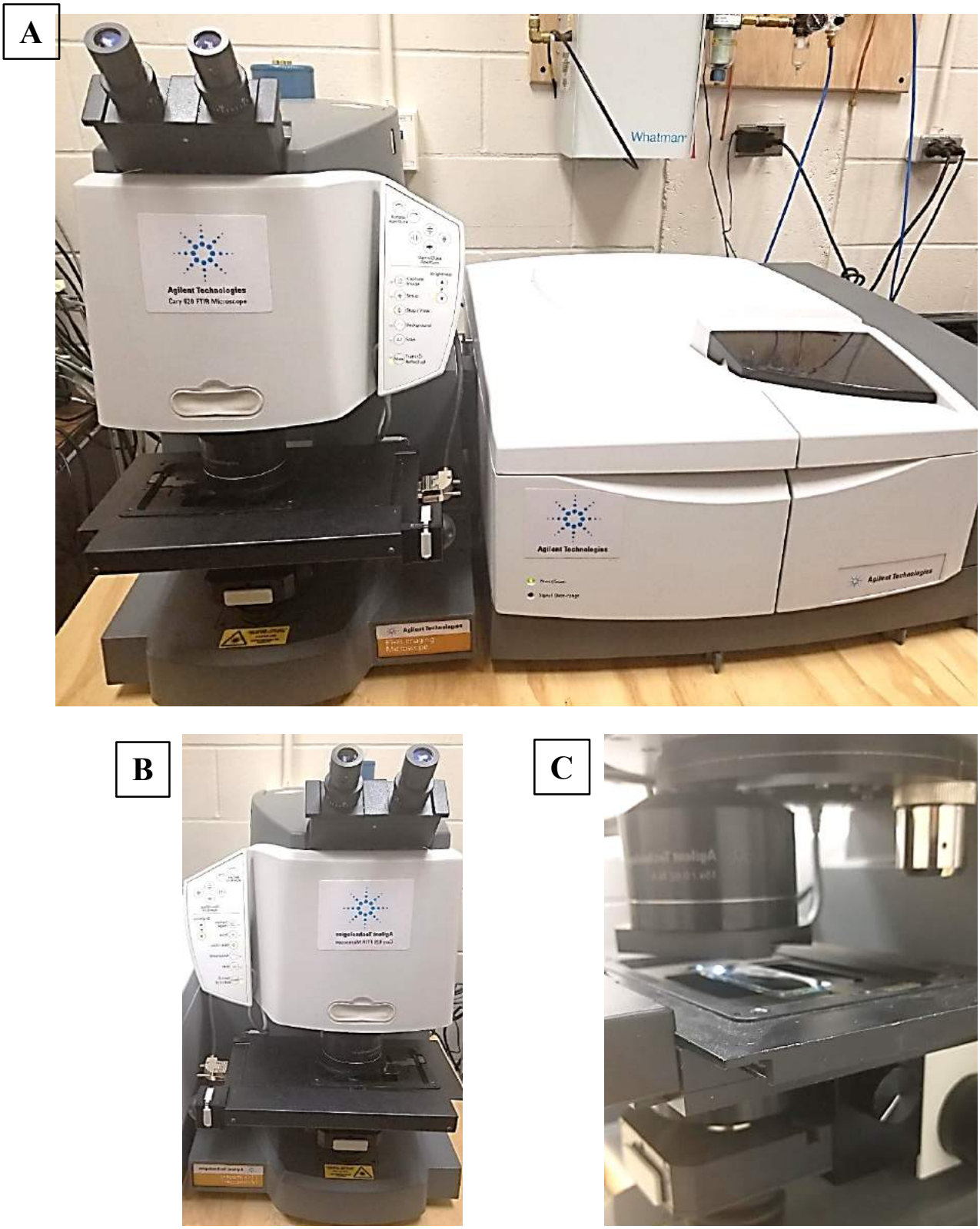

Figure 3.4. A- The Agilent-Cary 620 FTIR Microscope and 670 spectrometer used in this thesis. B) Agilent-Cary 620 IR Microscope (C) Close-up of the sample stage.

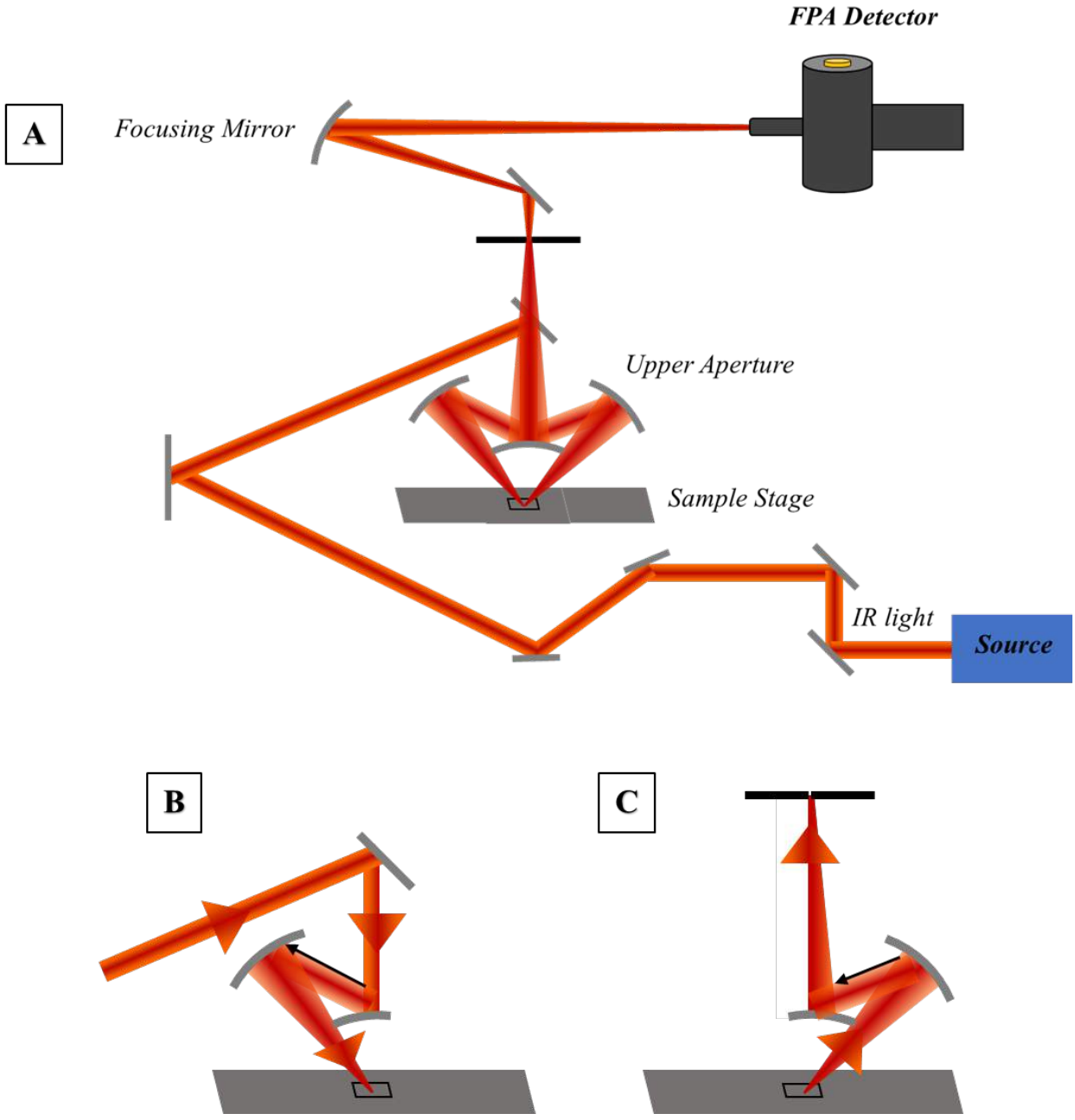

Figure 3.5. Schematic representation of the FTIR microscope in transflectance mode. A) Schematic of IR microscope. B) The incident light on the sample. C) Reflected light from the sample.

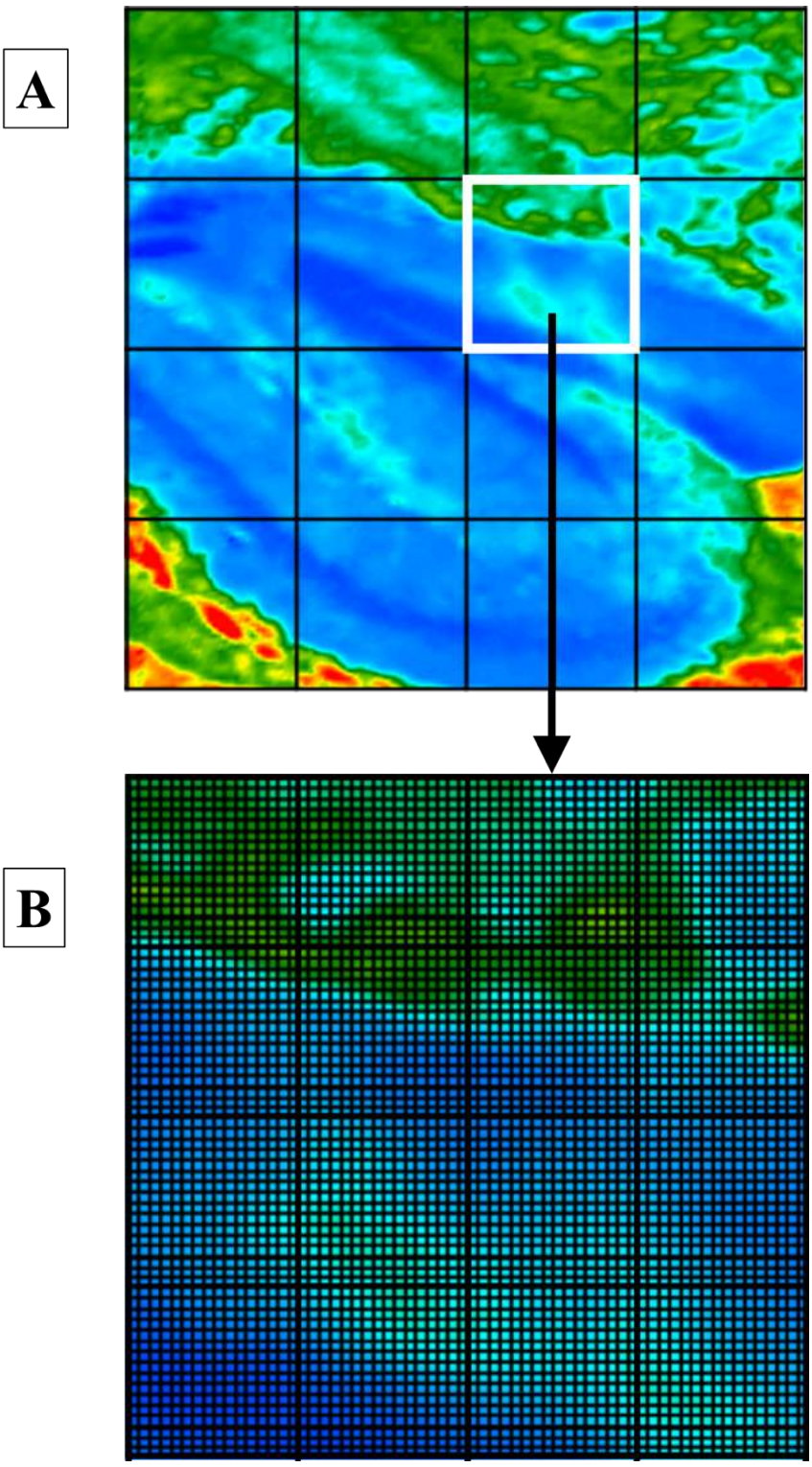

Figure 3.6A-B. Diagram of a 4×4-tile mosaic of brain tissue from 3xTg mouse, demonstrating FPA imaging. A) 4×4-tile mosaic image of the hippocampus and B) a single tile image extracted from this mosaic. A is an array of 65,536 pixels (since every tile contains 4096 pixels = 4096 × 4 × 4) and B is (64 × 64 pixels = 4096 pixels).

3.4.1 Information Obtained from an Infrared Spectrum

An infrared spectrum is a plot of the amount of light absorbed versus wavenumber (equation 3.7). The infrared microscope generates spectra by recording the amount of light absorbed by the sample (Baker et al., 2014). The amount of light may be presented in percentage transmittance, percentage reflectance or absorbance. The intensity of an infrared absorption band is proportional to the concentration (Beer-Lambert Law). Therefore, IR spectra can be used for quantitative analysis, under certain circumstances (Baker et al. 2014).

$$A = - \log_{10} \frac{T}{T_0} = \varepsilon c l \qquad \text{.....(3.6)}$$

Equation 3.6 is Beer-Lambert Law equation, where A is absorbance, T is the intensity of transmitted light, T_0 is the intensity of incident light, ε is absorptivity, c is concentration and *l* is path length (distance traveled by light through the substrate).

The absorbance spectrum is preferred as mathematical data changes such as spectral subtraction, baseline correction, quantitative analysis and band fitting are valid only on this linear format (ordinate axis is linear with sample concentration). This is because percentage absorbance is directly proportional to concentration (i.e. a linear relationship). The position of infrared absorption peaks is measured in either wavenumber $1/\lambda$ (cm^{-1}) or wavelength λ in μm (Griffiths, 2007).

3.4.2 Spatial Resolution of FTIR Spectroscopy

One of the limitations of infrared spectroscopy is the spatial resolution which is restricted by the wavelength of infrared light (Lasch & Naumann, 2006). Equation 3.7 describes the main limitations of spatial resolution in far-field microscopy.

$$R = \frac{1.22\,\lambda}{n \sin\theta} \qquad \ldots\ldots\ldots\ldots\ldots\ldots\ldots\ldots 3.7$$

Where $n \sin\theta$ is the numerical aperture (NA) of the objective, n is the index of refraction and λ is the wavelength of the incident light.

The limit of resolution of a microscope refers to its ability to differentiate between two close Airy disks in the diffraction pattern. The numerical aperture of the objective is derived from Rayleigh's criterion that states that any two points can be resolved if the center of one Airy disk coincides with the first minimum of the second Airy pattern. As per equation 3.7, one limitation is that the wavelength range of the mid-infrared region means that the limits to pixel resolution are on the order of microns(λ= 2.5-25 μm); this does not allow us search for nanoscale details (Lasch & Naumann, 2006).

3.5 Infrared Spectroscopy Applied to Biological Samples

All biomolecules absorb light within the mid-infrared region, i.e. wavelengths 2.5-25 μm and wavenumbers 4000-400 cm^{-1}(R. Dyer,1965, Chapter 2). The mid-IR spectra are typically divided into two regions of interest. The higher energy region (2700-3500 cm^{-1}) is dominated by heavy-

atom-light atom stretching modes i.e. OH, NH and CH stretches. The mid-infrared region from 1800-900 cm^{-1} is also called the fingerprint region as it is rich in vibrational modes that are characteristic of most functional groups. These molecules absorb light associated with the vibrational motion of their chemical bonds such as bending, stretching, rocking, wagging or scissoring. FTIR measures the energy absorbed, producing spectra with bands representing the chemical composition in the given sample at each pixel (Baker et al., 2014).

3.5.1 IR Spectroscopy of Brain Tissue

The brain is a pivotal body organ that contains a range of biomolecules such as proteins, carbohydrates, DNA, RNA, blood, carbohydrates, neurons, neurotransmitters, phosphates, lipids and so on. The brain is composed of an outer grey matter layer and inner white matter core. The grey matter is made up of neuron cell bodies, dendrites and axons whereas the white matter is composed of oligodendrocytes, astrocytes and a dense network of myelinated axons. Myelin plays a critical role in insulating the axons for secure signal propagation and improving electrical conductivity (Hussain et al., 2019). Brain tissue consists of 70-83 % water, 7.5-8.5 % protein and 5-15 % lipids with a higher lipid concentration in white matter (15 %) and lower lipid concentration in grey matter (5 %) (Krafft et al., 2005). The brain contains various types of lipids, but the most abundant ones are the phospholipids and the steroid cholesterol. Table 3.1 summarizes the relative distribution of lipids in the grey matter and white matter of normal brain tissue (Krafft et al., 2005).

Table 3.1. Lipid composition in grey matter & white matter of normal brain tissue (in % of total lipid) adapted from (Krafft et al., 2005).

Lipid	Grey Matter	White Matter
Cholestrole	19.6	26.9
Phosphatidylethanolamine	30.7	19.6
Phosphatidylcholine	25.1	11.8
Galactocerebroside	7.2	18.4
Phosphatidylserine	7.2	9.0
Phosphatidylinositol	3.9	4.0
Sphingomyelin	3.2	4.4
Sulfatid	0.7	5.1
Phosphatidic acid	0.5	0.4
Unidentified	1.9	0.4

Figure 3.7 shows an IR spectrum from the brain of a 3xTg/transgenic mouse recorded for this thesis. The brain tissue spectrum is comprised of CH stretches both symmetric and anti-symmetric stretches, the Amide I and Amide II protein bands, carbonyl (C=O) stretches, and phosphate bands and other functional groups (sugars, nucleic acids, etc.) The CH region has strong peaks at 2956 and 2922 cm^{-1} associated with anti-symmetric CH_3 and CH_2 stretching modes and weaker peaks at 2871 and 2851 cm^{-1} due to symmetric CH_3 and CH_2 stretching. As per previous work published by Gough's group, the neuron cell bodies are identified based on CH stretches (Gallant et al., 2006 & Rak et al., 2007). The regions with the strongest CH_2 bands correspond to areas of high lipid content, typically the white matter of the brain, whereas the regions of neuron bodies (soma) have

lower lipid content and hence weaker lipid peaks. Thus, the neuron cell bodies are identified on the basis of CH stretches and are evaluated for markers of disease. This is further explained in chapter 4 of this thesis. In this study, we are mostly interested in creatine levels as a disease marker discussed in section 3.7 of this chapter.

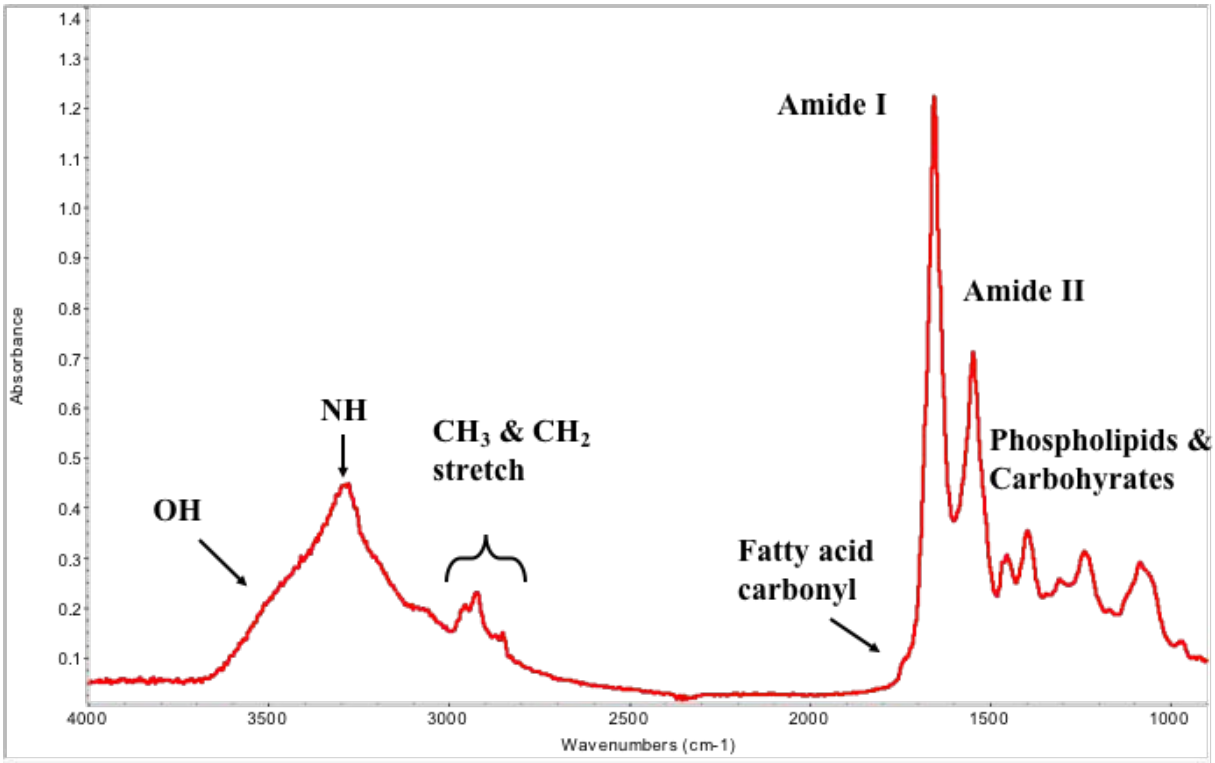

Figure 3.7. Generic IR spectrum of mouse brain tissue (Z.Abyat).

3.6 Animal Models of AD

Animal models are crucial in medical research. They have contributed to our understanding of genetics, mechanisms associated with various diseases, the efficacy and the toxicity of potential therapeutics. Transgenic mouse models have been used to identify some of the genetic mechanisms that lead to AD-type alterations in behavior and brain structure (Price & Sisodia 1994). Transgenic mouse models have broadened our understanding of AD pathology and have shed light on potential

therapeutics. Familial AD (FAD) mutations have been used to develop transgenic mouse models. The FAD is an early onset AD caused by specific genetic mutations within families. FAD provides a genetic lesion that has been used in AD modeling in transgenic animals. Mice are genetically very similar to humans; 95 % identical at the genomic level (Langley, 2009). The mouse genome sequencing was established earlier than that of the human genome, and mouse genetic manipulation is a well-established technique. Apart from genetic homology, mice and humans have many physiological similarities. Despite genomic similarities, there are phenotype differences between the two species. Many proposed pharmaceuticals that appeared to be promising in mice were found to fail in humans (Uhl & Warner 2015).

Because mice have similar brain networks and neurobiology with humans, they have been extensively utilized for the study of neurodegenerative diseases (Kitazawa, Medeiros and LaFerla, 2012). Apart from that, mouse models have a relatively affordable maintenance cost and are easy to modify genetically. Several transgenic mouse models with various FAD-associated combinations are available. These mice develop Aβ plaques and cognitive decline in an age-dependent manner. However, they do not fully recapitulate the disease course. Mice do not undergo neuronal loss and brain atrophy as humans would. Also, Aβ plaques expressed by transgenic mouse models are neuropathologically different from senile plaques (Maeda et al., 2007). Apart from that, mouse models need higher levels of APP expression to develop Aβ pathology, i.e., at least eight times more than the endogenous levels. This is opposite to human cases in which a 50 % increase in APP is enough for the development of AD-like pathology in Down syndrome (Duff & Suleman, 2004). However, more than 50 therapeutics have undergone clinical trials for AD, and most of them have been established through testing in transgenic mice models (Kitazawa et al., 2012).

3.6.1 C57BL/6 (Background/Control) Mice

C57BL/6 is a common inbred strain of laboratory mouse. This mouse model is used frequently for genetic modifications that replicate human diseases. C57BL/6 is the most widely used mouse strain in biomedical research owing to its congenic strains' availability, easy breeding, robustness and capability of learning various tasks (Bryant, 2011). C57BL/6J mice are the background strain used to produce the transgenic mouse line used in this study. This mouse model is used as a control group. The background mice used in this study were subjected to either a creatine-enriched diet or normal diet (non-creatine) to study the effect of dietary creatine enrichment in these mice versus the transgenic mice.

3.6.2 Triple Transgenic Mice (3xTg)

The transgenic mouse model used in this study develops both Aβ and tau pathology. This mouse model was originally developed by Oddo et al. and was first described in Oddo et al., 2003. This transgenic mouse model is generated by crossing three independent FAD mutant genes: The Swedish mutation (K670N/ M671L), the preselinin mutation (PS1M146V) and the tau mutation (P301L) (Oddo et al., 2003). The THY1.2 promoter is used to drive the transgene expression in AD-relevant areas. The APP and tau transgenes are microinjected into a single cell embryo from the PS1M146V knock-in mouse. The primary advantage of this mouse line is that multiple transgenes are introduced in the animal without altering the background genetic constitution, thus avoiding an essential confounding factor. This transgenic mouse model develops age-dependent Aβ and tau pathologies. The transgenic mouse experiences intracellular Aβ accumulation before tangle formation, consistent with the amyloid cascade hypothesis. Intracellular Aβ deposition

begins at 6 months of age while Aβ plaques begin to accumulate at 9 to 12 months of age. The tau and NFT form in the CA1 neurons at the later stages. (Oddo et al., 2003).

Another study investigated the possibility of tau-mediated AD neurodegeneration using the same mouse model i.e. 3xTg (Winton et al, 2011). This study attempted to distinguish Aβ peptide from Aβ epitopes within APP through immunohistochemical analysis. A panel of antibodies were used to distinguish Aβ from cleaved Aβ peptides (Aβ plaques). It was reported that the intraneuronal material shared epitopes with APP but not free Aβ. The intraneuronal material from this mouse model (3xTg) was compared with 3xTg mice deficient for β-secretase (3xTg-BACE) i.e. mice that do not produce Aβ. This was done to prove and confirm the presence of intraneuronal APP and absence of Aβ peptides. Immunoblots for 3xTg-BACE showed powerful intranueronal APP and absence of Aβ. However, the tau levels were similar in 3xTg and 3xTg-BACE mice. Thus, tau pathology is independent from Aβ peptide generation in 3xTg mouse model. This study confirms that the 3xTg mouse model develops both free or cleaved Aβ and tau pathology, but these pathologies form independently (Winton et al, 2011).

A recent study used 3xTg mouse model to investigate the implication of brain energy metabolism in AD (Adlimoghaddam et al, 2019). Brain metabolic activity in 3xTg and age-matched controls was measured using Fluorodeoxyglucose Positron Emission Tomography (FDG-PET). 11-month old 3xTg were used to evaluate brain metabolism since at this age the mice develop both plaque and tau pathology. The study reported significant decline in brain metabolism in the cortical piriform and insular regions relative to age-matched controls. The activity of mitochondrial protein levels (complex I-V) also decreased tremendously. Thus hypometabolism coupled with impaired oxidative phosphorylation results in decrease in mitochondrial energy levels and neurodegeneration. There is an association between hypometabolism and reduced

mitochondrial function. However, there is no association between metabolic activity and neuropathological (Aβ, tau, and astrocytes) changes in AD. This implies that alterations in brain metabolism precedes AD pathology. Thus early stage metabolic changes in cortical and piriform regions can be a biomarker for early AD therapeutics development and neurogenesis preservation (Adlimoghaddam et al, 2019).

The 3xTg mice present age and pathology dependent cognitive decline, hence mimicking the neuropathology of AD. Thus, this mouse model is suitable for testing therapeutic interventions and assessing their effectiveness in ameliorating AD lesions and their progression. 3xTg mice have been used in many studies since their introduction in 2003. In this study, the 3xTg mice are used to assess the distribution of a putative disease marker, i.e., creatine and the effect of a therapeutic, i.e., dietary creatine in creatine distribution and localization in brain tissue from 3xTg mice.

3.7 IR Spectroscopy of Creatine

The objective of this study is to identify neurodegeneration in AD using the 3xTg transgenic mouse model. IR spectra of brain sections of transgenic mice are assessed and compared to sections from background mice. The deposition and distribution of creatine in the tissue sections is determined from characteristic creatine band intensities. The effect of a potential therapeutic, i.e. creatine ingestion is assessed to establish whether a creatine enriched diet may be used as a therapeutic for the prevention or delay of AD pathology.

3.7.1 *In Vitro* IR Spectroscopy of creatine

FTIR spectroscopy has been used to study markers of altered energy metabolism. Research from the Gough group reported the novel discovery of large crystalline creatine microdeposits in tissue

sections from post mortem demented human brains and a different transgenic mouse model, TgCRND8, possessing a double mutant form of human APP695 (with K670N/M671L and V717F) (Gallant et al., 2006). These creatine deposits were larger and more numerous in post mortem demented brains compared to non-demented ones. Similar results were reported for TgCRND8 mouse tissue sections compared to those of controls where these deposits were either absent or lower in the non-transgenic litter mate controls. The study concluded that creatine molecule could be a marker of the disease process in AD. A subsequent extension of this study reported an association among creatine, amyloid plaque and lipid in the hippocampus in tissue sections of the TgCRND8 mouse brains (Kuzyk et al., 2010). The study examined the distribution of creatine, lipids and amyloid plaque deposits in animals at a range of ages, *viz*. 5, 8, 11, 14 and 17 months. As before, FTIR images from tissue sections from TgCRND8 mice were compared with age-matched littermate control mice. All the TgCRND8 mice had creatine deposits with deposition extent increasing with age. The oldest littermate control mice had minor creatine deposits. The creatine was always deposited in the grey matter of the brain across the hippocampus and not in the white matter. The lipid distribution was similar in TgCRND8 and age-matched littermate controls at all ages. The dense core plaques were always surrounded by lipids. This was confirmed by examining several serial sections.

In the dietary creatine study undertaken for this thesis, the creatine distribution was analyzed by integrating peak areas for 1305 cm^{-1} and 1400 cm^{-1} bands which are established markers for creatine crystals as per the earlier work that was done by our lab (Gallant et al., 2006 & Kuzyk et al., 2010).

Skoczen et al. studied the effect of the ketogenic diet (KD) on creatine accumulation in the hippocampus and dentate gyrus of rat brains using synchrotron-FTIR (SR-FTIR) spectroscopy.

Adult male Wistar rats were used for this study. The animals were divided into three groups comprised of a control group with standard laboratory diet and two groups with a ketogenic diet of ratio 5:1 (KD1) and 9:1 (KD2) respectively. For quantitative verification of differences in creatine distribution between the analyzed animal groups, the median, minimal and maximal value of creatine deposits were evaluated for the sector 3 of cornu Ammonis (CA3), dentate gyrus (DG) and the walls for hippocampal cell layers. It was reported that creatine band intensities increased within CA3 and DG regions of ketogenic diet rats compared to standard diet fed rats. The results confirmed the applicability of FTIR spectro-microscopy for studying the creatine accumulation within nervous tissue. This study suggested that rats with a higher ketogenic diet experienced a boost in hippocampal energy production capacity (Skoczen et al., 2017).

Chapter 4. A pilot study of dietary creatine supplementation in 3xTg & C57BL/6 mice.

4.1 Outline of the Experiments

One of the objectives of this thesis was to use FTIR spectroscopy to identify biochemical alterations linked to AD using the 3xTg mouse model. FTIR mosaic images were used to assess creatine distribution, the proposed disease biomarker for altered energy metabolism, i.e., . The effect of the therapeutic, i.e., the creatine-enriched diet, was assessed to establish whether dietary creatine might prevent or delay the onset of disease pathology. Creatine levels were assessed by FTIR imaging of brain tissue sections, primarily from the hippocampus and the cerebellum of background mice and the 3xTg mouse model. Over the course of the project, a second objective became necessary, namely to establish a sample preparation methodology that would yield consistent and reproducible creatine spectra. We hypothesized that the high (5.5 micron) spatial resolution possible with FTIR along with our expertise in creatine spectroscopy would provide a measurement of creatine levels that is reflective of the *in vivo* condition (Gallant 2006, Rak 2007 & Kuzyk et al., 2010).

4.1.1 Animals Used in This Study

All animals were maintained in standard cages at the animal holding facility at St. Boniface Hospital Alberchtsen Research Centre. A total of 12 mice (6 background & 6 transgenic) were used in this study. These animals, i.e. this pilot group of animals, were provided by Dr. Albensi from a slightly larger dietary study (Snow, et al, 2017). Eighteen animals were used in the parallel dietary study by Dr. Albensi's group; to date, only data on male mice have been published (Snow, et al, 2017). Genders were not matched in this pilot group of animals; the control mice were all male; the 3xTg were mixed, in uneven numbers. Dr. Gough did not participate in gender selection. The control and transgenic animals had been divided into two groups of n = 3 to be fed regular or

creatine-enriched diets. Dietary intervention (3 %, w/w creatine added to standard diet) began at the age of 7 months and continued for eight weeks. Before seven months, all mice were on a regular, creatine-free diet. Mice were exposed to 12-hour cycles of light and dark in a room maintained at 22° C. Animals were sacrificed at the age of 9 months, and their brains were extracted as decribed in previous papers (list our other mice papers); snap-frozen tissue encased in OCT(optimum cutting temperature,Tissue-Tek) were stored at -80°C. This task had been completed prior to the commencement of this Master's thesis. All experiments were approved by the University of Manitoba Animal Care and Use Committee which conforms to the Canadian Council for Animal Care's Guide to the Care and Use of Experimental Animals.

Table 4.1. Gender and diet of 3xTg/AD & C57BL/6/background Mice.

Mouse Type	**Mouse Code** (from Dr. Albensi's lab)	**Gender**	**Diet Type**
3xTg/Transgenic	B0100130381	Female	Control
	B0100130382	Female	
	B0100130383	Male	
	B0100130362	Male	Creatine
	B0100160363	Female	
	B01001600365	Female	
C57BL/6/Background	13MICE0005	Male	Control
	13MICE006	Male	
	13MICE0007	Male	
	13MICE0016	Male	Creatine
	13MICE0018	Male	
	13MICE0019	Male	

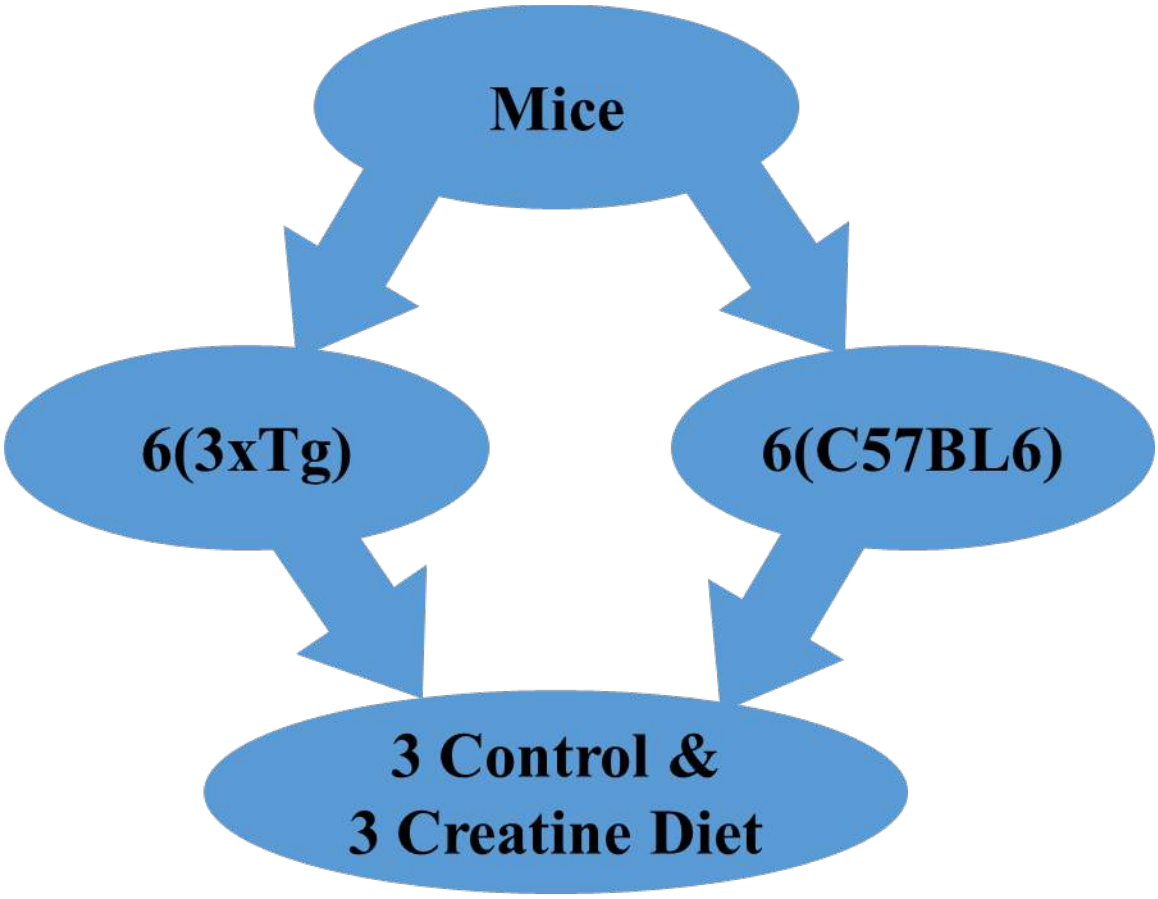

Figure 4.1. Design of experiments.

There were similarities that were controlled but some critical differences were identified retrospectively: gender mismatch, animals sacrificed at different times, differences in sample preparation, freezing and the storage conditions. Some of these differences, i.e., gender mismatch in 3xTg mice and sample preparation were not considered during the design of experiments. We established the impact of these variations on the outcome only post-sacrifice and imaging of these brain tissue sections (discussed in chapter 6).

54.2 Detailed Experimental Methods

The following sections describe the various protocols used for this research.

4.2.1 Brain Tissue Preparation

The animals were sacrificed by inhalation of isoflurane in 2013 at RCFFN (Richardson Centre for Functional Foods & Nutraceuticals). This was performed by Dr. Gough and Dr. Suh from RCFFN. Catherine Findlay and Margret Rak (former Ph.D. students from Dr. Gough's laboratory) also assisted in this procedure. The animals were treated in accordance with the guidelines of the Canadian Council on Animal Care, and the protocols were approved by the University of Manitoba. The brains were extracted and bisected sagittally along the midline (Gallant et al., 2006, Rak et al., 2007, & Kuzyk et al., 2010). Each hemisphere of the brain was covered with optimum cutting temperature medium (OCT) compound (Sakura, Tokyo, Japan), placed cut-side up on a small piece of cork and was frozen with liquid nitrogen. Tissue samples were not fixed since tissue fixation with formaldehyde washes away creatine, which is highly soluble in water. The unfixed brain tissue was flash frozen in isopentane cooled with liquid nitrogen and stored in a freezer at -80°C until sectioning. The tissue was cryosectioned (-20°C) into 7 μm thick sections in the sagittal plane, around 0.5 mm from the midline. Several sections were acquired at different depths by cutting a few millimeters deeper through the brain tissue. The unfixed brain tissue sections were mounted on glass slides, IR reflective slides (Low-e MirrIR^{TM}, Kevley Technologies, Chesterland, OH) or BaF_2 windows. The slides were then transported in a Styrofoam box containing dry ice at -80°C to the University of Manitoba for FTIR imaging. The tissue sections were dried for a minimum of one night to avoid traces of water that would interfere with infrared measurements. The tissue sections were dried by placing them in a desiccator containing silica gel pellets for 24 hours, in the dark. The desiccators were stored in a wooden cabinet at room temperature. It is

essential to dry the brain tissues in the dark to avoid lipid oxidation (Stitt et al., 2012). Some of the brains were sectioned in summer 2013, and some were stored in a sealed plastic slide case at -80 °C. Some of these frozen slides were thawed and imaged in 2013. The remaining frozen slides from 2013 and the slides for sections acquired in 2017 were imaged in 2017-2019. It was then discovered that the storage time had affected the creatine appearance and distribution that was observed during the course of this study. This issue is addressed in chapter 6 of this thesis.

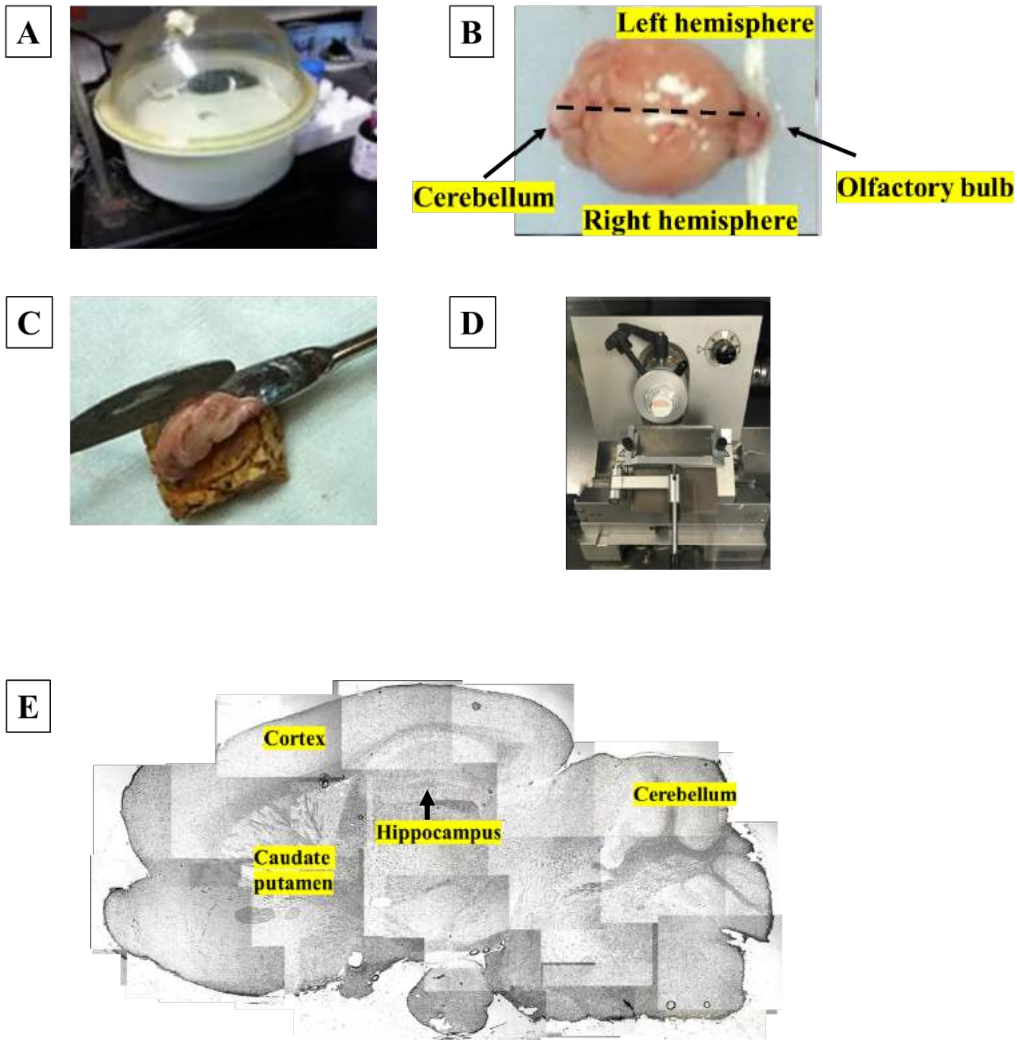

Figure 4.2. Brain tissue preparation procedure. A) Mouse undergoing anesthesia with isoflurane at St. Boniface Hospital Albrechtsen Research Centre. The 3xTg mice were sacrificed at RCFFN. B) Top view of extracted mouse brain lying on wax block, ready to be bisected sagittally along the midline. C) Left hemisphere of mouse brain being mounted on cork base, coated with OCT. D) Cryosectioning of the frozen brain tissue at -20°C. E) Visible light image of a sagittal section of brain tissue from this dietary study.

4.2.2 IR Microscopy

Data collection was performed at the University of Manitoba. FTIR-FPA mosaics were recorded with an Agilent Cary 670 FTIR Spectrometer coupled to an Agilent Cary 620 FTIR microscope. The Cary 620 FTIR microscope is a focal plane array (FPA) chemical imaging microscope. The

microscope has a 64 × 64 pixel FPA detector capable of simultaneously acquiring 4096 spectra over a single tile, which covers an area of 352 x 352 μm^2, at 5.5 μm per pixel. Most of the images were mosaics of 5×5 tiles containing 102,400 spectra per mosaic. All the data were collected in transflectance mode with 4 cm^{-1} spectral resolution. A total of 16-32 scans were coadded for sample measurement and 516 scans for background measurement. It is critical to record a background spectrum before recording a sample spectrum. This is because FTIR spectrometer is inherently a single beam instrument. A background spectrum is collected with no sample in the infrared beam. For the case of this study, a background is recorded using the clean imaging substrate, i.e., clean MirrIR slide or BaF_2 window. The background spectrum serves to measure the contribution of environment and instrument to the spectrum. These effects are then eliminated by ratioing the sample beam spectrum to the background spectrum.

4.3 IR Spectral Analysis & Data Processing

All spectral processing was done at the University of Manitoba using Agilent ResolutionsPro™ software (version 5.3.01964). The spectra were processed using the established assignment of IR bands in bio-spectroscopy (Parker, 1983, Gallant et al., 2006, Rak et al., 2007, Kuzyk et al., 2010 & Findlay et al., 2015). The areas of peaks associated with specific tissue components were represented on a false color scale. The exact parameters used to process brain tissue mosaics are outlined in Table 4.2.

Table 4.2. Processing parameters used for brain tissue maps (Gallant 2006, Rak 2007 & Kuzyk et al., 2010).

Function	**Band (cm^{-1})**	**Baseline (cm^{-1})**
Lipid		
CH_2 symmetric stretch (2852)	2856-2845	2996-2802
Lipid Carbonyl	1751-1738	1764-1728
Protein (β-sheet amyloid)		
Amide I band (1630)	1630-1620	1642-1610
Creatine		
Band 1 (1306)	1314-1298	1316-1296
Band 2 (1400)	1406-1391	1406-1390

4.4. Identifying Hippocampal Neurons using lipid bands

IR mapping was initially performed in the hippocampus of each sample as this is one of the first regions affected by AD in both transgenic mice and humans (Apostolova et al. 2006). Several mosaics of the hippocampus were acquired for both background and 3xTg mice. The mosaics included the CA1, CA2, CA3 and the dentate gyrus neurons, the neuropil and the white matter of the corpus callosum. The major brain tissue components were identified on the basis of lipid distribution as established by previous work done by Gough's group (Gallant et al., 2006, Rak et al., 2007, & Kuzyk et al., 2010). The neurons in the grey matter correspond to areas of lowest lipid band intensities, whereas the neuropil has a higher lipid content, and the white matter (enriched with myelin) has the highest symmetric CH_2 stretch bands (area under the curve between 2856 and

2845 cm^{-1}) (Gallant 2006, Rak 2007 & Kuzyk et al., 2010). The integrated area under every band is analyzed for every spectrum in the mosaic and results are displayed as a false color image. False color images are spectrochemical images which give an impression of tissue morphology based on functional group distribution. Figure 4.3 shows single pixel spectra of white matter, neuropil and the neuron cell bodies processed on lipid band intensity, i.e. the integrated intensity of the band centered at 2852 cm^{-1}. Figure 4.4 shows the corresponding false color images processed for lipids at 2852 cm^{-1} band. As per scale, the red color represents areas with high lipid concentration.

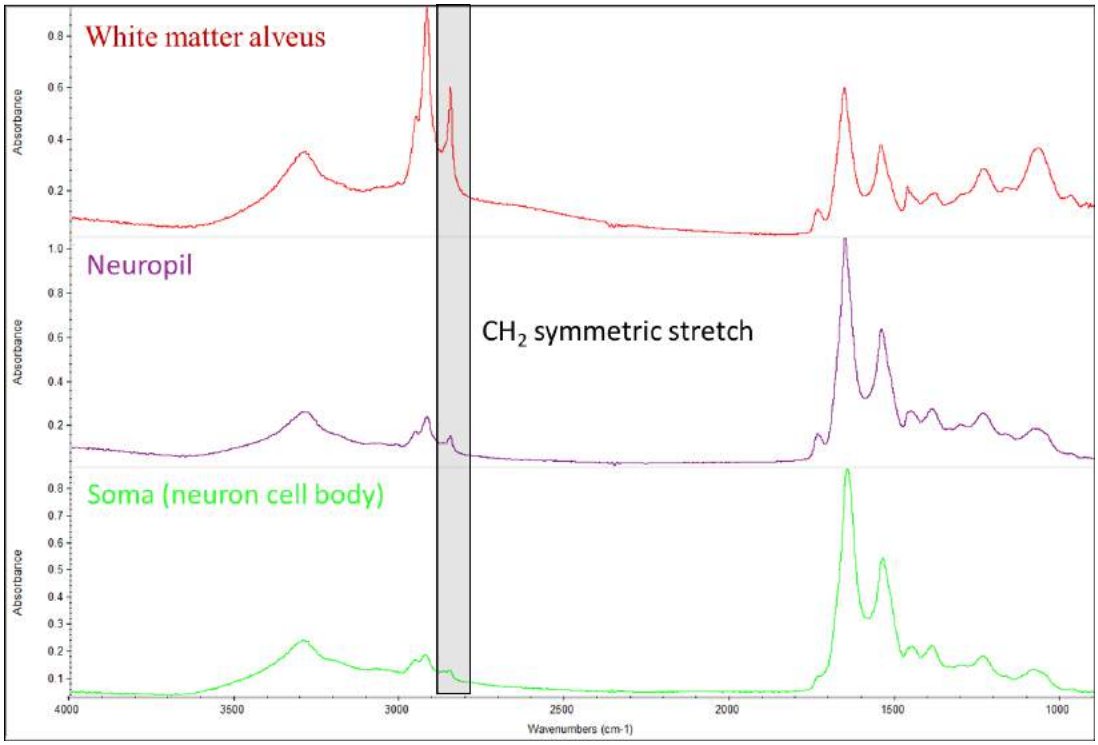

Figure 4.3. Scattered single-pixel spectra of white matter, neuropil, and neurons in brain tissue. The spectra are processed with Agilent ResolutionsPro^{TM} software (version 5.3.01964). The neurons are identified by spectrochemically masking them on the basis of the integrated band intensity of the symmetric CH_2 stretch modes. The neurons in the grey matter correspond to areas of lowest lipid band intensity (red spectrum), whereas the neuropil has a higher lipid content (purple spectrum), and the white matter (enriched with myelin) has the highest (green spectrum.

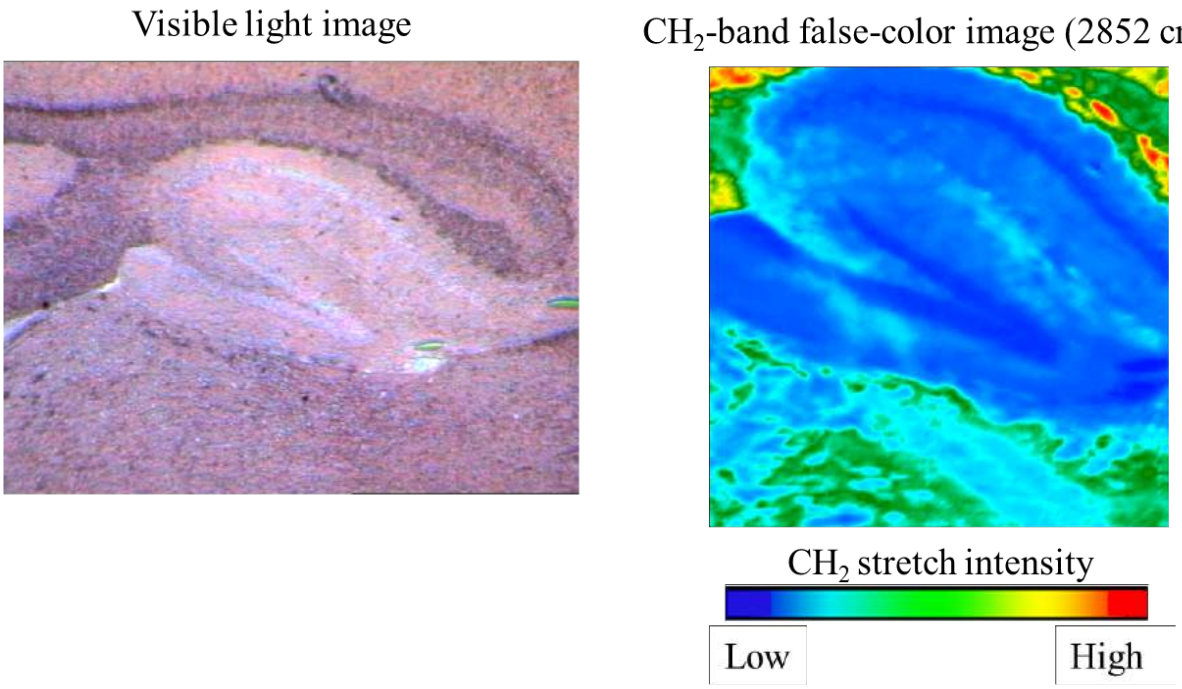

Figure 4.4 Spechtrochemical image of the hippocampus processed for lipid distribution (2856 cm^{-1}). The red color represents regions with high lipid content i.e. white matter enriched with myelin and the blue color represnts the grey matter i.e. neurons (that has lowest lipid content).

4.4.1 Assessing Creatine Localization in Hippocampal Neurons

Previous work done by Dr. Gough's group demonstrated that the existence of elevated creatine crystals in brain tissue might be associated with AD (Gallant et al., 2006, Kuzyk et al., 2010). Gallant and co-workers reported the discovery of crystalline creatine deposits in the hippocampus, cortex and the caudate of transgenic/TgCRND8 mice. The creatine crystals were revealed through processing IR maps of brain tissue sections based on the band intensity and absorbance at 1306 cm^{-1} and 1400 cm^{-1}. The area of a sharp peak (located between 1314 and 1298 cm^{-1}, baseline 1316–1296 cm^{-1}) and a doublet (located between 1406 and 1391 cm^{-1}, baseline 1406-1390 cm^{-1}) was found to be adequate for detection of all creatine deposits within the tissue. Spectral images

processed for distribution of lipid and creatine are overlaid to demonstrate tissue composition, i.e., white matter and grey matter and creatine colocalization (Figure 4.5 A-B). Figure 4.5 A-B depict various spectral markers, i.e. white matter, neuropil, neuron cell bodies (the soma), creatine in brain tissue and a spectrum of pure creatine. Creatine distribution was evaluated in the same manner in both background and 3xTg animals. The distribution was assessed over several sections mounted on MirrIR slides (Low-e MirrIR^{TM}, Kevley Technologies, Chesterland, OH). At least ten sections from each animal were examined to ensure a representative survey of each brain. The creatine deposition and distribution is described in detail in Chapter 5 of this thesis.

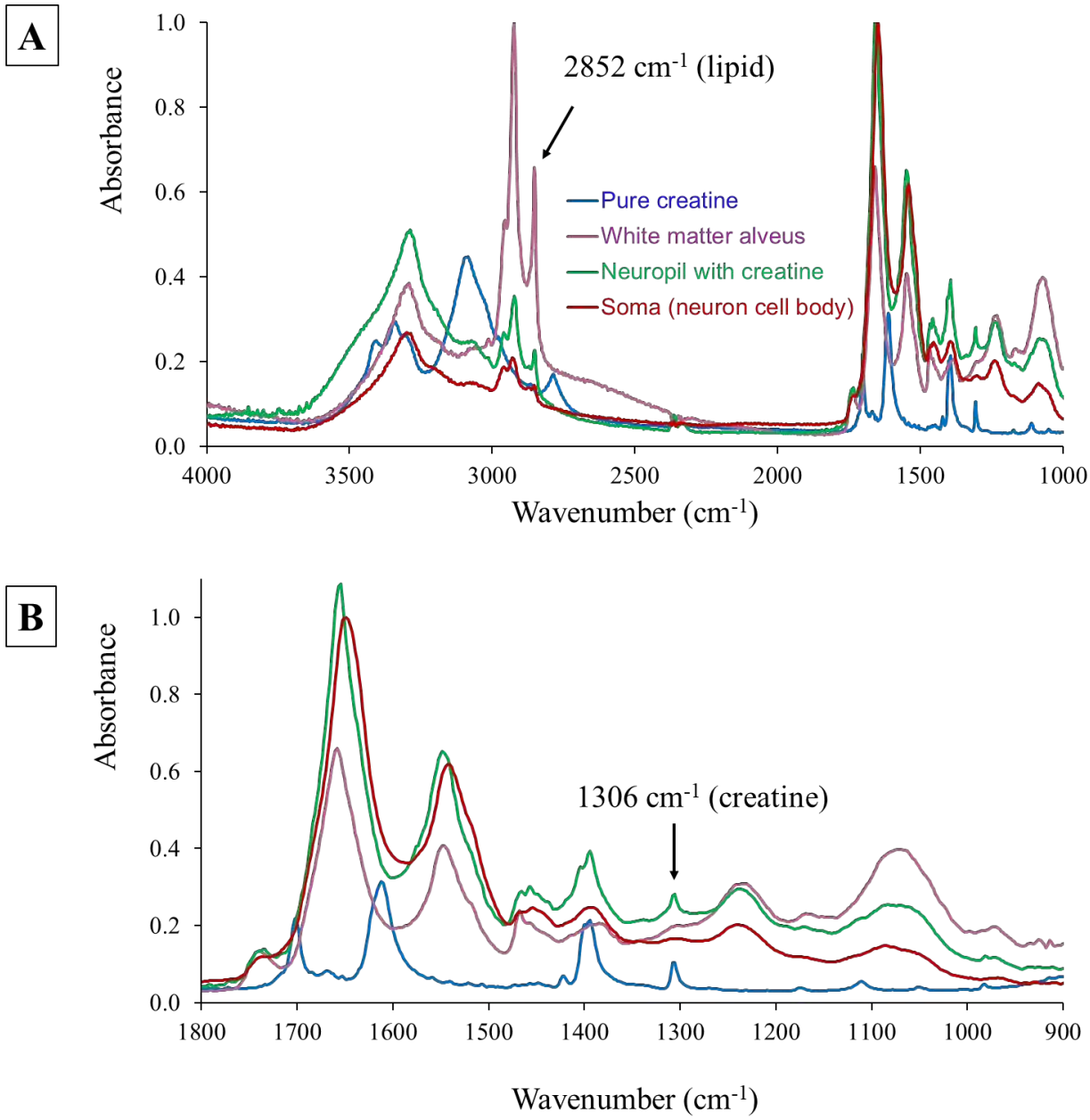

Figure 4.5. A) Typical spectra for neurons (soma) -, neuropil with creatine -, white matter -, & pure creatine -. **B)** Close-up of the finger print region with the chosen creatine marker band at 1306 cm^{-1}.

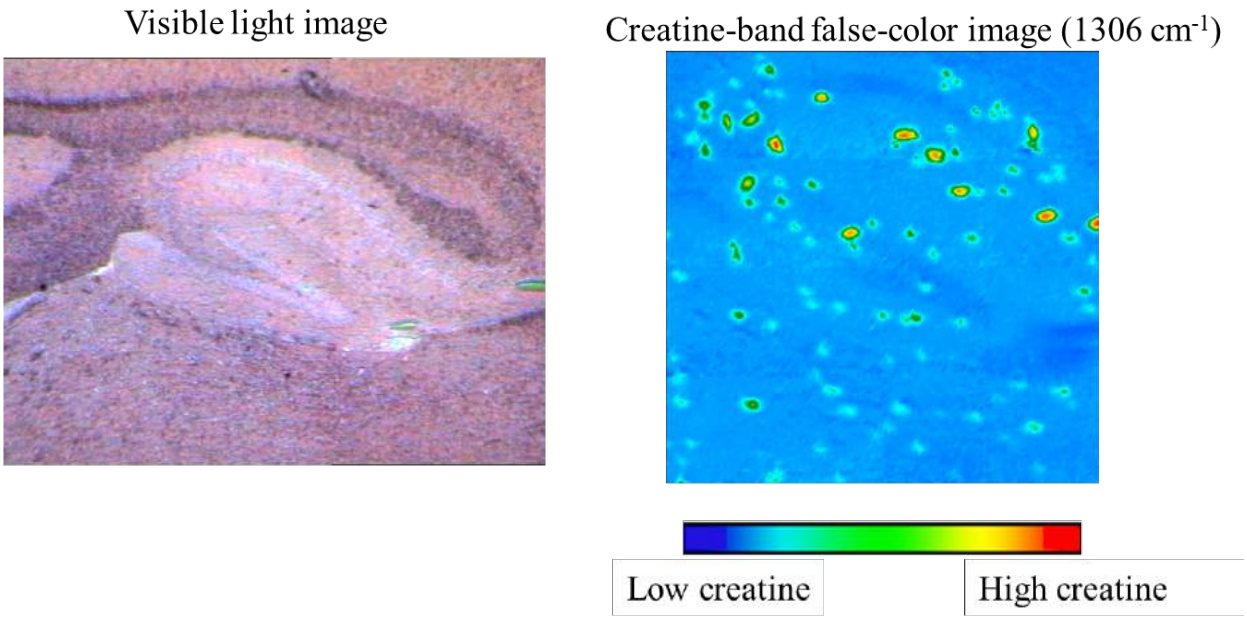

Figure 4.6. Spechtrochemical images processed for lipid and creatine distribution. Spectral images processed for distribution of lipid and creatine are overlaid to demonstrate tissue composition and creatine colocalization. The areas under the lipid and creatine peaks are integrated with parameters established in our lab, defined in chapter 4, Table 4.2

Chapter 5. Effect of Creatine Diet on Creatine Accumulation & Localization

5.1 Overview

The effect of 3 % w/w dietary creatine supplementation was tested in transgenic 3xTg mice and age-matched background mice (C57BL/6). The transgenic mice were maintained on a C57BL/6 background for more than eight generations. The transgenic mice harbored the APP_{695}, $PS1_{M146V}$ and Tau_{P301L} mutations that lead to both Aβ and tau pathology. The study involved a total of 12 mice (n = 6 per group) where one group was transgenic, i.e., 3xTg mice, and the other group was age-matched background C57BL/6 mice. The control and creatine-enriched diet program started when the mice were seven months old and continued for eight weeks. Post sacrifice at 9 months, brains were removed and frozen; the brain tissue was cryosectioned and prepared for IR imaging as described in chapter 4.

Animals from this dietary study were imaged using far-field FTIR imaging technique. Thermal source FTIR images were obtained with an Agilent-Cary 620 microscope and 64 × 64 focal plane array detector (FPA) at the University of Manitoba. FTIR images were used for evaluating the effect of dietary creatine in background mice and age-matched 3xTg mice. This pilot study was originally designed as a dietary study; however during the course of the dietary study, several problems arose that necessitated a change in the direction, towards methods development. This dietary study was a part of a bigger parallel dietary study by Dr. Albensi's group. There were several confounding factors in the experimental design that were not controlled. Gender imbalance was one of these variables. This study involved a total of 12 animals (n = 6 (3xTg) & n = 6 (C57BL/6)). As described in chapter 4 (Table 4.1), these animals were divided into two groups i.e. the creatine-enriched diet animals (n = 3) and the control/standard diet animals (n = 3). The creatine-enriched and standard diet animals included both female and male genders; the 3xTg group had n = 2 male animals and n = 4 female animals whereas the background mice were all

male. The gender imbalance made it impossible to conduct a statistical analysis for creatine distribution.

Apart from the gender imbalance, there were inconsistencies in creatine crystal morphology and creatine distribution, even in sections from the same animals that were acquired at the same time. Further, it was not possible to conduct statistical analysis since there was not an adequate number of sections from each animal. A minimum of 5 sections from each animal were needed for statistical analysis. The animals in this dietary study were sacrificed in 2013 and freeze-stored -80°C as either intact hemispheres of brain or or as brain tissue sections mounted on Kevly imaging slides until 2017 and 2018 when they were sectioned or imaged. Some of these sections were imaged in 2013 with a few weeks of cryosectioning. Others remained frozen until this study. The freeze-storage affected the tissue quality that was not anticipated in the experimental design. In some cases, the tissue quality was quite poor that most sections acquired were either torn or sections that were full of folds. As a result, in some animals, only 1 section could be obtained that would be useful for imaging. Because of insufficient and inconsistent number of sections from each animal statistical analysis was not conducted. Table 5.1 summarizes the number of sections acquired and imaged from each animal, the imaging dates, and the number of useful sections for FTIR imaging.

Table 5.1. Sectioning & imaging history

Animals	Animal type/Diet	Number of sections acquired in 2013		Imaging date		Sections acquired in 2017-2018	Number of useful sections
		BaF_2	Kevley	*2013-2014	*2017-2018		
B-0100130381	3xTg/Control	5	16	0	15	0	15
B-0100150382	3xTg/Control	3	9	1	8	0	8
B-0100130383	3xTg/Control	3	9	2	8	0	8
B-0100160362	3xTg/Creatine	3	16	0	16	0	8
B-0100130363	3xTg/Creatine	3	8	0	8	0	7
B-0100160365	3xTg/Creatine	4	10	0	7	0	5
13MICE0005	C57BL/6/Control	1	0	1	0	131	6
13MICE0006	C57BL/6/Control	1	0	1	0	0	1
13MICE0007	C57BL/6/Control	0	0	0	3	53	3
13MICE0016	C57BL/6/Creatine	2	0	2	0	0	2
13MICE0018	C57BL/6/Creatine	2	0	2	0	10	8
13MICE0019	C57BL/6/Creatine	0	0	0	9	50	2

*Some images were recorded in 2013-2014 by Catherine Findlay & Peter Trokajlo, while some were recorded in 2017-2018 by Zahra Abyat.

In some of the stored sections, it was found that creatine crystals which had been detectable when imaged initially were no longer present when the samples were imaged post 6 years of freeze storage. These anomalies in creatine appearance shifted the focus of the study to a methodology study aimed at optimizing a sample preparation methodology that would yield consistent and reproducible creatine spectra reflective of the *in vivo* state of the animals. Several sample preparation variables were investigated to establish their effect on creatine crystal structure and distribution. A series of freeze-thaw experiments and cryosectioning experiments were designed to study the effect of sample preparation on creatine appearance. The results of this work are described in detail in Chapter 6 of this thesis.

As a result of the problems described above, the material presented in Chapter 5 addresses three main topics:

- A full tissue section survey acquired by LDIR
- A survey of tissue data from this thesis and from previous work in the Gough lab
- A summary of the results for the 12 animals in the dietary study

During the course of this study, some images were acquired with a novel method called laser direct infrared (LDIR) as a demonstration trial of new imaging capabilities by the Agilent personnel. These results are presented in Section 5.2, as they influenced the planning and method development for brain tissue imaging.

Next, the general distribution and morphology of creatine crystals were surveyed from animals from this study as well as animals not included in this dietary study (Section 5.2 & 5.3). This was done to evaluate the effect of sample preparation on creatine morphology, using the distribution recorded through this thesis and a comparison with historical data from Dr. Gough's lab. FTIR images of 3xTg and background mice on a standard diet and creatine diet are discussed in this chapter, separated by gender (Section 5.3).

Finally, the data acquired for the dietary study are presented and analyzed insofar as possible, in light of the unforeseen complications (Section 5.4). The results are separated according to animal type, diet and gender.

5.2 LDIR imaging of mouse brain tissue

Because some memory and learning is governed by processes in the hippocampus, previous work in Dr. Gough's lab had been directed to imaging the hippocampus primarily (Gallant 2006, Rak 2007 & Kuzyk et al., 2010), with occasional small surveys of cortical regions. An Agilent

applications specialist offered to demonstrate the capability of a novel instrument known as laser direct infrared (LDIR) for rapid detection of distinct features. Brain tissue sections from a 3xTg mouse (not from this dietary study) were prepared (cryosectioned and dried) and provided to the Agilent team for LDIR imaging. LDIR images were acquired using the Agilent 8700 at the Agilent facility in Santa Clara, California, US. The Agilent 8700 system uses a quantum cascade laser (QCL) to direct infrared light of a specific chosen wavelength to the sample. In transflectance mode he light is then reflected from the sample and directed to the detector. The QCL laser, together with rapid optics in this system, allowed the acquisition images of large sample areas, even the entire tissue section, targeting a specific compound at a given frequency, in a very short time, sometimes in minutes.

LDIR imaging was used to assess the creatine distribution across the entire brain section of a 3xTg mouse, *viz*., 3xTg-448 (B0103200448), a 12-month female on the standard diet. This was an elder mouse compared to the 9 month old mice used in this dietary study. This mouse was sacrificed and cyosectioned in 2015. Figure 5.1 shows visible light images of 3xTg-448 and Figure 5.2 shows the corresponding LDIR images of this brain section. Figure 5.1B shows the hippocampus and its sub regions i.e. the CA1, CA2, CA3 and the dentate gyrus. Degeneration in the hippocampus is considered to be among the early symptoms of AD. However, hippocampal degeneration does not occur uniformly. The CA1 region is the first region that undergoes degeneration and neuronal loss in 3xTg brain. The LDIR images of 3xTg-448 show creatine crystals distributed throughout the hippocampus, cortex and the cerebellum, i.e., the grey matter of the brain (Figure 5.2A-C). LDIR images revealed for the first time that there were significant creatine crystals in the cerebellum. Previously most images were focused on hippocampus because it is an area of early degeneration. This outcome influenced methods development and imaging

planning. Based on this outcome, creatine distribution was assessed in both the hippocampus and the cerebellum for all mice in this study, i.e. (3xTg & background group).

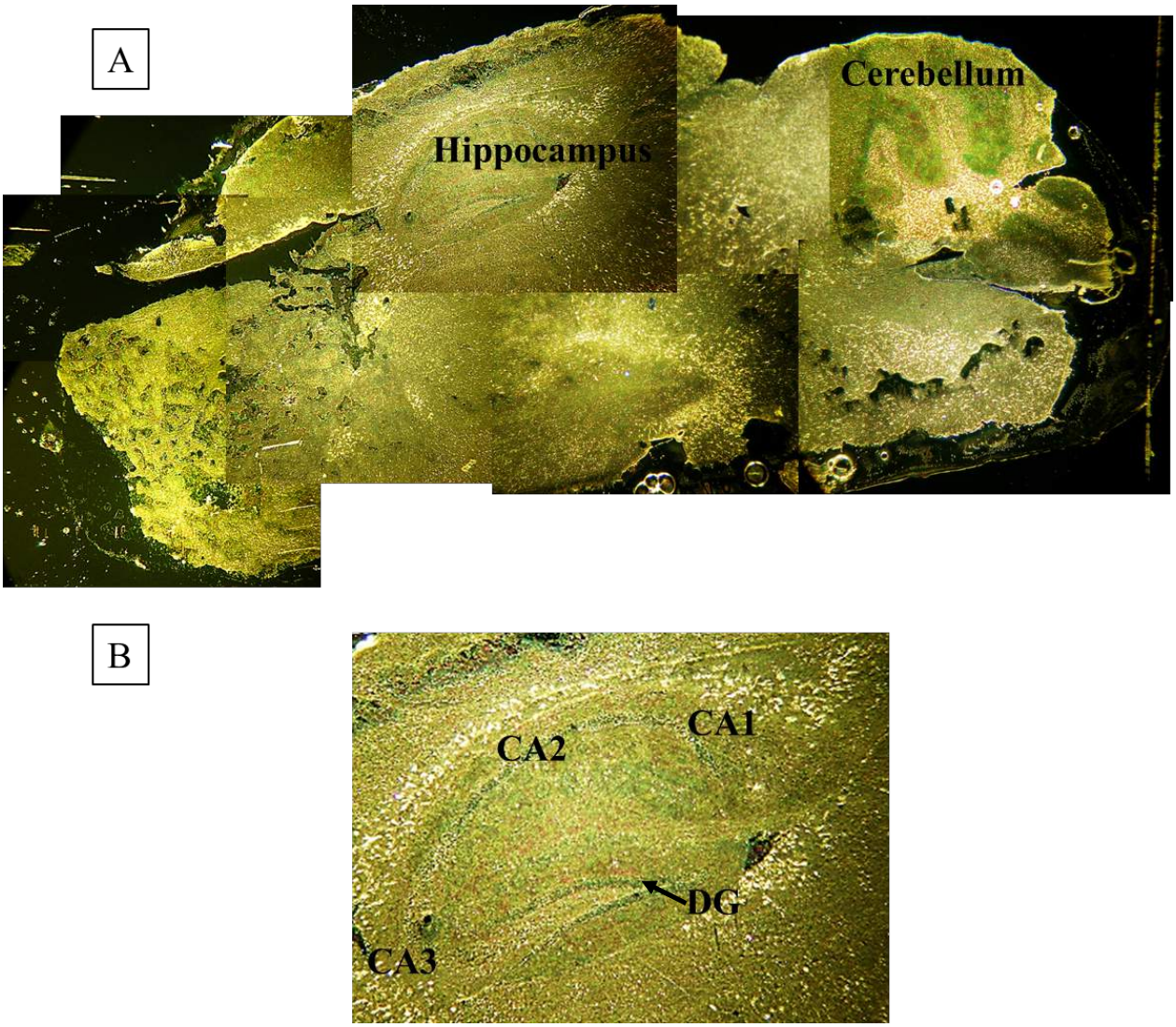

Figure 5.1. Morphology of sagittal section of a female 3xTg mouse brain (B0103200448). A)Visible light image of an unstained section from a 12-month-old 3xTg female mouse on a standard diet mounted on a gold-coated silicon wafer. Note: This mouse was not from the group used in this dietary study. **B)** A close-up of the hippocampus and its sub regions i.e. locations of CA1, CA2, CA3 and dentate gyrus neurons. Degeneration in AD occurs in the hippocampus and its sub regions.

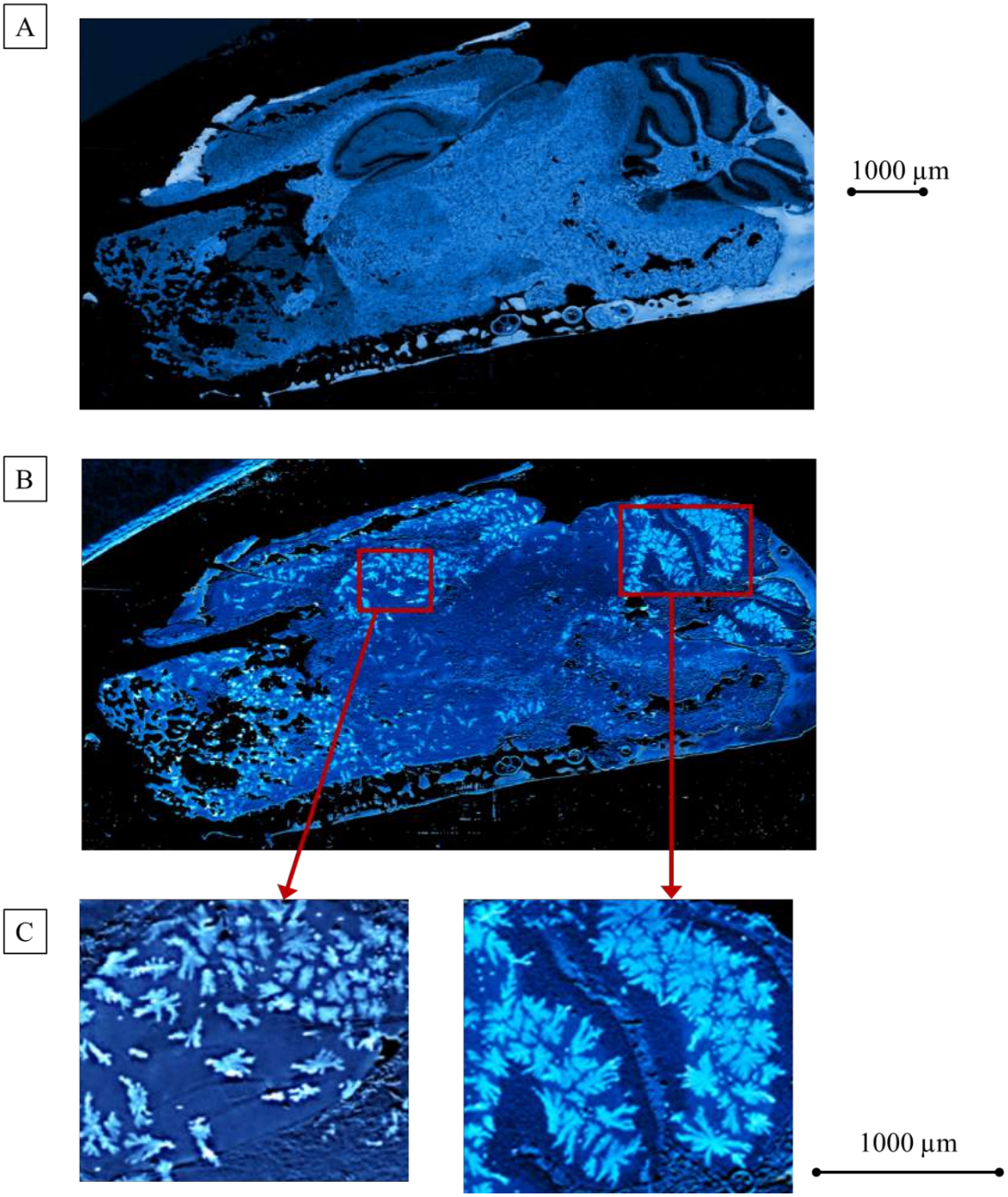

Figure 5.2. LDIR images of the entire mouse brain (3xTg-448) collected in 1 hour. **A)** LDIR image showing white and grey matter distribution (imaged on lipid carbonyl at 1735 cm^{-1}) at 1 µm pixel resolution. **B)** LDIR image showing creatine crystal distribution throughout the brain (imaged on creatine peak at 1307 cm^{-1}) at 1 µm pixel resolution. **C)** Close-up LDIR images of the hippocampus (left) and cerebellum (right) in 3xTg showing sharp dendritic creatine crystals in the grey matter of brain; the hippocampus, the folia of the cerebellum and the cortex.

5.2.1 Dendritic crystal pattern of creatine deposits

The LDIR images (Figure 5.2A-C) displayed a creatine crystal morphology that was not previously remarked upon in detail, namely the existence of dendritic morphology. Dendritic crystals are formed by a diffusion-controlled crystallization process (Holden. A & Morrison. P, 1982). Examination of previously acquired FTIR images for another transgenic mouse model, viz. TgCRND8 mice revealed that a similar pattern occurred in some cases (Figure 5.3). Figure 5.3 depicts dendritic creatine crystallization (Kuzyk et al., 2010). The 8-month, 11-month & 17-month TgCRND8 had either dendritic creatine crystals or a mixture of dendritic and irregular creatine crystals (Figure 5.3). On the other hand, images obtained from the dietary study in this thesis had a different creatine morphology. The creatine crystals from this study were always in the form of single solid irregular crystals of varying size from 1 μm to 1 mm. The creatine crystallization process is complex. Diffusion-controlled crystallization is dependent on the amount of solute, i.e., creatine crystals, and the local temperature gradient. There were some differences in the sample preparation methods; temperature difference in freezing medium (temperature of isopentane cooled in liquid nitrogen < temperature of liquid nitrogen), duration of immersion in freezing medium, storage conditions and freeze-thaw procedure. This may have affected the crystallization process and the crystal morphology. Experiment to explore these possibilities are described in detail in chapter 6 of this thesis.

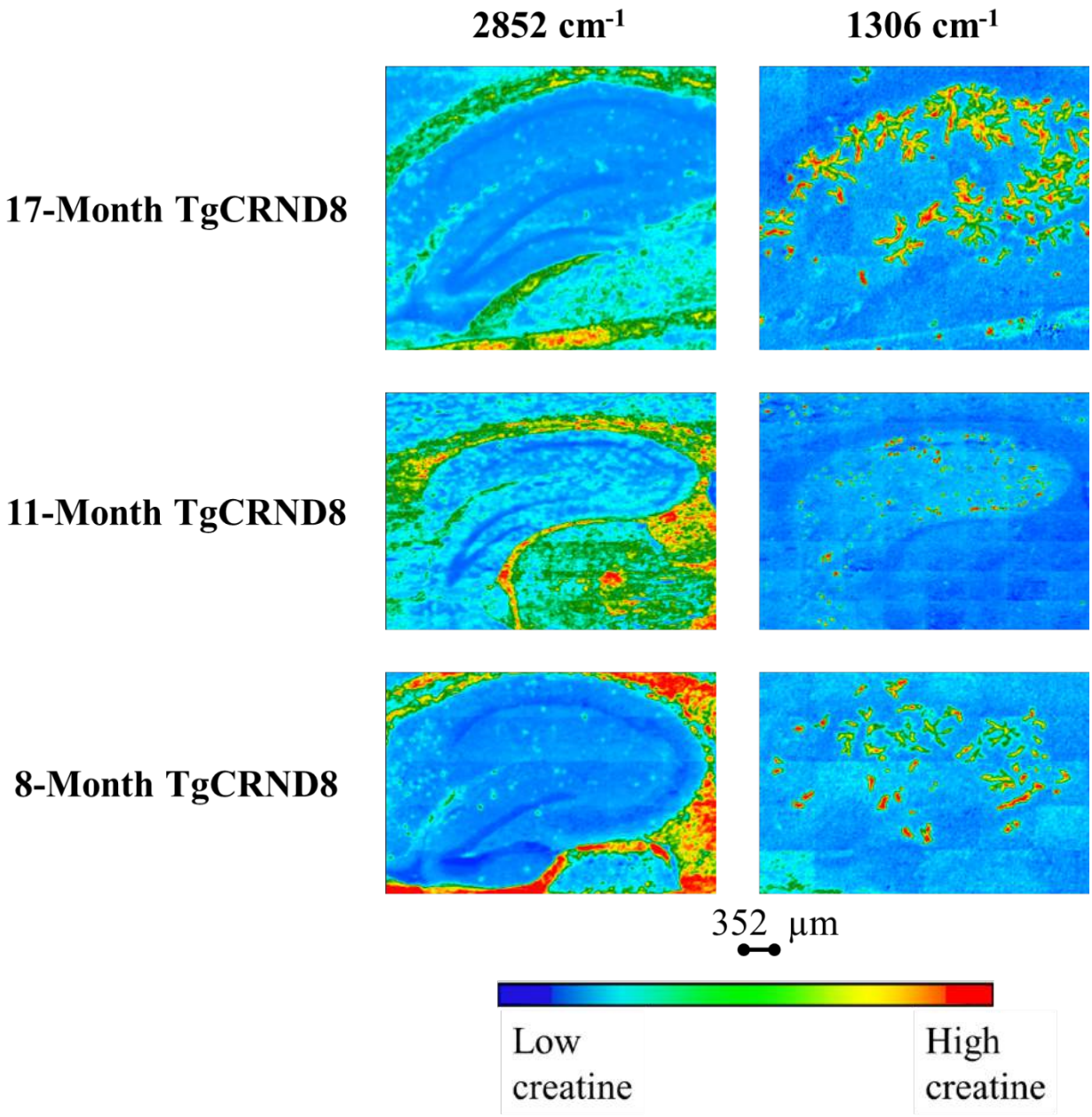

Figure 5.3. Dendritic creatine deposits in hippocampus of TgCRND8 mice (Kuzyk et al., 2010). These hippocampal images were previously acquired and published (Kuzyk et al., 2010) but were reprocessed using the parameters employed in this thesis. As per false color scale, the red color represents areas of high creatine content. FPA images are mosaics of 7 × 6, 7 × 5 & 6 × 4 tiles respectively. One tile = 64 × 64 pixels = 352 × 352 µm.

5.3 Effect of creatine diet on creatine distribution

As described in section 5.1, the dietary pilot study in this thesis was affected by gender imbalance and sample storage. This pilot study involved (n = 6) 3xTg and (n = 6 C57BL/6) animals that were divided into two groups i.e. the creatine-enriched diet animals (n = 3) and the control/creatine-free diet animals (n = 3). The creatine-enriched and control diet animals included both female and male genders. The 3xTg group of animals involved n = 2 male and n = 4 female animals. The sample size and gender imbalance made statistical analysis challenging since gender may be a factor impacting the creatine distribution. The FTIR images obtained from the 12 animals in this study were analyzed qualitatively based on visual appearance of creatine crystals in the spechtrochemical images. The results are discussed and separated by gender in the following sub-sections (5.3.1-5.3.3).

5.3.1Effect of creatine diet on C57BL/6/background mice (control group)

A total of 6 background mice were used in this study where n=3 were on control diet and n=3 on creatine diet. Spectrochemical images of brain tissue from these animals were processed on lipid (2852 cm^{-1}) band to show grey and white matter of the brain. The creatine band (1306 cm^{-1}) was used to assess creatine distribution and localization within the grey and white matter of the brain. Creatine distribution was assessed over several sections in each animal (at least 5). However, in some animals only 1 or 2 good quality sections could be obtained due to long term storage that impacted the tissue quality. Figure 5.4A, 5.4 B & 5.4C depict spectrochemical images of the hippocampus of brain tissue sections from C57BL/6 mice that were on 3 % w/w. The visual inspection of spectrochemical images revealed creatine crystals that appeared in a different form

i.e. pools of creatine crystals running a few millimeters in length (crystals in form of streaks) (Figure 5.4A ;13MICE0016, Figure 5.4B; 13MICE0018). This creatine crystallization pattern was only noticed in these sections. Examination of lab notes revealed an unusual storage and transport conditions. These animals (13MICE0016 &13MICE0018) were sacrificed in 2013. The unfixed brain tissue from these animals was flash frozen in isopentane cooled with liquid nitrogen. The brain sections were acquired shortly after the animal sacrifice at RCFFN. The brain tissue sections were mounted on BaF_2 slides. The slides were on dry ice at -80° C for 12 hours while being transported to Synchrotron Radiation Centre (SRC). These slides were then refrigerated at -20 ° C and thawed for imaging at SRC. Post imaging the slides were returned on dry ice and stored in a fridge at 4°C until the next imaging. The slides were maintained in a fridge to avoid any lipid oxidation. The slides were stored and transported at a range of temperatures (-80°, - 20° & 4° C). The storage and transport conditions may have affected the crystallization, since this crystallization pattern was only noticed in these slides. This unusual crystallization pattern demonstrates the effect of sample preparation that will be addressed in chapter 6.

Creatine crystals in form of streaks were observed in some of the sections obtained from 13MICE0016 &13MICE0018 i.e. the C57BL/6 animals on creatine-enriched diet (Figure 5.4A & Figure 5.4B). There were only 2 sections that were imaged for 13MICE0016 that both had creatine crystals. Out of 10 sections imaged for 13MICE0018, 6 sections had creatine crystals appearing visually in some regions of the hippocampus. Figure 5.4B depicts representative images of some of these sections. Full set of spectrochemical images for all animals in this study are presented in the appendix (Chapter 8, Appendix I, Figure 8.1-8.24) of this thesis. Animal 13MICE0019 (another C57BL/6 mouse on creatine-enriched diet) did not contain creatine crystals (Figure 5.4C). Out of 9 imaged sections, none of the spechtrochemical images contained creatine crystals.

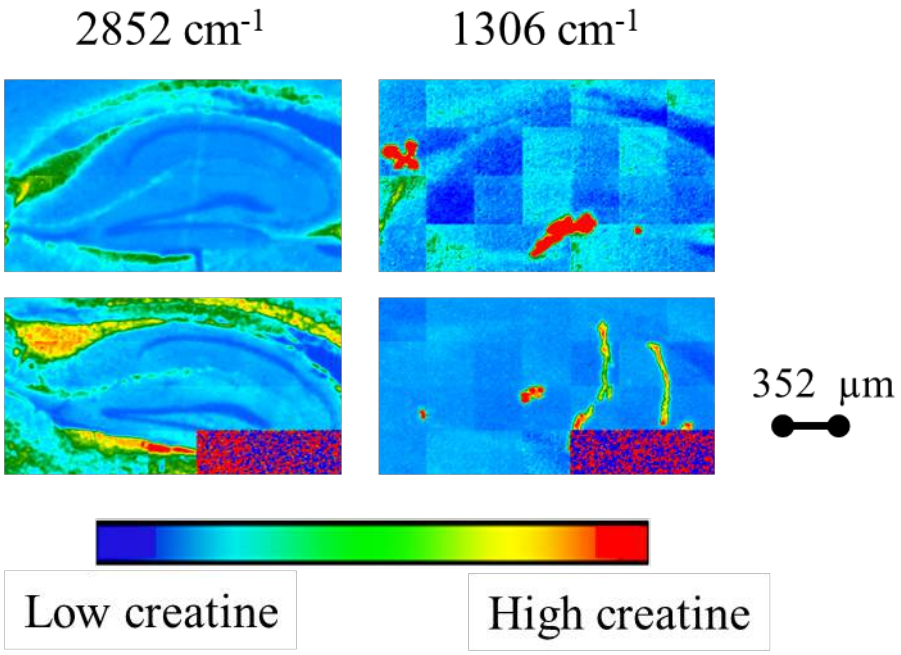

Figure 5.4A. Spectrochemical images of hippocampus for creatine distribution in 13MICE0016 (9-month background male mouse on 3% creatine enriched diet). The spectrochemical images were processed for distribution of lipids (2852 cm^{-1}) to establish tissue morphology and creatine (1306 cm^{-1}) to assess creatine localization. The images were processed with methods outlined in table 4.1. FPA images are mosaics of 7 × 4 tiles. One tile = 64 × 64 pixels = 352 × 352 µm. As per scale, the red color represents areas with high creatine concentration. Creatine crystals in form of streaks were observed in these sections possibly due to variable freezing and transportation conditions (transportation over a range of temperatures i.e. (– 80 °, – 20 ° & 4 ° C). Upper scale = 0.5395, Lower scale = - 0.0277. Corresponds to areas of zero signal as the detector warmed up. Note: These images were recorded by Peter Trokajlo in 2013 (a previous summer student in Dr. Gough's lab).

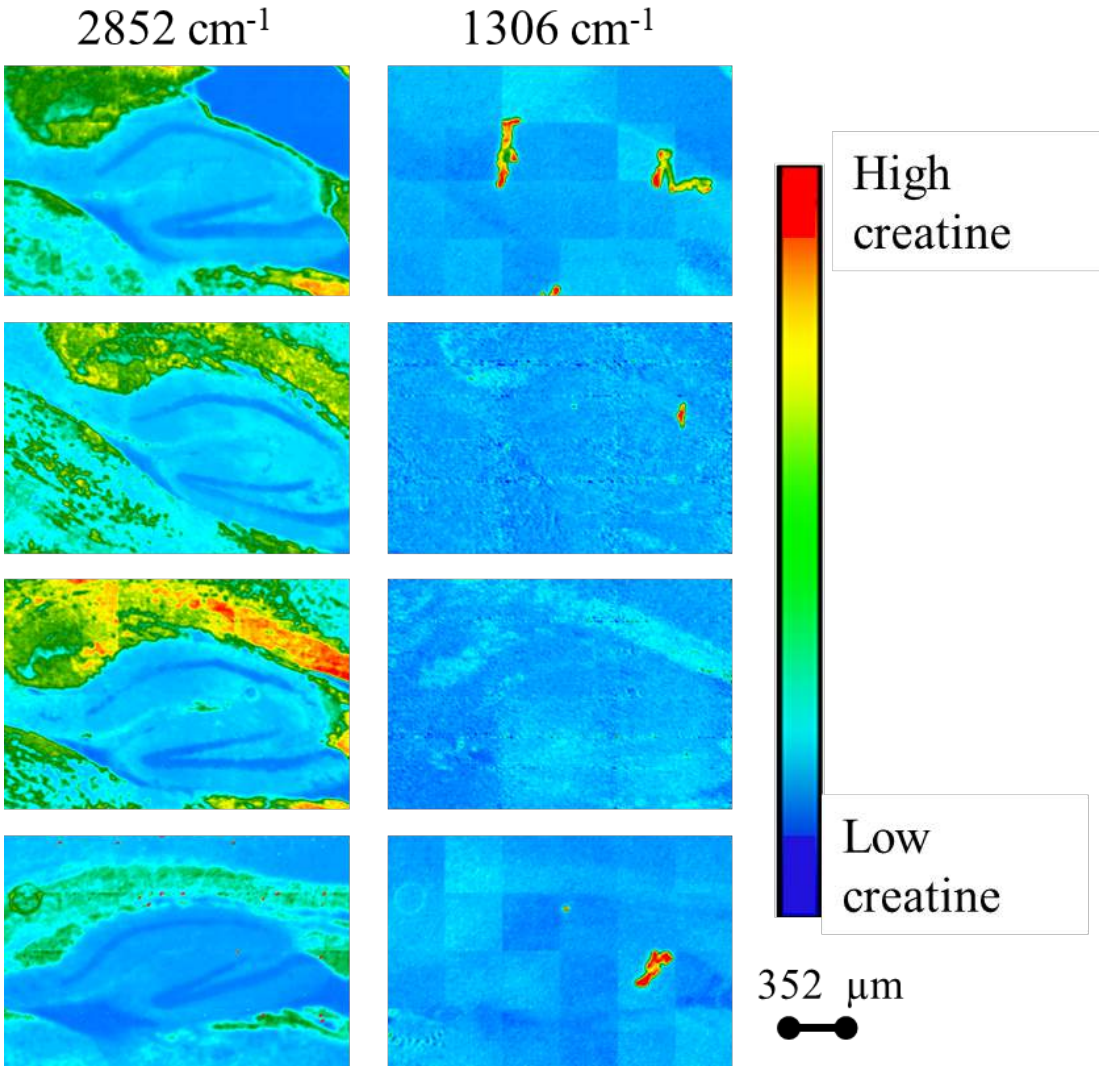

Figure 5.4B. Representative spectrochemical images of hippocampus for creatine distribution in 13MICE0018 (9-month background male mouse on 3% creatine enriched diet). The spectrochemical image was processed for distribution of lipids (2852 cm^{-1}) to establish tissue morphology and creatine (1306 cm^{-1}) to assess creatine localization. The images were processed with methods outlined in table 4.1. FPA images include mosaics of 6 × 4 & 5 × 5 tiles. One tile = 64 × 64 pixels = 352 × 352 µm. As per scale, the red color represents areas with high creatine concentration. Creatine in form of streaks appeared in some of the sections. Upper scale = 0.4656, Lower scale = - 0.088. Note: 2 of these images were recorded by Peter Trokajelo in 2013 (a previous member of Dr. Gough's lab).

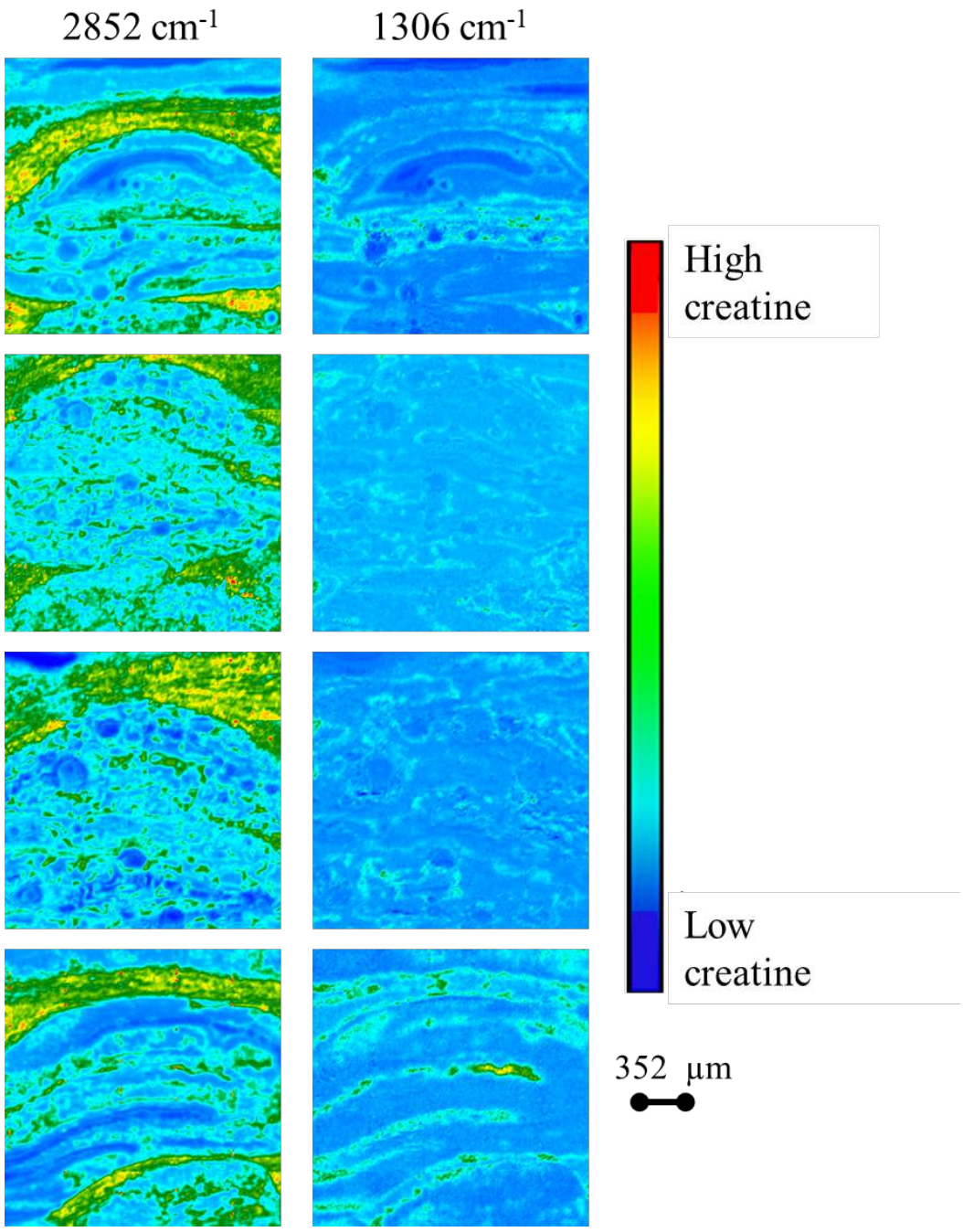

Figure 5.4C. Representative spectrochemical images of hippocampus for creatine distribution in 13MICE0019 (9-month background male mouse on 3% creatine enriched diet). The spectrochemical images were processed for distribution of lipids (2852 cm^{-1}) to establish tissue morphology and creatine (1306 cm^{-1}) to assess creatine localization. The images were processed with methods outlined in table 4.1. FPA images are mosaics of 5 × 5 tiles. One tile = 64 × 64 pixels = 352 × 352 µm. As per scale, the red color represents areas with high creatine concentration. There was no evidence of creatine in this animal (1306 cm^{-1}). Upper scale = 2.560, Lower scale = -0.6970.

Figure 5.5A, 5.5B & 5.5C depict spectrochemical images for creatine distribution in C57BL/6 mice on control diet. The corresponding mice on control diet i.e. 13MICE0005 & 13MICE0006 also displayed creatine localization in some of the hippocampal sections (Figure 5.5A & Figure 5.5B).

The background (C57BL/6) animals on control diet were mostly stored as frozen brain from 2013 until 2017 when they were sectioned and imaged. These animals were cryosectioned in 2017 but the tissue quality was poor. Long term storage had affected the tissue quality tremendously. Most of the sections obtained were distorted. There were only 1 or 2 sections for 13MICE0005 & 13MICE0006 on BaF_2 slides that were acquired in 2013. The animal 13MICE0007 had a few decent quality sections i.e. 3 (Table 5.1) acquired in 2017 that were imaged (Figure 5.5C). There was no evidence of creatine in any of the sections imaged for 13MICE0007. All the background mice were males, so there is no data for female C57BL/6 mice. It is not clear whether creatine diet had impacted the creatine distribution in these mice, due to inconsistencies in creatine appearance in sections obtained from the same animal, limited number of sections available for imaging in some animals due to long term storage effect and absence of quantitative analysis.

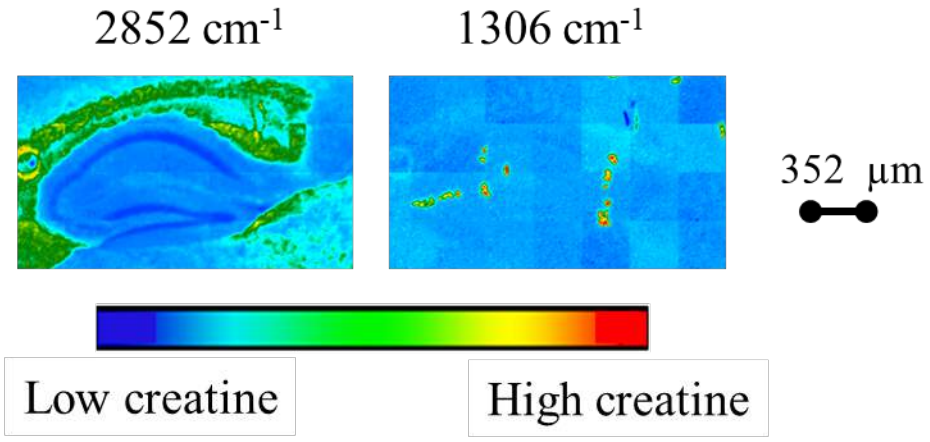

Figure 5.5A. Spectrochemical image of hippocampus for creatine distribution in 13MICE0005 (9-month background male mouse on control diet). The spectrochemical image was processed for distribution of lipids (2852 cm^{-1}) to establish tissue morphology and creatine (1306 cm^{-1}) to assess creatine localization. The image was processed with methods outlined in table 4.1. FPA image is a mosaic of 7 × 4 tiles. One tile = 64 × 64 pixels = 352 × 352 µm. As per scale, the red color represents areas with high creatine concentration. Creatine in form of punctate was detected in this section (the only optimum quality section available for animal 13MICE0005). Upper scale = 0.4325, Lower scale = -0.6970. Note: This image was recorded by Peter Trokajelo in 2013.

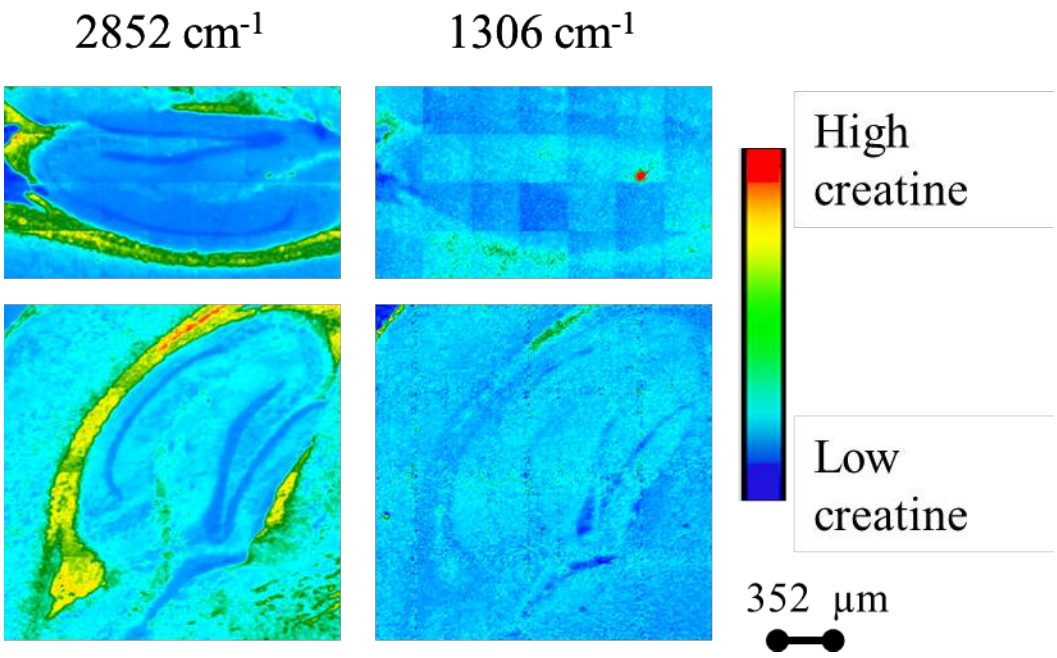

Figure 5.5B. Spectrochemical images of hippocampus for creatine distribution in 13MICE0006 (9-month background male mouse on control diet). The spectrochemical images were processed for distribution of lipids (2852 cm^{-1}) to establish tissue morphology and creatine (1306 cm^{-1}) to assess creatine localization. The images were processed with methods outlined in table 4.1. FPA images are mosaics of 7 × 4 & 5 × 5 tiles. One tile = 64 × 64 pixels = 352 × 352 µm. As per scale, the red color represents areas with high creatine concentration. Creatine in form of punctate was observed one of these sections. Upper scale = 0.2650, Lower scale = -0.022.

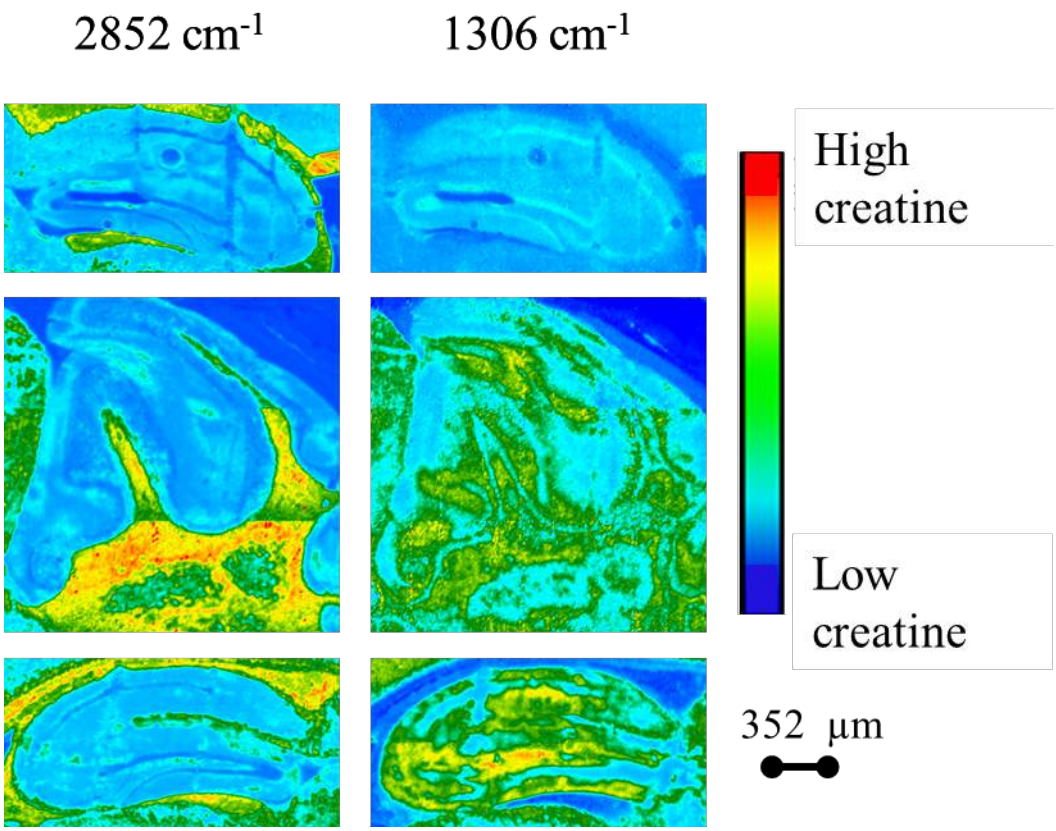

Figure 5.5C. Spectrochemical images of hippocampus for creatine distribution in 13MICE0007 (9-month background male mouse on control diet). The spectrochemical images were processed for distribution of lipids (2852 cm^{-1}) to establish tissue morphology and creatine (1306 cm^{-1}) to assess creatine localization. The images were processed with methods outlined in table 4.1. FPA images are mosaics of 4 × 2, 3 × 3 & 4 × 2 tiles. One tile = 64 × 64 pixels = 352 × 352 µm. As per scale, the red color represents areas with high creatine concentration. There was no evidence of creatine in this animal. Upper scale = 2.060, Lower scale = -0.6270.

5.3.2 Effect of creatine diet on 3xTg male mice compared to control diet

In this study, there were only two 3xTg male mice, one of which was on the creatine diet (3xTg-362) while the other was on the control diet (3xTg-383). A total of 16 sections were examined for mouse 3xTg-362 and 8 sections for 3xTg-383. Representative images of these animals are shown in Figure 5.6 A & Figure 5.6B. Images of all the sections for these animals are presented in the appendix (Chapter 8, Appendix I, Figure 8.11-8.18). Out of 16 sections imaged for 3xTg-362, 10 were loaded with creatine throughout the hippocampus and the cerebellum (Figure 5.6A (i) & Figure 5.6 (ii)). The remaining 6 sections had no evidence of creatine presence (Chapter 8, Appendix I, Figure 8.11-8.15). The majority of the sections imaged for this animal i.e. 10 out of 16 had visual appearance of creatine. 6 out of 10 sections however did not contain creatine. The long term freeze storage may have affected the distribution of creatine (detected based on visual appearance of creatine in false color images). These animals were sacrificed in 2013. Post cryosectioning, the sections were mounted on MirrIR slides (Low-e MirrIR^{TM}, Kevley Technologies, Chesterland, OH) slides and were stored at – 80 ° C until 2017 when they were thawed and imaged.

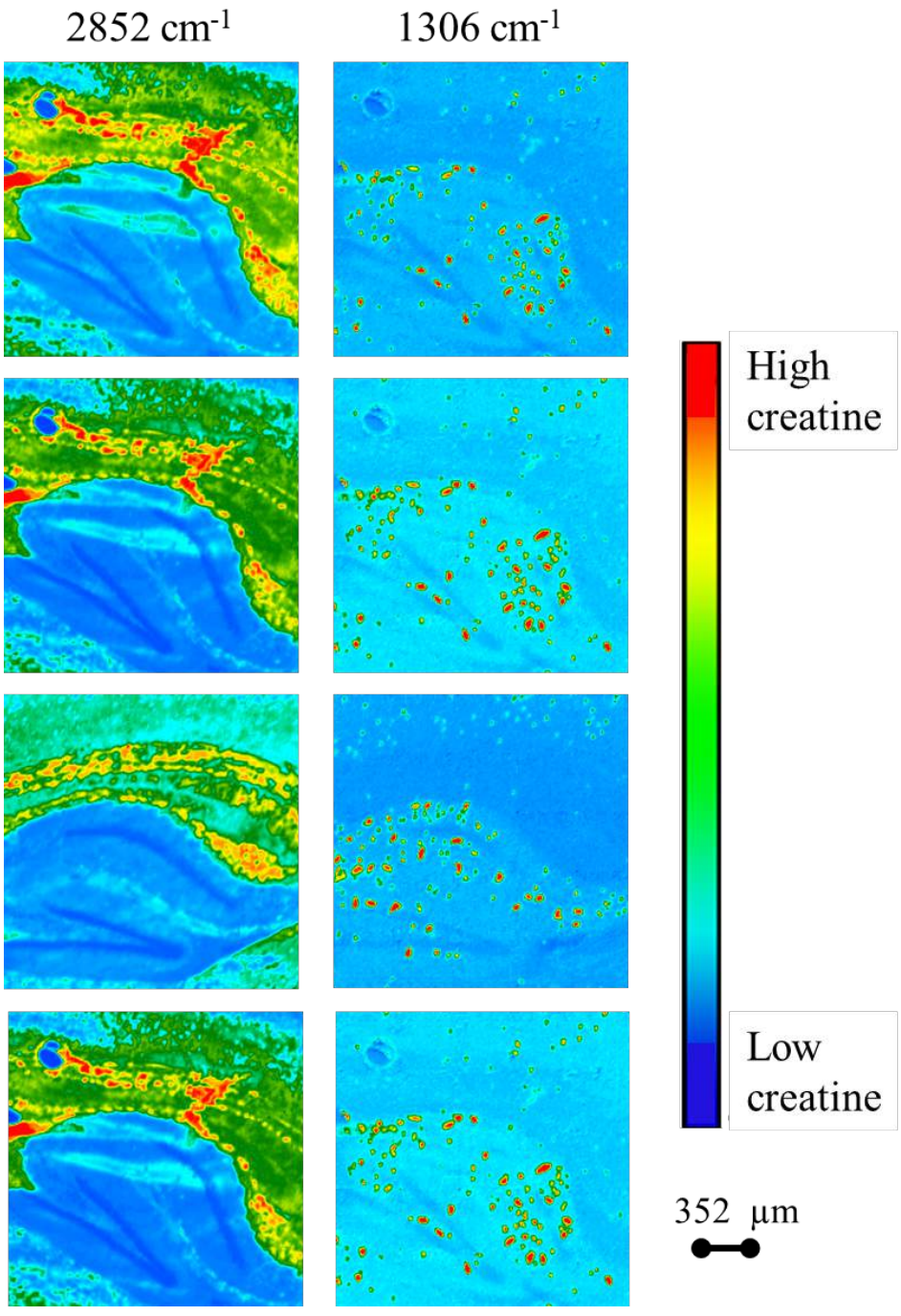

Figure 5.6A (i). Representative spectrochemical images of the hippocampus for creatine distribution in 3xTg male mouse on creatine diet (serial sections from 3xTg-362). The spectrochemical images were processed for distribution of lipids (2852 cm^{-1}) to establish tissue morphology and creatine (1306 cm^{-1}) to assess creatine localization. The images were processed with methods outlined in table 4.1. All FPA images are mosaics of 5 × 5 tiles. One tile = 64 × 64 pixels = 352 × 352 µm. As per scale, the red color represents areas with high creatine concentration. There are creatine crystals throughout the hippocampus. Upper scale = 0.6216, Lower scale = -0.1540.

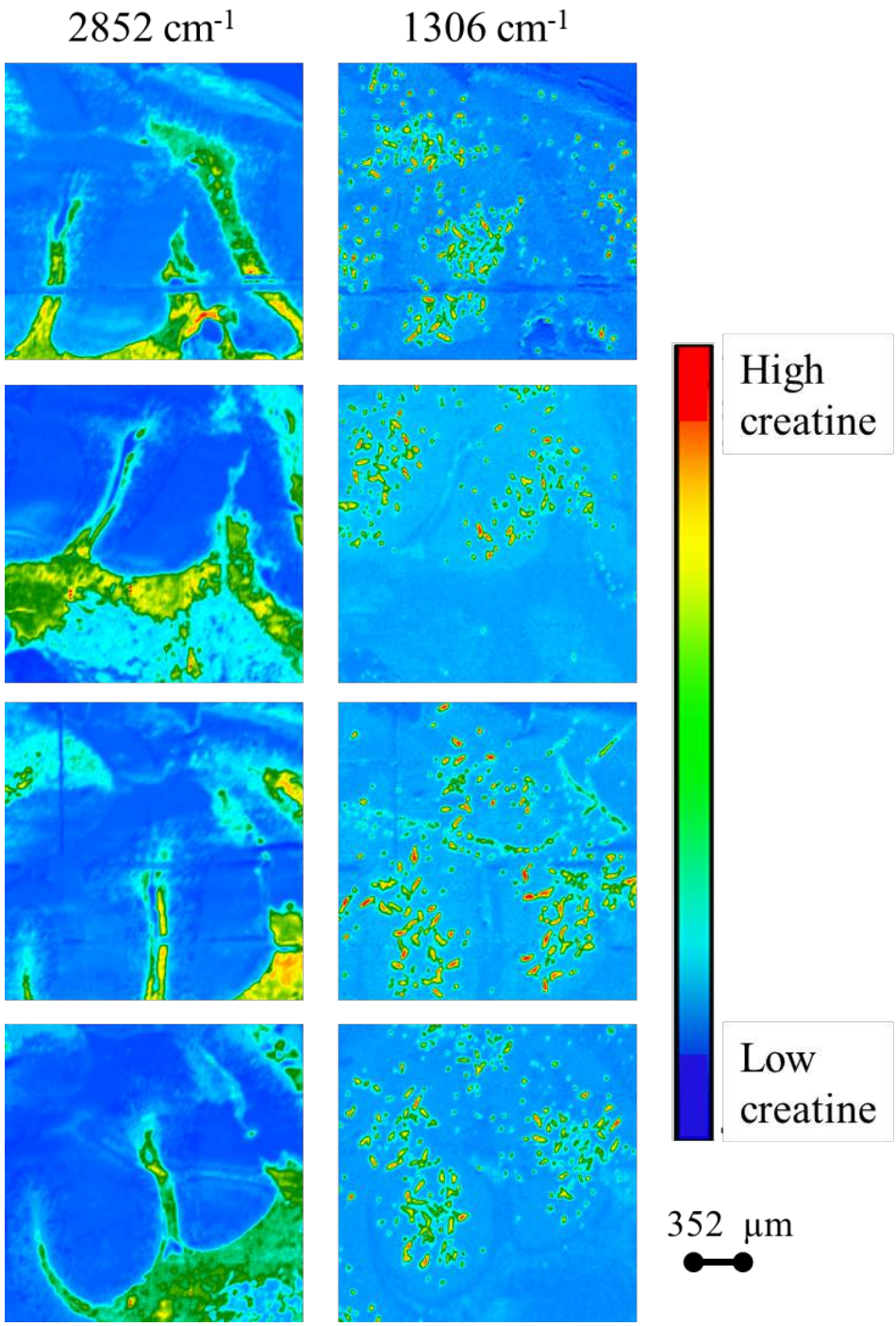

Figure 5.6A (ii). Spectrochemical images of the cerebellum for creatine distribution in 3xTg male mouse on creatine diet (serial sections from 3xTg-362). The spectrochemical images were processed for distribution of lipids (2852 cm^{-1}) to establish tissue morphology and creatine (1306 cm^{-1}) to assess creatine localization. The images were processed with methods outlined in table 4.1. All FPA images are mosaics of 5 × 5 tiles. One tile = 64 × 64 pixels = 352 × 352 µm. As per scale, the red color represents areas with high creatine concentration. The cerebellum images have extensive appearance of creatine crystals. Upper scale = 0.6617, Lower scale = -0.1540

For the counterpart of this male mouse on the control diet, i.e., 3xTg-383 (Figure 5.6B), there was no evidence of creatine appearance in any of the 8 sections that were imaged. Representative images are shown in Figure 5.6B and remaining sections are presented in the appendix. (Chapter 8, Appendix I, Figure 8.17-8.18). Thus, the 3xTg male mouse on creatine diet had extensive localization of creatine throughout the hippocampus (figure 5.6A (i & ii)) whereas the corresponding 3xTg male mice on standard/control diet did not contain creatine crystals (Figure 5.6B). It can not be confirmed whether the extensive appearance of creatine was associated with the creatine enrichment. This is because the sample size is inadequate for this gender i.e. only two 3xTg male mice where one (3xTg-362) was on creatine-enriched diet while the other one (3xTg-383) was on control diet. The absence of creatine crystals in 3xTg-383 might also be attributed to freeze storage effect since these sections were stored as frozen slides for more than 6 years prior to imaging. Hence with all these uncertainties, it is not possible to establish the effect of creatine dietary enrichment in this pilot study. Instead the study was directed and focused on optimizing methods of tissue preparation and storage to establish a working methodology for future studies.

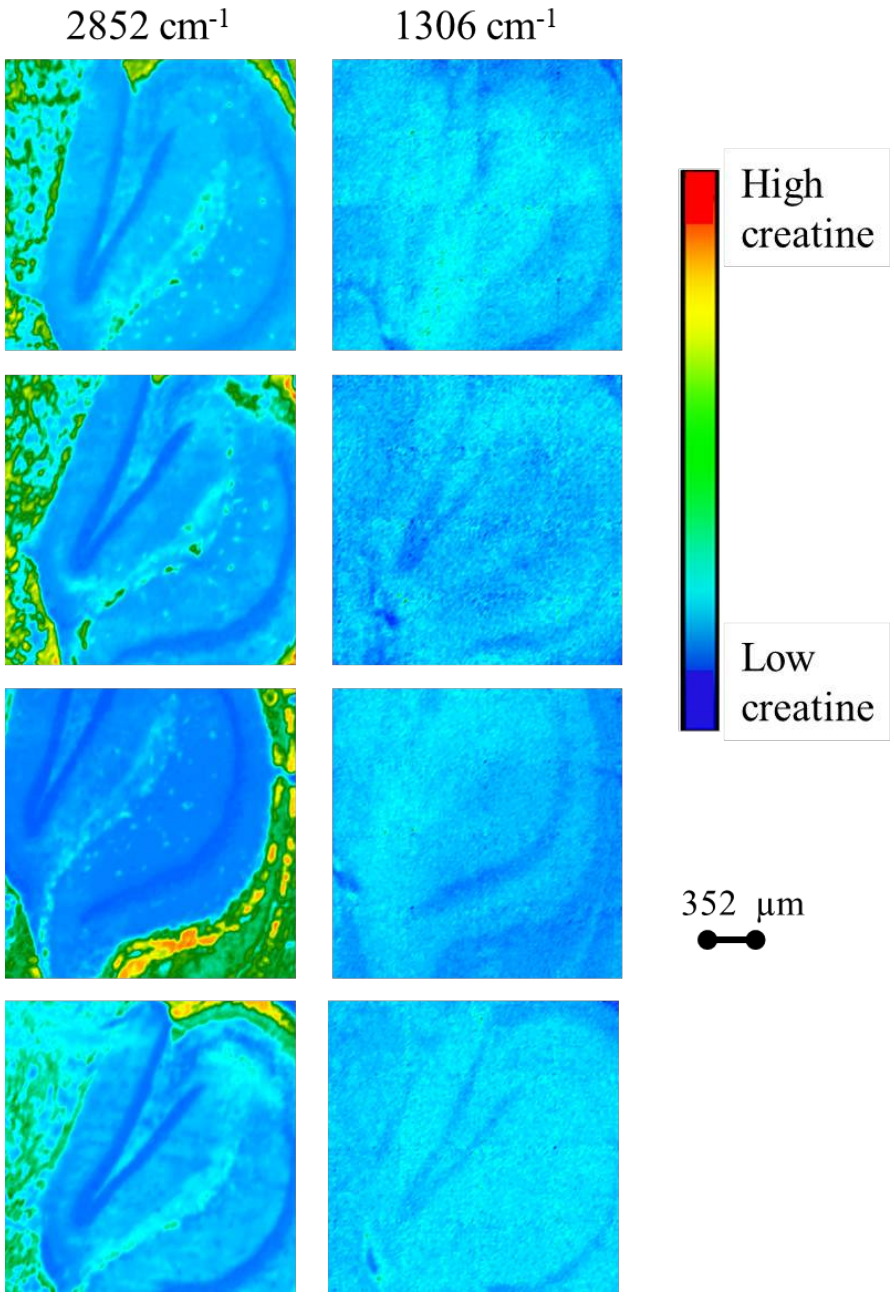

Figure 5.6B. Representative spectrochemical images of hippocampus for creatine distribution in 3xTg male mouse on a standard diet (3xTg-383). The spectrochemical images were processed for distribution of lipids (2852 cm^{-1}) to establish tissue morphology and creatine (1306 cm^{-1}) to assess creatine localization. The images were processed with methods outlined in table 4.1. All FPA images are mosaics of 5 × 5 tiles. One tile = 64 × 64 pixels = 352 × 352 µm. As per scale, the red color represents areas with high creatine concentration. The hippocampal spectrochemical images of this animal (3xTg-383) did not contain any evidence of creatine crystals. In contrary, the corresponding 3xTg male mouse on creatine diet (3xTg-362, Figure 5.6A(i)) had an extensive appearance of creatine throughout the hippocampus. Upper scale = 0.2711, Lower scale = -0.0230.

5.3.3 Effect of creatine diet on 3xTg/AD female mouse compared to control diet

Figures 5.7A & 5.7B and Figure 5.8A & 5.8B represent spectrochemical images of representative sections from female 3xTg mice on creatine diet (3xTg-363 & 3xTg-365) and the counterpart female mice on control diet (3xTg-381 & 3xTg-382) respectively. Several sections were examined from the female 3xTg mice on creatine and control diet group; however, a few are represented in Figure 5.7A & B. A full set of images is presented in the appendix (Chapter 8, Appendix I, Figure 8.18-8.20). For the female 3xTg mouse on creatine diet, out of 7 hippocampal sections from 3xTg-363, none of the sections had creatine appearance (Figure 5.7A). This was similarly observed in the second female 3xTg mouse on creatine diet, i.e., 3xTg-365 where out of 7 sections that were imaged, none of the sections had evidence of creatine appearance.

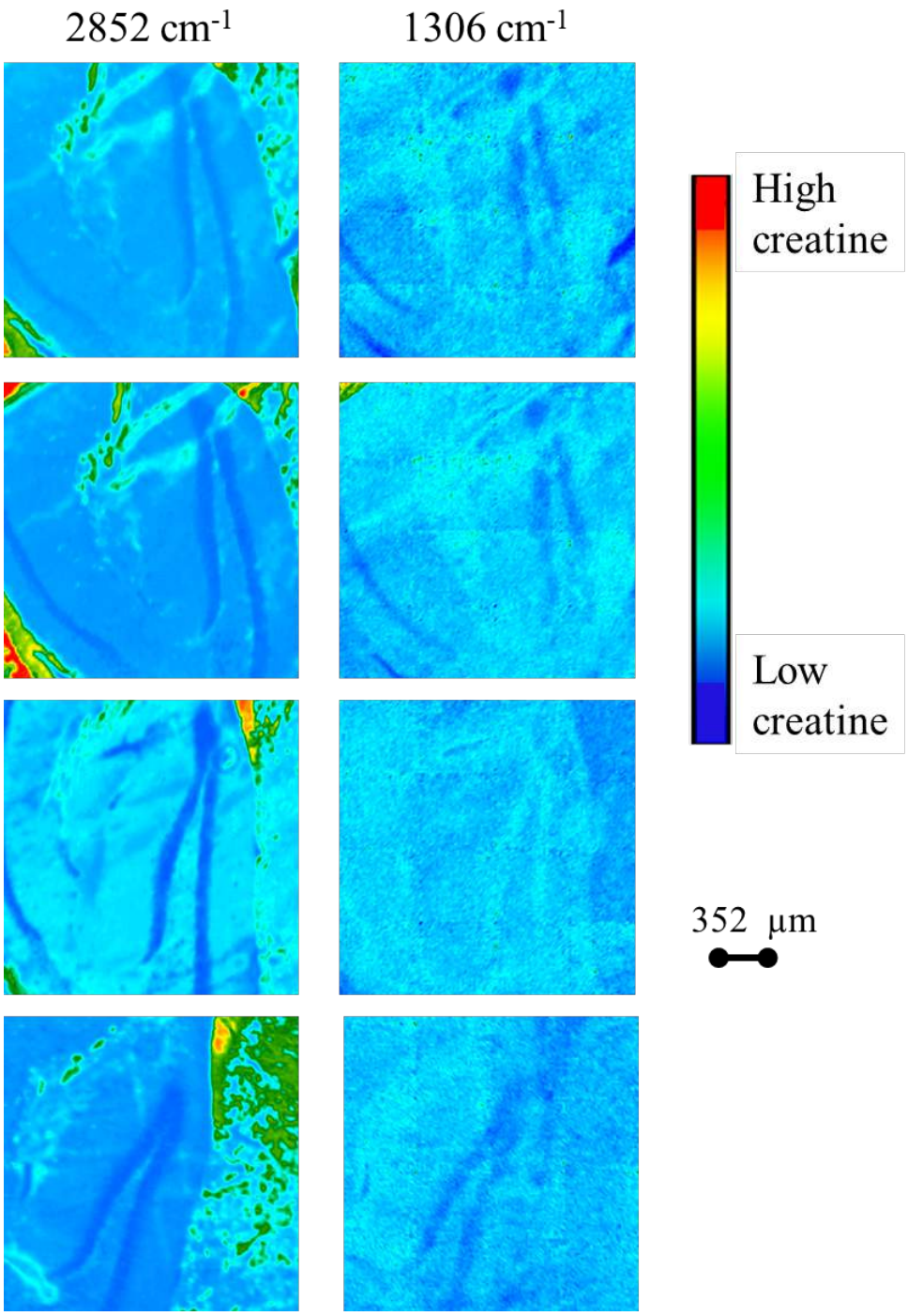

Figure 5.7A. Representative spectrochemical images of creatine distribution in 3xTg female mouse on creatine diet (3xTg-363). The spectrochemical images were processed for distribution of lipids (2852 cm^{-1}) to establish tissue morphology and creatine (1306 cm^{-1}) to assess creatine localization. The images were processed with methods outlined in table 4.1. FPA images are mosaics of 5 × 5 tiles. One Tile = 64 × 64 pixels = 352 × 352 µm. As per scale, the red color represents areas with high creatine concentration. There was no evidence of creatine appearance in these images. Upper scale = 0.2610, Lower scale = -0.0220.

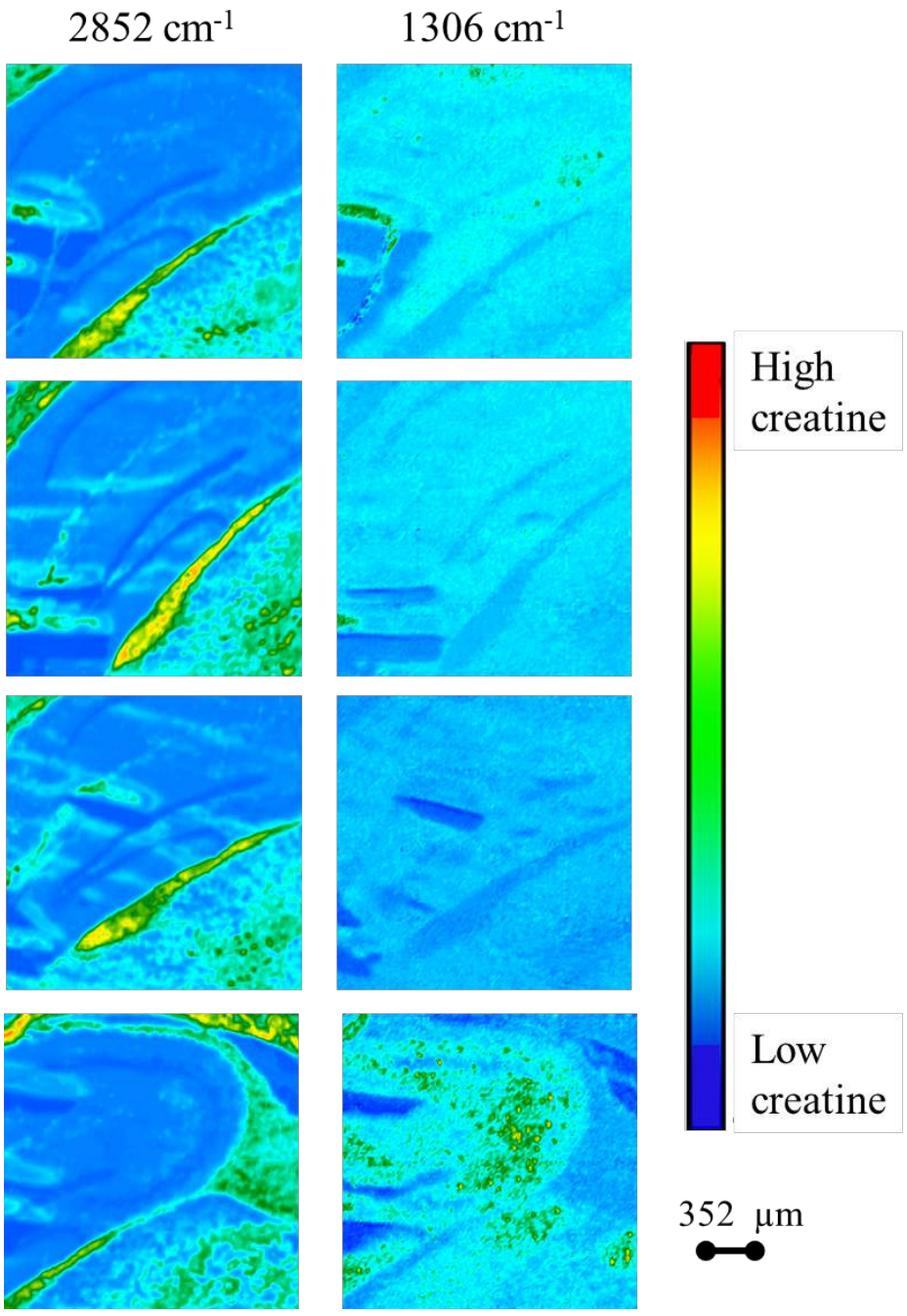

Figure 5.7B. Representative spectrochemical images of creatine distribution in 3xTg female mouse on creatine diet (3xTg-365). The spectrochemical images were processed for distribution of lipids (2852 cm^{-1}) to establish tissue morphology and creatine (1306 cm^{-1}) to assess creatine localization. The images were processed with methods outlined in table 4.1. FPA images are mosaics of 5 × 5 tiles. One Tile = 64 × 64 pixels = 352 × 352 µm. As per scale, the red color represents areas with high creatine concentration. The visual inspection of these sections did not show any evidence of creatine presence. This was similarly observed in 3xTg-363 (Figure 5.7A). Upper scale = 0.2610, Lower scale = -0.0220.

In comparison, the two female 3xTg mice on the control diet had creatine crystals (representative images in Figure 5.8A & B). All the spectrochemical images for these animals are presented in the appendix (Appendix I, Chapter 8, 8.21-8.26). Out of 15 sections that were imaged for 3xTg-381, 6 sections were loaded with creatine crystals, 5 sections had a few scattered solid creatine crystals (punctate crystals), and 5 sections had traces of creatine, i.e., a few small creatine crystals. However, the second female 3xTg mouse on the control diet had creatine appearance only in one section out of the 8 sections that were imaged. Thus, the visual inspection of false color images from female 3xTg mice depicts presence of creatine in the control group. Conversely, the female mice on creatine diet did not show any evidence of creatine in all the hippocampal sections that were imaged. It is not clear why the female transgenic mice on creatine diet did not contain any creatine crystals. This is opposite to the creatine appearance in the male transgenic mice. The male 3xTg mouse on control diet (3xTg-383, Figure 5.6B) did not show any evidence of creatine crystals whereas the male 3xTg mouse on creatine diet (3xTg-362, Figure 5.6A) demonstrated extensive appearance of creatine crystals in most of the sections that were imaged i.e. 10 out of 16 sections. There seems to be a difference in response to creatine diet between the female and male transgenic mice. However, this can not be ascertained with this sample size. The sample size for each gender was too small i.e. only two male transgenic mice and 4 female transgenic mice.

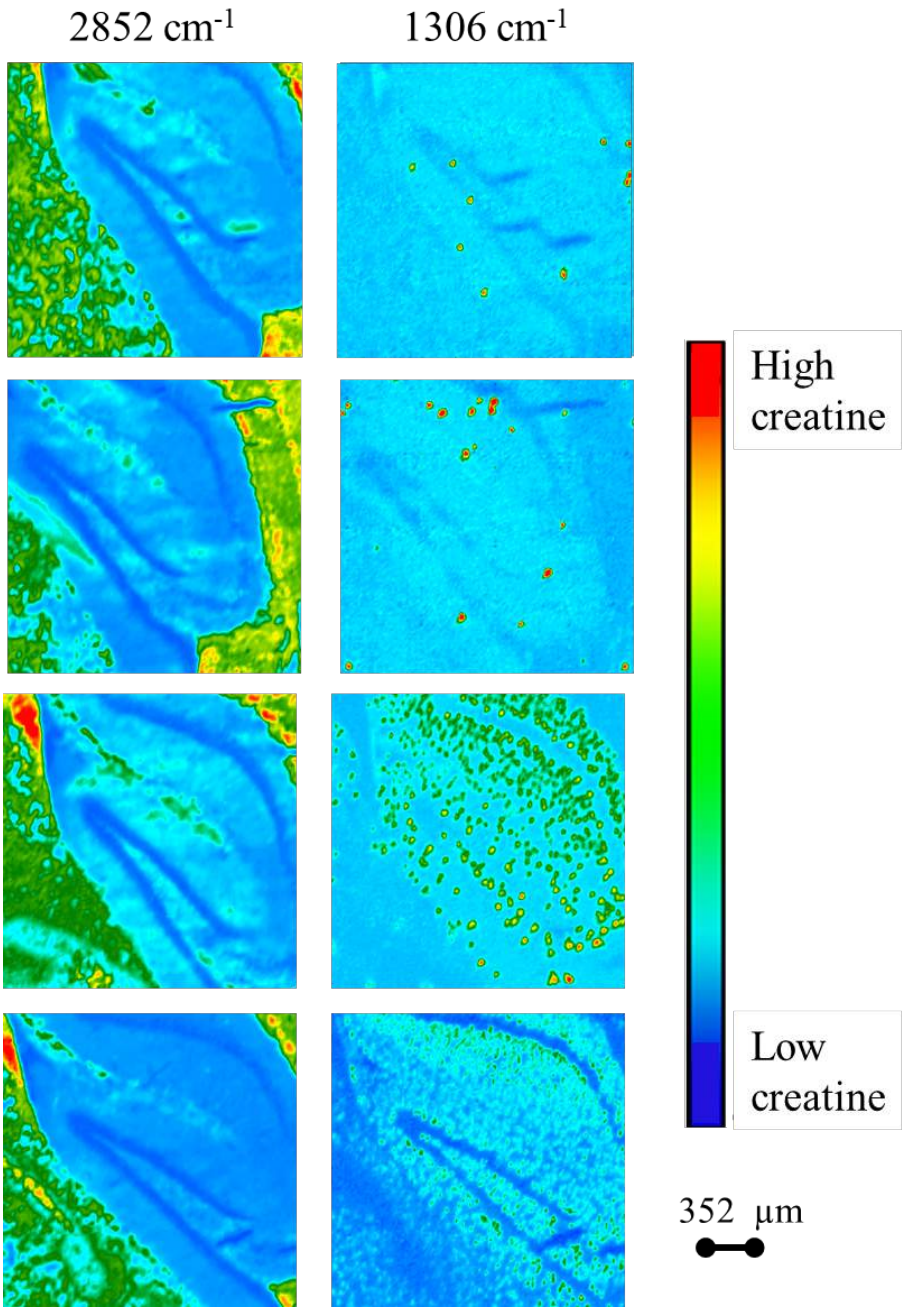

Figure 5.8A. Representative spectrochemical images of creatine distribution in 3xTg female mouse on control diet (3xTg-381). The spectrochemical images were processed for distribution of lipids (2852 cm^{-1}) to establish tissue morphology and creatine (1306 cm^{-1}) to assess creatine localization. The images were processed with methods outlined in table 4.1. FPA images are mosaics of 5 × 5 tiles. One tile = 64 × 64 pixels = 352 × 352 µm. As per scale, the red color represents areas with high creatine concentration. 3xTg-381 contained creatine crystals that were scattered throughout the hippocampus. Some of the sections demonstrated creatine presence, in contrast, the female mice on creatine diet did not contain creatine. Upper scale = 0.2610, Lower scale = -0.0220.

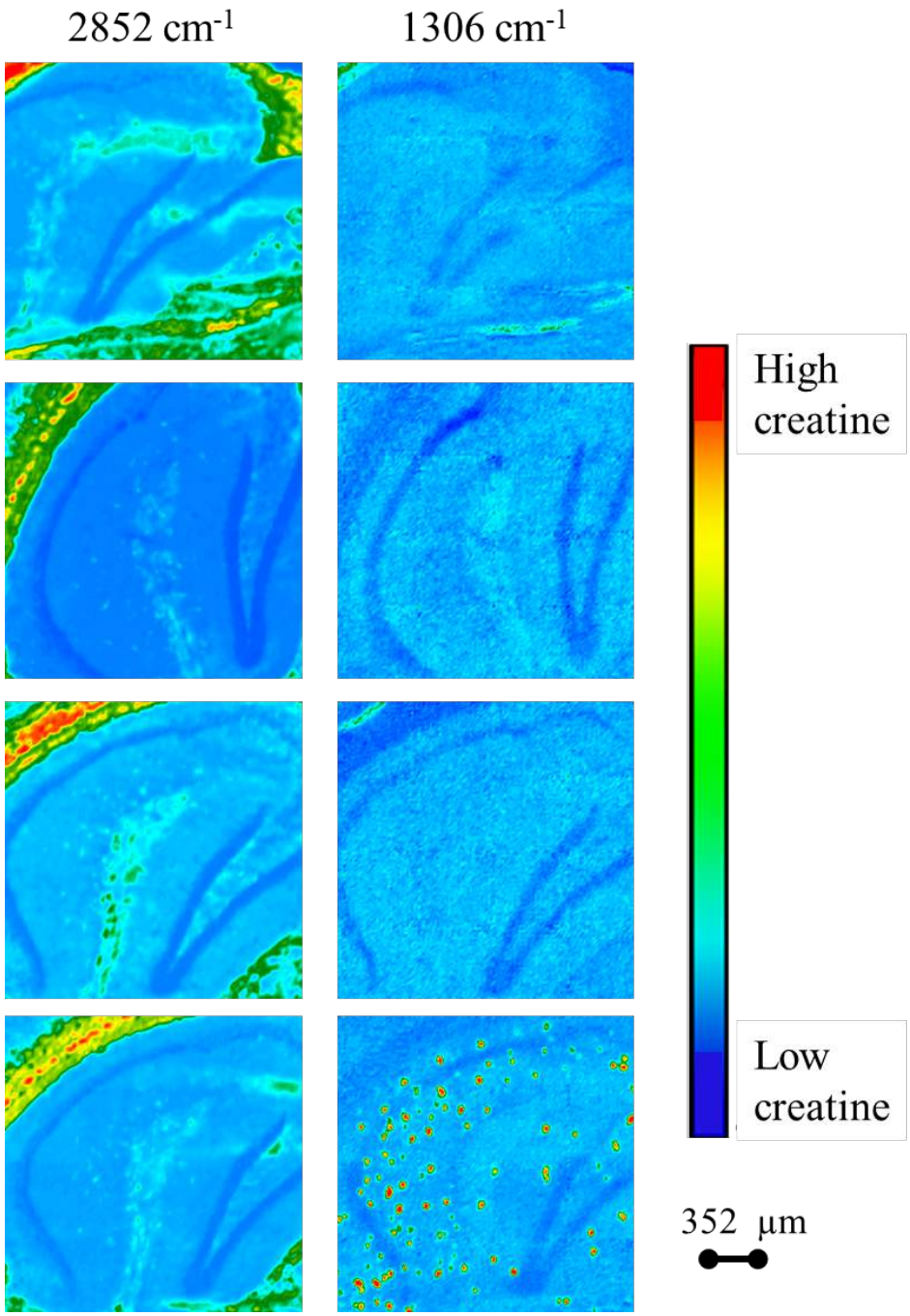

Figure 5.8B. Representative spectrochemical images of creatine distribution in 3xTg female mouse on control diet (3xTg-382). The spectrochemical images were processed for distribution of lipids (2852 cm^{-1}) to establish tissue morphology and creatine (1306 cm^{-1}) to assess creatine localization. The images were processed with methods outlined in table 4.1. FPA images are mosaics of 5 × 5 tiles. One tile = 64 × 64 pixels = 352 × 352 µm. As per scale, the red color represents areas with high creatine concentration. Most of the sections did not contain creatine, only one of the imaged sections contained creatine (extensive creatine presence). Upper scale = 0.2610, Lower scale = -0.0220.

55.4 Effect of dietary creatine enrichment on the hippocampal creatine accumulation

FTIR spectrochemical imaging was used to examine brain tissue sections from 9-month old 3xTg mice expressing triple mutations of PSI_{M146V}, APP_{Swe}, tau_{P301L} transgenes and age-matched background mice (C57BL/6). A total of 12 mice (6 3xTg & 6 C57BL/6) were used in this study. 3xTg and C57BL/6 animals were each divided into two groups (n = 3) to be fed regular or creatine-enriched diets. The 3xTg mice included mice from both genders, whereas the C57BL/6 mice were male mice. Effect of 3 % w/w dietary creatine supplementation was then evaluated in these mice. Table 5.1 is a summary of the results obtained from this dietary study.

Table 5.2. Creatine localization (based on visual appearance in spectrochemical images) in 9-month 3xTg & C57BL/6 mice.

Diet	**Background Mice (C57BL/6)**			**Transgenic Mice (3xTg)**		
Control	Minor/Traces	Minor/Traces	None	Ocassional Presence	Occasional Presence	Minor
Creatine	Occasional presence	Occasional presence	None	None	None	Extensive

The visual inspection of spectrochemical images of C57BL/6 (background mice) on 3 % creatine diet (Figure 5.4A-C) revealed an occasional presence of creatine crystals in these mice. In comparison the C57BL/6 mice on a standard diet (Figure 5.5 A-C) had hardly contained creatine. However, this can not be confirmed since the number of sections imaged were not adequate for statistical analysis. Sometimes there was only one section due to poor tissue quality resulting from long term freeze storage of the whole un-sectioned tissue. Apart from that creatine distribution was

not uniform even on sections obtained from the same animal and mounted on the same slide. Thus, with all these inconsistencies, it was not possible to draw any conclusions. The 3xTg male mouse on creatine diet (section 5.6A) had extensive appearance of creatine (10 out of 16 sections) whereas the counterpart male mice on standard diet (Figure 5.6B) had almost no creatine appearance (only 1 or two small crystals were observed).

The visual appearance of creatine in this study i.e. extensive appearance in 3xTg male mouse and occasional appearance in C57BL/6 mice on 3 % creatine diet is in line with results obtained from the same dietary study by Dr. Albensi's group for the same cohort of mice (Snow et al., 2018). The study investigated the effects of dietary creatine enrichment (3%) on hippocampal-dependent functions of C57BL/6 mice. A total of 18 C57BL/6 mice were used that were either on control diet (n=8) or creatine supplemented diet (n=10). Morris water maze (MWM) tests and mitochondrial oxygen consumption rates were examined to assess the cognitive function in these mice before and after creatine supplementation. The levels of transcription factors and various types of proteins critical to memory formation and cognitive function were measured using Western blot analysis. These included mitochondrial proteins such as electron transport chain complex I and mitochondrial fission protein, transcription factors and their associated proteins i.e. IκB (NF-κB inhibitor indicative of NF-κB activity), CREB (cAMP response element binding protein) and Egrl (early growth factor protein) and plasticity-related proteins such as CaMKII (calcium/calmodulin-dependent protein kinase II), PSD95 (postsynaptic density protein95) and Egr2 (another transcription protein). It was reported that creatine ingestion decreased the escape latency/time in the MWM test and increased coupled respiration rate in hippocampal mitochondria. The creatine concentration the hippocampus increased by 8.7 % in the creatine supplemented group. The levels of CaMKII, PSD-95, and Complex I proteins increased in mice that were on

creatine enriched diet. The IκB level, which is a measure of NF-κB-mediated signaling decreased. The data demonstrated that dietary creatine supplementation could improve learning, memory and mitochondrial function in male background mice.

Conversely, the female 3xTg mice on creatine diet in this FTIR study did not show any evidence of creatine localization in the hippocampus (Figure 5.7A & Figure 5.7B). Instead, the 3xTg female mice on control diet contained creatine (Figure 5.8A & Figure 5.8B). There is no comparable data for female C57BL/6 mice in this study. Despite the fact that the number of animals from each gender is small, table 5.2 indicates that there maybe a gender related difference in response to creatine enriched diet. However, this can not be ascertained with this sample size. The sample size for each gender was small i.e. only two male transgenic mice and 4 female transgenic mice. This gender related difference in response is further described in the following section (section 5.5).

5.5 The impact of gender on the hippocampal accumulation of creatine

The creatine diet may have impacted the distribution and appearance of creatine in male 3xTg and C57BL/6 mice. However, this cannot be ascertained owing to gender mismatch and discrepancy in the creatine distribution over brain tissue sections from the same animals. There were a limited number of 3xTg female and male mice that were randomly assigned to either creatine or control diet. There were 4 female 3xTg mice (n = 2 creatine diet group & n = 2 control diet group) and 2 male 3xTg mice (n = 1 creatine diet group & n = 1 control diet group). There were no female C57BL/6 mice in this dietary study for gender effect comparison. All C57BL/6 mice were male mice (n = 6).

Gender mismatch may have impacted the results of this study in several ways. Several studies have reported that neuropathology development is dependent on age and gender. A study by Oh et al. reported age and gender dependent pathology in 3xTg mice (Oh et al., 2010). Both male and female 3xTg mice were used. The 9-month male mice had no plaque pathology whereas the female age-matched mice had already developed plaque pathology at this age. In another study, the male transgenic mice (3xTg) only developed extracellular plaques in the hippocampus at the age of 15 months whereas the tau helical filaments only developed starting from 18 months and proceeded to the age of 26 months (Mastrangelo & Bowers 2008). Another study reported that Aβ 1–40 and 1–42 were only detectable at the age of 16 months in male 3xTg-AD mice (Hirata-Fukae et al., 2008). There is evidence of a variation in the onset age for the development of AD pathology that may be attributed to several factors such as phenotype loss associated with progressive breeding of the animals, or due to housing conditions for each animal colony (Mastrangelo & Bowers 2008, Oh et al, 2010, Hirata-Fukae et al, 2008). Thus, based on literature, it appears that the male 3xTg mice develop plaque pathology beyond 9 months of age. The dietary study in this thesis involved only two 9-month 3xTg male mice (3xTg-362 & 3xTg-383). The 3xTg-362 had extensive appearance of creatine (10 out of 16 sections) whereas 3xTg-383 did not exhibit any evidence of creatine presence (Figure 5.6A & Figure 5.6B). The creatine diet might have assisted in maintaining brain bioenergetics. However, the sample size for this gender, i.e., only two 3xTg male mice used in this study, and anomalies in creatine distribution patterns that had to do with sample preparation (Chapter 6), makes it impossible to conclude so.

The female 3xTg mice experience earlier and more severe plaque pathology compared to age-matched male mice (Oh et al., 2010). Another study evaluated the effect of gender difference

on AD pathology development in 3xTg mice. AD pathology, i.e., Aβ load and tau were compared between female and male 3xTg at 9, 16 and 23 months of age (Hirata-Fukae et al., 2008). Aβ production and degradation were also examined by checking the levels of soluble APP cleaved at the β site (sAPPbeta) and neprilysin (Aβ degrading enzyme) as indicators. It was reported that the 3xTg female mice have more aggressive Aβ pathology compared to age-matched male mice. The female mice had significantly higher beta-secretase activity compared to male mice at 9 months of age. Neprilysin levels decreased with aging in both female and male 3xTg mice, but the extent of decrease was greater in female 3xTg mice. This is because neprilysin activity is regulated by estrogen in females. This study suggests that the female mice are more affected by Aβ pathology as they experienced both up-regulation of Aβ production and down-regulation of Aβ degradation with aging (Hirata-Fukae et al., 2008).

Apart from the difference in AD pathology, the males and females store, metabolize and utilize creatine in a sex-specific manner (Ellery et al., 2016). A study on rats reported that the creatine kinase activity (CK activity) is dependent on the sex hormone regulation cycle. The CK activity was found to be directly proportional to estrogen levels and was in synchrony with the estrous cycle (Sömjen et al., 1991). Another study investigated the effect of 2 % and 4 % dietary creatine on depression-related hippocampal gene expression and behaviors in rats in the presence and absence of sex steroids (Allen et al., 2015). The effect of creatine diet on sham and gonadectomized female and male rats was compared to rats on a regular diet, i.e., control group. Creatine had no effect on gene expression or behavior in sham, gonadectomized and ovariectomized, rats without hormone replacement. Instead, creatine together with sex hormones improved the performance of rats in forced swim test, a test used to evaluate depressive behavior. This study suggested that sex hormones are necessary to achieve the neuroprotective effects of

creatine. Gender, sex hormones, and metabolic status affect the behavioral and neurochemical effect of creatine supplementation (Allen et al., 2015).

Chapter 6. Effect of sample preparation on creatine distribution & build-up

6.1 Anomalies in creatine distribution among serial sections of brain tissue

Review of data presented in chapter 5 and section 6.2 led to a hypothesis concerning the factors affecting the crystallization process, and experiments were designed to elucidate this process. This chapter is an exploration of anomalies in creatine appearance and the experiments conducted to unravel this problem.

In reviewing data of creatine distribution in mice, numerous variations in crystal pattern were evident. There were anomalies in creatine appearance and differences in crystal patterns (morphology) even on sections from the same animal mounted on the same slide (Chapter 5, section 5.3). Historical data were reviewed from both 3xTg and TgCRND8 studies; both published (Gallant 2006, Rak 2007 & Kuzyk et al., 2010) and un-published data. A notable example of crystal morphology variation was observed in previous studies (described in section 6.2). In reviewing these results and consulting older notebooks, it was found that the sample preparation and storage was not always the same. It was hypothesized that methods of tissue acquisition, freezing, storage, transport all could play a role in the ultimate formation of the crystal. Experiments were designed to test some of these possible factors. The objective of these experiments was to at least recreate the freeze-thaw artifact. This chapter will present an overview of crystal morphology variation from this study and previous studies as described in section 6.2. Results of experiments designed to recreate the freeze-thaw artifact are presented in section 6.3.

During the course of this study, several inconsistencies in creatine distribution were observed (Chapter 5, section 5.3). Apart from variation in crystal pattern, there were inconsistencies in creatine crystal presence that were noticed during repeatability experiments. Figure 6.1A-D demonstrates the variation in creatine crystal morphology observed in data obtained from brain tissue from this study and other studies from Dr. Gough's lab. Figure 6.1A shows

irregular crystal morphology observed in brain tissue sections from 3xTg mice from this dietary study (Chapter 5). The creatine crystals from this study were in the form of solid irregular crystals with size varying from 1μm to 1 mm. Figure 6.1B presents irregular crystal morphology observed in brain tissue sections from background mice, i.e., C57BL/6 mice from this dietary study. The creatine distribution pattern was not uniform in brain tissue sections from these mice. The creatine crystal appearance was variable; it appeared as a single massive irregular crystal or irregular crystals in the form of streaks (Figure 6.1B). This crystal morphology in these animals, i.e., 3xTg and C57BL/6 varied even in brain tissue sections from the same animal that were mounted on the same slide.

Figure 6.1C depicts dendritic crystal morphology observed in brain tissue sections from another transgenic mouse line; TgCRND8, from a previous study in Dr. Gough's lab (Kuzyk et al., 2010). This study was a continuation of a previous study that had reported the discovery of elevated creatine deposits in TgCRND8 brain tissue sections (Gallant et al., 2006). The study examined the distribution of creatine, lipids and dense core plaque deposits in brain tissue of TgCRND8 mice. Brain tissue sections from 5, 8, 11, 14 & 17-month old TgCRND8 and littermate control mice were analyzed with FTIR spectroscopy. The study reported that creatine deposits were detected in all TgCRND8 mice and the extent of deposition increased with age. Figure 6.1C (i) & (ii) show sections from 8 and 17-month TgCRND8 mice respectively from this study (Kuzyk et al., 2010). The 17-month TgCRND8 had dendritic crystals throughout the hippocampus (Figure 6.1 C (i)) whereas the 8-month TgCRND8 had a mixture of dendritic and irregular crystals (Figure 6.1 C (ii)). Figure 6.1 D shows irregular crystal morphology observed in the 11-month TgCRND8 brain tissue from the same study (Kuzyk et al., 2010). This crystal appearance pattern demonstrates that crystal morphology, i.e., dendritic or irregular crystals, is independent of the age

of animals. The 8, 11 & 17-month TgCRND8 had either dendritic creatine crystals or a mixture of dendritic and irregular creatine crystals (Figure 6.1C & D). The crystal morphology observed in Figure 6.1C & D demonstrates that crystal morphology had nothing to do with the age of mice but with sample preparation methods.

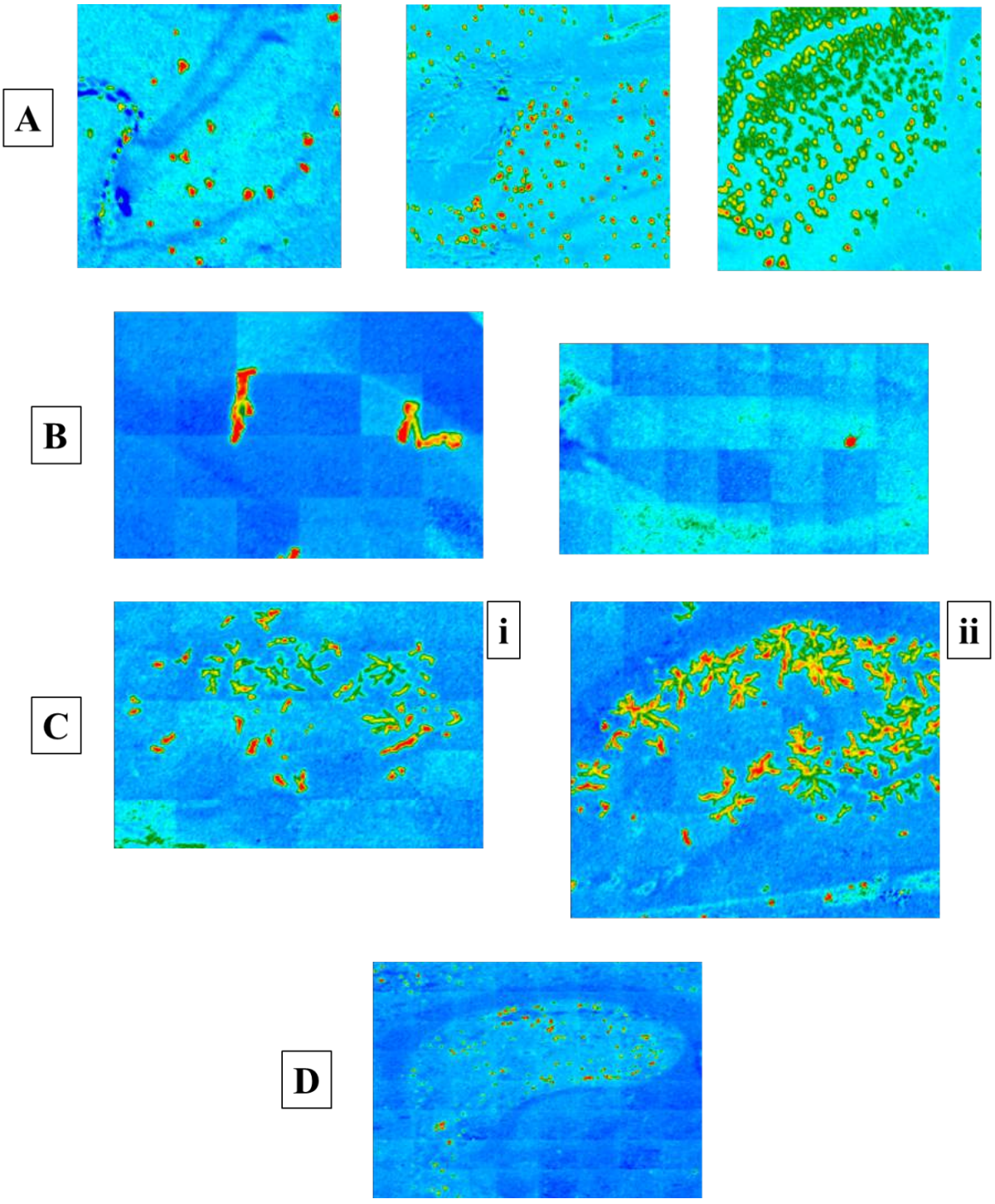

Figure 6.1 A-D. Spectrochemical images of variable creatine morphology**.** A) Irregular crystal morphology in 3xTg male mice on creatine diet. B) Irregular crystal morphology in male C57BL/6 mice on creatine diet. C) Dendritic crystal morphology in 3xTg (TgCRND8) mice on standard diet (Kuzyk et al., 2010). C (i) shows a mixture of irregular and dendritic creatine crystals in 8-month TgCRND8 mouse, whereas C(ii) shows dendritic crystals in 17-month TgCRND8 mouse. D) Irregular crystal morphology in 11-monthTgCRND8 mice (Kuzyk et al., 2010).

6.2 Evaluation of possible causes for anomalies in creatine crystal appearance

The creatine deposition in this dietary study as described in chapter 5 (section 5.3) was different from one section to another. This may be attributed to the fact that the creatine formation *ex vivo* is a diffusion-controlled crystallization process. The crystal growth has not been consistent even in sections of the same animals mounted on the same slide. The shape of growing crystals in diffusion controlled crystallization process is dependent on several factors such as the temperature and pressure involved, concentration of solute, the chemistry and the structure of the mother phase and chemical and heat transport properties of the crystal (Heaney.P, 1997). The creatine crystals in this study were formed by a freeze-thaw crystallization process which could have been affected by temperature, storage conditions, amount of creatine present in brain and impurities that could be entrapped in the crystal lattice. Even the speed of the freezing and thawing process affects the crystallization pattern. The crystallization process itself is an art (Holden.A & Morrison.P, 1982 & "Growing Quality Crystals," n.d). In the case of brain tissue, crystallization is more challenging since the brain composition is not uniform throughout the brain (variable lipids, proteins, etc.).

Another possible cause for the difference in creatine crystallization pattern for crystals from this study and crystals from previous studies (Kuzyk et al.,2010) may be variation in temperature control. There were some differences in the creatine crystallization temperatures involved in this dietary study and the previous studies by Dr. Gough's group (Kuzyk et al., 2010). Previously the freezing was done by immersing a hemisphere of the fresh brain in liquid nitrogen (at -196 °C) whereas in this dietary study, the brain tissue was immersed in isopentane cooled in liquid nitrogen (at -176 °C). The freeze-thaw process with liquid nitrogen frequently yielded dendritic crystals, whereas the freeze-thaw process with isopentane cooled in liquid nitrogen yielded a mixture of single nuclei crystals, irregular crystals and sometimes dendritic crystals. The

temperature gradient involved in freeze-thaw with liquid nitrogen is steeper compared to isopentane cooled in liquid nitrogen that was used in this dietary study. This variation in temperature may have affected the crystallization process.

The speed of crystallization is another factor that influences the crystal shape. The crystallization process in this study was faster, compared to the previous method due to higher temperature involved (isopentane cooled in liquid nitrogen at -176 °C versus liquid nitrogen -196 °C). This faster crystallization process at -176 °C yielded irregular crystals whereas the slower crystallization process at -196 °C yielded dendritic crystals. The fast crystallization process involved in this study may not have provided the crystals enough time to grow into dendritic crystals. Instead, a collection of small irregular crystals was obtained.

The storage period is another factor that may have affected the crystallization process. The tissue sections used in this study were not acquired at one time. Some brain tissue was sectioned in 2013, others in 2017. Post cryosectioning in 2013, the sections were mounted on MirrIR slides and stored in a freezer at - 80˚C. Some of the brain tissue was frozen either as sections mounted on slides or as brain hemispheres at - 80˚C for over six years. This storage period affected the tissue quality that was obvious during cryosectioning in 2017. Upon examining FTIR images of sections of the same animal that were acquired in both 2013 and 2017, inconsistencies in creatine presence were observed. Figure 6.2 A shows the FPA image of the cerebellum from a background mouse brain, i.e., 13MICE0019. The brain tissue from this mouse was freeze stored at - 80˚C for more than six years post animal sacrifice. The tissue was freeze-thawed in 2018. Figure 6.2C shows that creatine crystals were identified on the periphery of the cerebellum. The creatine crystals appeared within the OCT compound outer surface layer, used to embed the brain tissue during freeze sectioning at - 20˚C. Figure 6.2E shows the hippocampus of the same mouse, i.e.,

13MICE0019 having creatine crystals appearing at the edges of the tissue and the OCT (Figure 6.2G). This is clear evidence of creatine migration from brain tissue surface due to the long term storage effect.

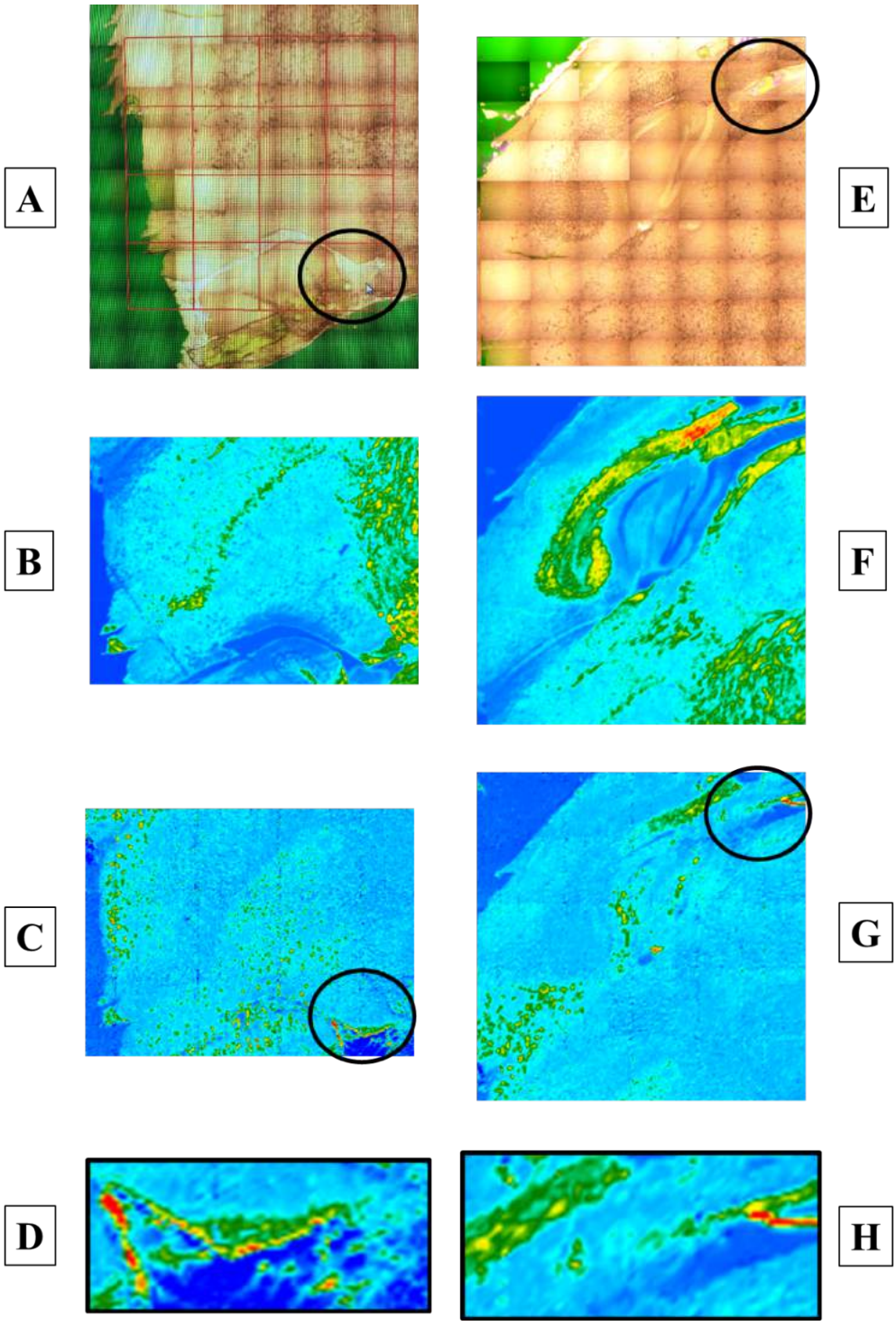

Figure 6.2.A-H Creatine crystals appearing at the periphery of the A) cerebellum. C) The circled region shows creatine crystals on the periphery of the cerebellum, within the OCT outer surface layer. D) is a close-up of the circled region in C). And E) Creatine crystals appearing on the hippocampus. G) The circled region depicts creatine crystals appearing at the edges of the tissue and the OCT. H) is a close-up of the circled region in G). As per scale, the red color represents areas with high creatine concentration. Upper scale = 0.6070, Lower scale = -0.1323

6.3 Experiments designed to recreate the freeze-thaw artifact

Given the anomalies in creatine crystal pattern and the inconsistencies in creatine presence (described in chapter 5, section 5.3) a series of freeze-thaw experiments were conducted. The objective of these experiments was to study the effect of sample preparation in creatine appearance and distribution. The hypothesis was that sample preparation methods, i.e., methods of tissue acquisition, freezing, storage, and transport, could play a role in the ultimate formation of the crystal. The first part of these experiments aimed to evaluate the effect of sectioning conditions on creatine crystal formation and morphology (crystal pattern). The second part of these experiments focused on evaluating the effect of freeze storage and freeze-thaw conditions on creatine crystal appearance and morphology. These experiments are explained in the following sections (section 6.3.1 & 6.3.2).

6.3.1 Effect of Cryosectioning Conditions on Creatine Crystal Formation

Animal 3xTg-448 was chosen for cyrosectioning experiments since this animal had been studied previously and there was information about it. The brain tissue was cryosectioned and almost all the sections including the ones with slight folds were mounted on Kevley slides (Low-e MirrIR^{TM}, Kevley Technologies, Chesterland, OH). Occasionally a few sections were mounted on glass slides, but the focus was to get the maximum number of sections on Kevley slides and study them with FTIR imaging. This was done to ensure that most sections would be imaged and to observe any inconsistencies in creatine crystal appearance occurring as a result of cryosectioning conditions. The sections were acquired with variable cryosectioning conditions. These conditions included cryosectioning with exposure to wind (while the fan was blowing to cool the cryostat, Figure 6.3B) and sheltered wind blow (the sectioning would be stopped while sheltering the brain

tissue from wind and resume sectioning when the cooling cycle ceases, Figure 6.3A). The cool air circulates through the sample compartment to maintain the temperature of the cryochamber. The objective of this experiment was to check whether the wind blow affects the quality of the brain tissue sections or creatine crystal formation. A series of sections were acquired and imaged with FTIR. The evaluation of these FTIR spectrochemical images did not lead to any conclusive results. These images are presented in the appendix (Chapter 9, Appendix II, Figure 9.1-9.13). The cryosectioning conditions do not impact the creatine crystal formation.

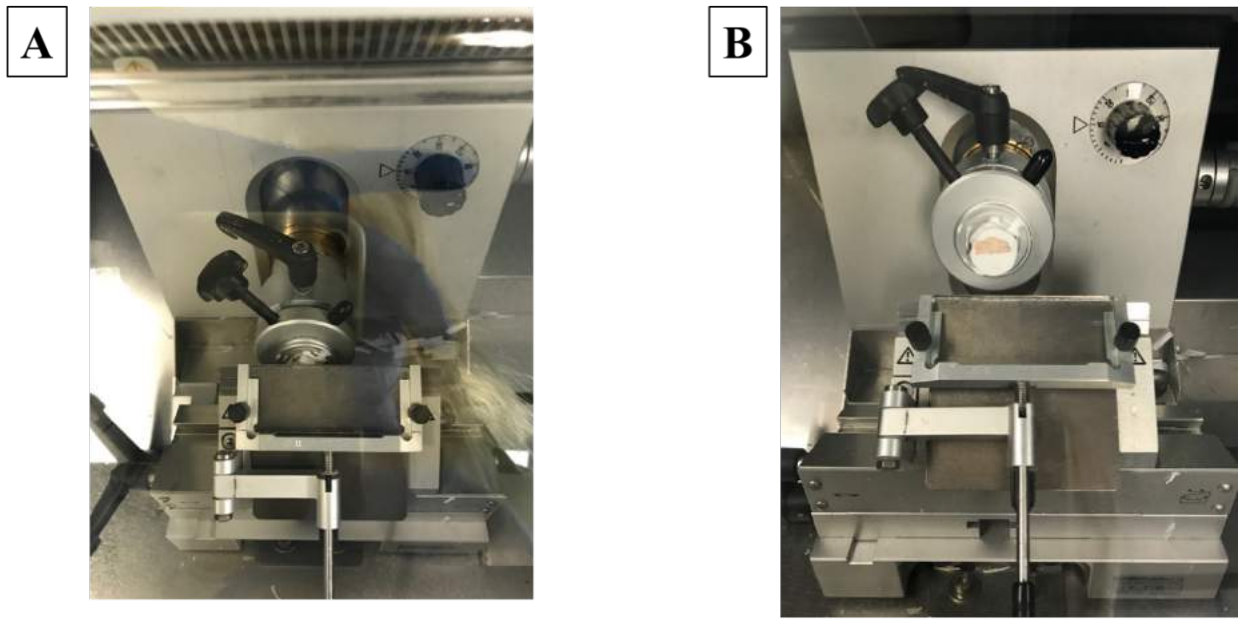

Figure 6.3. Cryosectioning Conditions (sheltered & exposed sectioning)

6.3.2 Effect of Freeze-Thaw conditions on Creatine Crystal Formation

A slide that was previously FTIR imaged and had inconsistencies in creatine distribution was chosen (3xTg-381) for this experiment. The results from 3xTg-381 were described in chapter 5 (section 5.3.3, Figure 5.8A). Figure 6.4 shows the creatine distribution in 8 sections from 3xTg-381 that were mounted on the same slide. The creatine appearance was not consistent across these 8 sections (Figure 6.4). Some sections had creatine crystals throughout the hippocampus (3xTg-381-5 & 6), some had a few scattered creatine crystals (3xTg-381-1, 2, 3, 4 & 7) and 1 section that had no appearance of creatine (3xTg-381-8). The chosen slide for 3xTg-381 was subjected to a series of freeze-thaw experiments. The slide was stored in the freezer at - 80˚C for 24 hours. The slide was then thawed at room temperature for 3 hours. This slide was then returned to the freezer at - 80˚C for 3 hours. This freeze-thaw procedure was repeated 5 times. Then the slide was dried in a desiccator containing silica beads, for 24 hours. All the 8 sections from this slide were FTIR imaged after this repeated freeze-thaw process. The FTIR images were acquired using the same FTIR parameters as images before freeze-thaw experiments. The FTIR images before and after freezing were compared to evaluate the effect of freeze-thaw conditions on creatine distribution. The results are described below.

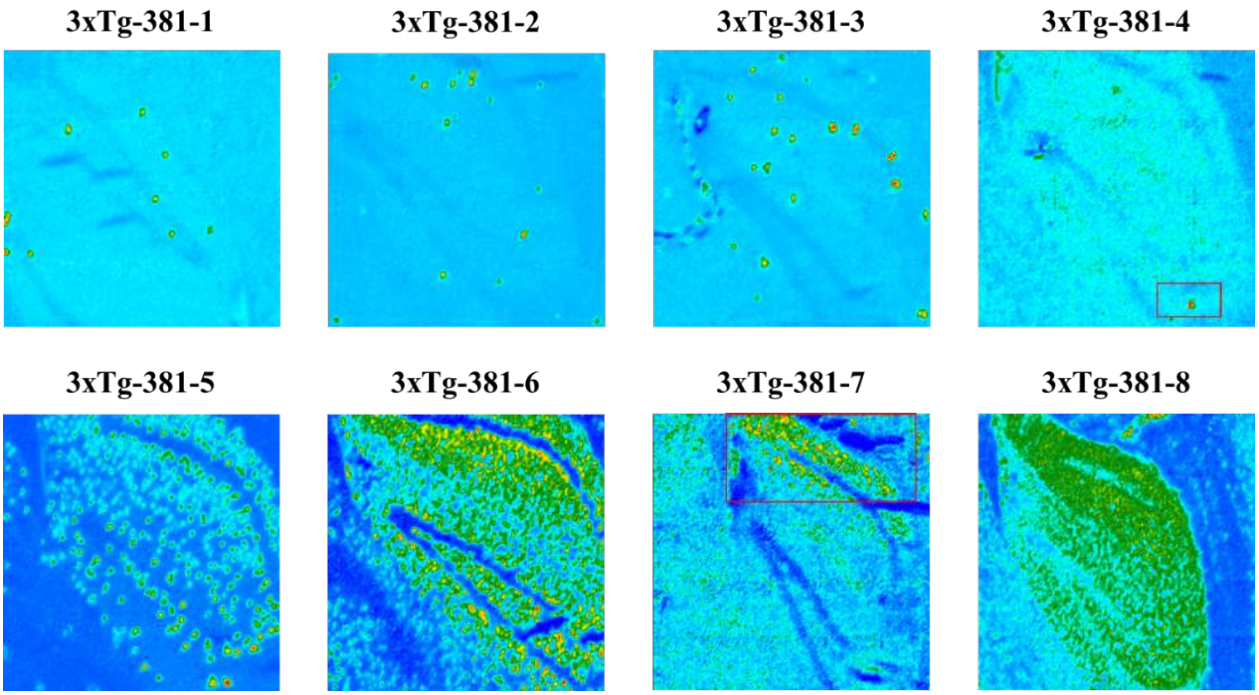

Figure 6.4. Creatine distribution over several sections from 3xTg-381. The creatine distribution varied across the 8 sections, with some sections having a few scattered creatine crystals as shown by arrows and others none. FPA images are mosaics of 5 × 5 tiles . One tile = 64 × 64 pixels = 352 × 352 μm.

Figure 6.5 depicts spectrochemical images of section (3xTg-381-5) before (6.5 A & B) and after the freeze-thaw experiment (6.5 C & D). The spectrochemical images from 3xTg-381-5 were processed for lipid and creatine distribution using 2852 and 1306 cm^{-1} band intensities respectively. Prior to freezing this section (3xTg-381-5) was loaded with creatine crystals (Figure 6.5 B) that disappeared post the freeze-thaw experiment (Figure 6.5 D). Figure 6.6 shows a single pixel spectrum of 3xTg-381-5 before & after freezing. The spectrum had a sharp creatine band that disappeared post the freeze-thaw procedure. The disappearance of creatine crystals post the freeze-thaw procedure is a clear evidence of the impact of sample preparation and storage procedures on the appearance of creatine crystals.

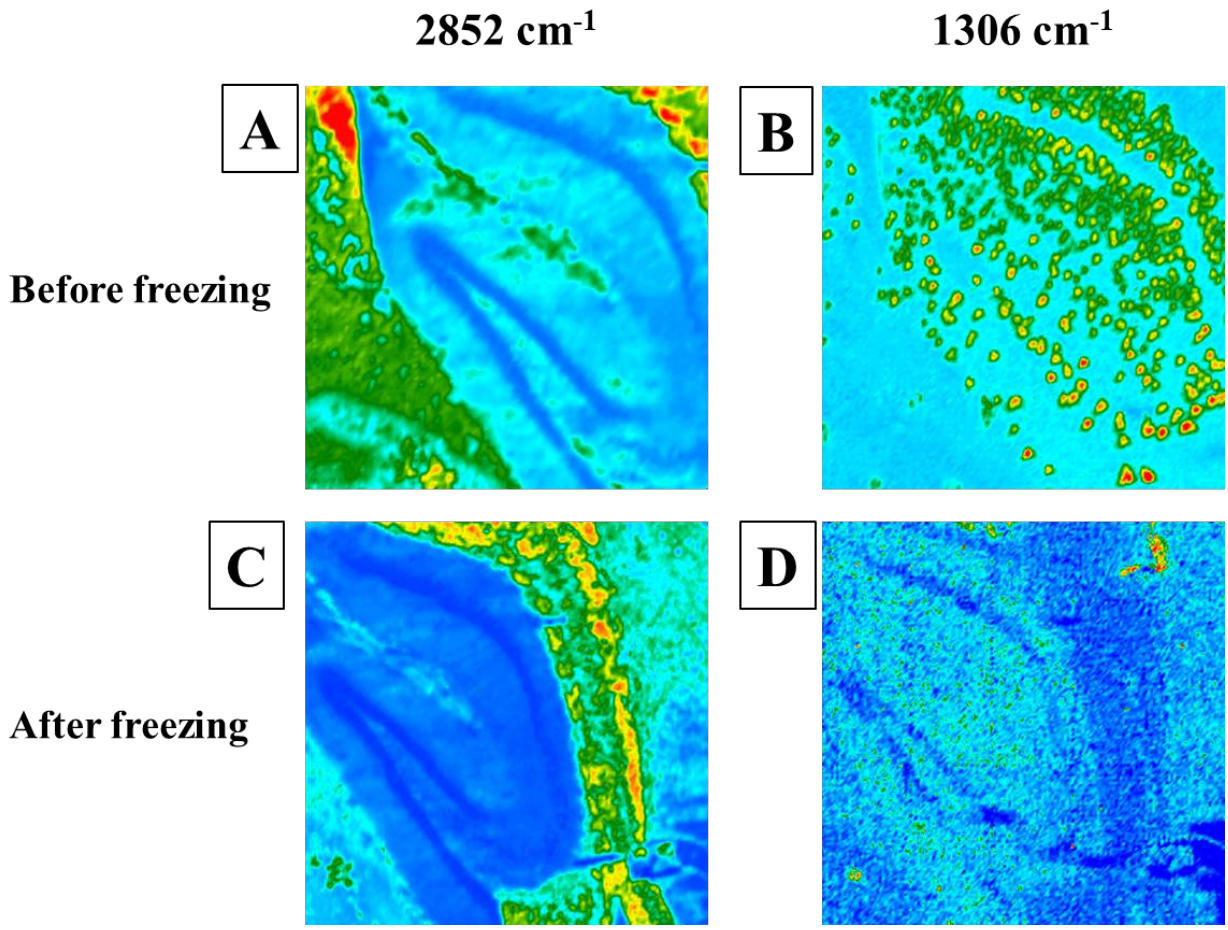

Figure 6.5. Comparison of spectrochemical images of 3xTg-381-5 before & after the freeze-thaw process. These spectrochemical images were processed for lipid and creatine distribution using 2852 and 1306 cm^{-1} band intensities respectively. Prior to freezing this section (3xTg-381-5) was loaded with creatine crystals that disappeared post the freeze-thaw experiment. Note: A small creatine crystal is seen in D in the upper right at the edge of cortex but this part was not imaged before freezing. FPA images are mosaics of 5 × 5 tiles . One tile = 64 × 64 pixels = 352 × 352 μm. As per scale, the red color represents areas with high creatine concentration.

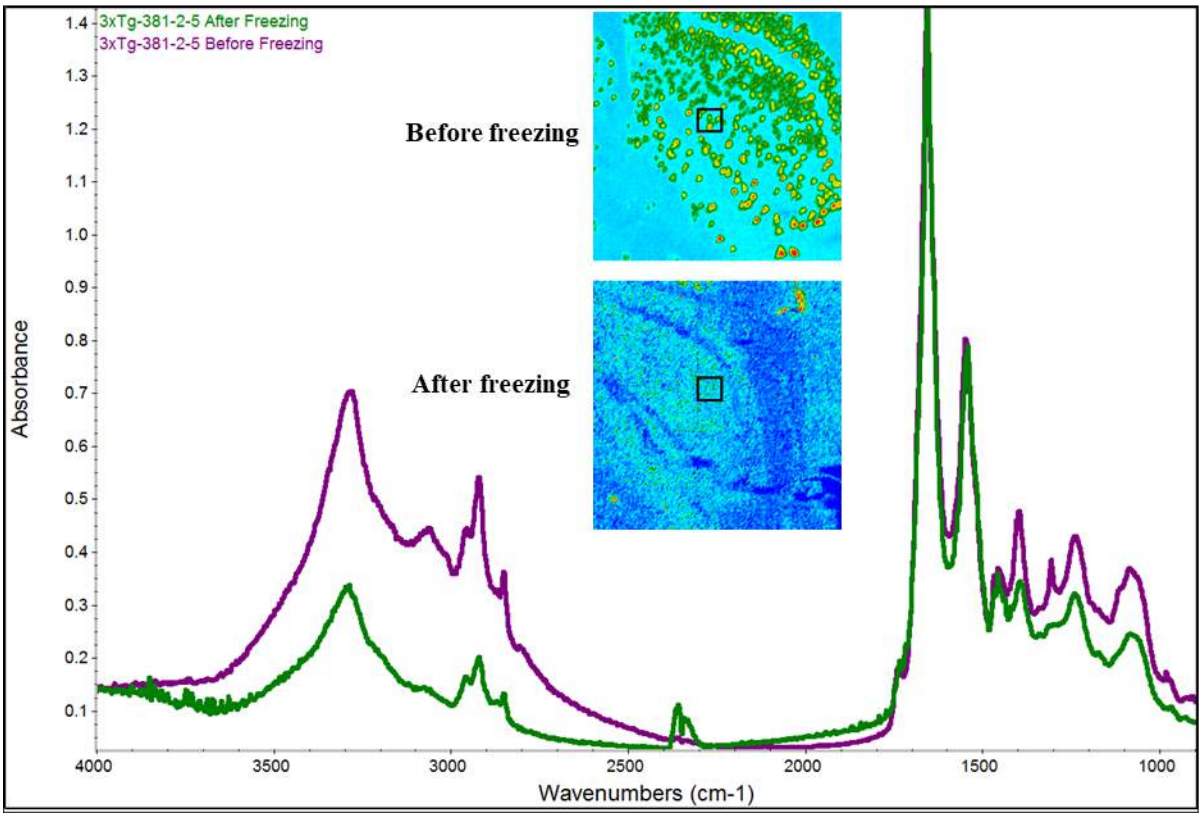

Figure 6.6. Single pixel spectrum of 3xTg-381-5 before & after freezing. The sharp creatine band present before freezing disappeared post-freezing. Note: Pixels in the vicinity of the chosen region were also examined for creatine. No creatine was found in any of these pixels. The disappearance of creatine crystals post the freeze-thaw procedure is a clear evidence of the impact of sample preparation and storage procedures on the appearance of creatine crystals.

Figure 6.7 shows another section, i.e., 3xTg-381-7 that had undergone the freeze-thaw experiment. Figure 6.7 A & B correspond to 3xTg-381-7 before freezing, processed for lipid and creatine respectively, whereas figure 6.7 C & D are corresponding spectrochemical images of the same section post the freeze-thaw experiment. There were a few creatine crystals before the freeze-thaw procedure (Figure 6.7 B) that were no longer present post the freeze-thaw experiment (Figure 6.7 D). This result was further supported by a comparison of spectra from this section prior and post

freeze-thaw. Figure 6.8 is a comparison of a single pixel spectrum of 3xTg-381-7 before & after freeze-thaw. The sharp creatine band disappeared post-freeze-thaw procedure.

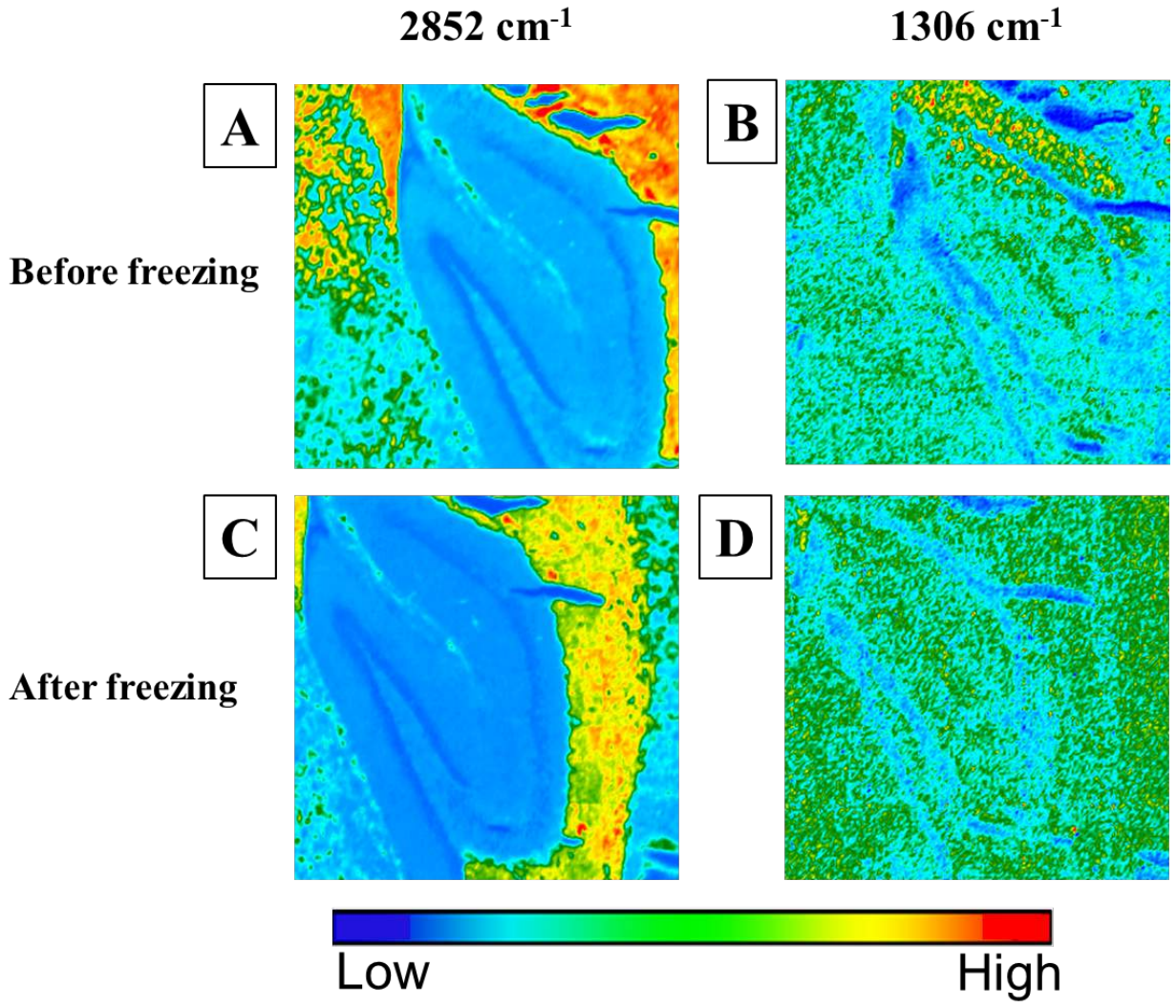

Figure 6.7. Comparison of spectrochemical images of 3xTg-381-7 before & after the freeze-thaw procedure. The spectrochemical images were processed for lipid and creatine distribution using 2852 (figure 6.7A & C) and 1306 cm^{-1} band intensities respectively (figure 6.7 B & D). There were a few creatine crystals before the freeze-thaw procedure (figure 6.7B) that were no longer present (figure 6.7D). As per scale, the red color represents areas with high creatine concentration. FPA images are mosaics of 5 × 5 tiles. One tile = 64 × 64 pixels = 352 × 352 μm. As per scale, the red color represents areas with high creatine concentration.

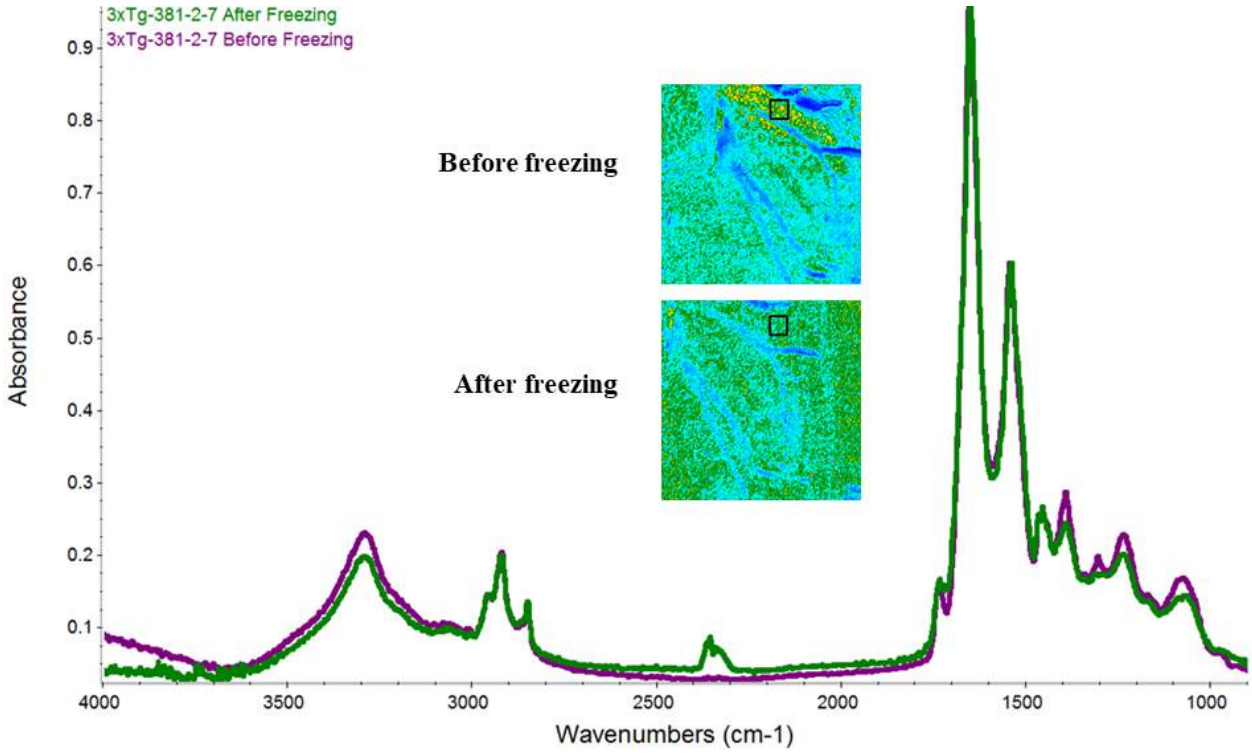

Figure 6.8 Comparison of single pixel spectrum of 3xTg-381-7 before & after freeze-thaw procedure. The sharp creatine band present before the freeze-thaw disappeared post the freeze-thaw procedure. Note: Pixels in the vicinity of the chosen region were also examined for creatine. No creatine was found in any of these pixels.

Despite the fact section 3xTg-381-7 was loaded with creatine crystals prior to freezing, there were a few areas that were free of creatine (broad creatine bands). These spectra had broad creatine bands that made it impossible to establish if these bands were creatine bands. A total of 14 single pixel spectra from this section (3xTg-381-7) were overlaid and summed. There is evidence of creatine bands at positions 1306 & 1400 cm^{-1} in the summed spectrum (Figure 6.9). The other bands in this region are inherently much weaker than the 1306 cm^{-1} singlet and 1400 cm^{-1} doublet bands, so they would not contain creatine. This demonstrates that the creatine crystals may be scattered throughout the brain tissue resulting in a spectrum with broad/weak creatine bands. Thus, the creatine appearance is dependent on sample preparation.

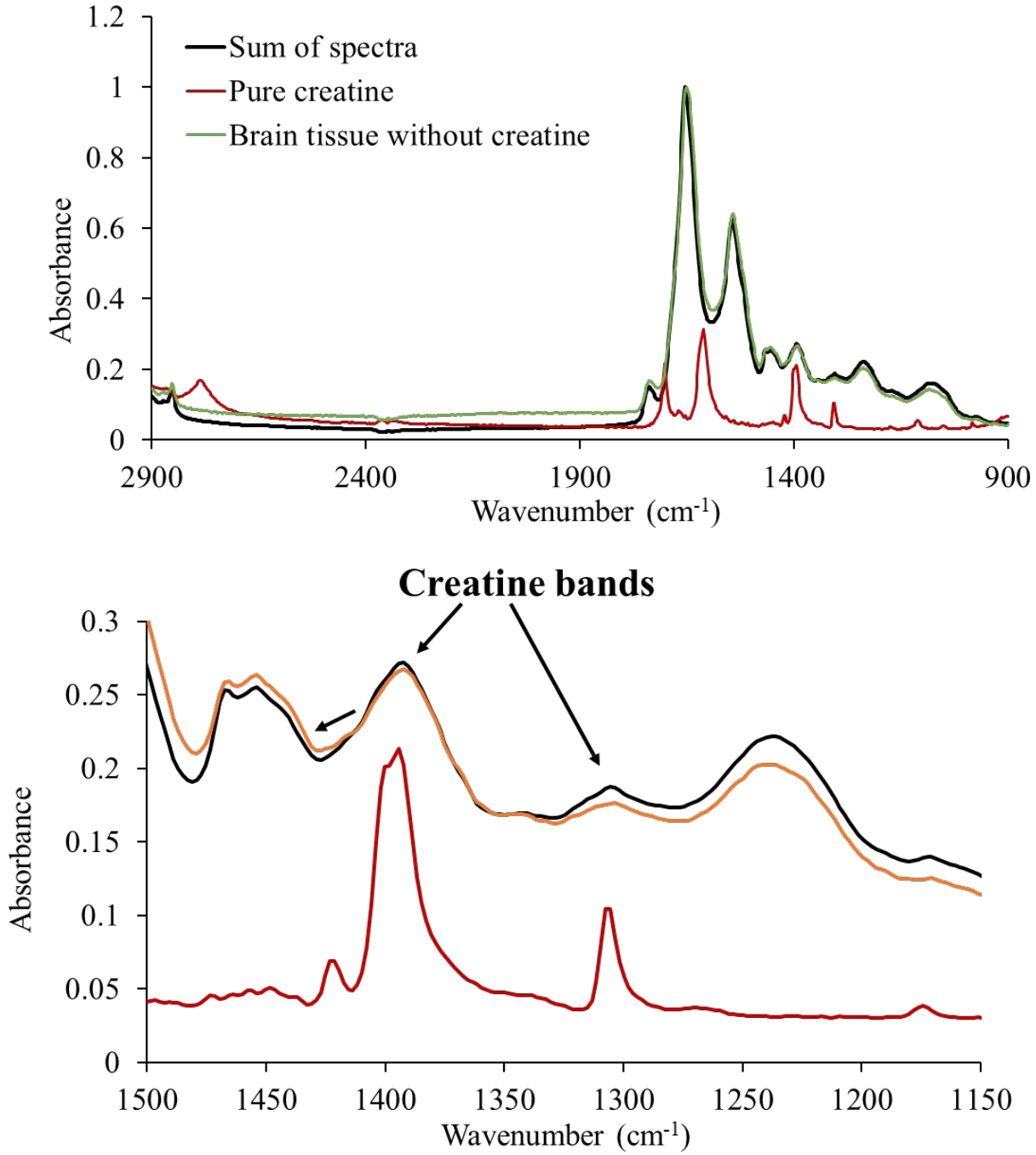

Figure 6.9 Summation of 14 single pixel spectra of 3xTg-381-7 (spectra of regions wihout creatine before the freeze-thaw procedure). There is evidence of creatine bands at positions 1306 & 1400 cm^{-1} in the summed spectrum. The other bands in this region are inherently much weaker than the 1306 cm^{-1} singlet and 1400 cm^{-1} doublet bands, so they would not contain creatine. These broad bands may appear because the creatine crystals are thinly dispersed in brain tissue.

Figure 6.10 depicts spectrochemical images from 3xTg-381-3 prior (Figure 6.10 A & B) and post the freeze-thaw procedure (Figure 6.10 C & D). There were numerous medium-sized irregular creatine crystals in the hippocampus (Figure 6.10 C). Post the freeze-thaw experiment the creatine crystals were absent (Figure 6.10D).

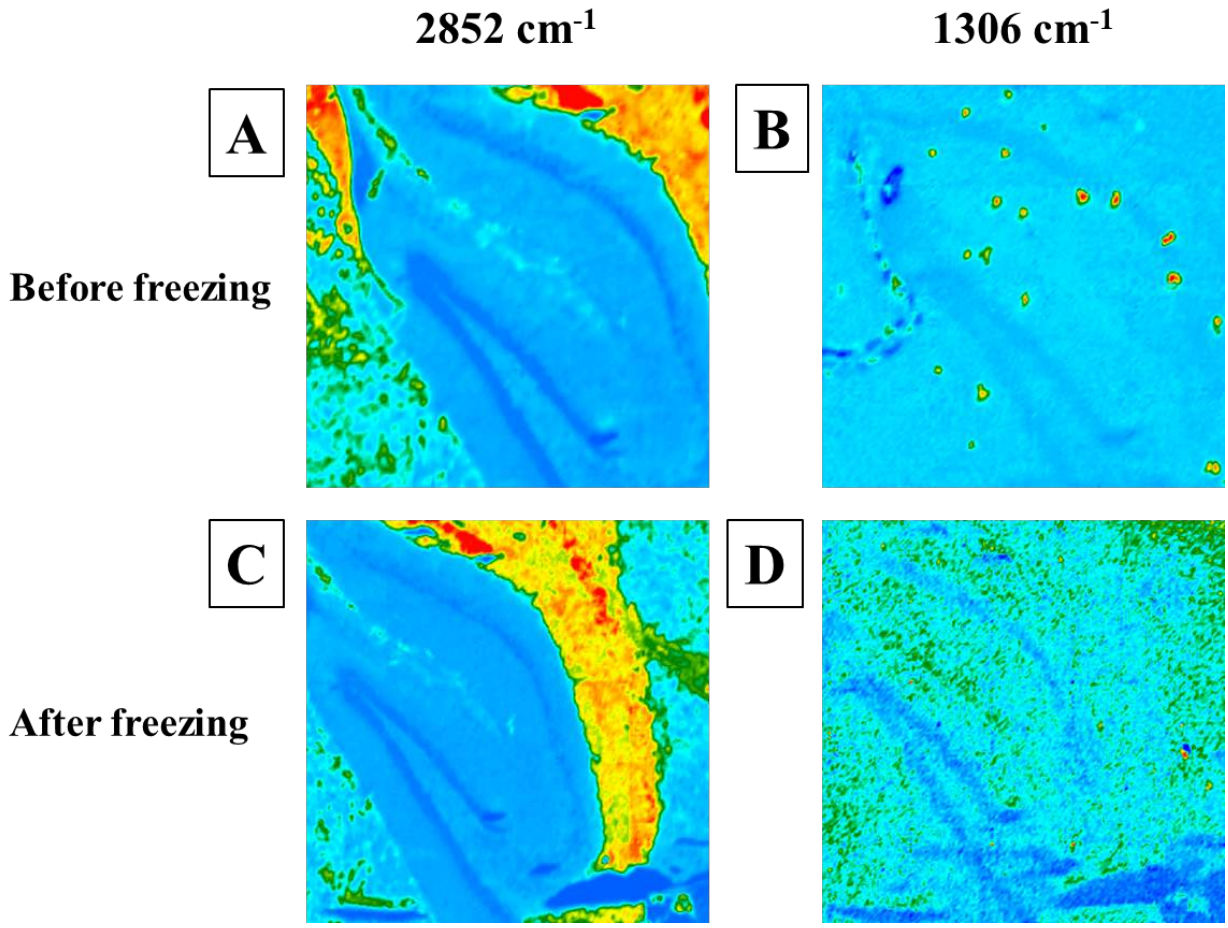

Figure 6.10. Comparison of spectrochemical images of 3xTg-381-3 before & after the freeze-thaw process. The spectrochemical images were processed for lipid and creatine distribution using 2852 (Figure 6.10A & C) and 1306 cm^{-1} band intensities respectively (Figure 6.10 B & D). There were scattered creatine crystals before the freeze-thaw procedure (Figure 6.10B) that were no longer present (Figure 6.10D). As per scale, the red color represents areas with high creatine concentration. Note: The areas imaged are a little different in the before and after, but the critical regions have been captured in both. FPA images are mosaics of 5 × 5 tiles. One tile = 64 × 64 pixels = 352 × 352 μm. As per scale, the red color represents areas with high creatine concentration.

Overview of literature reports on creatine crystals in brain tissue:

A number of studies have attempted to assess the distribution of creatine at the cellular level. The discovery that creatine could be detected in brain tissue section with FTIR imaging was first reported by Gallant et al., (2006). These creatine deposits, suggestive of altered energetic status, were detected by synchrotron infrared spectrochemical imaging. In a continuation of this study, the distribution of creatine, lipid and dense core plaque deposits in the hippocampus of 5, 8, 11, 14 & 17-month old TgCRND8 and littermate control mice were explored with thermal source FPA (Kuzyk et al., 2010). The FTIR study reported that creatine deposits were detected in all TgCRND8 mice and the extent of deposition increased with age. The creatine deposits were only found in the hippocampal grey matter and not the white matter. The creatine deposits were not physically connected in adjacent sections. It was concluded that the crystalline creatine crystals were deposited within the tissue as a result of the freeze-thaw process. It was not possible to determine how the extracellular or intracellular creatine eventually formed crystalline crystals. However, because the creatine distribution varied slightly between serial sections, it was inferred that crystalline deposits do not exist *in vivo* and are an *ex vivo* freeze-thaw artifact (Kuzyk et al., 2010).

A similar study reported crystalline creatine deposits as a marker of localized ischemia in cerebral malaria (Hackett et al, 2015). Creatine levels in this study were evaluated using synchrotron FTIR spectroscopy; however, the synchrotron light is polarized. The study reported crystalline creatine deposits that were identified as an *in vivo* state of elevated creatine to phosphorcreatine ratio. However, the variation in the orientation of creatine crystals to the synchrotron light source was misidentified as evidence of both creatine and phosphocreatine.

Previous work by Dr. Gough's group revealed polarization dependent variations between creatine spectra recorded with thermal source (un-polarized) and synchrotron (polarized) FPA

(Khamenhfar, 2011, MSc thesis, University of Manitoba). Figure 6.11 shows creatine spectra collected using the thermal source FPA with a polarizer angle set at 0, 45 and 90° relative to the orientation of pure, elongated creatine crystals (University of Manitoba). The 1306 band completely disappears at 90° while appearing as a sharp band at 0° (Figure 6.11). Thus, the creatine bands vanish if the crystal lies at the wrong orientation relative to polarized light.

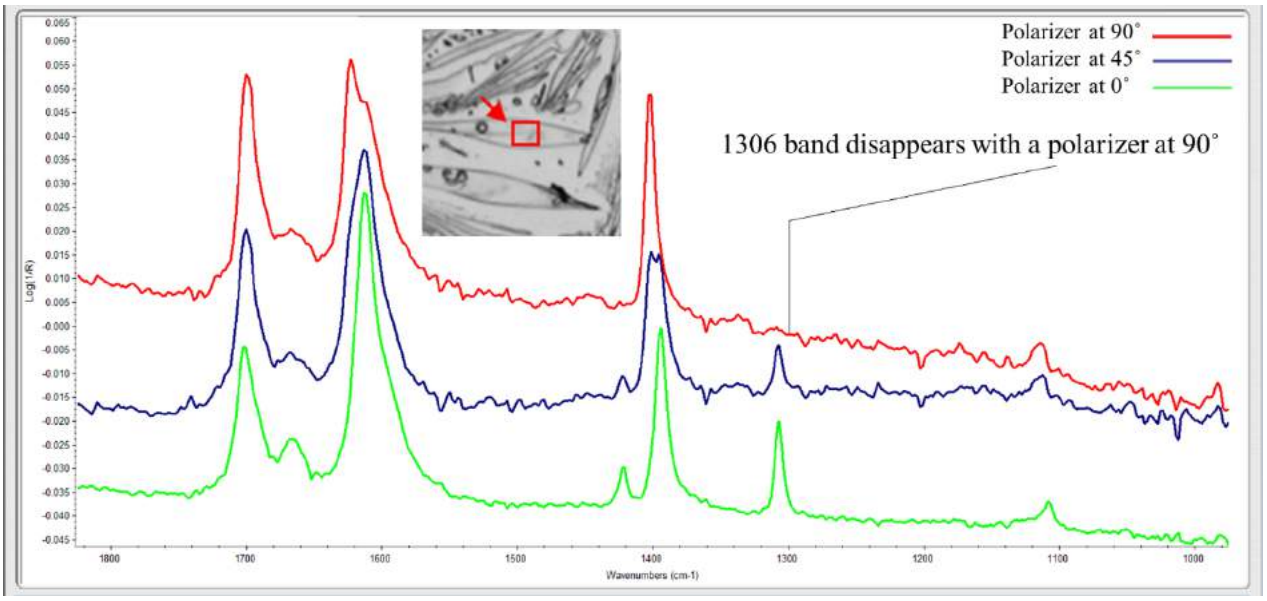

Figure 6.11 Creatine spectra collected using Agilent Cary 670 FTIR Spectrometer coupled to an Agilent Cary 620 FTIR microscope at the University of Manitoba with polarizer angles of 0, 45 and 90°. The 1306 cm^{-1} band completely disappears at 90° while appearing as a sharp band at 0°.

A recent study by Skoczen et al. evaluated the effect of the ketogenic diet (KD) on creatine accumulation in the hippocampus of rat brains using synchrotron FTIR (SR-FTIR) spectroscopy (Skoczen et al., 2017). Adult male Wistar rats were used for this study. The animals were divided into three groups comprised of a control group (N) with standard laboratory diet and two groups

with a ketogenic diet of ratio 5:1 (KD1) and 9:1 (KD2) respectively. The appearance of creatine was evaluated only in the Cornu Ammonis (CA3) and the dentate gyrus (DG). Similar levels of creatine deposits were reported in N and KD1 groups. The creatine band intensities were higher KD2 group (the group with a higher ketogenic diet ratio) compared to standard diet fed rats. The results from this study suggest a similar problem of inconsistent and irregular appearance of creatine crystals as observed in this thesis. However, this study had a limited scope, owing to instrument limitation. SR-FTIR spectroscopy has a drawback of small sample size analysis and long imaging times (hours). As a result, creatine analysis was confined to only the Cornu Ammonis (CA3) and the dentate gyrus (DG) of the hippocampal formation. These regions were analyzed by raster scanning over the tissue surface. It appears that only a single section from each animal was evaluated. The small regions examined in this study possibly are likely not representative of the creatine accumulation status in the entire hippocampus that has been reported in previous studies (Kuzyk et al., 2010).

In this thesis, creatine deposits suggestive of altered energetic status were detected by FTIR spectroscopy in all animals (3xTg & C57BL/6 mice on creatine-enriched diet & standard diet). However, the creatine appearance and crystal morphology was not uniform even in serial sections acquired from the same animal at the same cryo-sectioning time. Through a series of freeze-thaw experiments, it was confirmed that the sample preparation methods, i.e., methods of tissue acquisition, freezing, storage, and transport, affect the formation of the crystal. Creatine crystals can get washed away or migrate from tissue surface during the freeze-thaw procedure. This is likely to happen because creatine is highly soluble in water. For creatine levels that are truly representative of *in vivo* condition, it is recommended to cryostat the brain tissue within a few days

after the animal sacrifice and dry the cryosectioned sections at room temperature immediately post sectioning.

Chapter 7. Conclusions & Future Work

7.1 Conclusions

The following conclusions were drawn from this thesis:

- Creatine deposits suggestive of altered energetic status were detected by infrared spectrochemical imaging in all the animals in this study.

- Gender-related differences in response were found in parallel animals. The female 3xTg had shown evidence of creatine crystals in the control group and not in the creatine diet group. Conversely, the male 3xTg/AD mouse on creatine diet had extensive creatine appearance and almost no evidence of creatine in 3xTg mouse on control diet. However, this can not be verified statistically due to small sample size for each gender (n = 2 male 3xTg & n = 4 female 3xTg).

- Creatine deposition was found to be extensive in the hippocampal sections of male 3xTg mouse on creatine diet. In comparison, the male 3xTg mouse on control diet did not contain creatine crystals. It is not possible to establish whether the creatine dietary enrichment has impacted the creatine localization. This is because of sample size (gender) limitation (n = 1 creatine diet & n = 1 control diet) and inconsistency in creatine distribution over sections from the same animals.

- Based on results obtained from this study, the female mice on creatine diet did not experience creatine deposition. It is not clear why the female transgenic mice on creatine diet did not contain any creatine crystals.

- Freeze-thaw experiments confirmed that the sample preparation methods, i.e., methods of tissue acquisition, freezing, storage, and transport, affect the formation of the crystal. Creatine crystals can get washed away or migrate from tissue surface during the freeze-thaw procedure. This is possible because creatine is highly soluble in water.

7.2 Future Work

Dietary creatine may assist cognitive protection, in early-stage AD. Future research is required to establish the therapeutic potential of creatine in AD. The following can be done:

- A future study to be conducted involving both isopentane cooled in liquid nitrogen and liquid nitrogen as a freezing medium during the freeze-thaw procedure. A comparison of these would provide information about their effect on creatine crystallization pattern.

- The freeze-thaw conditions are critical in the creatine distribution and should be considered in future studies. The creatine distribution is dependent on the sample preparation. Freeze storage of the cryosectioned brain tissue sections does affect the creatine distribution. The best sample preparation method is to dry the cryosectioned brain tissue at room temperature immediately after sectioning. Also, it is best to cryotome the brain tissue within a few days after animal sacrifice.

- Creatine administration prior to 9 months should be considered for female 3xTg mice in future studies, because females experience earlier pathology (before 9 months) and also the creatine metabolism in females is dependent on estrogen levels (sex hormone regulation cycle). Future studies should include records of sex hormone levels and disease pathology.

- This study was limited by a small number of animals from each gender (n = 2 for male 3xTg, n = 4 female 3xTg & n = 6 for male C57BL/6, no female C57BL/6). A future study with a large sample size for each gender (e.g. n = 5 for each gender & diet) would provide a better understanding of gender-related differences in response.

- Future studies involving AD and C57BL/6 mice of variable ages and genders would provide more information with regards to gender-related differences in pathology.

Appendix I

Spectrochemical Images of C57BL/6 & 3xTg Mice on Creatine & Control Diet

Appendix I

This Appendix contains spectrochemical images of all brain tissue sections from the dietary pilot study. The study involved a total of 12 animals (n = 6 3xTg & n = 6 C57BL/6). These animals were divided into two groups i.e. the creatine-enriched diet animals (n = 3) and the control/standard diet animals (n = 3). The creatine-enriched and standard diet animals included both female and male genders. The 3xTg group had n = 2 male animals and n = 4 female animals whereas the background mice were all male mice.

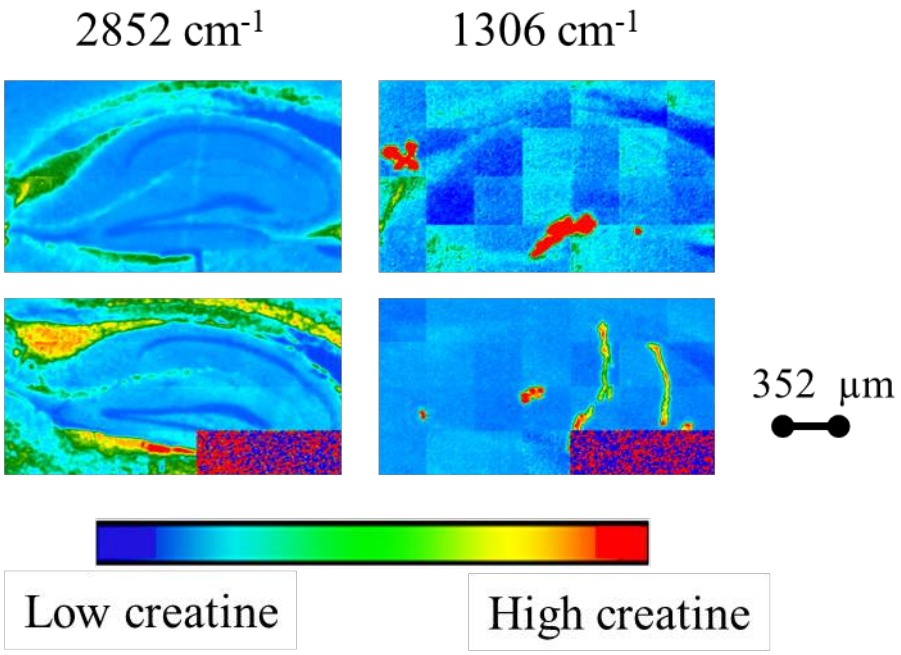

Figure 8.1. Creatine appearance from 13MICE0016 (9-month background male mouse on 3% creatine enriched diet). The spectrochemical image was processed for distribution of lipids (2852 cm^{-1}) to establish tissue morphology and creatine (1306 cm^{-1}) to assess creatine localization. The image is processed with methods outlined in table 4.1. Upper scale = 0.5395, Lower scale = -0.0277. Corresponds to areas of zero signal as the detector warmed up.

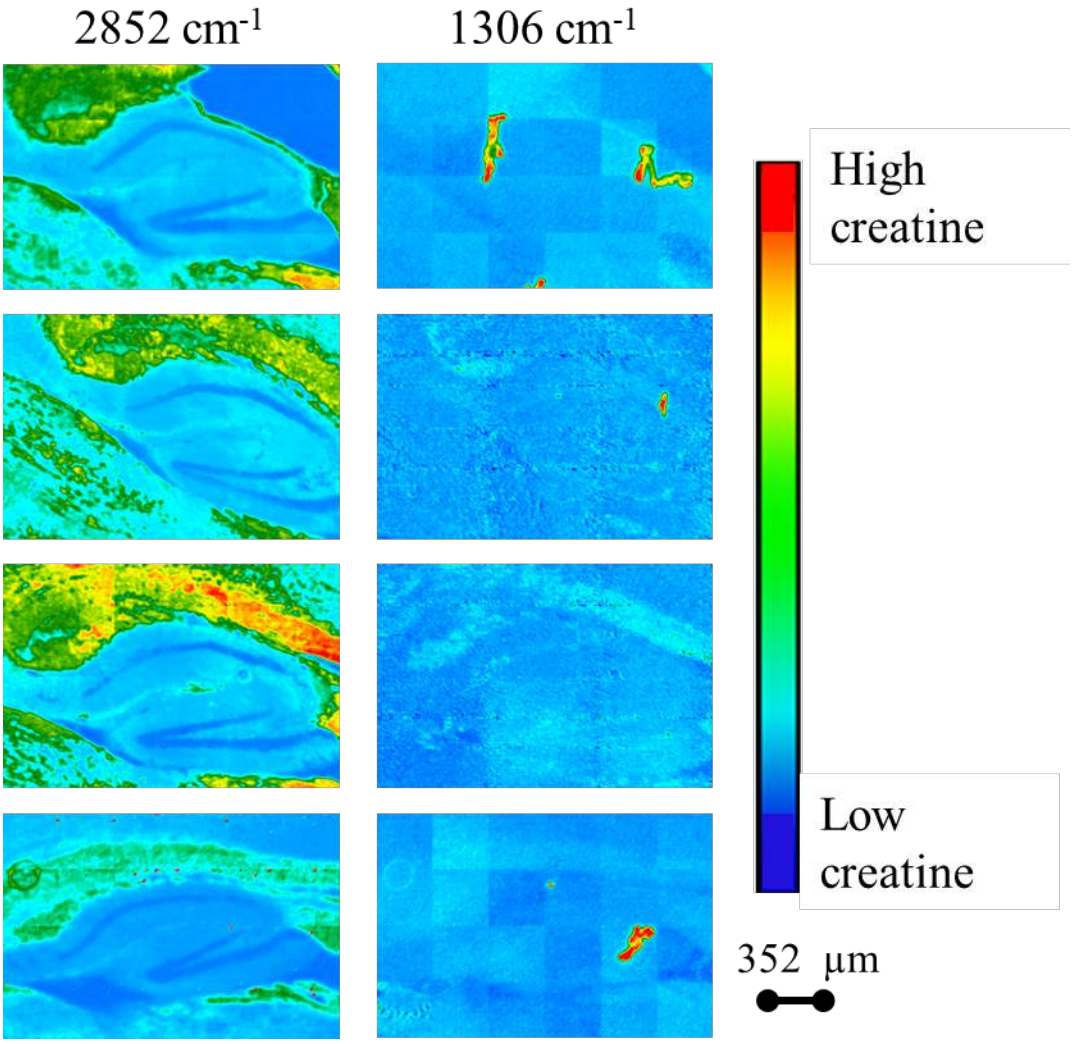

Figure 8.2. Creatine appearance from 13MICE0018 (9-month background male mouse on 3% creatine enriched diet). The spectrochemical image was processed for distribution of lipids (2852 cm^{-1}) to establish tissue morphology and creatine (1306 cm^{-1}) to assesss creatine localization. The image is processed with methods outlined in table 4.1. As per scale, the red color represents areas with high creatine concentration. Upper scale = 0.4656, Lower scale = - 0.088.

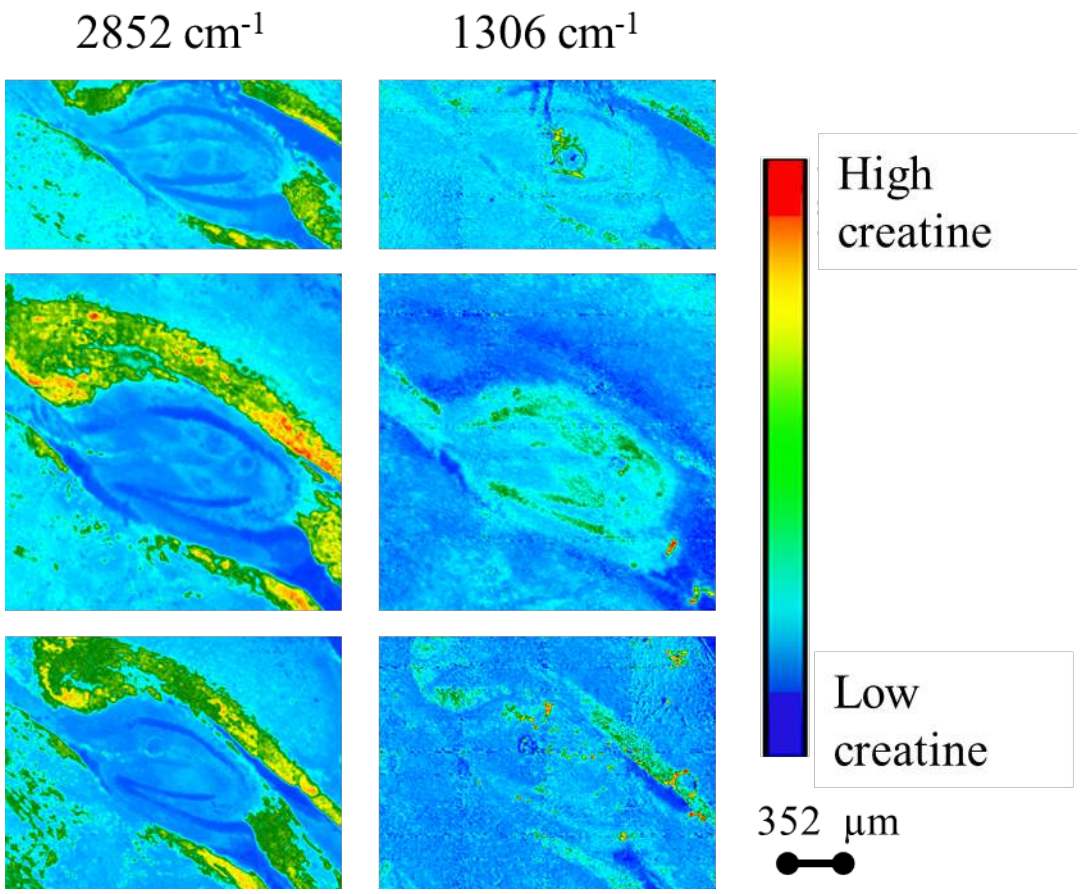

Figure 8.3. Creatine appearance from 13MICE0018 (9-month background male mouse on 3% creatine enriched diet). The spectrochemical image was processed for distribution of lipids (2852 cm^{-1}) to establish tissue morphology and creatine (1306 cm^{-1}) to assess creatine localization. The image is processed with methods outlined in table 4.1. One tile = 64 × 64 pixels = 352 × 352 µm. As per scale, the red color represents areas with high creatine concentration. Upper scale = 2.560, Lower scale = -0.6970.

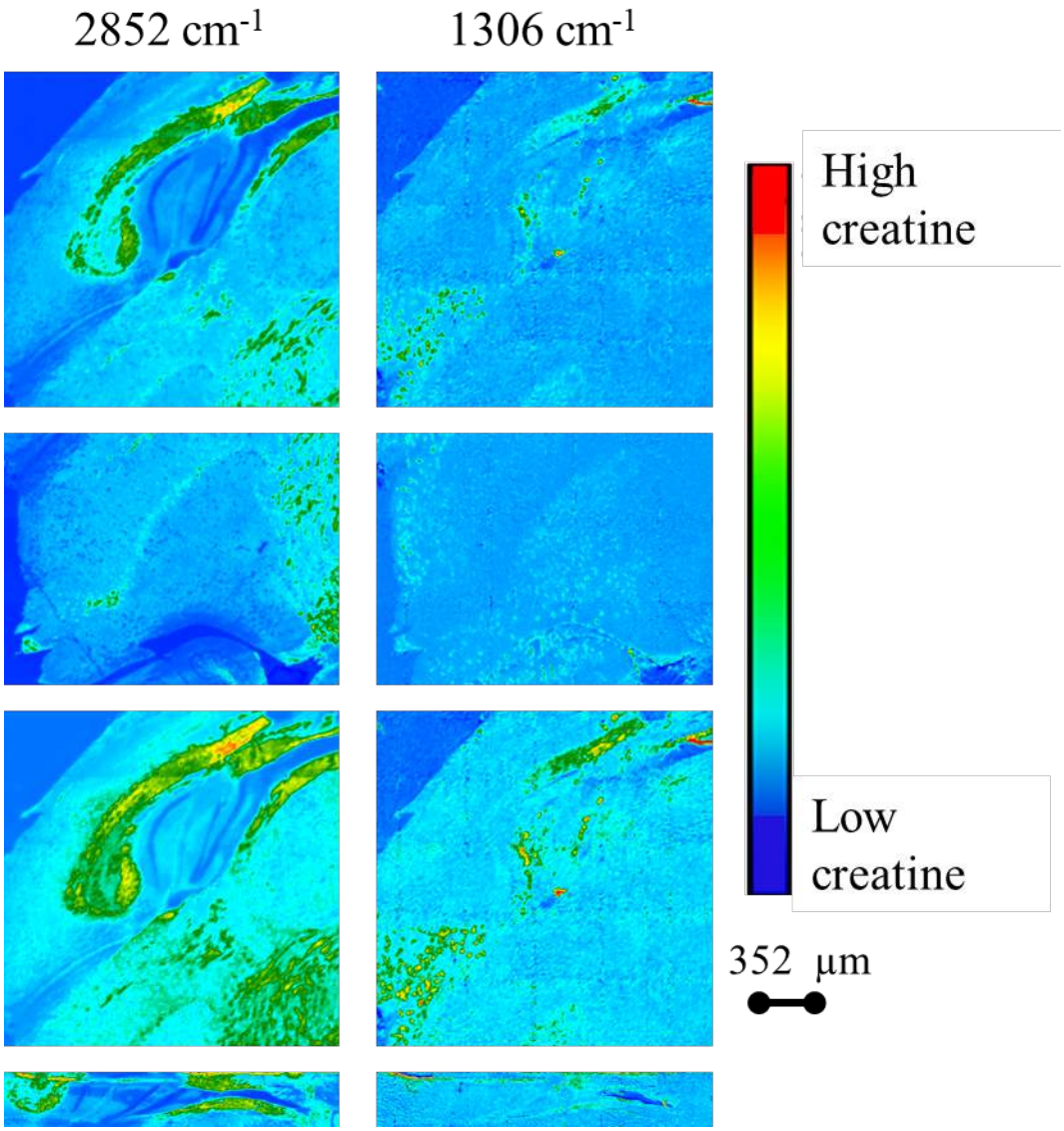

Figure 8.4. Creatine appearance from 13MICE0018 (9-month background male mouse on 3% creatine enriched diet). The spectrochemical image was processed for distribution of lipids (2852 cm^{-1}) to establish tissue morphology and creatine (1306 cm^{-1}) to assess creatine localization. The image is processed with methods outlined in table 4.1. Upper scale 2.560; Lower scale -0.6970.

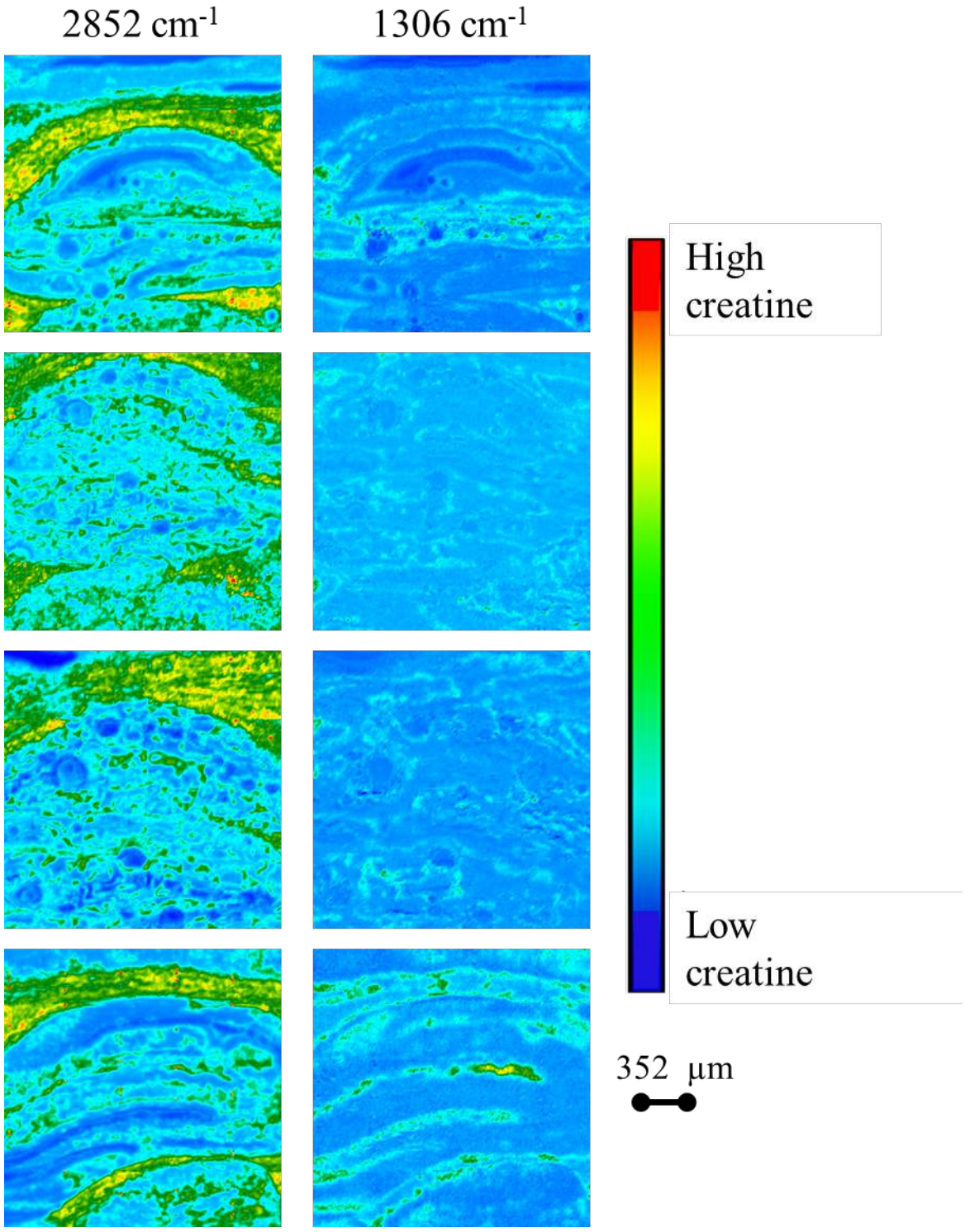

Figure 8.5. Creatine appearance from 13MICE0019 (9-month background male mouse on 3% creatine enriched diet). The spectrochemical image was processed for distribution of lipids (2852 cm^{-1}) to establish tissue morphology and creatine (1306 cm^{-1}) to assess creatine localization. The image is processed with methods outlined in table 4.1. Upper scale 2.560; Lower scale -0.6970.

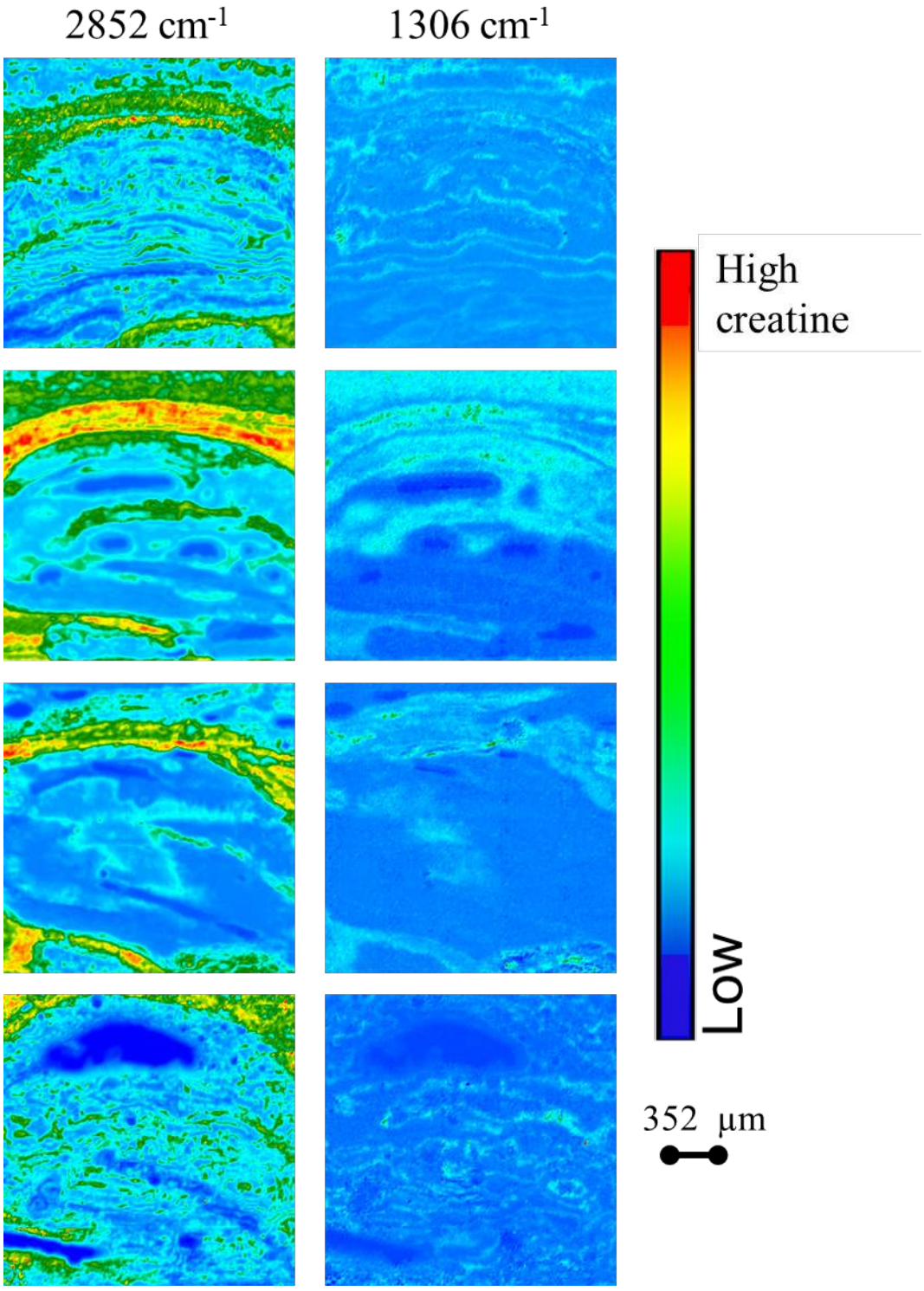

Figure 8.6. Creatine appearance from 13MICE0019 (9-month background male mouse on 3% creatine enriched diet). The spectrochemical image was processed for distribution of lipids (2852 cm^{-1}) to establish tissue morphology and creatine (1306 cm^{-1}) to assess creatine localization. The image is processed with methods outlined in table 4.1. Upper scale 2.560; Lower scale -0.6970.

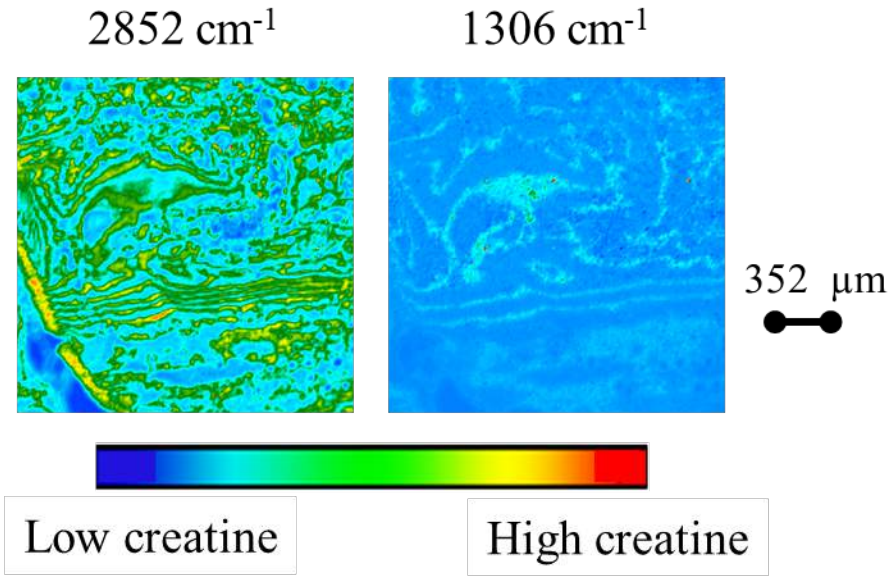

Figure 8.7. Creatine appearance from 13MICE0019 (9-month background male mouse on 3% creatine enriched diet). The spectrochemical image was processed for distribution of lipids (2852 cm^{-1}) to establish tissue morphology and creatine (1306 cm^{-1}) to assess creatine localization. The image is processed with methods outlined in table 4.1. Upper scale 2.560; Lower scale -0.6970.

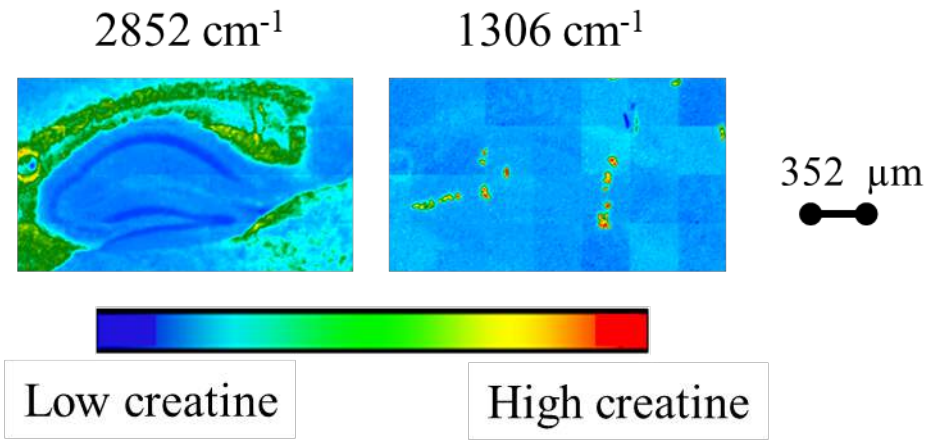

Figure 8.8. Creatine appearance from 13MICE0005 (9-month male background mouse control diet). The spectrochemical image was processed for distribution of lipids (2852 cm^{-1}) to establish tissue morphology and creatine (1306 cm^{-1}) to assess creatine localization. The image is processed with methods outlined in table 4.1. As per scale, the red color represents areas with high creatine concentration. Upper scale = 0.4325, Lower scale = -0.6970.

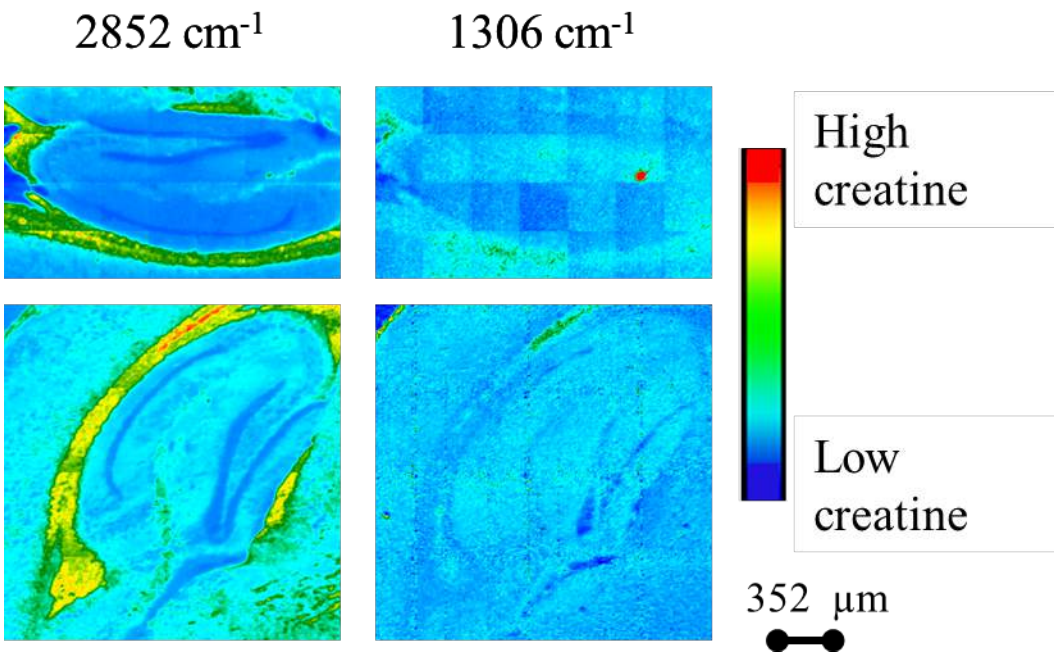

Figure 8.9. Creatine appearance from 13MICE0006 (9-month male background mouse control diet). The spectrochemical image was processed for distribution of lipids (2852 cm^{-1}) to establish tissue morphology and creatine (1306 cm^{-1}) to assess creatine localization. The image is processed with methods outlined in table 4.1. As per scale, the red color represents areas with high creatine concentration. Upper scale = 0.2650, Lower scale = -0.022.

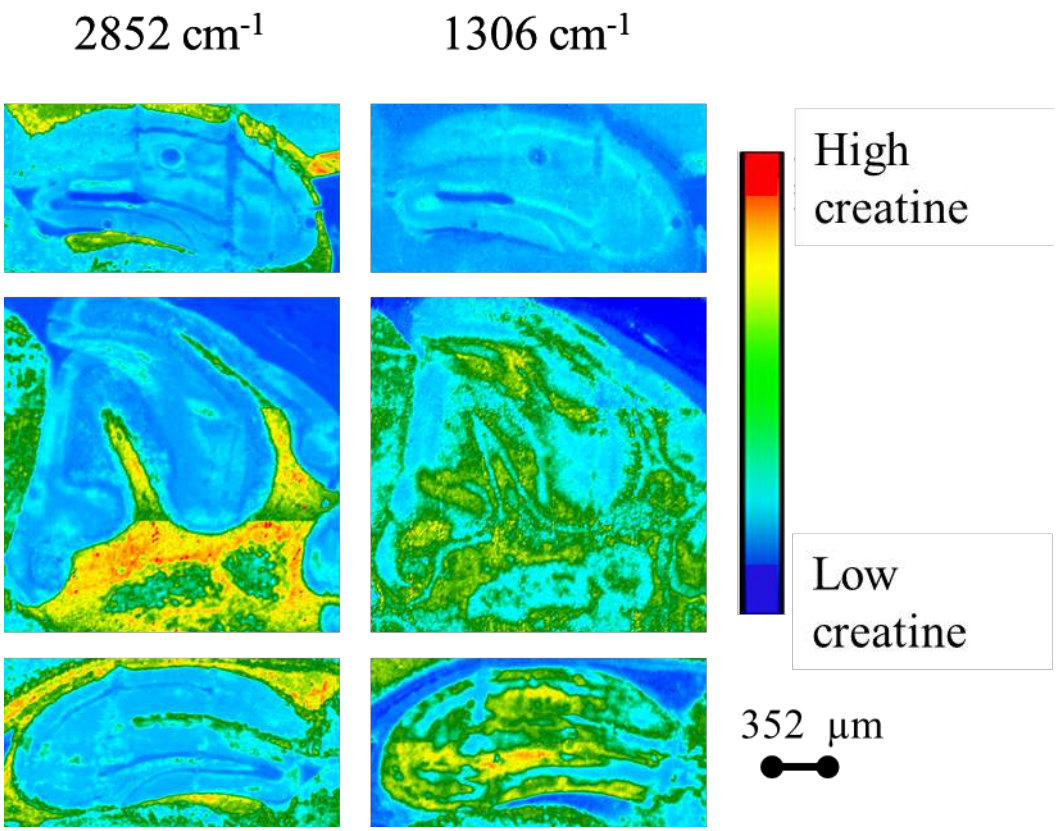

Figure 8.10. Creatine appearance from 13MICE0007 (9-month male background mouse control diet). The spectrochemical image was processed for distribution of lipids (2852 cm^{-1}) to establish tissue morphology and creatine (1306 cm^{-1}) to assess creatine localization. The image is processed with methods outlined in table 4.1. As per scale, the red color represents areas with high creatine concentration. Upper scale = 2.060, Lower scale = -0.6270.

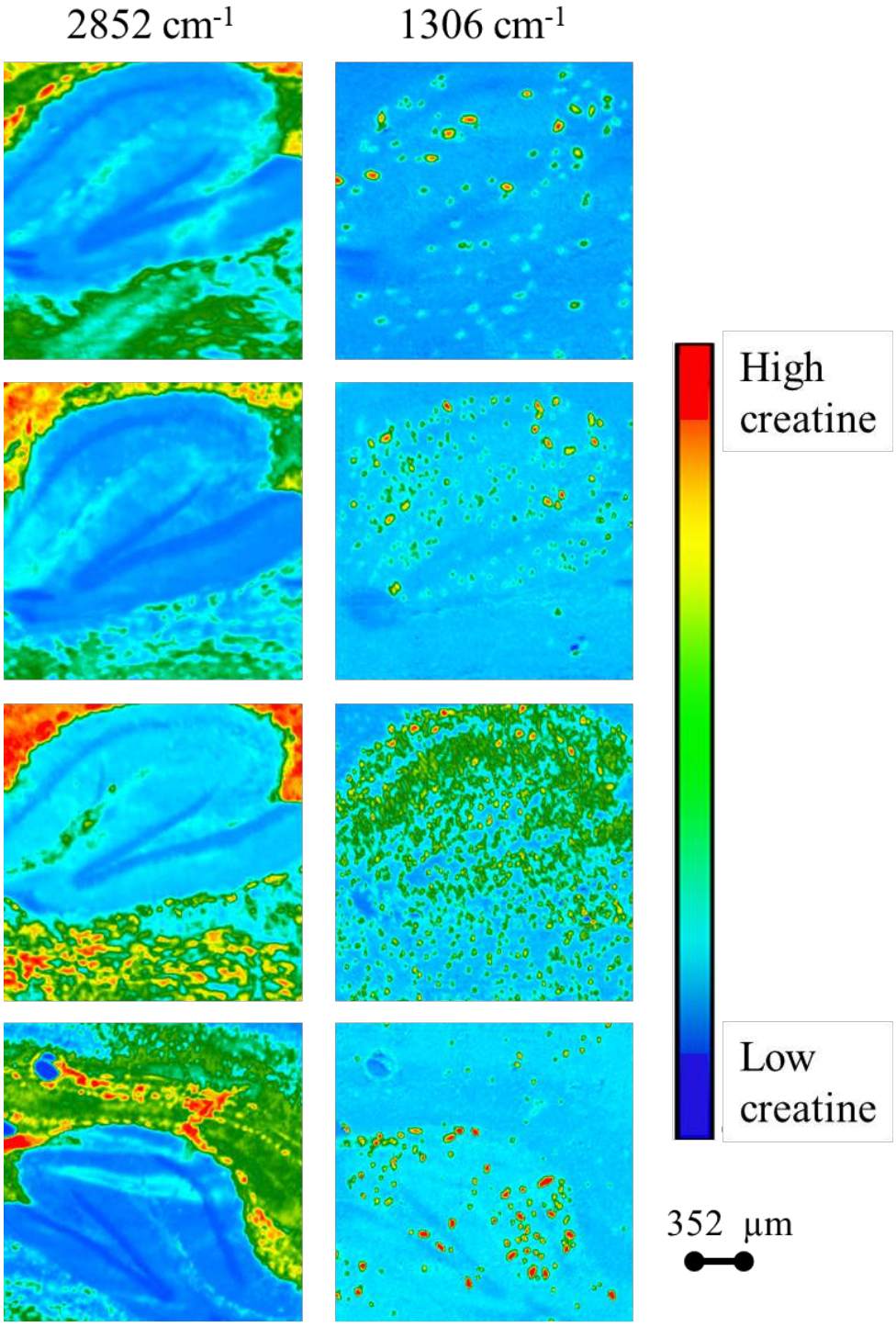

Figure 8.11. Creatine appearance from 3xTg-362 (9-month male transgenic mouse creatine diet). The spectrochemical image was processed for distribution of lipids (2852 cm^{-1}) to establish tissue morphology and creatine (1306 cm^{-1}) to assess creatine localization. The image is processed with methods outlined in table 4.1. As per scale, the red color represents areas with high creatine concentration. Upper scale = 0.6216, Lower scale = -0.1540.

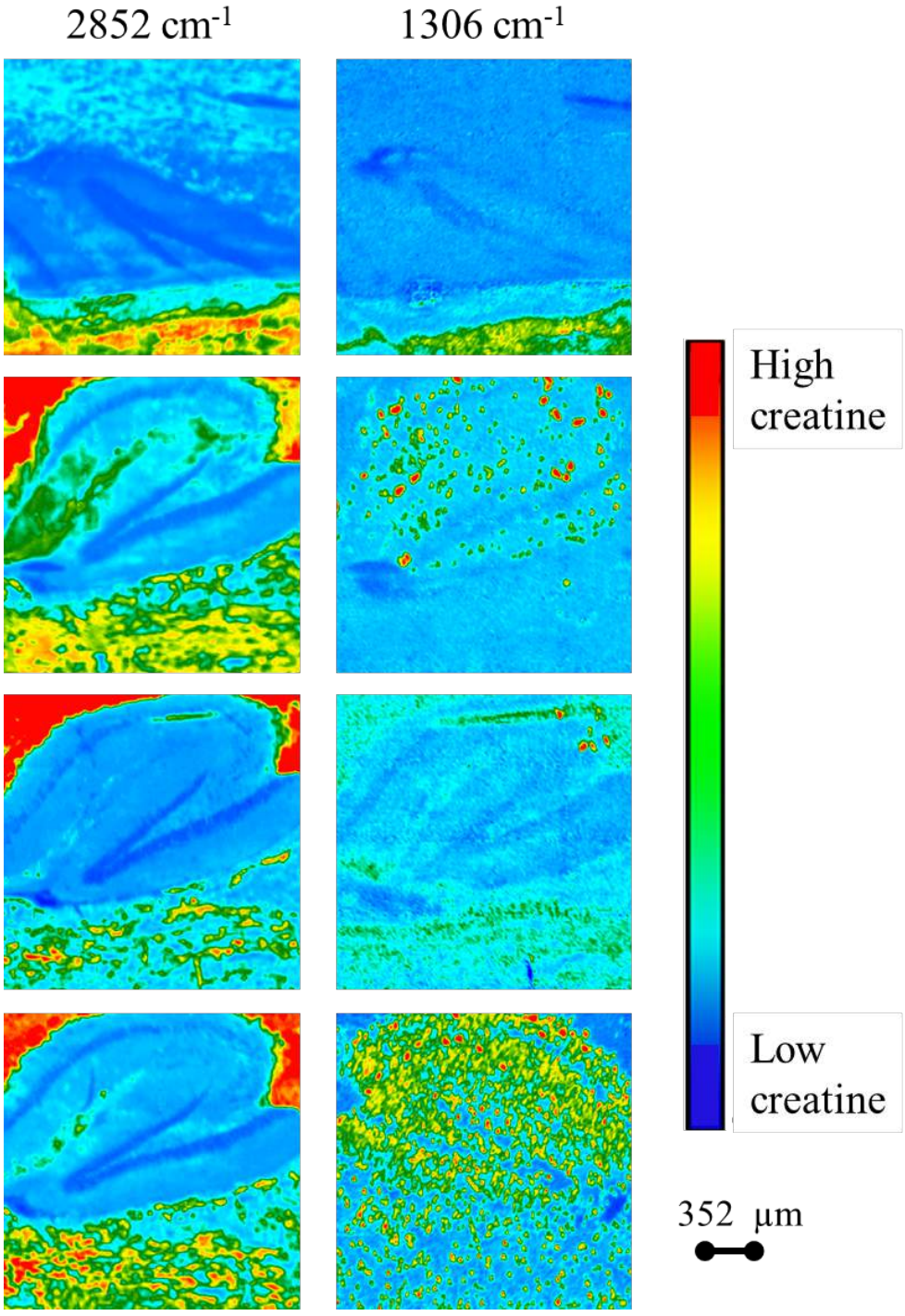

Figure 8.12. Creatine appearance from 3xTg-362 (9-month male transgenic mouse creatine diet). The spectrochemical image was processed for distribution of lipids (2852 cm^{-1}) to establish tissue morphology and creatine (1306 cm^{-1}) to assess creatine localization. The image is processed with methods outlined in table 4.1. As per scale, the red color represents areas with high creatine concentration. Upper scale = 0.6216, Lower scale = -0.1540.

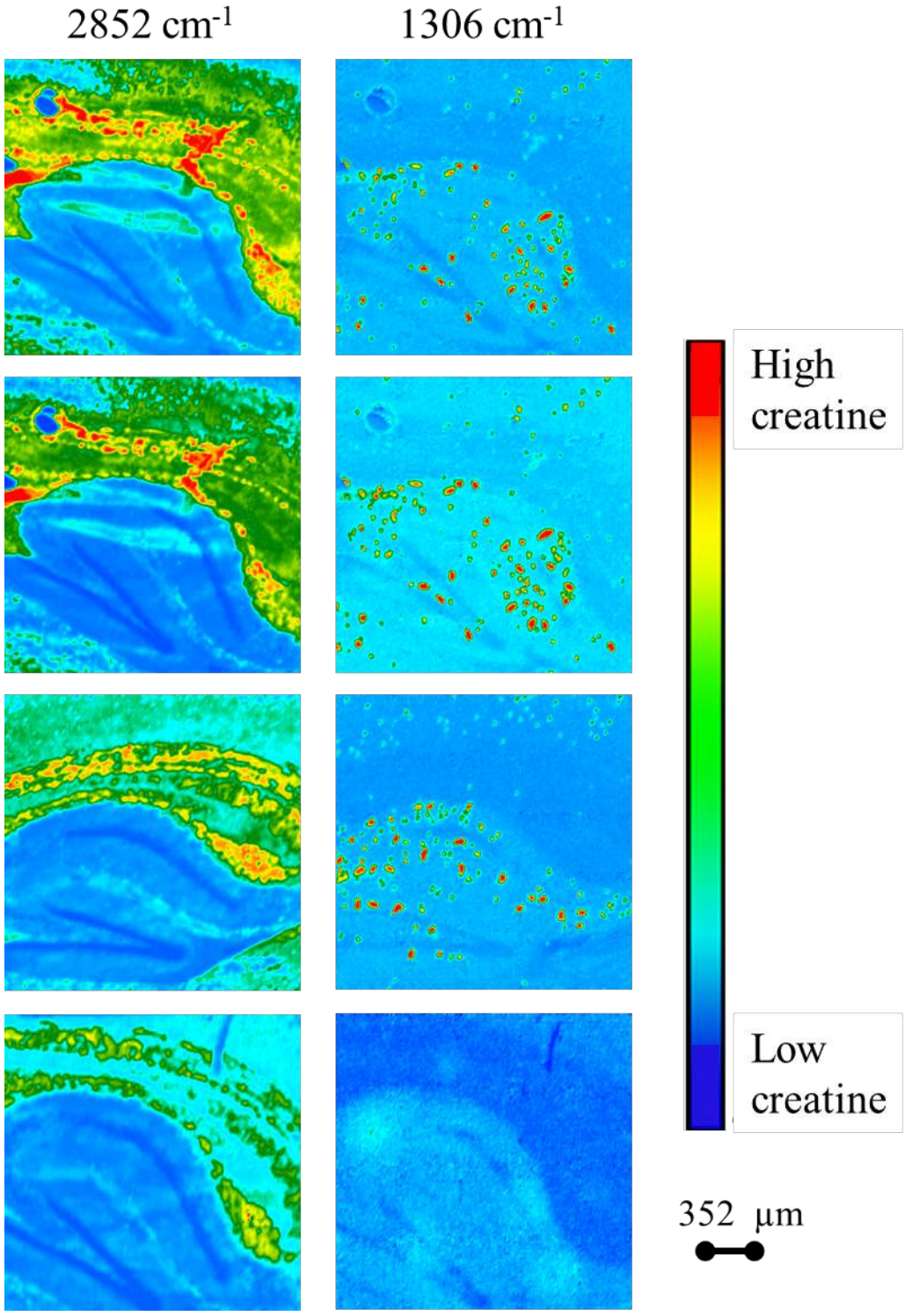

Figure 8.13. Creatine appearance from 3xTg-362 (9-month male transgenic mouse creatine diet). The spectrochemical image was processed for distribution of lipids (2852 cm^{-1}) to establish tissue morphology and creatine (1306 cm^{-1}) to assess creatine localization. The image is processed with methods outlined in table 4.1. As per scale, the red color represents areas with high creatine concentration. Upper scale = 0.6216, Lower scale = -0.1540.

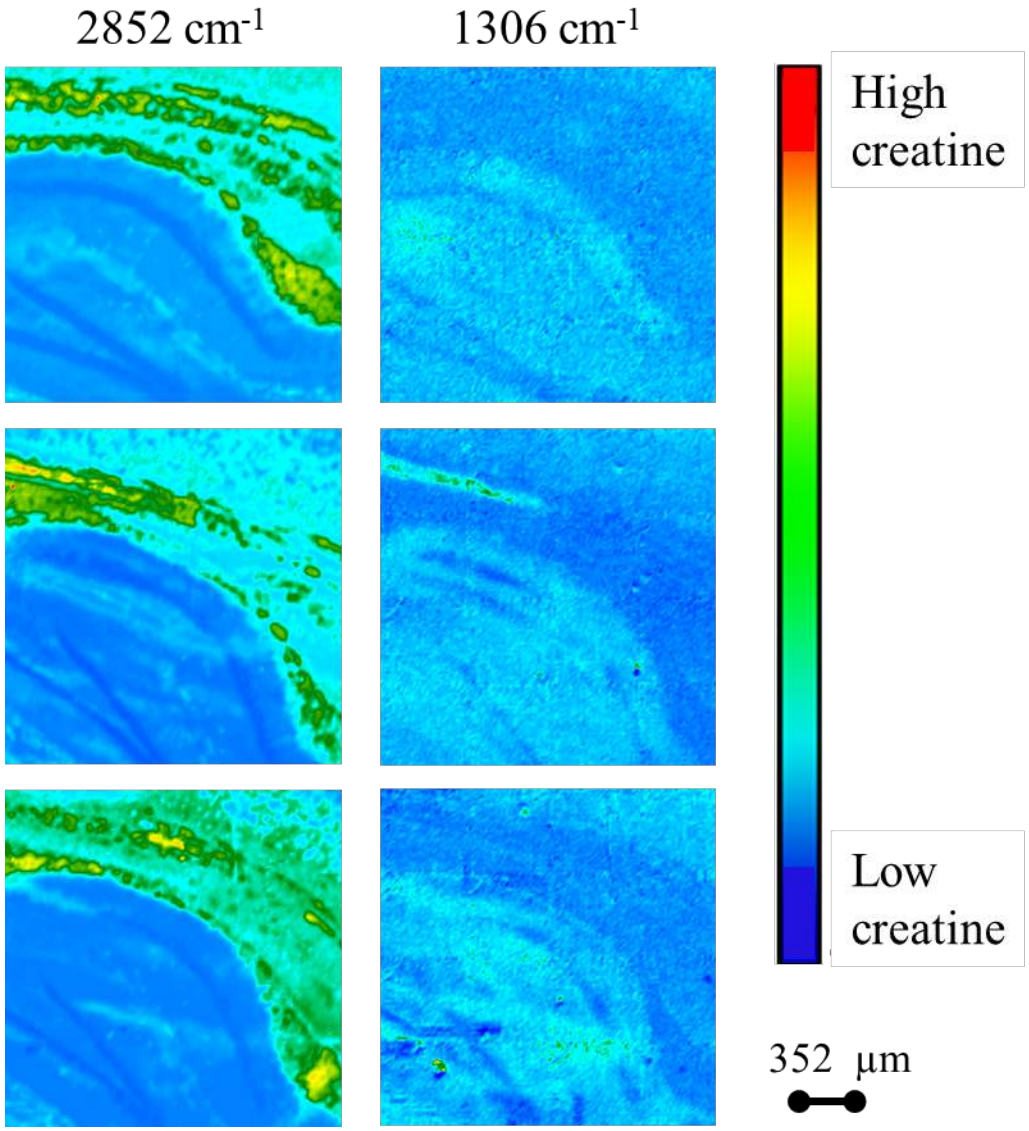

Figure 8.14. Creatine appearance from 3xTg-362 (9-month male transgenic mouse creatine diet). The spectrochemical image was processed for distribution of lipids (2852 cm^{-1}) to establish tissue morphology and creatine (1306 cm^{-1}) to assess creatine localization. The image is processed with methods outlined in table 4.1. As per scale, the red color represents areas with high creatine concentration. Upper scale = 0.6216, Lower scale = -0.1540.

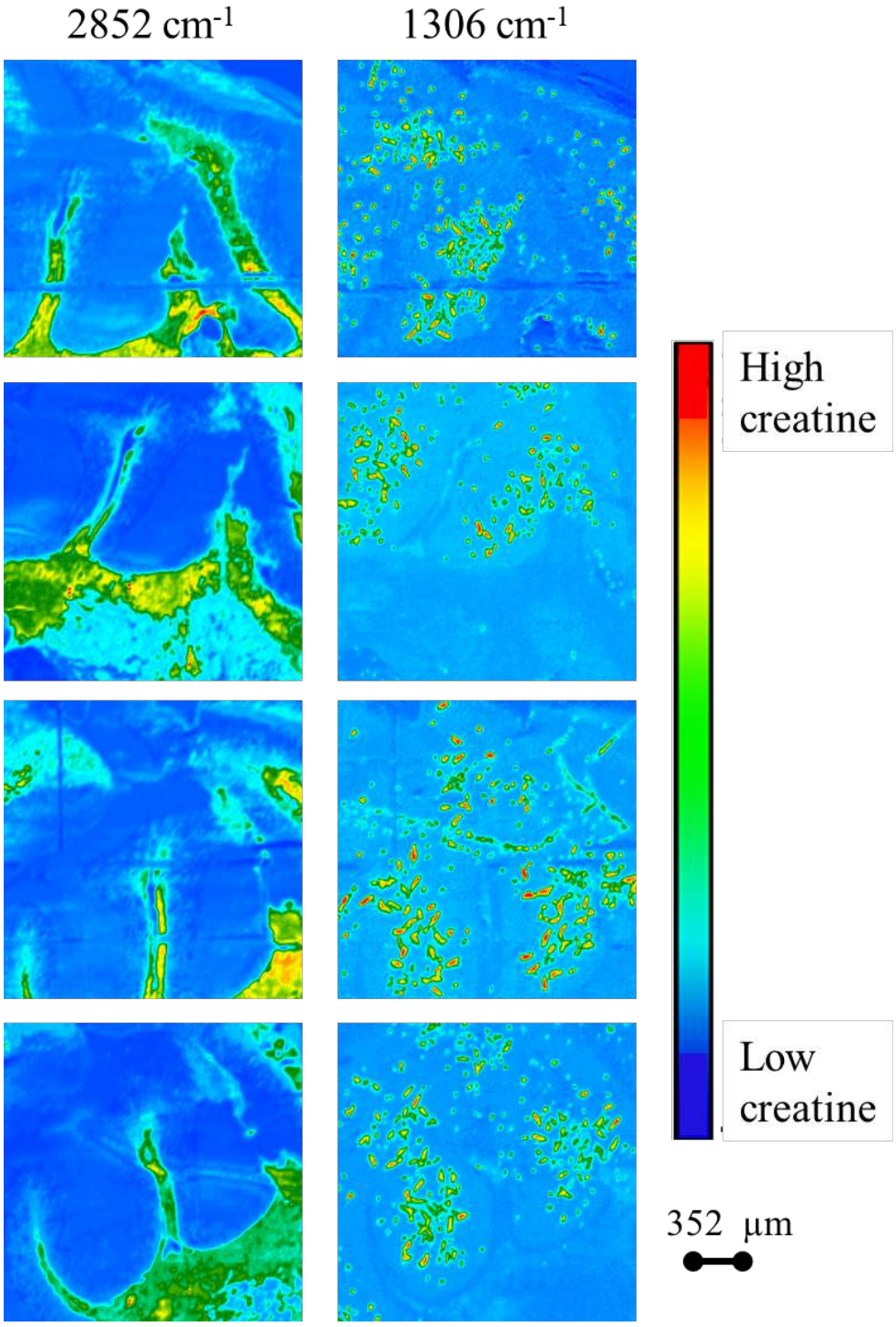

Figure 8.15. Creatine appearance in the cerebellum of 3xTg-362 (9-month male transgenic mouse creatine diet). The spectrochemical image was processed for distribution of lipids (2852 cm^{-1}) to establish tissue morphology and creatine (1306 cm^{-1}) to assess creatine localization. The image is processed with methods outlined in table 4.1. As per scale, the red color represents areas with high creatine concentration. Upper scale = 0.6617, Lower scale = -0.1540.

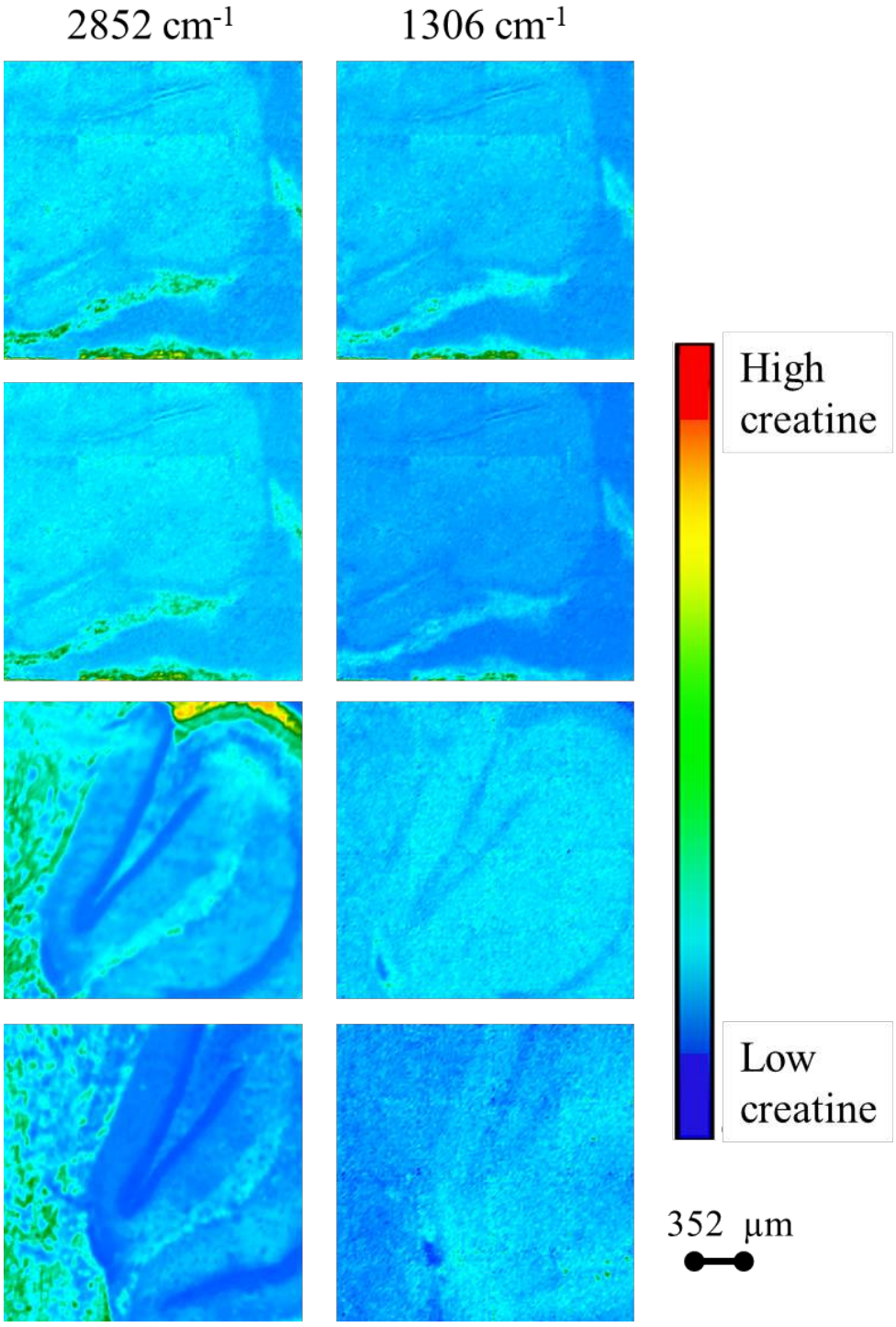

Figure 8.17. Creatine appearance in the hippocampus of 3xTg-383 (9-month male transgenic mouse control diet). The spectrochemical image was processed for distribution of lipids (2852 cm^{-1}) to establish tissue morphology and creatine (1306 cm^{-1}) to assess creatine localization. The image is processed with methods outlined in table 4.1. As per scale, the red color represents areas with high creatine concentration. Upper scale = 0.2711, Lower scale = -0.0230.

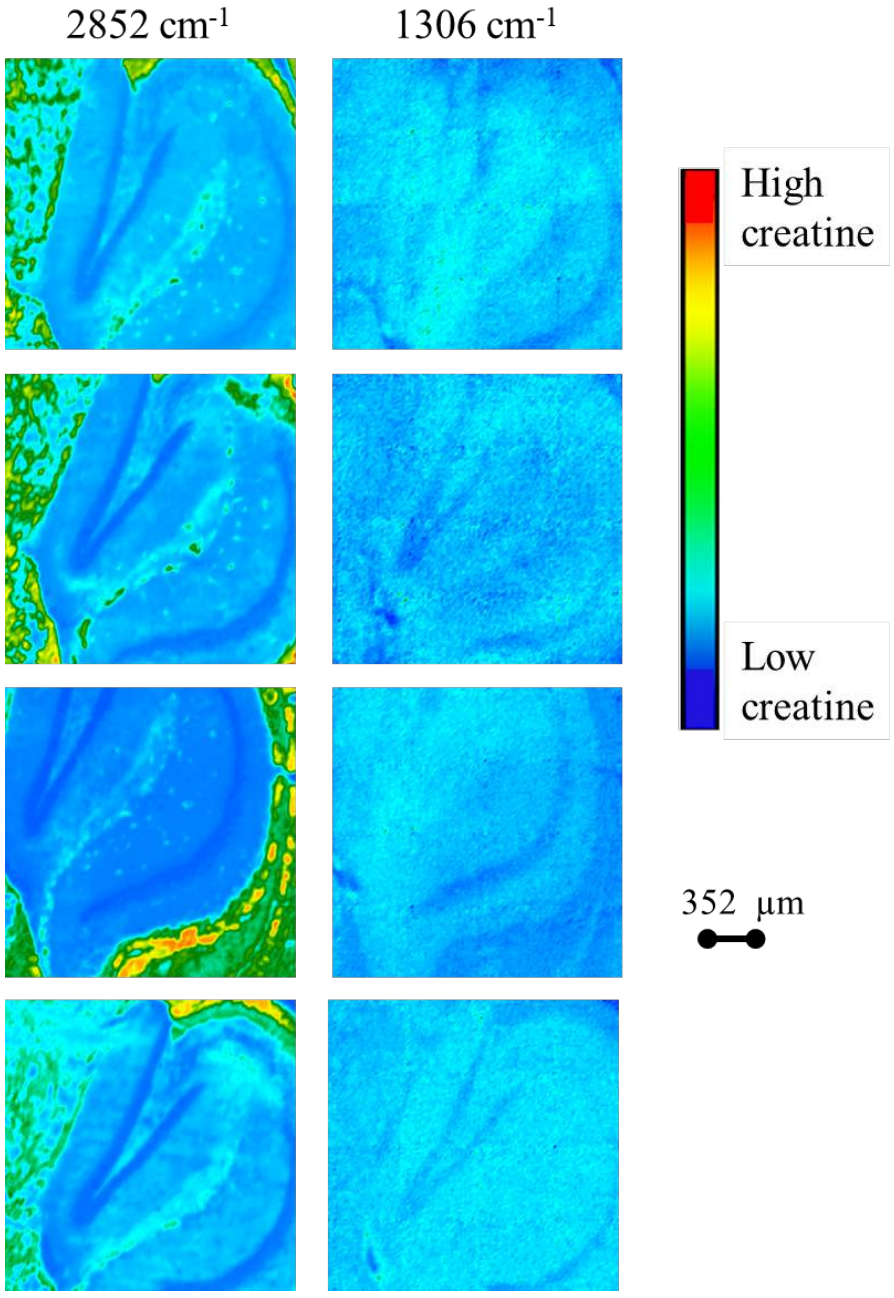

Figure 8.18. Creatine appearance in the hippocampus of 3xTg-383 (9-month male transgenic mouse control diet). The spectrochemical image was processed for distribution of lipids (2852 cm^{-1}) to establish tissue morphology and creatine (1306 cm^{-1}) to assess creatine localization. The image is processed with methods outlined in table 4.1. As per scale, the red color represents areas with high creatine concentration. Upper scale = 0.2711, Lower scale = -0.0230.

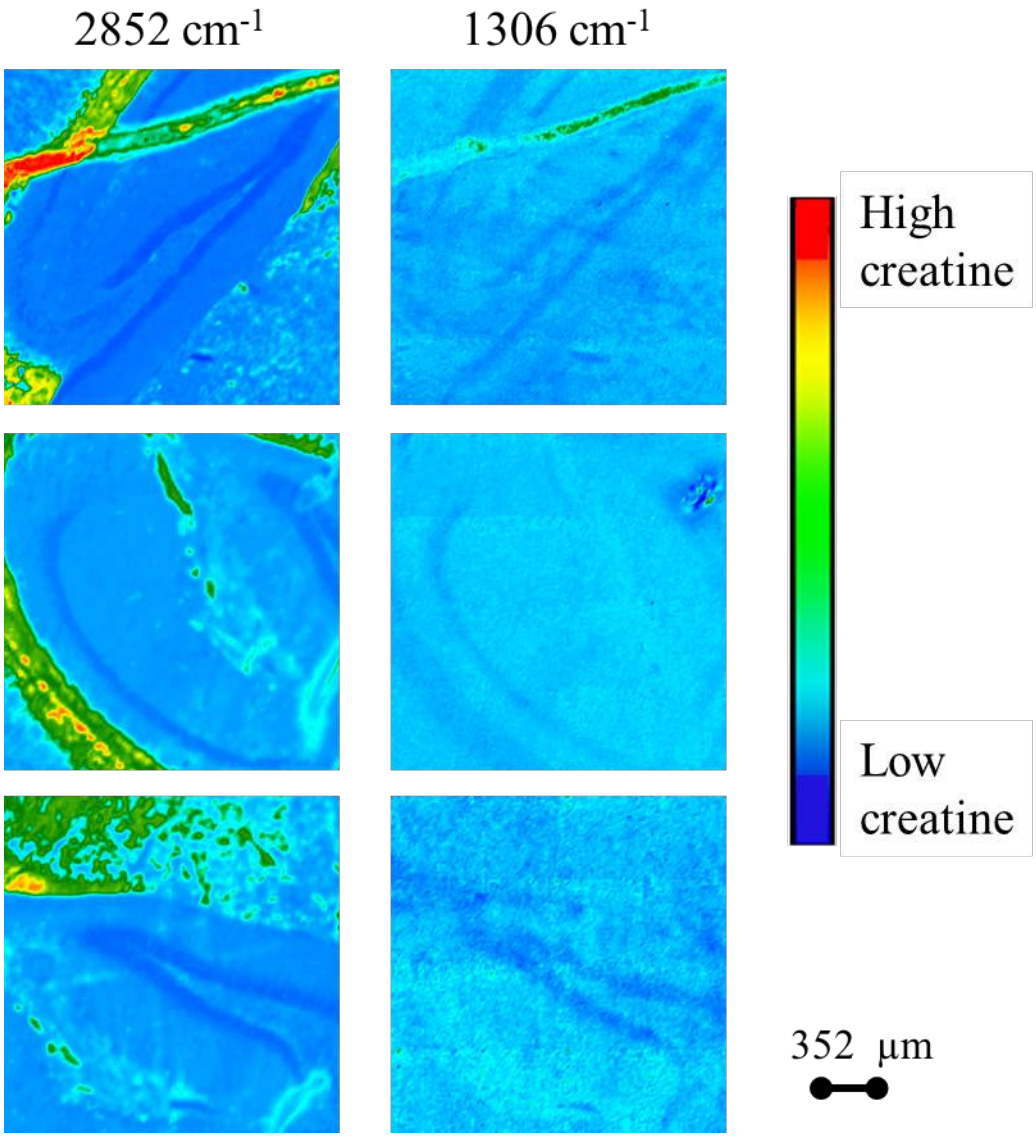

Figure 8.18. Creatine appearance in the hippocampus of 3xTg-363 (9-month female transgenic mouse creatine diet). The spectrochemical image was processed for distribution of lipids (2852 cm^{-1}) to establish tissue morphology and creatine (1306 cm^{-1}) to assess creatine localization. The image is processed with methods outlined in table 4.1. As per scale, the red color represents areas with high creatine concentration. Upper scale = 0.2610, Lower scale = -0.0220.

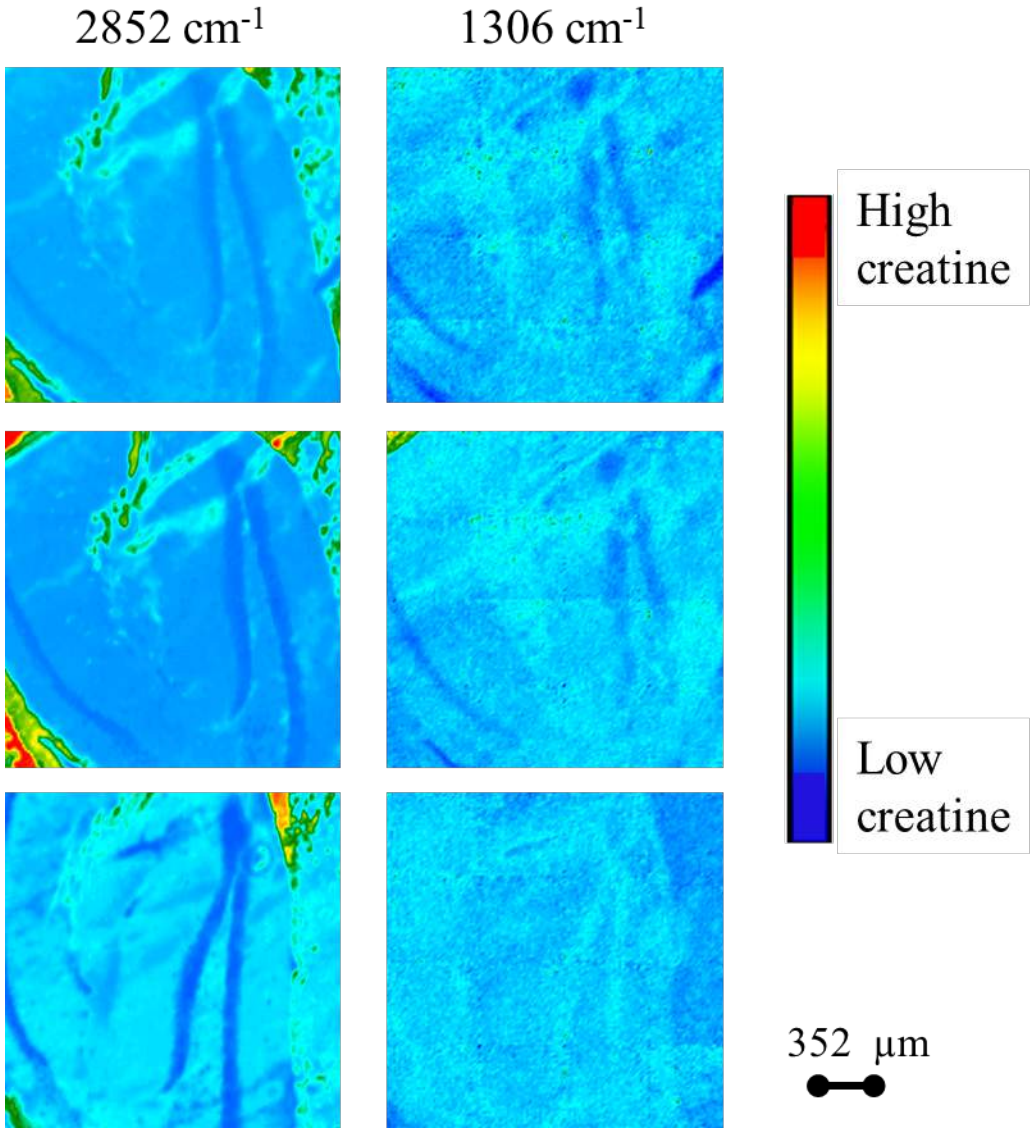

Figure 8.19. Creatine appearance in the hippocampus of 3xTg-363 (9-month female transgenic mouse creatine diet). The spectrochemical image was processed for distribution of lipids (2852 cm^{-1}) to establish tissue morphology and creatine (1306 cm^{-1}) to assess creatine localization. The image is processed with methods outlined in table 4.1. As per scale, the red color represents areas with high creatine concentration. Upper scale = 0.2610, Lower scale = -0.0220.

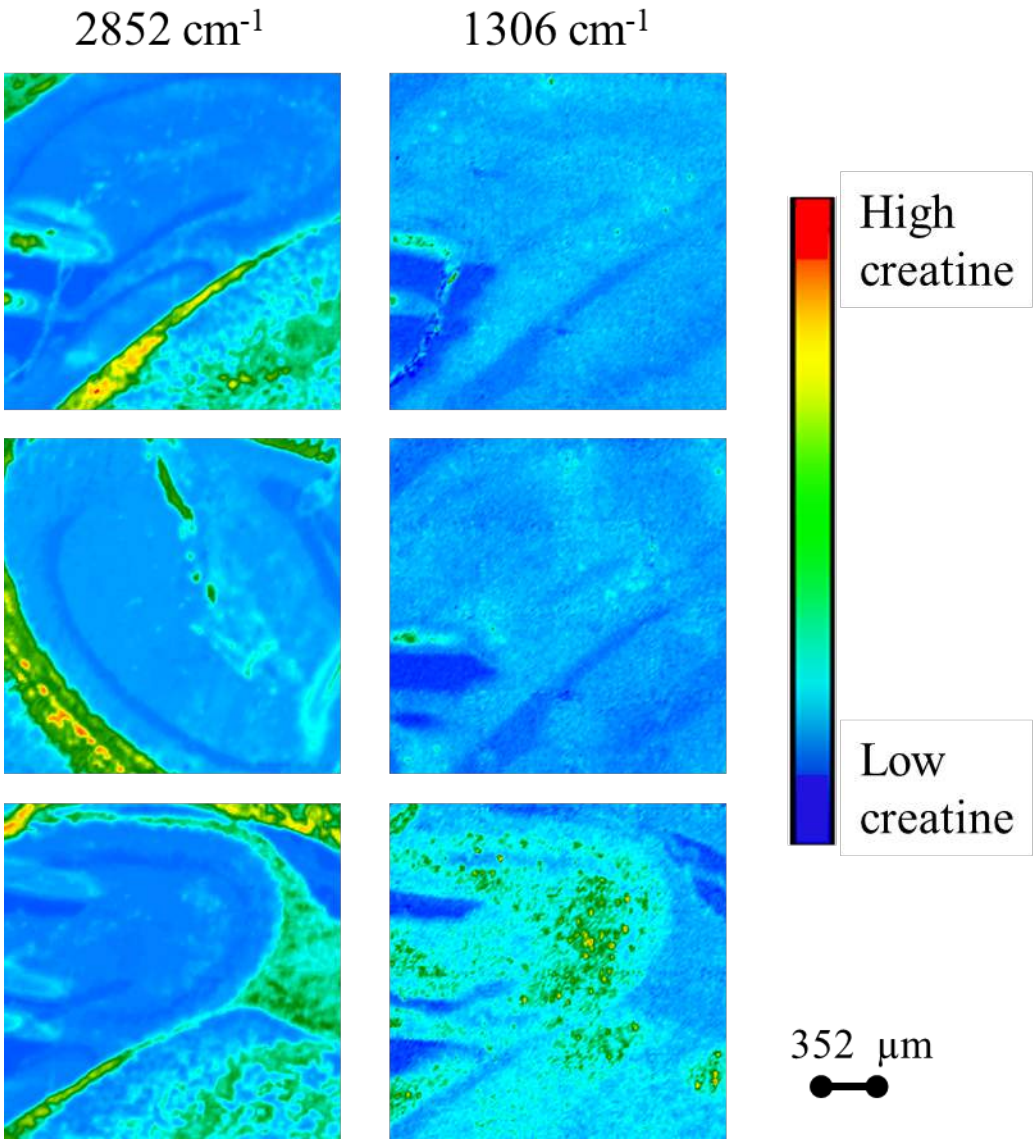

Figure 8.20. Creatine appearance in the hippocampus of 3xTg-365 (9-month female transgenic mouse creatine diet). The spechtrochemical image was processed for distribution of lipids (2852 cm^{-1}) to establish tissue morphology and creatine (1306 cm^{-1}) to assess creatine localization. The image is processed with methods outlined in table 4.1. Upper scale 0.3573; Lower scale - 0.0988.

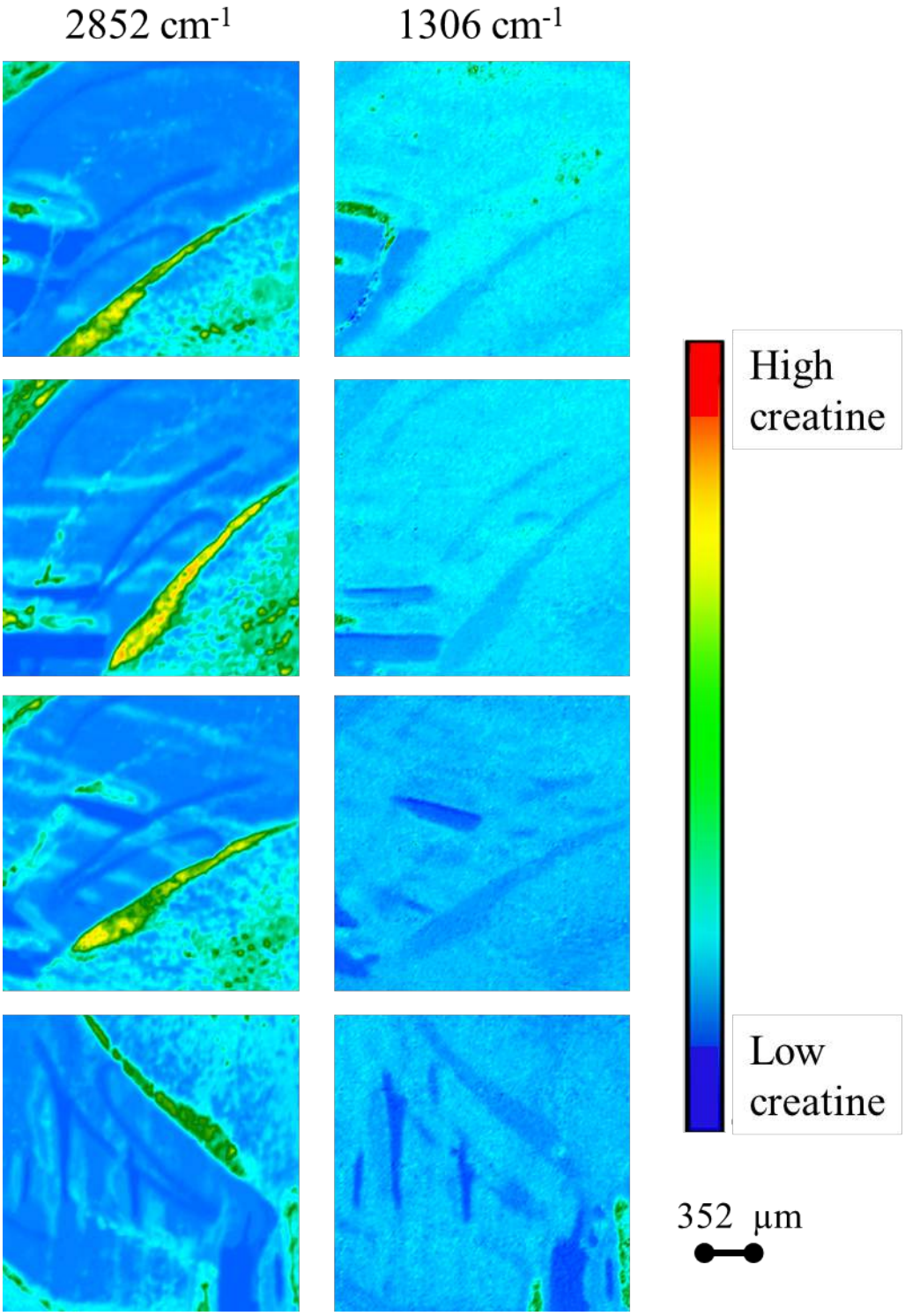

Figure 8.20. Creatine appearance in the hippocampus of 3xTg-365 (9-month female transgenic mouse creatine diet). The spechtrochemical image was processed for distribution of lipids (2852 cm^{-1}) to establish tissue morphology and creatine (1306 cm^{-1}) to assess creatine localization. The image is processed with methods outlined in table 4.1. Upper scale 0.3573; Lower scale - 0.0988.

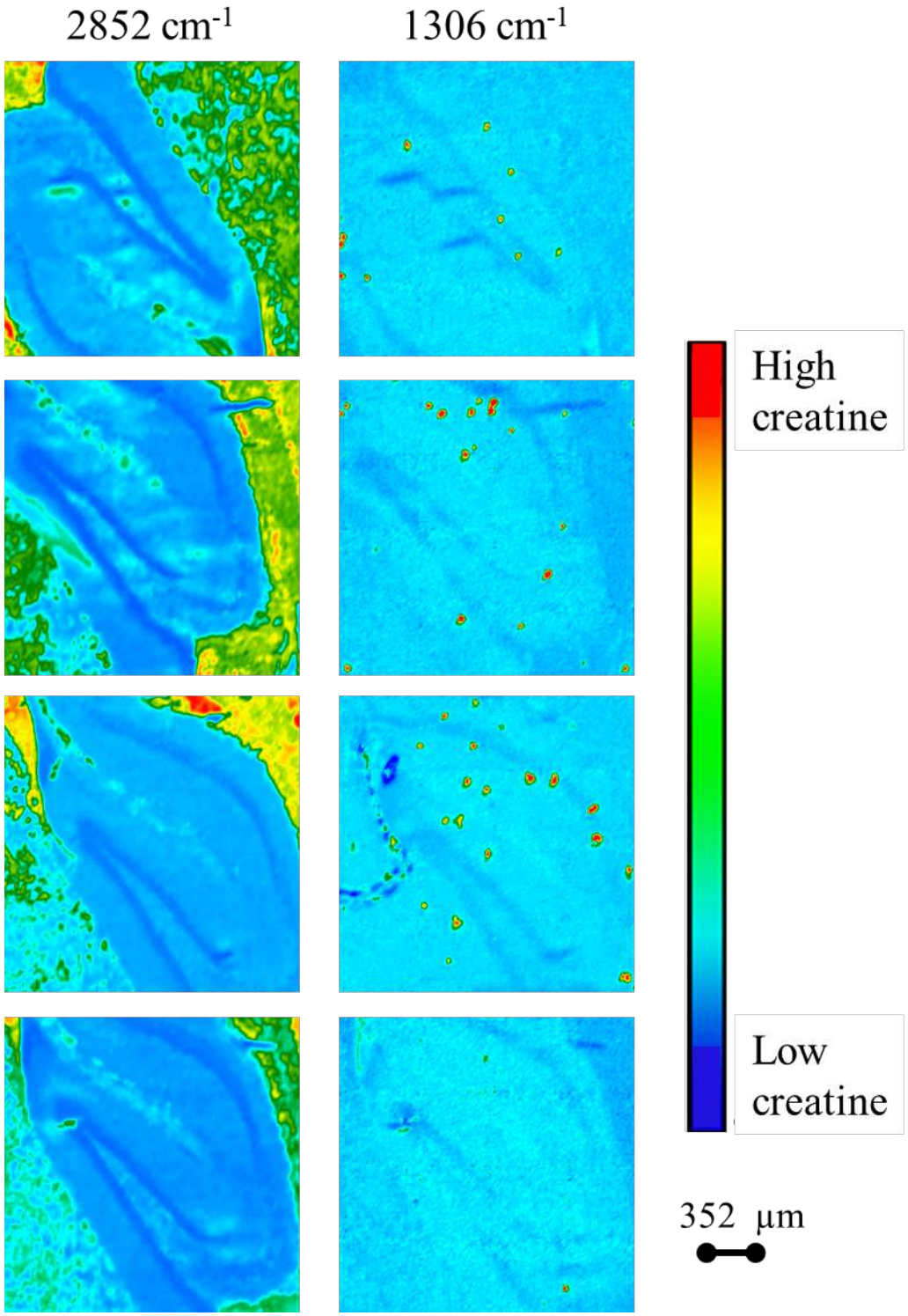

Figure 8.21. Creatine appearance in the hippocampus of 3xTg-381 (9-month female transgenic mouse control diet). The spectrochemical image was processed for distribution of lipids (2852 cm^{-1}) to establish tissue morphology and creatine (1306 cm^{-1}) to assess creatine localization. The image is processed with methods outlined in table 4.1. Upper scale 0.3717; Lower scale - 0.0823.

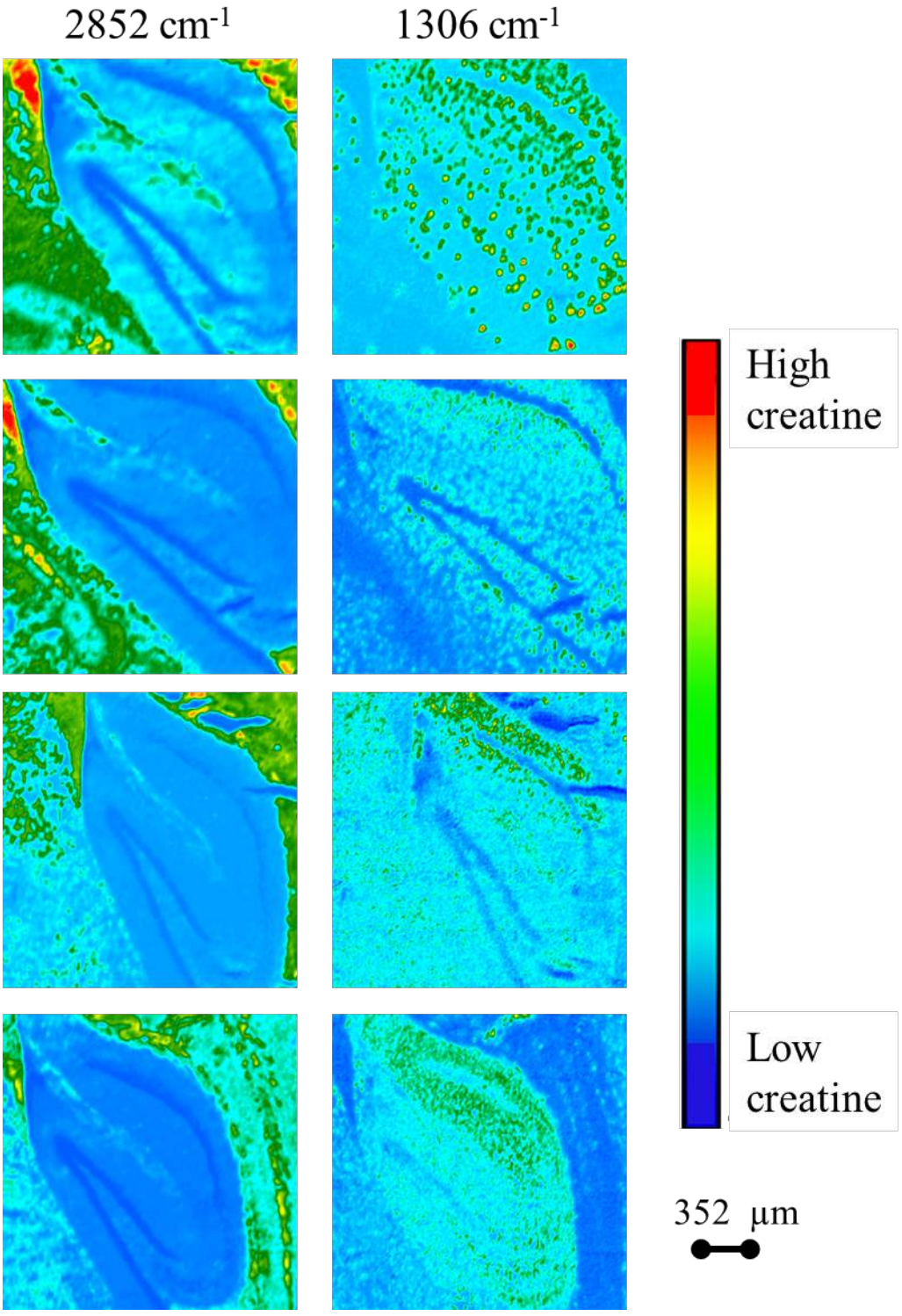

Figure 8.22. Creatine appearance in the hippocampus of 3xTg-381 (9-month female transgenic mouse control diet). The spectrochemical image was processed for distribution of lipids (2852 cm^{-1}) to establish tissue morphology and creatine (1306 cm^{-1}) to assess creatine localization. The image is processed with methods outlined in table 4.1. Upper scale 0.3717; Lower scale - 0.0823.

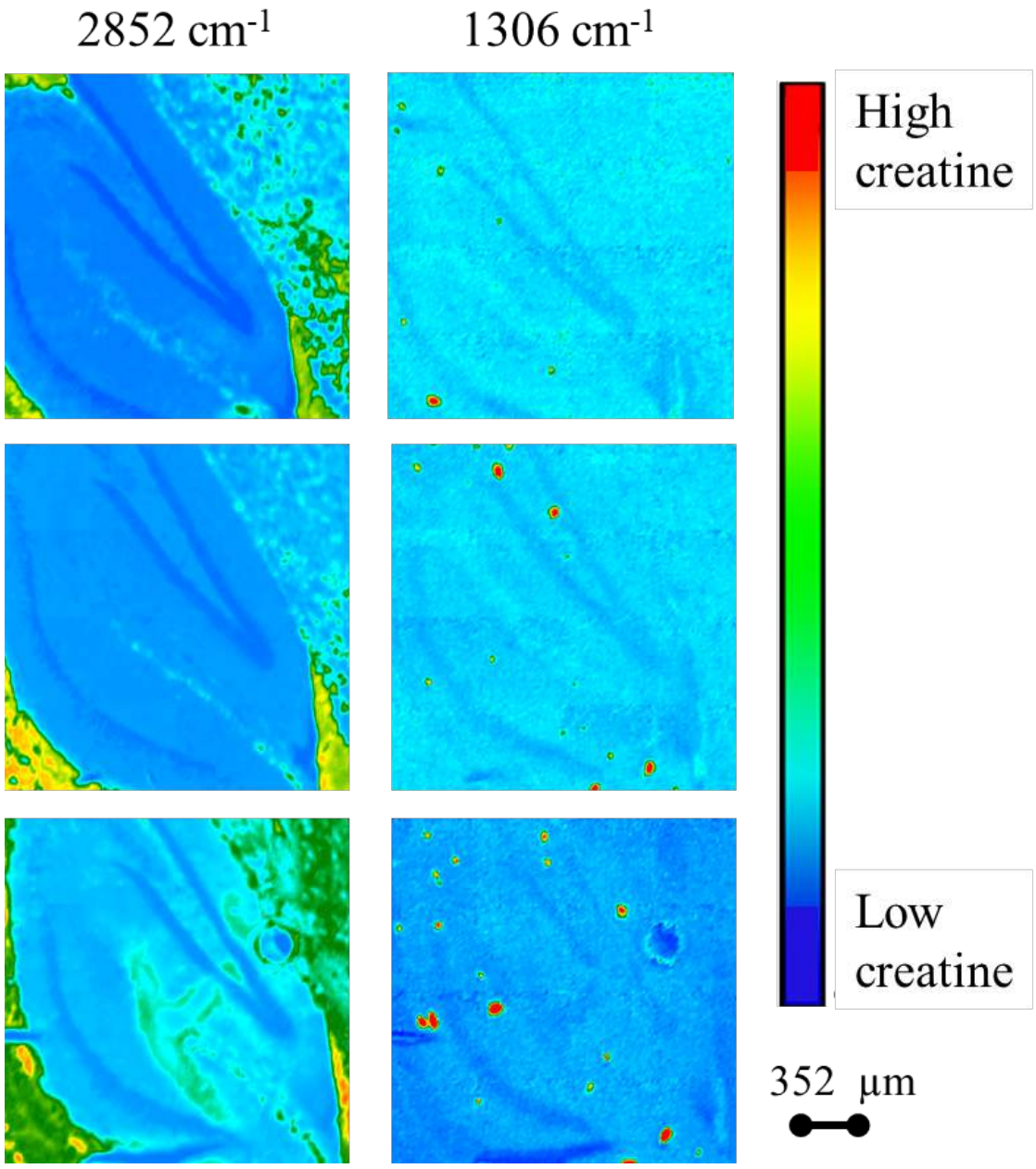

Figure 8.23. Creatine appearance in the hippocampus of 3xTg-381 (9-month female transgenic mouse control diet). The spectrochemical image was processed for distribution of lipids (2852 cm^{-1}) to establish tissue morphology and creatine (1306 cm^{-1}) to assess creatine localization. The image is processed with methods outlined in table 4.1. Upper scale 0.3717; Lower scale - 0.0823.

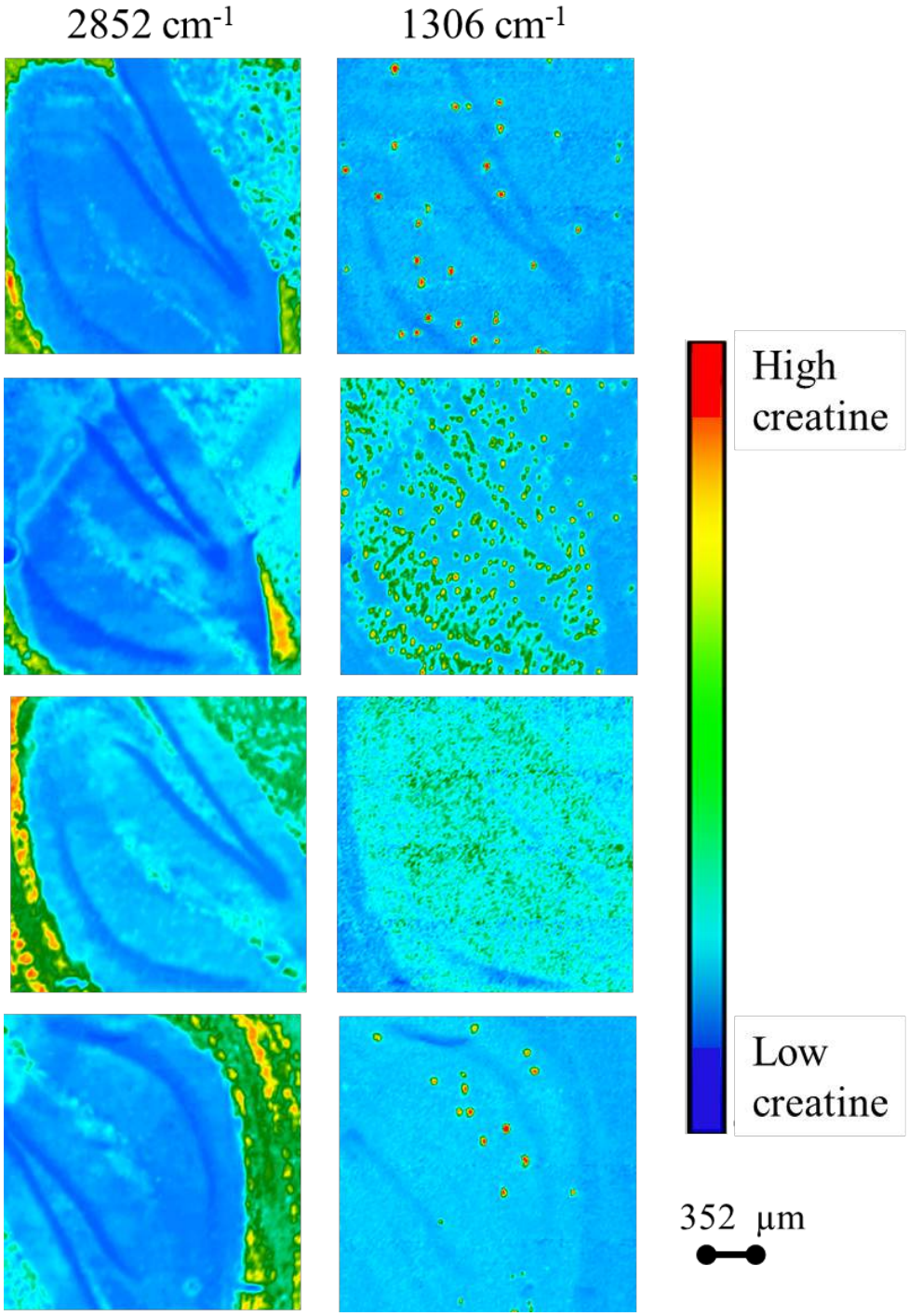

Figure 8.24. Creatine appearance in the hippocampus of 3xTg-381 (9-month female transgenic mouse control diet). The spectrochemical image was processed for distribution of lipids (2852 cm^{-1}) to establish tissue morphology and creatine (1306 cm^{-1}) to assess creatine localization. The image is processed with methods outlined in table 4.1. Upper scale 0.3717; Lower scale - 0.0823.

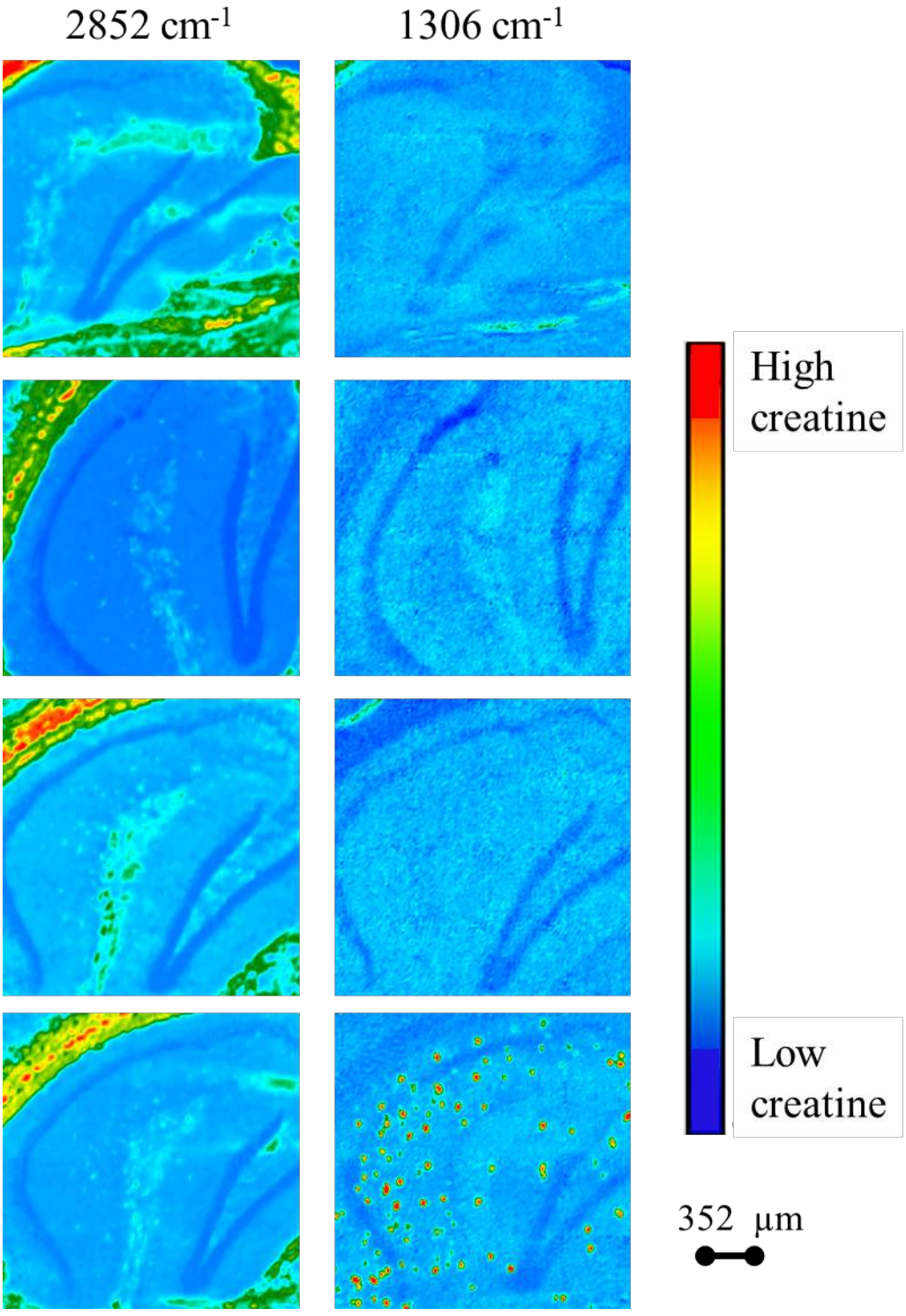

Figure 8.25. Creatine appearance in the hippocampus of 3xTg-382 (9-month female transgenic mouse control diet). The spectrochemical image was processed for distribution of lipids (2852 cm^{-1}) to establish tissue morphology and creatine (1306 cm^{-1}) to assess creatine localization. The image is processed with methods outlined in table 4.1. Upper scale 0.4431; Lower scale -0.0401.

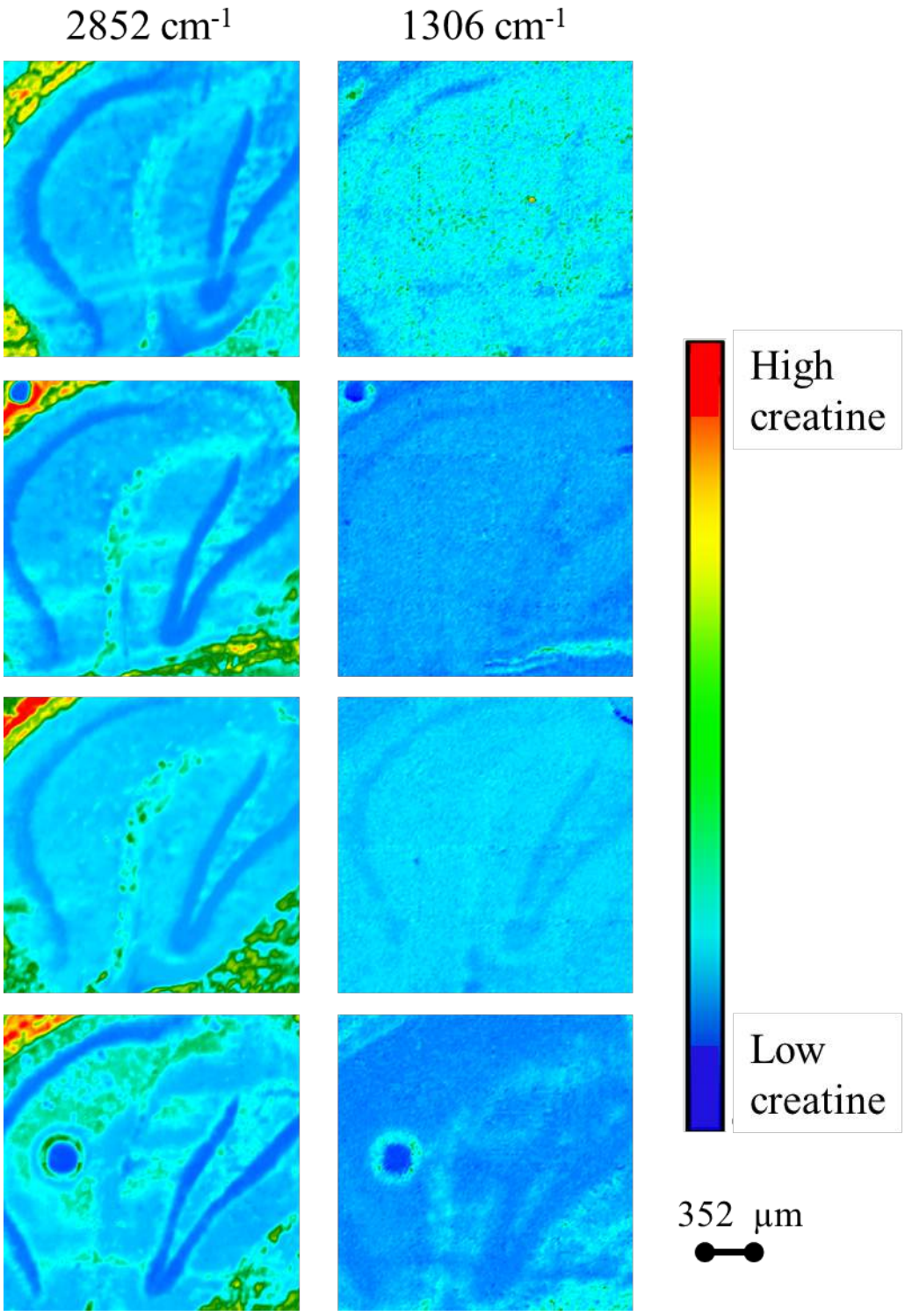

Figure 8.26. Creatine appearance in the hippocampus of 3xTg-382 (9-month female transgenic mouse control diet). The spectrochemical image was processed for distribution of lipids (2852 cm^{-1}) to establish tissue morphology and creatine (1306 cm^{-1}) to assess creatine localization. The image is processed with methods outlined in table 4.1. Upper scale 0.4431; Lower scale -0.0401.

Appendix II

FTIR Spechtrochemical Images of Cryosectioning Conditions

Appendix II

This chapter contains spectrochemical images obtained from crysectioning experiments (Figure 9.1-9.13). These experiments were conducted to determine whether sectioning conditions affect tissue quality and creatine crystal formation. All the sections that were imaged did not show evidence of creatine crystals. Thus, the cryosectioning conditions do not have an impact on creatine appearance and localization in brain tissue sections.

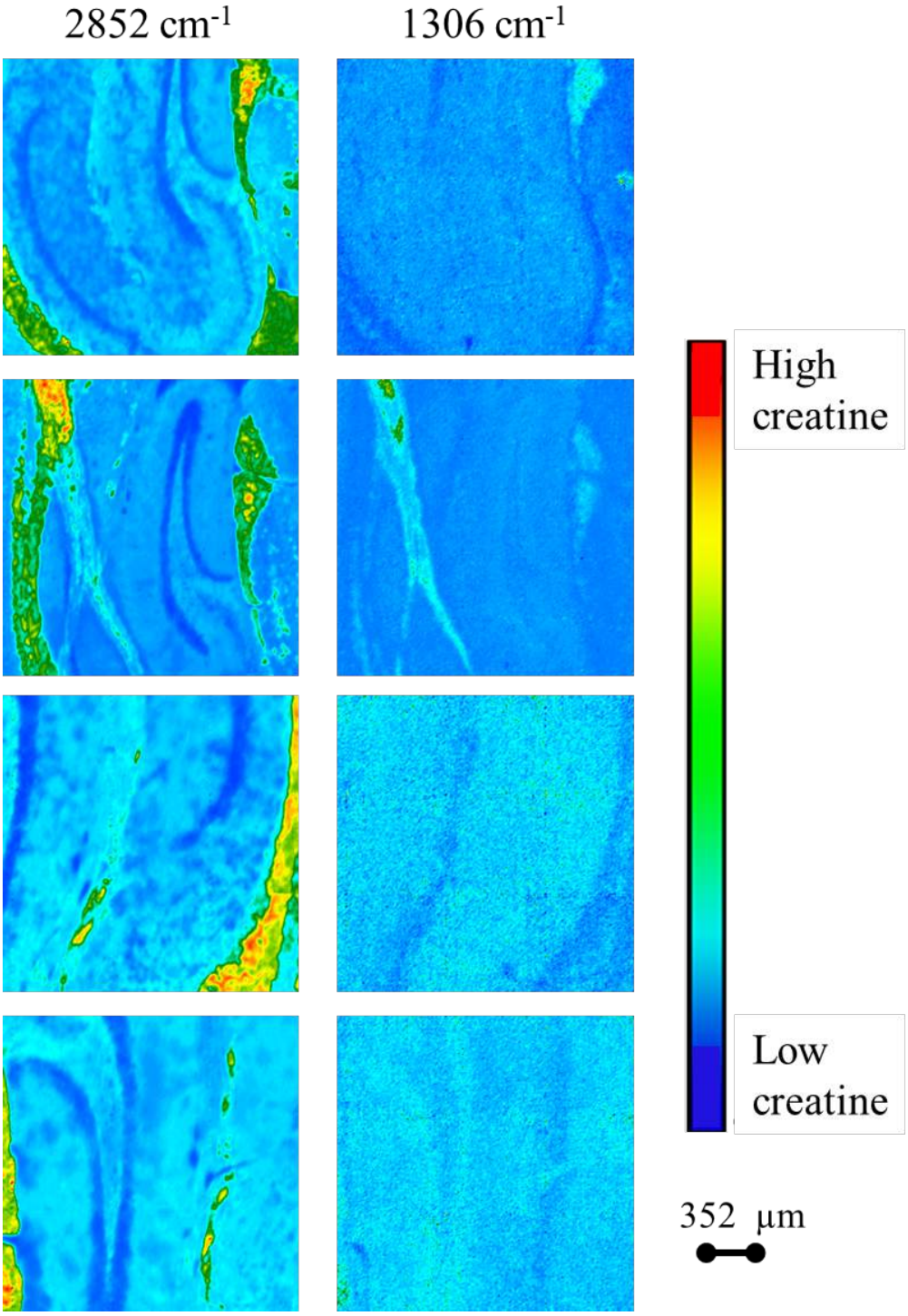

Figure 9.1 Creatine appearance in the hippocampus of 3xTg-448 (3xTg mouse on standard diet) acquired with exposed wind blowing on the brain tissue (tissue exposed to wind). The spectrochemical images were processed for distribution of lipids (2852 cm^{-1}) to establish tissue morphology and creatine (1306 cm^{-1}) to assess creatine localization. The image is processed with methods outlined in table 4.1. Upper scale 0.4320, Lower scale -0.0974.

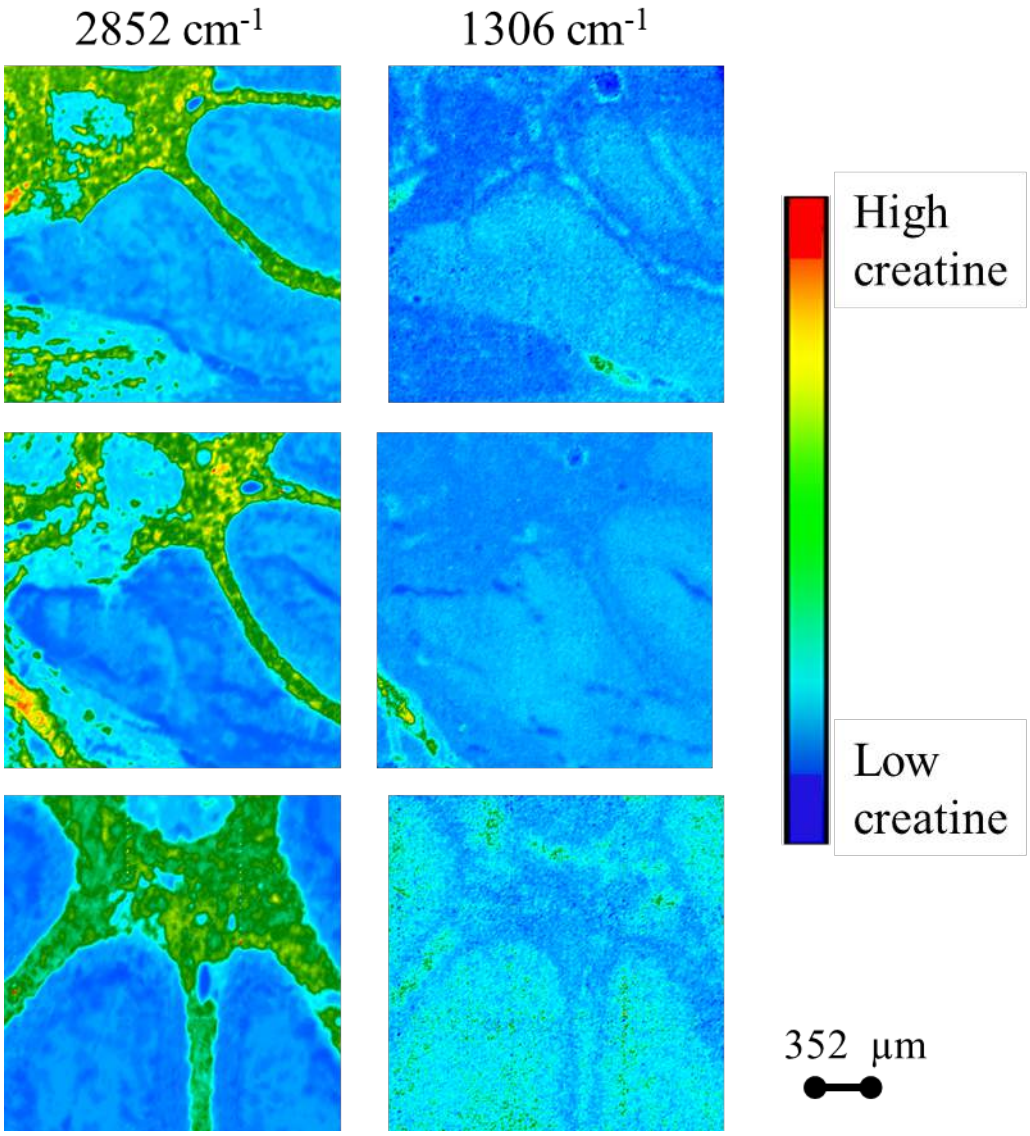

Figure 9.2. Creatine appearance in the cerebellum of 3xTg-448 (3xTg mouse on standard diet) acquired with wind blowing on the brain tissue (tissue exposed to wind). The spectrochemical images were processed for distribution of lipids (2852 cm^{-1}) to establish tissue morphology and creatine (1306 cm^{-1}) to assess creatine localization. The image is processed with methods outlined in table 4.1. Upper scale 0.4320, Lower scale -0.0974.

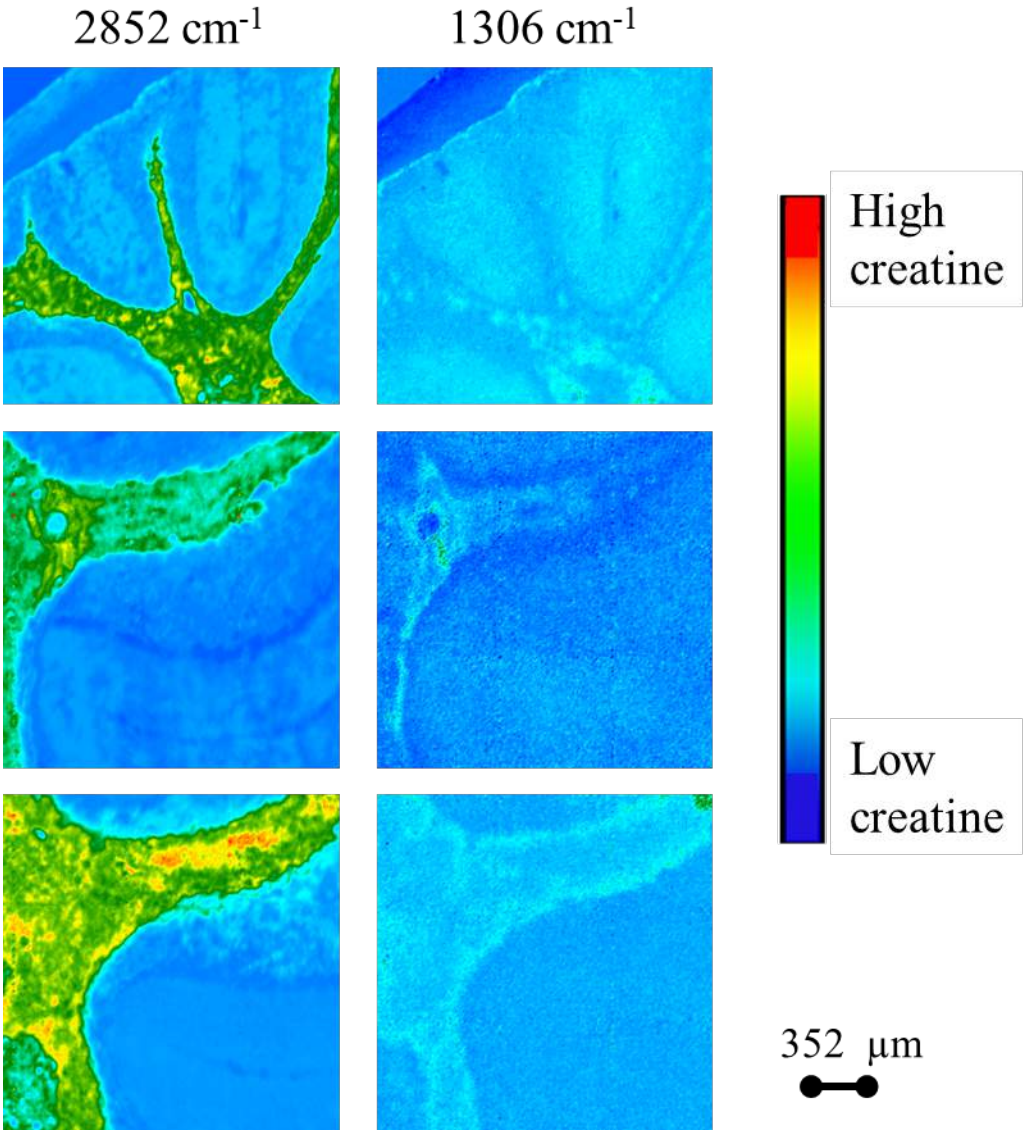

Figure 9.3. Creatine appearance in the cerebellum of 3xTg-448 (3xTg mouse on standard diet) acquired with wind blowing on the brain tissue (tissue exposed to wind). The spectrochemical images were processed for distribution of lipids (2852 cm^{-1}) to establish tissue morphology and creatine (1306 cm^{-1}) to assess creatine localization. The image is processed with methods outlined in table 4.1. Upper scale 0.4320, Lower scale -0.0974.

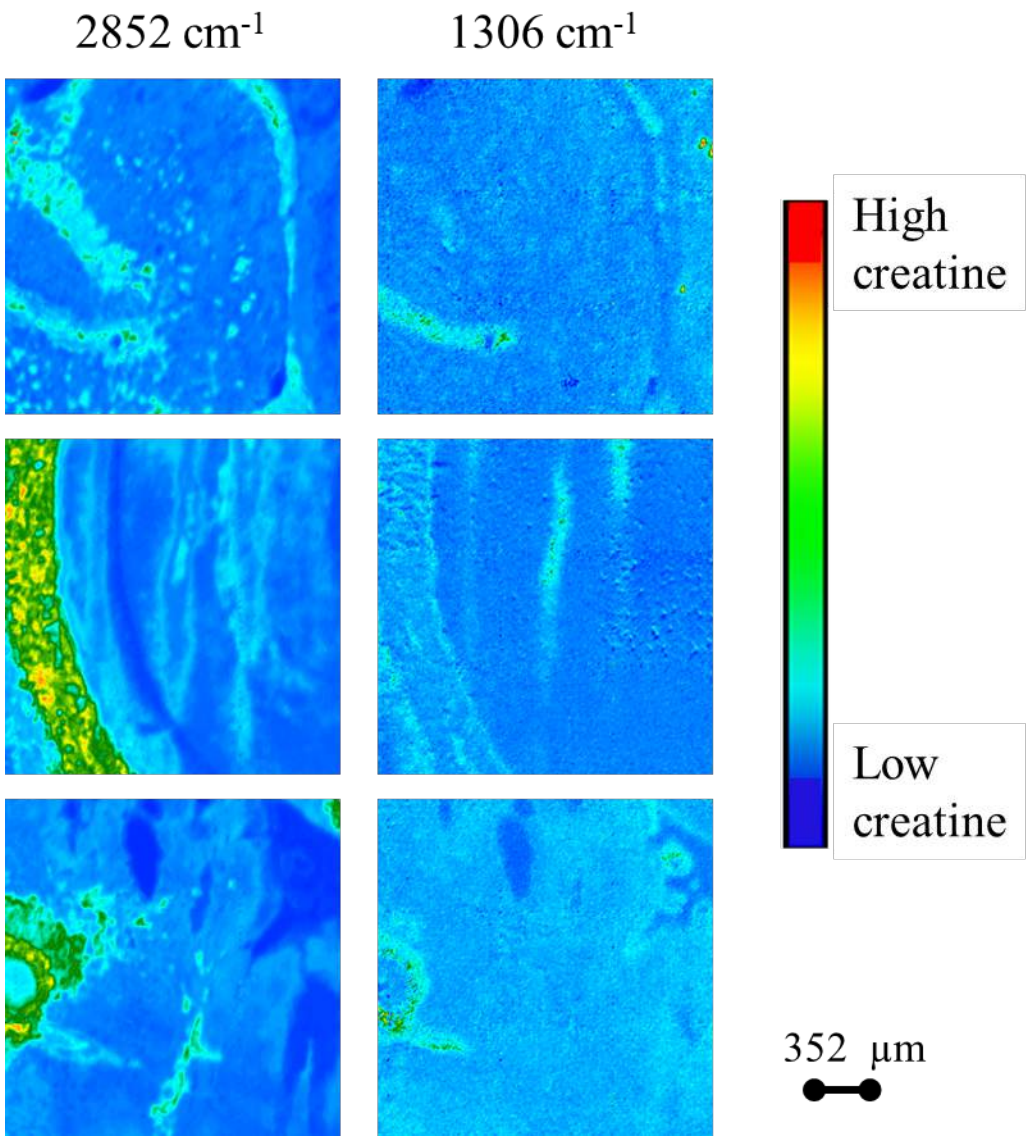

Figure 9.4. Creatine appearance in the hippocampus of 3xTg-448 (3xTg mouse on standard diet) acquired post the completion of a cycle of exposed wind blowing on the brain tissue. The spectrochemical images were processed for distribution of lipids (2852 cm^{-1}) to establish tissue morphology and creatine (1306 cm^{-1}) to assess creatine localization. The image is processed with methods outlined in table 4.1. Upper scale 0.4320, Lower scale -0.0974.

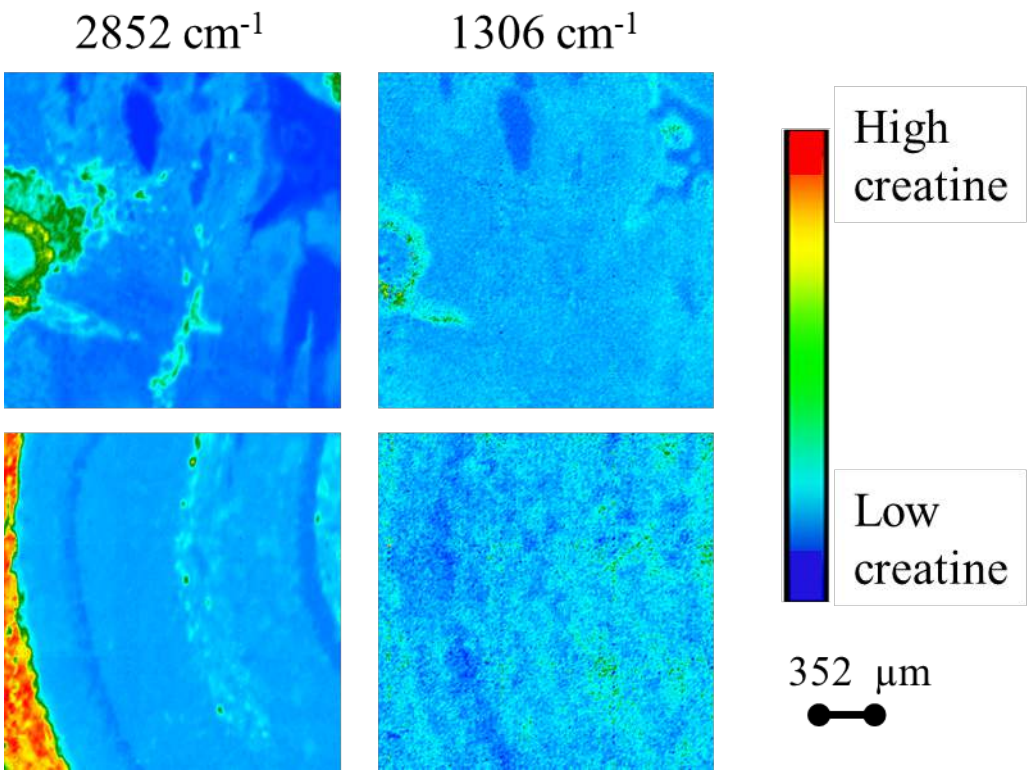

Figure 9.5. Creatine appearance in the hippocampus of 3xTg-448 (3xTg mouse on standard diet) acquired post the completion of a cycle of exposed wind blowing on the brain tissue. The spectrochemical images were processed for distribution of lipids (2852 cm^{-1}) to establish tissue morphology and creatine (1306 cm^{-1}) to assess creatine localization. The image is processed with methods outlined in table 4.1. Upper scale 0.4320, Lower scale -0.0974.

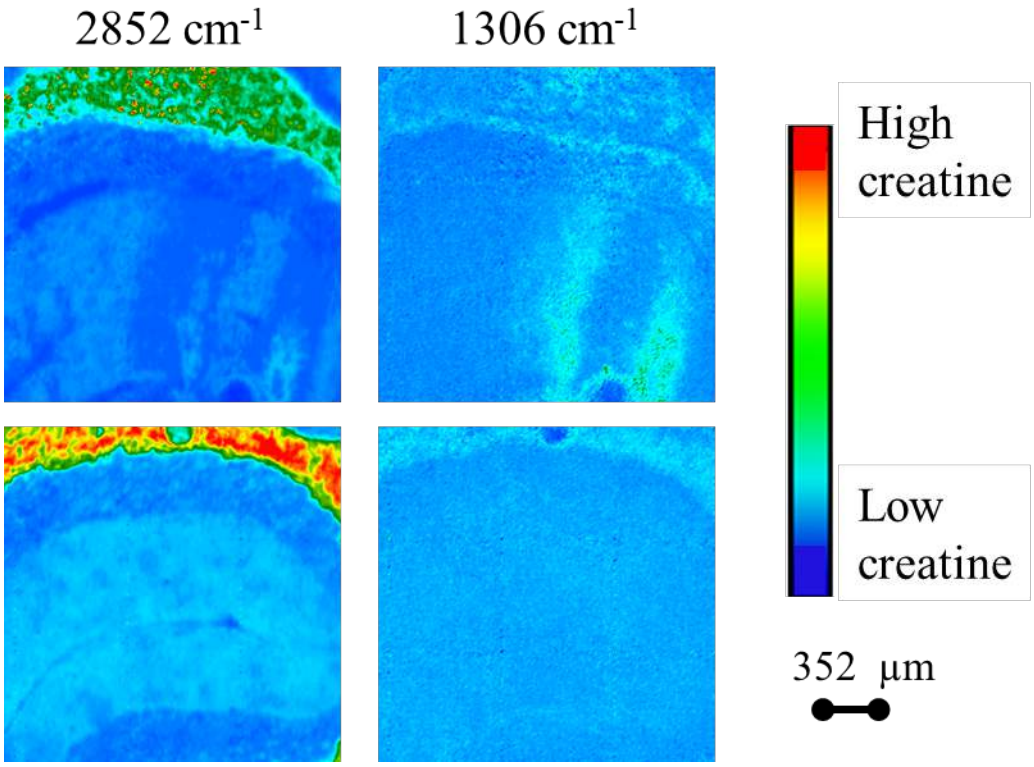

Figure 9.6. Creatine appearance in the cerebellum of 3xTg-448 (3xTg mouse on standard diet) acquired post the completion of a cycle of exposed wind blowing on the brain tissue. The spectrochemical images were processed for distribution of lipids (2852 cm^{-1}) to establish tissue morphology and creatine (1306 cm^{-1}) to assess creatine localization. The image is processed with methods outlined in table 4.1. Upper scale 0.4320, Lower scale -0.0974.

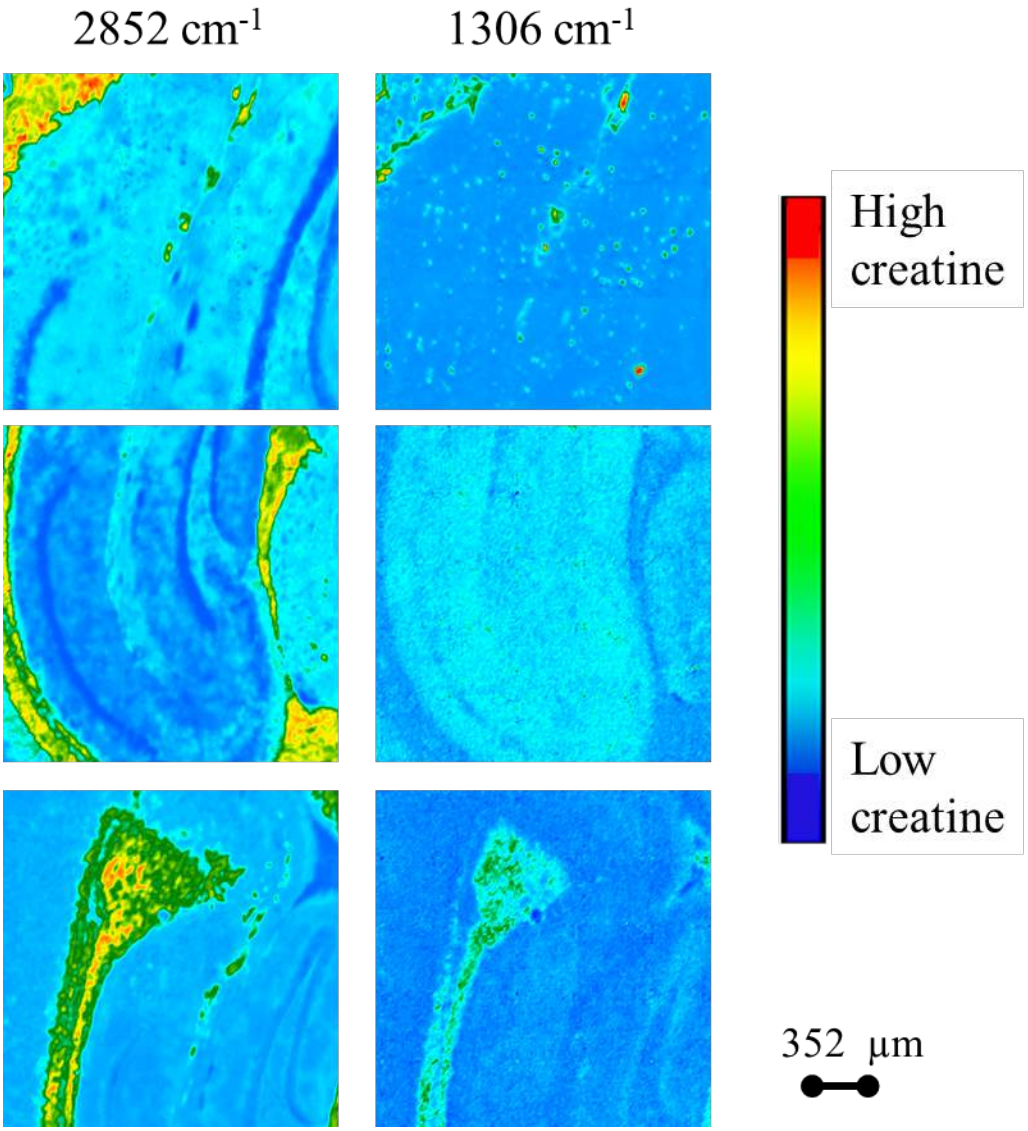

Figure 9.7. Creatine appearance in the hippocampus of 3xTg-448 (3xTg mouse on standard diet) acquired with sheltered wind blowing. These sections were acquired when the cryostat cooler blowing while the brain tissue was covered/sheltered. The spectrochemical images were processed for distribution of lipids (2852 cm^{-1}) to establish tissue morphology and creatine (1306 cm^{-1}) to assess creatine localization. The image is processed with methods outlined in table 4.1. Upper scale 0.4320, Lower scale -0.0974.

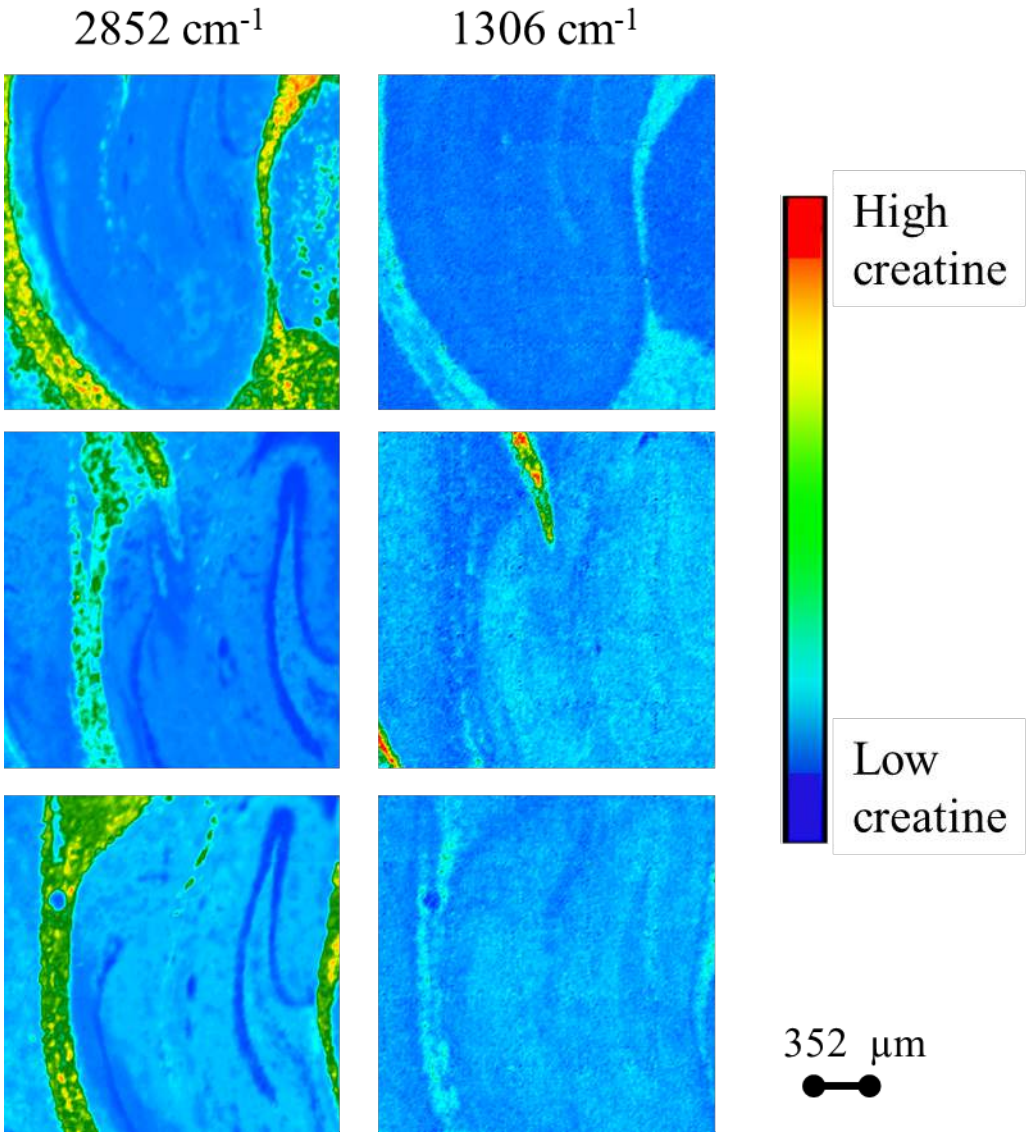

Figure 9.8. Creatine appearance in the hippocampus of 3xTg-448 (3xTg mouse on standard diet) acquired with sheltered wind blowing. These sections were acquired when the cryostat cooler blowing while the brain tissue was covered/sheltered. The spectrochemical images were processed for distribution of lipids (2852 cm^{-1}) to establish tissue morphology and creatine (1306 cm^{-1}) to assess creatine localization. The image is processed with methods outlined in table 4.1. Upper scale 0.4320, Lower scale -0.0974.

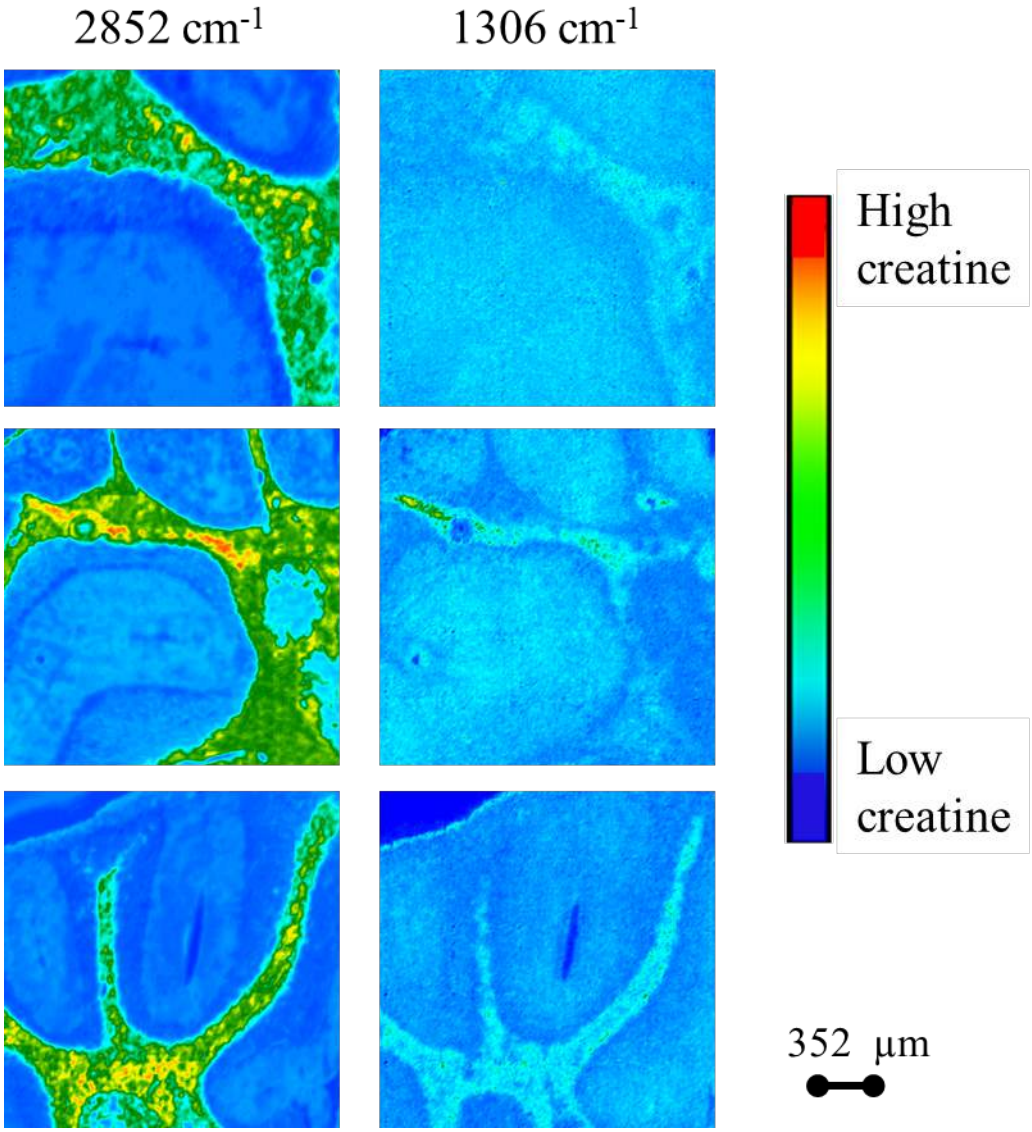

Figure 9.9. Creatine appearance in the cerebellum of 3xTg-448 (3xTg mouse on standard diet) acquired with sheltered wind blowing. These sections were acquired when the cryostat cooler blowing while the brain tissue was covered/sheltered. The spectrochemical images were processed for distribution of lipids (2852 cm^{-1}) to establish tissue morphology and creatine (1306 cm^{-1}) to assess creatine localization. The image is processed with methods outlined in table 4.1. Upper scale 0.4320, Lower scale -0.0974.

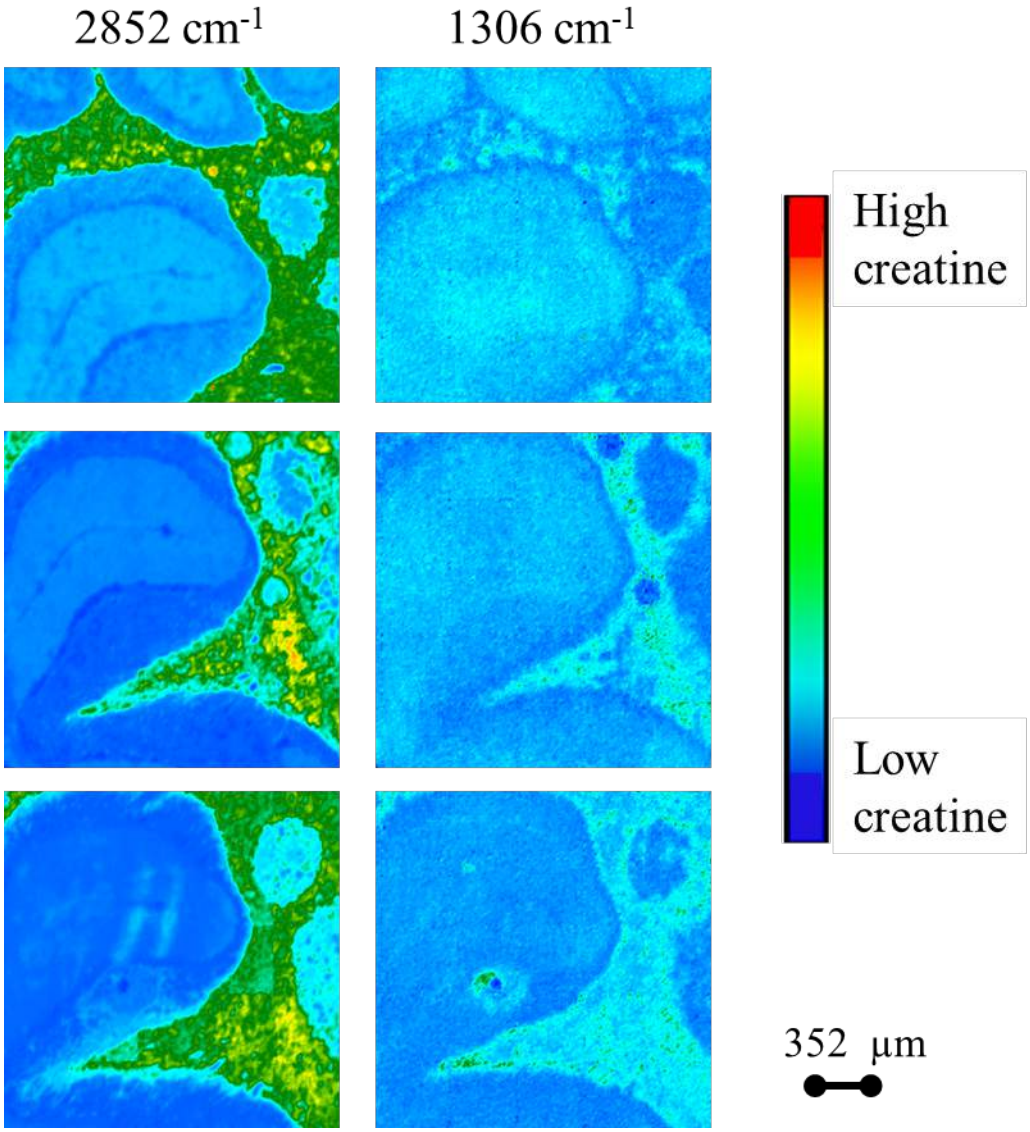

Figure 9.10. Creatine appearance in the cerebellum of 3xTg-448 (3xTg mouse on standard diet) acquired with sheltered wind blowing. These sections were acquired when the cryostat cooler blowing while the brain tissue was covered/sheltered. The spectrochemical images were processed for distribution of lipids (2852 cm^{-1}) to establish tissue morphology and creatine (1306 cm^{-1}) to assess creatine localization. The image is processed with methods outlined in table 4.1. Upper scale 0.4320, Lower scale -0.0974.

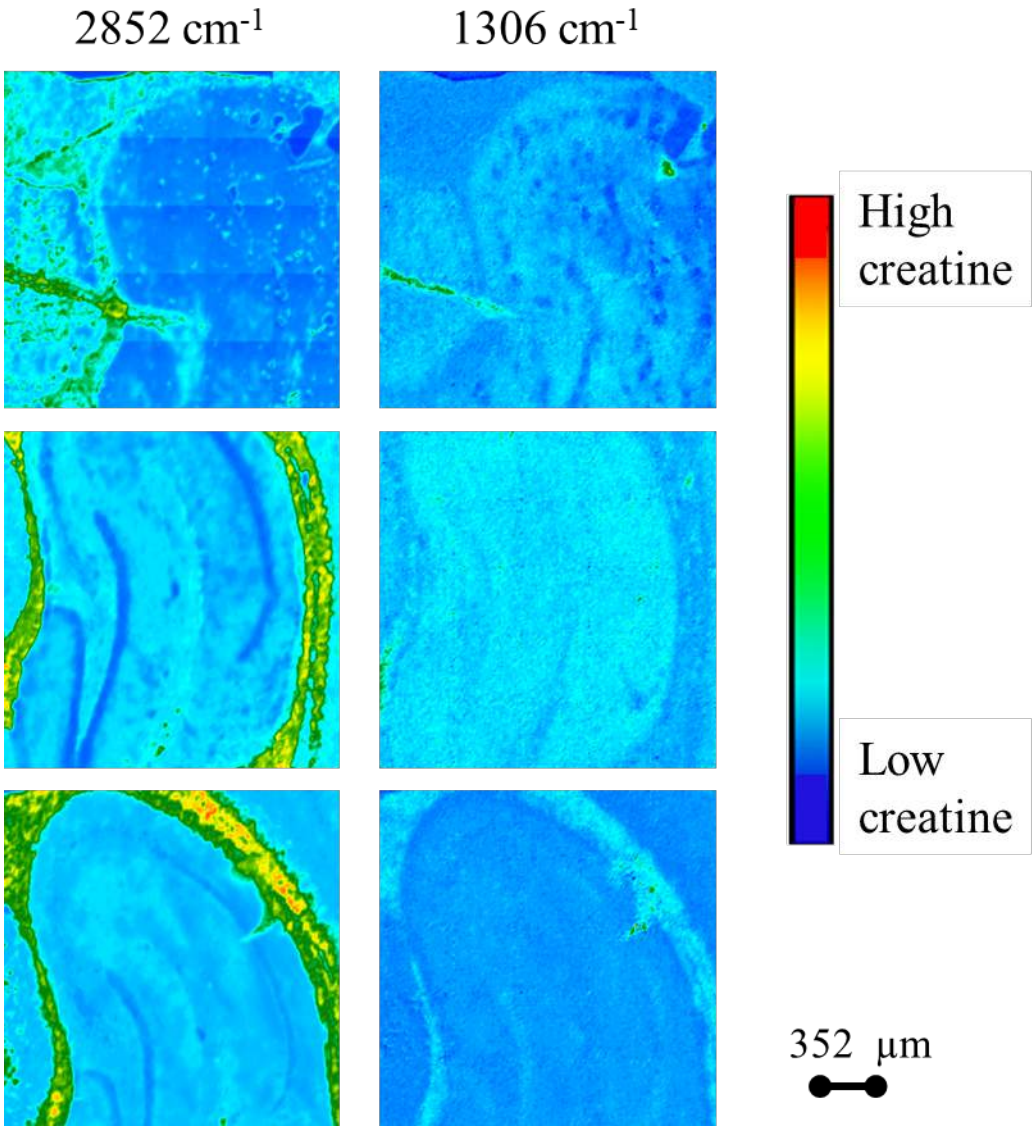

Figure 9.11. Creatine appearance in the hippocampus of 3xTg-448 (3xTg mouse on standard diet) acquired post a cycle of sheltered wind blowing. These sections were acquired when the cryostat cooler blowing while the brain tissue was covered/sheltered. The spectrochemical images were processed for distribution of lipids (2852 cm^{-1}) to establish tissue morphology and creatine (1306 cm^{-1}) to assess creatine localization. The image is processed with methods outlined in table 4.1. Upper scale 0.4320, Lower scale -0.0974.

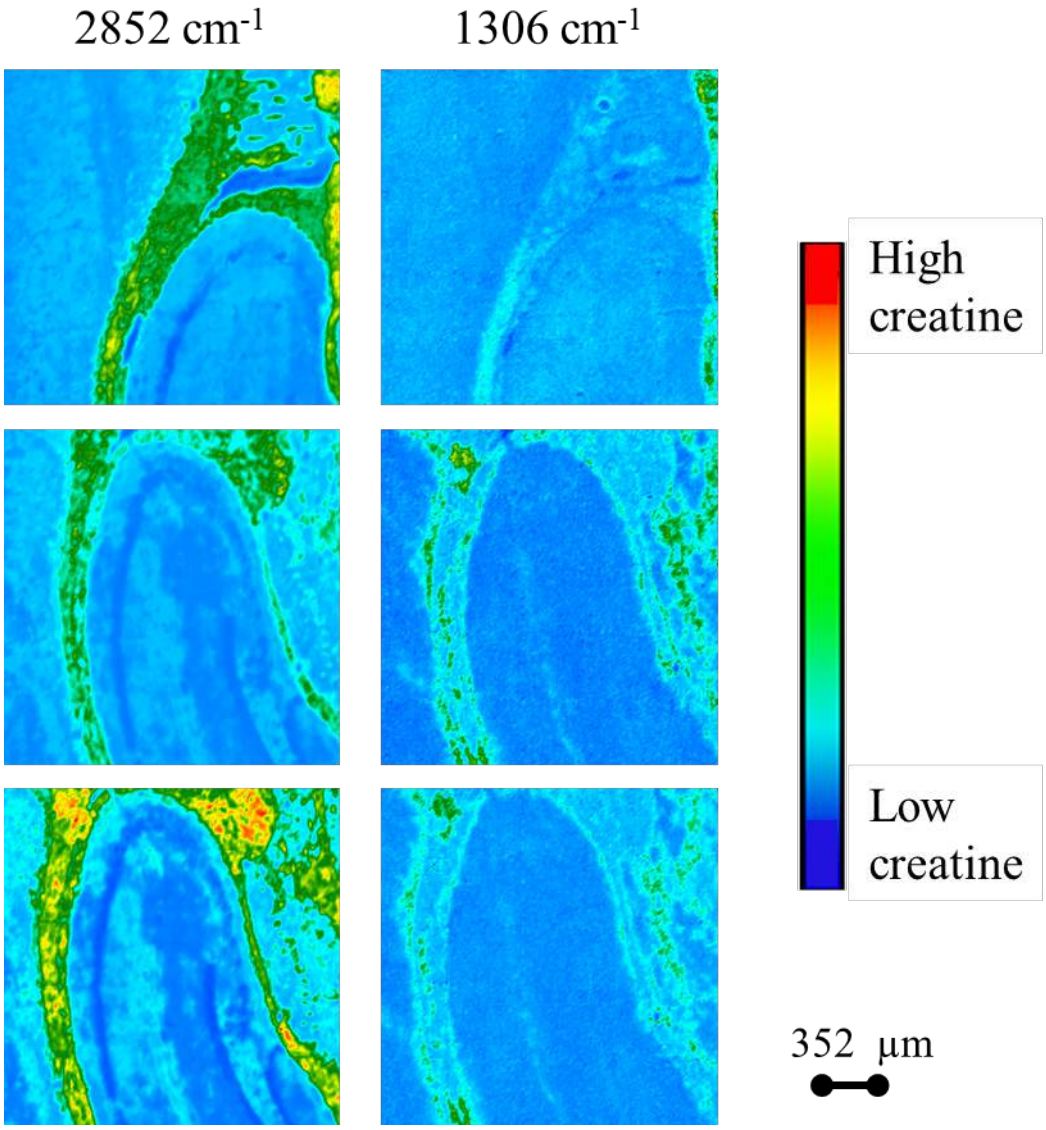

Figure 9.12. Creatine appearance in the hippocampus of 3xTg-448 (3xTg mouse on standard diet) acquired post a cycle of sheltered wind blowing. These sections were acquired when the cryostat cooler was on having wind blowing to brain tissue while it was covered/sheltered. The spectrochemical images were processed for distribution of lipids (2852 cm^{-1}) to establish tissue morphology and creatine (1306 cm^{-1}) to assess creatine localization. The image is processed with methods outlined in table 4.1. Upper scale 0.4320, Lower scale -0.0974.

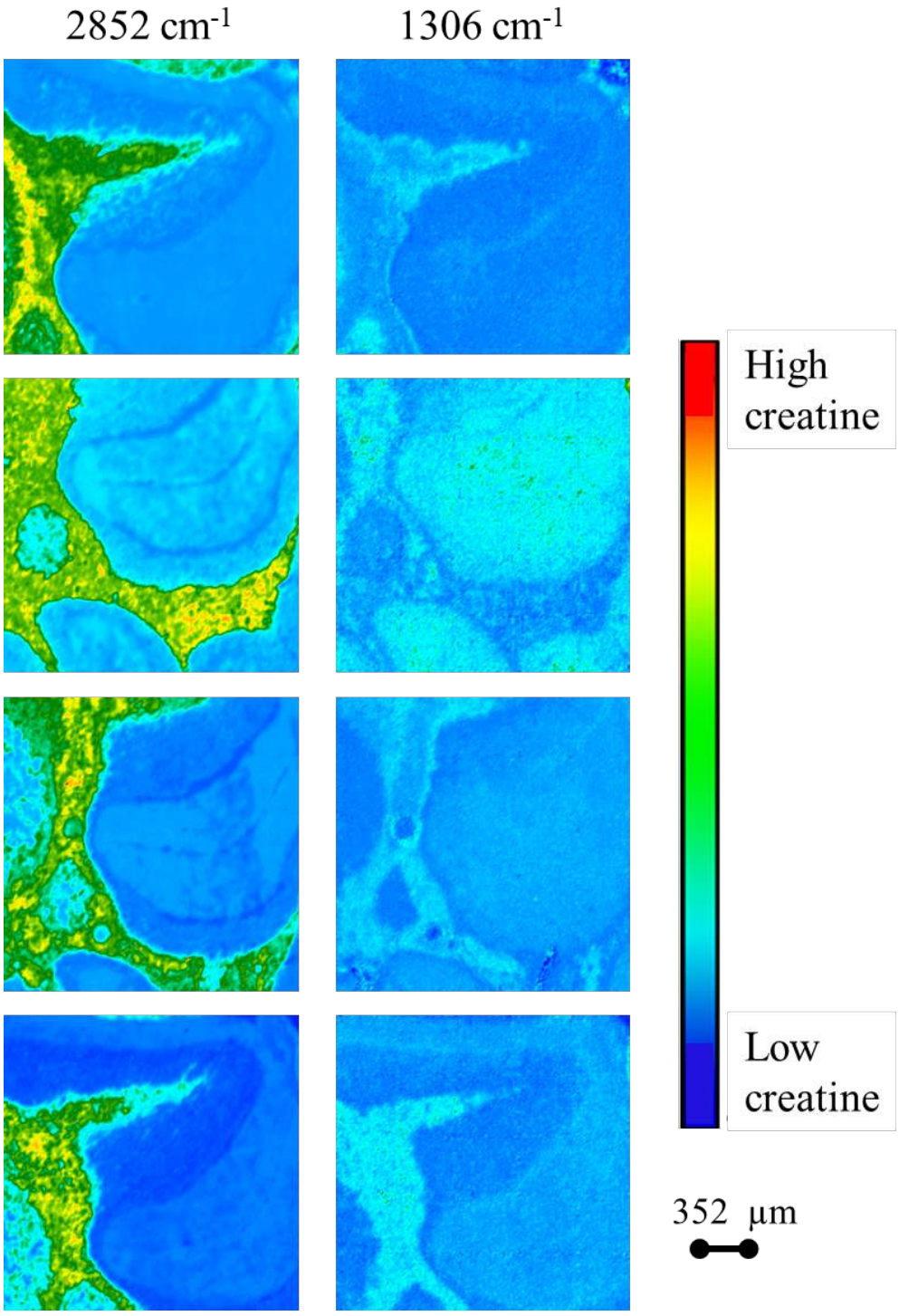

Figure 9.13. Creatine appearance in the cerebellum of 3xTg-448 (3xTg mouse on standard diet) acquired post a cycle of sheltered wind blowing. These sections were acquired when the cryostat cooler blowing wind on the brain tissue while covered/sheltered. The spectrochemical images were processed for distribution of lipids (2852 cm^{-1}) to establish tissue morphology and creatine (1306 cm^{-1}) to assess creatine localization. The image is processed with methods outlined in table 4.1. Upper scale 0.4320, Lower scale -0.0974.

References

2015 Alzheimer's disease facts and figures. (2015). *Alzheimer's & Dementia : The Journal of the Alzheimer's Association*, *11*(3), 332–384.

Adlimoghaddam, A., Snow, W. M., Stortz, G., Perez, C., Djordjevic, J., Goertzen, A. L., & Albensi, B. C. (2019). Regional hypometabolism in the 3xTg mouse model of Alzheimer's disease. *Neurobiology of disease*, *127*, 264-277.

Allen, P. J., DeBold, J. F., Rios, M., & Kanarek, R. B. (2015). Chronic high-dose creatine has opposing effects on depression-related gene expression and behavior in intact and sex hormone-treated gonadectomized male and female rats. *Pharmacology, Biochemistry, and Behavior*, *130*, 22–33.

Alzheimer's Association Canada. (2018). Retrieved from https://alzheimer.ca/en/Home/About-dementia/What-is-dementia/Dementia-numbers

Apostolova, L. G., Dinov, I. D., Dutton, R. A., Hayashi, K. M., Toga, A. W., Cummings, J. L., & Thompson, P. M. (2006). 3D comparison of hippocampal atrophy in amnestic mild cognitive impairment and Alzheimer's disease. *Brain : A Journal of Neurology*, *129*(Pt 11), 2867–2873.

Armstrong, R. A. (2011). The pathogenesis of Alzheimer's disease: a reevaluation of the "amyloid cascade hypothesis." *International Journal of Alzheimer's Disease*, *2011*, 1–6.

Association, A., & others. (2018). 2018 Alzheimer's disease facts and figures. *Alzheimer's & Dementia*, *14*(3), 367–429.

Baker, M. J., Trevisan, J., Bassan, P., Bhargava, R., Butler, H. J., Dorling, K. M., … others. (2014). Using Fourier transform IR spectroscopy to analyze biological materials. *Nature*

Protocols, *9*(8), 1771.

Bender, A., Auer, D. P., Merl, T., Reilmann, R., Saemann, P., Yassouridis, A., … others. (2005). Creatine supplementation lowers brain glutamate levels in Huntington's disease. *Journal of Neurology*, *252*(1), 36–41.

Benseny-Cases, N., Klementieva, O., Cotte, M., Ferrer, I., & Cladera, J. (2014). Microspectroscopy (muFTIR) reveals co-localization of lipid oxidation and amyloid plaques in human Alzheimer disease brains. *Analytical Chemistry*, *86*(24), 12047–12054.

Bloom, G. S. (2014). Amyloid-β and tau: the trigger and bullet in Alzheimer disease pathogenesis. *JAMA Neurology*, *71*(4), 505–508.

Brewer, G. J., & Wallimann, T. W. (2000). Protective effect of the energy precursor creatine against toxicity of glutamate and $β$-amyloid in rat hippocampal neurons. *Journal of Neurochemistry*, *74*(5), 1968–1978.

Bryant, C. D. (2011). The blessings and curses of C57BL/6 substrains in mouse genetic studies. *Annals of the New York Academy of Sciences*, *1245*, 31–33.

Bürklen, T. S., Schlattner, U., Homayouni, R., Gough, K., Rak, M., Szeghalmi, A., & Wallimann, T. (2006). The creatine kinase/creatine connection to Alzheimer's disease: CK-inactivation, APP-CK complexes and focal creatine deposits. *Journal of Biomedicine & Biotechnology*, *2006*(3), 35936.

Carroll, J. C., Rosario, E. R., Chang, L., Stanczyk, F. Z., Oddo, S., LaFerla, F. M., & Pike, C. J. (2007). Progesterone and estrogen regulate Alzheimer-like neuropathology in female 3xTg-AD mice. *The Journal of Neuroscience : The Official Journal of the Society for Neuroscience*, *27*(48), 13357–13365.

Cerf, E., Sarroukh, R., Tamamizu-Kato, S., Breydo, L., Derclaye, S., Dufrene, Y. F., …

Raussens, V. (2009). Antiparallel beta-sheet: a signature structure of the oligomeric amyloid beta-peptide. *The Biochemical Journal*, *421*(3), 415–423.

Chamberlain, K. A., Chapey, K. S., Nanescu, S. E., & Huang, J. K. (2017). Creatine enhances mitochondrial-mediated oligodendrocyte survival after demyelinating injury. *Journal of Neuroscience*, *37*(6), 1479–1492.

Chemistry, M. D. of. (n.d.). *Growing Quality Crystals*. Retrieved from https://web.mit.edu/x-ray/cystallize

Chiang, K., & Koo, E. H. (2014). Emerging therapeutics for Alzheimer's disease. *Annual Review of Pharmacology and Toxicology*, *54*, 381–405.

Choo, L. P., Wetzel, D. L., Halliday, W. C., Jackson, M., LeVine, S. M., & Mantsch, H. H. (1996). In situ characterization of beta-amyloid in Alzheimer's diseased tissue by synchrotron Fourier transform infrared microspectroscopy. *Biophysical Journal*, *71*(4), 1672–1679.

Correia, M., Lopes, J., Silva, R., Rosa, I., Henriques, A., Ivonne Delgadillo, S. O., & Nunes, A. (2016). FTIR Spectroscopy - A Potential Tool to Identify Metabolic Changes in Dementia Patients. *Journal Alzheimers Neurodegener*, *2*(2), 7–9.

Costantini, L. C., Barr, L. J., Vogel, J. L., & Henderson, S. T. (2008). Hypometabolism as a therapeutic target in Alzheimer's disease. *BMC Neuroscience*, *9*, S16.

Dong, S., Duan, Y., Hu, Y., & Zhao, Z. (2012). Advances in the pathogenesis of Alzheimer's disease: a re-evaluation of amyloid cascade hypothesis. *Translational Neurodegeneration*, *1*(1), 18.

Duff, K., & Suleman, F. (2004). Transgenic mouse models of Alzheimer's disease: how useful have they been for therapeutic development? *Briefings in Functional Genomics &*

Proteomics, *3*(1), 47–59.

Dyer, J. R. (1965). *Applications of absorption spectroscopy of organic compounds*. Englewood Cliffs, N.J.: Prentice-Hall.

El-Amouri, S. S., Zhu, H., Yu, J., Marr, R., Verma, I. M., & Kindy, M. S. (2008). Neprilysin: An enzyme candidate to slow the progression of Alzheimer's disease. *American Journal of Pathology*, *172*(5), 1342–1354.

Ellery, S. J., Walker, D. W., & Dickinson, H. (2016). Creatine for women: a review of the relationship between creatine and the reproductive cycle and female-specific benefits of creatine therapy. *Amino Acids*, *48*(8), 1807–1817.

Ellis, D. I., & Goodacre, R. (2006). Metabolic fingerprinting in disease diagnosis: biomedical applications of infrared and Raman spectroscopy. *The Analyst*, *131*(8), 875–885.

Findlay, C. R., Wiens, R., Rak, M., Sedlmair, J., Hirschmugl, C. J., Morrison, J., … Gough, K. M. (2015). Rapid biodiagnostic ex vivo imaging at 1 μm pixel resolution with thermal source FTIR FPA. *Analyst*, *140*(7), 2493–2503.

Frisoni, G. B., Fox, N. C., Jack, C. R., Scheltens, P., & Thompson, P. M. (2010). The clinical use of structural MRI in Alzheimer disease. *Nature Reviews Neurology*, *6*, 67–77.

Gallant, M., Rak, M., Szeghalmi, A., Del Bigio, M. R., Westaway, D., Yang, J., … Gough, K. M. (2006). Focally elevated creatine detected in amyloid precursor protein (APP) transgenic mice and Alzheimer disease brain tissue. *The Journal of Biological Chemistry*, *281*(1), 5–8.

Goate, A., Chartier-Harlin, M. C., Mullan, M., Brown, J., Crawford, F., Fidani, L., … Hardy, J. (1991). Segregation of a missense mutation in the amyloid precursor protein gene with familial Alzheimer's disease. *Nature*, *349*(6311), 704–706.

Griffiths, P. R., & De Haseth, J. A. (2006). Fourier Transform Infrared Spectrometry: Second

Edition. In *Fourier Transform Infrared Spectrometry: Second Edition*.

Hackett, M. J., Britz, C. J., Paterson, P. G., Nichol, H., Pickering, I. J., & George, G. N. (2015). In situ biospectroscopic investigation of rapid ischemic and postmortem induced biochemical alterations in the rat brain. *ACS Chemical Neuroscience*, *6*(2), 226–238.

Hackett, M. J., Lee, J., El-Assaad, F., McQuillan, J. A., Carter, E. A., Grau, G. E., … Lay, P. A. (2012). FTIR imaging of brain tissue reveals crystalline creatine deposits are an ex vivo marker of localized ischemia during murine cerebral malaria: General implications for disease neurochemistry. *ACS Chemical Neuroscience*, *3*(12), 1017–1024.

Hardy, J. A., & Higgins, G. A. (1992). Alzheimer's disease: The amyloid cascade hypothesis. *Science*, *256*(5054), 184–185.

Hardy, J., & Selkoe, D. J. (2002). The amyloid hypothesis of Alzheimer's disease: Progress and problems on the road to therapeutics. *Science*, *297*(5590), 2209.

Harris, F. M., Brecht, W. J., Xu, Q., Tesseur, I., Kekonius, L., Wyss-Coray, T., … Huang, Y. (2003). Carboxyl-terminal-truncated apolipoprotein E4 causes Alzheimer's disease-like neurodegeneration and behavioral deficits in transgenic mice. *Proceedings of the National Academy of Sciences*, *100*(19), 10966–10971.

Hatami, A., Albay, R. 3rd, Monjazeb, S., Milton, S., & Glabe, C. (2014). Monoclonal antibodies against Aβ42 fibrils distinguish multiple aggregation state polymorphisms in vitro and in Alzheimer disease brain. *The Journal of Biological Chemistry*, *289*(46), 32131–32143.

Heaney.P. (1997). Crystal growth-fast and slow. Retrieved from http://www.minsocam.org/msa/

Hellström-Lindahl, E., Ravid, R., & Nordberg, A. (2008). Age-dependent decline of neprilysin in Alzheimer's disease and normal brain: Inverse correlation with Aβ levels. *Neurobiology of Aging*, *21*(2), 210–221.

Hersh, L., & Rodgers, D. (2008). Neprilysin and Amyloid Beta Peptide Degradation. *Current Alzheimer Research*, *5*(2), 225–231.

Hirata-Fukae, C., Li, H.-F., Hoe, H.-S., Gray, A. J., Minami, S. S., Hamada, K., … Matsuoka, Y. (2008). Females exhibit more extensive amyloid, but not tau, pathology in an Alzheimer transgenic model. *Brain Research*, *1216*, 92–103.

Holden, A., & Morrison, P. (1999). *Crystals and crystal growing*. Cambridge, Mass: MIT Pr.

Holtzman, D. M. (2004). In vivo effects of ApoE and clusterin on amyloid-beta metabolism and neuropathology. *Journal of Molecular Neuroscience : MN*, *23*(3), 247–254.

Humm, A., Fritsche, E., Steinbacher, S., & Huber, R. (1997). Crystal structure and mechanism of human L-arginine:glycine amidinotransferase: A mitochondrial enzyme involved in creatine biosynthesis. *EMBO Journal*, *16*(12), 3373–3385.

Hussain, G., Anwar, H., Rasul, A., Imran, A., Qasim, M., Zafar, S., … Muhammad Umair, A. (2019). Lipids as biomarkers of brain disorders. *Critical Reviews in Food Science and Nutrition*, 1–24.

Jack, C. R., Albert, M. S., Knopman, D. S., McKhann, G. M., Sperling, R. A., Carrillo, M. C., … Phelps, C. H. (2011). Introduction to the recommendations from the National Institute on Aging-Alzheimer's Association workgroups on diagnostic guidelines for Alzheimer's disease. *Alzheimer's and Dementia*, *7*(3), 257–262.

Jack, C. R., Lowe, V. J., Weigand, S. D., Wiste, H. J., Senjem, M. L., Knopman, D. S., … Petersen, R. C. (2009). Serial PIB and MRI in normal, mild cognitive impairment and Alzheimers disease: Implications for sequence of pathological events in Alzheimers disease. *Brain*, *132*(5), 1355–1365.

Khamenehfar, A, (2011), Examination of creatine deposits and environs in TgCRND8 mouse

brain by Raman and FTIR microspectroscopy (Masters dissertation).

Kim, J., Basak, J. M., & Holtzman, D. M. (2009). The Role of Apolipoprotein E in Alzheimer's Disease. *Neuron*, *63*(3), 287–303.

Kitazawa, M., Medeiros, R., & Laferla, F. M. (2012). Transgenic mouse models of Alzheimer disease: developing a better model as a tool for therapeutic interventions. *Current Pharmaceutical Design*, *18*(8), 1131–1147.

Klivenyi, P., Ferrante, R. J., Matthews, R. T., Bogdanov, M. B., Klein, A. M., Andreassen, O. A., … Beal, M. F. (1999). Neuroprotective effects of creatine in a transgenic animal model of amyotrophic lateral sclerosis. *Nature Medicine*, *5*(3), 347–350.

Komatsu, H., Liu, L., Murray, I. V. J., & Axelsen, P. H. (2007). A mechanistic link between oxidative stress and membrane mediated amyloidogenesis revealed by infrared spectroscopy. *Biochimica et Biophysica Acta (BBA) - Biomembranes*, *1768*(8), 1913–1922.

Krafft, C., Neudert, L., Simat, T., & Salzer, R. (2005). Near infrared Raman spectra of human brain lipids. *Spectrochimica Acta. Part A, Molecular and Biomolecular Spectroscopy*, *61*(7), 1529–1535.

Kuzyk, A., Kastyak, M., Agrawal, V., Gallant, M., Sivakumar, G., Rak, M., … Gough, K. M. (2010). Association among amyloid plaque, lipid, and creatine in hippocampus of TgCRND8 mouse model for Alzheimer disease. *The Journal of Biological Chemistry*, *285*(41), 31202–31207.

Lambert, J. B., Shurvell, H. F., & Cooks, R. G. (1987). Introduction to Organic Spectroscopy. In *Introduction to Organic Spectroscopy*. Macmillan Publishing Company.

Langley, G. (2009). The validity of animal experiments in medical research.*The Humane Society Institute for Science and Policy – ASR, 1*, 161-168.

Larkin, P. (2011). Infrared and Raman Spectroscopy; Principles and Spectral Interpretation. In *Infrared and Raman Spectroscopy; Principles and Spectral Interpretation*.

Lasch, P., & Naumann, D. (2006). Spatial resolution in infrared microspectroscopic imaging of tissues. *Biochimica et Biophysica Acta (BBA) - Biomembranes*, *1758*(7), 814–829.

Lewis, E. N., Treado, P. J., Reeder, R. C., Story, G. M., Dowrey, A. E., Marcott, C., & Levin, I. W. (1995). Fourier Transform Spectroscopic Imaging Using an Infrared Focal-Plane Array Detector. *Analytical Chemistry*, *67*(19), 3377–3381.

Liu, C. C., Kanekiyo, T., Xu, H., & Bu, G. (2013). Apolipoprotein e and Alzheimer disease: Risk, mechanisms and therapy. *Nature Reviews Neurology*, *9*(2), 106–118.

Luo, Y., Bolon, B., Kahn, S., Bennett, B. D., Babu-Khan, S., Denis, P., … Vassar, R. (2001). Mice deficient in BACE1, the Alzheimer's β-secretase, have normal phenotype and abolished β-amyloid generation. *Nature Neuroscience*, *4*(3), 231–232.

Maeda, J., Ji, B., Irie, T., Tomiyama, T., Maruyama, M., Okauchi, T., … Suhara, T. (2007). Longitudinal, quantitative assessment of amyloid, neuroinflammation, and anti-amyloid treatment in a living mouse model of Alzheimer's disease enabled by positron emission tomography. *The Journal of Neuroscience : The Official Journal of the Society for Neuroscience*, *27*(41), 10957–10968.

Martin, M. (2013). Measuring Restriction Sizes Using Diffusion Weighted Magnetic Resonance Imaging: A Review. *Magnetic Resonance Insights*, *6*, 59–64.

Mastrangelo, M. A., & Bowers, W. J. (2008). Detailed immunohistochemical characterization of temporal and spatial progression of Alzheimer's disease-related pathologies in male triple-transgenic mice. *BMC Neuroscience*, *9*, 81.

Miller, L. M., Bourassa, M. W., & Smith, R. J. (2013). FTIR spectroscopic imaging of protein

aggregation in living cells. *Biochimica et Biophysica Acta*, *1828*(10), 2339–2346.

Movasaghi, Z., Rehman, S., & ur Rehman, D. I. (2008). Fourier Transform Infrared (FTIR) Spectroscopy of Biological Tissues. *Applied Spectroscopy Reviews*, *43*(2), 134–179.

Mudher, A., & Lovestone, S. (2002). Alzheimer's disease-do tauists and baptists finally shake hands? *Trends in Neurosciences*, *25*(1), 22–26.

Multiple Sclerosis. (2018). Retrieved August 6, 2018, from https://www.webmd.com/multiple-sclerosis/secondary-progressive-multiple-sclerosis#1

My-MS Prognosis. (2018). Retrieved August 1, 2018, from https://my-ms.org/ms_prognosis.html

Nelson, P. T., Braak, H., & Markesbery, W. R. (2009). Neuropathology and cognitive impairment in Alzheimer disease: a complex but coherent relationship. *Journal of Neuropathology and Experimental Neurology*, *68*(1), 1–14.

Oddo, S., Caccamo, A., Shepherd, J. D., Murphy, M. P., Golde, T. E., Kayed, R., … LaFerla, F. M. (2003). Triple-transgenic model of Alzheimer's Disease with plaques and tangles: Intracellular Aβ and synaptic dysfunction. *Neuron*, *39*(3), 409–421.

Oh, K.-J., Perez, S. E., Lagalwar, S., Vana, L., Binder, L., & Mufson, E. J. (2010). Staging of Alzheimer's pathology in triple transgenic mice: a light and electron microscopic analysis. *International Journal of Alzheimer's Disease*, *2010*.

Ohno, M., Sametsky, E. A., Younkin, L. H., Oakley, H., Younkin, S. G., Citron, M., … Disterhoft, J. F. (2004). BACE1 Deficiency Rescues Memory Deficits and Cholinergic Dysfunction in a Mouse Model of Alzheimer's Disease. *Neuron*, *41*(1), 27–33.

Otellin, V. A., Korzhevskii, D. E., Kostkin, V. B., Balestrino, M., Lensman, M. V, & Polenov, S. A. (2003). The neuroprotective effect of creatine in rats with cerebral ischemia. *Doklady*

Biological Sciences : Proceedings of the Academy of Sciences of the USSR, Biological Sciences Sections, *390*, 197–199.

Parker, F. S. (1983). *Applications of Infrared, Raman, and Resonance Raman Spectroscopy in Biochemistry*. Springer US.

Perkins, W. D. (1987). Fourier transform infrared spectroscopy. Part II. Advantages of FT-IR. *Journal of Chemical Education*, *64*(11), A269.

Price, D. L., & Sisodia, S. S. (1994). Cellular and molecular biology of Alzheimer's disease and animal models. *Annual Review of Medicine*, *45*, 435–446.

Rae, C., Digney, A. L., McEwan, S. R., & Bates, T. C. (2003). Oral creatine monohydrate supplementation improves brain performance: a double-blind, placebo-controlled, cross-over trial. *Proceedings. Biological Sciences*, *270*(1529), 2147–2150.

Rak, M., Del Bigio, M. R., Mai, S., Westaway, D., & Gough, K. (2007). Dense-core and diffuse Aβ plaques in TgCRND8 mice studied with synchrotron FTIR microspectroscopy. *Biopolymers*, *87*(4), 207–217.

Reffner, J. A. (1998). Instrumental factors in infrared microspectroscopy. *Cellular and Molecular Biology (Noisy-Le-Grand, France)*, *44*(1), 1–7.

Rocchi, A., Pellegrini, S., Siciliano, G., & Murri, L. (2003). Causative and susceptibility genes for Alzheimer's disease: a review. *Brain Research Bulletin*, *61*(1), 1–24.

Scheuner, D., Eckman, C., Jensen, M., Song, X., Citron, M., Suzuki, N., … Younkin, S. (1996). Secreted amyloid β–protein similar to that in the senile plaques of Alzheimer's disease is increased in vivo by the presenilin 1 and 2 and APP mutations linked to familial Alzheimer's disease. *Nature Medicine*, *2*(8), 864–870.

Selkoe, D. J. (1994). Normal and abnormal biology of the beta-amyloid precursor protein.

Annual Review of Neuroscience, *17*, 489–517.

Serrano-Pozo, A., Frosch, M. P., Masliah, E., & Hyman, B. T. (2011). Neuropathological alterations in Alzheimer disease. *Cold Spring Harbor Perspectives in Medicine*, *1*(1), a006189.

Shen, J., & Kelleher, R. J. 3rd. (2007). The presenilin hypothesis of Alzheimer's disease: evidence for a loss-of-function pathogenic mechanism. *Proceedings of the National Academy of Sciences of the United States of America*, *104*(2), 403–409.

Sherrington, R., Rogaev, E. I., Liang, Y., Rogaeva, E. A., Levesque, G., Ikeda, M., … St George-Hyslop, P. H. (1995). Cloning of a gene bearing missense mutations in early-onset familial Alzheimer's disease. *Nature*, *375*(6534), 754–760.

Skoczen, A., Setkowicz, Z., Janeczko, K., Sandt, C., Borondics, F., & Chwiej, J. (2017). The influence of high fat diets with different ketogenic ratios on the hippocampal accumulation of creatine - FTIR microspectroscopy study. *Spectrochimica Acta. Part A, Molecular and Biomolecular Spectroscopy*, *184*, 13–22.

Smith, A. D. (2002). Imaging the progression of Alzheimer pathology through the brain. *Proceedings of the National Academy of Sciences of the United States of America*, *99*(7), 4135–4137.

Snow, W. M., Cadonic, C., Cortes-Perez, C., Roy Chowdhury, S. K., Djordjevic, J., Thomson, E., … Albensi, B. C. (2018). Chronic dietary creatine enhances hippocampal-dependent spatial memory, bioenergetics, and levels of plasticity-related proteins associated with NF-κB. *Learning & Memory (Cold Spring Harbor, N.Y.)*, *25*(2), 54–66.

Somjen, D., Weisman, Y., Mor, Z., Harell, A., & Kaye, A. M. (1991). Regulation of proliferation of rat cartilage and bone by sex steroid hormones. *The Journal of Steroid Biochemistry and*

Molecular Biology, *40*(4–6), 717–723.

Stitt, D. M., Kastyak-Ibrahim, M. Z., Liao, C. R., Morrison, J., Albensi, B. C., & Gough, K. M. (2012). Tissue acquisition and storage associated oxidation considerations for FTIR microspectroscopic imaging of polyunsaturated fatty acids. *Vibrational Spectroscopy*, *60*, 16–22.

Sullivan, P. G., Geiger, J. D., Mattson, M. P., & Scheff, S. W. (2000). Dietary supplement creatine protects against traumatic brain injury. *Annals of Neurology*, *48*(5), 723–729.

Surewicz, W. K., Mantsch, H. H., & Chapman, D. (1993). Determination of protein secondary structure by Fourier transform infrared spectroscopy: A critical assessment. *Biochemistry*, *32*(2), 389–394.

Swerdlow, R. H. (2007). Pathogenesis of Alzheimer's disease. *Clinical Interventions in Aging*, *2*(3), 347–359.

Swerdlow, R. H., Burns, J. M., & Khan, S. M. (2014). The Alzheimer's disease mitochondrial cascade hypothesis: progress and perspectives. *Biochimica et Biophysica Acta*, *1842*(8), 1219–1231.

Tanaka, D., Nakada, K., Takao, K., Ogasawara, E., Kasahara, A., Sato, A., … Hayashi, J.-I. (2008). Normal mitochondrial respiratory function is essential for spatial remote memory in mice. *Molecular Brain*, *1*, 21.

Turner, P. R., O'Connor, K., Tate, W. P., & Abraham, W. C. (2003). Roles of amyloid precursor protein and its fragments in regulating neural activity, plasticity and memory. *Progress in Neurobiology*, *70*(1), 1–32.

Uhl, E. W., & Warner, N. J. (2015). Mouse models as predictors of human responses: evolutionary medicine. *Current Pathobiology Reports*, *3*(3), 219–223.

Vincent, T. J., Thiessen, J. D., Kurjewicz, L. M., Germscheid, S. L., Turner, A. J., Zhilkin, P., … Martin, M. (2010). Longitudinal Brain Size Measurements in App/Ps1 Transgenic Mice. *Magnetic Resonance Insights*, *4*, MRI.S5885.

Wallimann, T., Wyss, M., Brdiczka, D., Nicolay, K., & Eppenberger, H. M. (1992). Intracellular compartmentation, structure and function of creatine kinase isoenzymes in tissues with high and fluctuating energy demands: the "phosphocreatine circuit" for cellular energy homeostasis. *The Biochemical Journal*, *281*(1), 21–40.

Who Health Organization. (2017). Retrieved August 1, 2018, from http://www.who.int/features/factfiles/dementia/en/

Winton, M. J., Lee, E. B., Sun, E., Wong, M. M., Leight, S., Zhang, B., ... & Lee, V. M. Y. (2011). Intraneuronal APP, not free Aβ peptides in 3xTg-AD mice: implications for tau versus Aβ-mediated Alzheimer neurodegeneration.

Wolozin, B. (2004). Cholesterol and the biology of Alzheimer's disease. *Neuron*, *41*(1), 7–10.

Xu, Q., Li, Y., Cyras, C., Sanan, D. A., & Cordell, B. (2000). Isolation and characterization of apolipoproteins from murine microglia. Identification of a low density lipoprotein-like apolipoprotein J-rich but E-poor spherical particle. *The Journal of Biological Chemistry*, *275*(41), 31770–31777.

Zhang, S., & Rich, A. (1997). Direct conversion of an oligopeptide from a β-sheet to an α-helix: A model for amyloid formation. *Proceedings of the National Academy of Sciences*, *94*(1), 23–28.

Zohdi, V., Whelan, D. R., Wood, B. R., Pearson, J. T., Bambery, K. R., & Black, M. J. (2015). Importance of tissue preparation methods in FTIR micro-spectroscopical analysis of biological tissues: "traps for new users". *PloS One*, *10*(2), e0116491.